



The University of Sheffield

**Particle Characterisation in Chemical Looping
Combustion with Solid Fuels**

PhD Thesis

Submitted by:

Chern Yean Sim (BEng, Grad EI)

Supervisors: Professor Vida Sharifi, Professor Jim Swithenbank

Department of Chemical and Biological Engineering

March 2013

SUMMARY

It is well known that carbon dioxide (CO₂) is a greenhouse gas that contributes to global warming. Nowadays, a third of the worldwide anthropogenic CO₂ emissions arise from fossil fuel fired power production. Meanwhile, fossil fuels continue to be the main source of energy for the foreseeable future. The increasing threat posed by enhanced global warming, as well as the requirement for sustainable energy supplies around the world, have led to the development of several novel technologies to produce clean energy from fuels. Among these new technologies is chemical looping combustion (CLC) that uses a solid metal oxide (oxygen carrier) to react with fuels. This technology has the potential advantage that it produces a pure stream of CO₂ that can then be sequestered. In a CLC process, the oxygen carrier is reduced by fuels in one reactor while being oxidised by air in a separate reactor. As the oxygen carrier circulates through the system, it is subjected to morphological and compositional changes such as sintering, attrition and reactions between various metal oxides and fuels. These changes tend to cause the reactivity of the oxygen carrier to decrease over time.

The main objective of this PhD study was to investigate and characterise the morphological and compositional changes of the oxygen carrier particles after they have undergone multiple reduction oxidation cycles in a CLC system. A single fluidised bed system was used in this study. Fuel was fed into a bed of oxygen carrier consisting of mechanically mixed iron oxide or wet impregnated copper oxide supported on alumina. The bed was fluidised by a stream of CO₂ and/or steam. Pyrolysis gases from the fuel gasification process reduced the oxygen carrier while forming char in the bed. Thus char was oxidised and the oxygen carrier was regenerated when the fluidising gas was switched to air.

Five different types of fuels were initially used in the tests. They were lignite coal, lignite char, activated carbon, US bituminous coal and Taldinski bituminous coal. The rates of gasification of the bituminous coal and activated carbon were much slower than those of the lignite coal and lignite char, resulting in an unfavourably large accumulation of char during the reduction stage. Subsequent experiments were conducted with UK bituminous coal to determine the effect of ash on the oxygen carrier particles over a long operational period.

The series of analytical tests included; stereo microscopy, porosimetry analysis, X-ray diffraction (XRD), X-ray fluorescence (XRF), inductively coupled plasma mass spectrometry (ICP-MS), scanning electron microscopy with an energy dispersive system (SEM/EDS) and

X-ray photoelectron spectroscopy (XPS). Tests were performed on both the fresh and reacted oxygen carriers.

Analytical results showed that when the pyrolysis gases react with the oxygen carrier, mineral matter left behind from the gasification process will deposit on the surface of the particles and diffuse into the core of the particles. This is due to the fact that mineral matter has a higher melting point compared to iron oxide and copper oxide. Iron oxide and copper oxide diffusing to the surface of the particles will replace those that are lost via attrition. As a result, the composition of the surface of these particles remains relatively unchanged. As more mineral matter diffuses into the core of the oxygen carrier particles, they can segregate metal oxide molecules located at the surfaces from those located at the core of the particles. When this occurs, there is a possibility that the segregated material formed will reduce the ability of oxygen to diffuse to the surface of the oxygen carrier particles. Hence this will reduce the conversion of the pyrolysis gases. This will thus lead to the reduction in the conversion of the pyrolysis gas and possibly in the deactivation of the oxygen carrier.

It was found that the support structure played a key role in maintaining the structural integrity of the metal oxide particles during repeated reduction and oxidation cycles. Experimental results showed that the rate of attrition initially increases with time indicating that the oxygen carrier structure weakens as it interacts with the mineral matter in ash.

Results from this research study have shown that the semi-batch chemical looping combustion of solid fuels is feasible provided reactive fuels that produce a large quantity of pyrolysis gases are used. Less reactive fuels will lead to the accumulation of a large inventory of char in the bed. The slow rate of gasification of char will then result in a lower carbon capture efficiency. In order to operate a semi-batch chemical looping combustion system with solid fuel, temperatures of above 1000°C are most likely required. However, this would exclude metal oxides with low melting points to act as potential oxygen carriers and may cause other problems such as ash fusion. A possible solution is to gasify the solid fuels in a separate reactor and channel the resulting pyrolysis gases into the chemical looping combustion system.

ACKNOWLEDGEMENTS

First and foremost, the author would like to extend his sincere gratitude to EPSRC for providing financial support which this project would not have been possible.

The author would like to express grateful appreciations to his supervisors, Professor Jim Swithenbank and Professor Vida Sharifi, for their invaluable guidance, advice, encouragement and help throughout the project. Without their advices and constructive ideas, this project would not be successfully accomplished.

It is also the author's outmost gratitude to Dr Stuart Scott, Dr John Dennis and Tamaryn Brown (University of Cambridge) for their assistance during the experimental work conducted at the University of Cambridge during the first year of this study.

The author would also like to thank Dr. Markus Neuroth (RWE Power AG), Edward Jamieson and Richard Hotchkiss (RWE Power UK) and Terry Coupe (Maltby Colliery) for supplying the coal samples. Special thanks to Dr Frank Alber (SASOL Germany GmbH) for supplying the alumina extrudates used for the preparation of the copper oxide particles.

The author would like to thank Dr Claire Hurley (Sheffield Surface Analysis Centre), Mr Chris Hill (Biomedical Science Electron Microscopy Unit), Mr Andrew Fairburn (Kroto Research Institute), Mr Steve Coulson and Mr Pilkington (Micromeritics Limited), Dr Adrian Cunliffe (University of Leeds) and Mr Robert Burton (Sheffield Hallam University) for their expertise, help and guidance in the usage of the analytical instruments.

Finally, the author would like to thank Mr Mike O'Meara, David Palmer and Adrian Lumby for their help and guidance in the fabrication of the experimental reactor and during the commissioning of the fluidised bed reactor.

A special thanks as well to the author's family and his friends for their support, understanding, motivation and encouragements.

Contents

SUMMARY	i
ACKNOWLEDGEMENTS	iii
LIST OF FIGURES	viii
LIST OF TABLES	xii
NONCLEMENTURES	xiii
Chapter 1 INTRODUCTION	1
1.1 Energy Demand & Supply	1
1.2 Climate Change	3
1.3 Legislation	7
1.3.1 Kyoto Protocol	7
1.3.2 Climate Change Act 2008	8
1.3.3 Carbon Budgets	8
1.3.4 Energy Act 2008	9
1.3.5 Renewables Obligation	9
1.3.6 Renewable Energy Strategy	10
1.4 Catalysis	10
1.5 Statement of Problem Addressed in this Thesis	11
1.6 Research Objectives	12
1.7 Layout of Thesis	12
Chapter 2 LITERATURE REVIEW	15
2.1 CO ₂ Capture & Storage	15
2.1.1 Post Combustion Capture	16
2.1.2 Pre-Combustion Capture	20
2.1.3 Oxyfuel Combustion Capture	22
2.2 Chemical Looping Combustion	26
2.3 Oxygen Carriers	27
2.3.1 General Particle Characteristics	27
2.3.2 Oxygen Carriers Preparation Methodologies	30
2.4 Oxygen Carrying Capacity	35
2.5 Chemical Looping Combustion with Solid Fuels	38
Chapter 3 THEORETICAL STUDY	43
3.1 Fluidisation	43

3.2	Minimisation of Gibbs Free Energy	49
3.3	Oxygen Carrier Chemistry and Thermodynamics	56
3.3.1	Iron Oxide	56
3.3.2	Copper Oxide	62
3.4	Particle Reaction Mechanism.....	67
3.5	Metal Oxide Deactivation.....	71
3.6	Mechanism of Interaction between Metal Oxide with Coal and Ash	77
3.7	Mechanism of Interaction between Metal Oxide with Coal and Ash via Surface Melting	80
Chapter 4	EXPERIMENTAL SETUP 1.....	82
4.1	Experimental Setup 1	82
4.1.1	Tar Trap Condenser	85
4.1.2	External Heater	86
4.1.3	Screw Feeder.....	86
4.1.4	Thermocouples	86
4.1.5	Gas Analyser.....	86
4.1.6	PC & Data Logger	87
4.1.7	Gas Cylinders.....	87
4.2	Operating Conditions	87
4.3	Procedures	88
4.3.1	Start Up Procedure.....	88
4.3.2	Shut Down Procedure	90
4.3.3	Fuels Preparation	90
4.3.4	Char Preparation	90
4.4	Fuel Analysis.....	91
4.5	Conversion Calculation Methodology	93
4.6	Separation of Oxygen Carriers from Ash.....	95
4.7	Iron Oxide.....	97
4.7.1	Exit Gas Profiles Analysis.....	97
4.7.2	Iron Oxide Conversion Analysis	107
4.8	Copper Oxide	109
4.8.1	Exit Gas Profiles.....	109
4.8.2	Copper Oxide Conversion Analysis.....	116
Chapter 5	EXPERIMENTAL SETUP 2.....	118

5.1	Experimental Setup 2	118
5.1.1	Fluidised Bed Reactor.....	121
5.1.2	External Heaters.....	121
5.1.3	Screw Feeder.....	121
5.1.4	Condensers.....	121
5.1.5	Thermocouples	121
5.1.6	Gas Analyser.....	122
5.1.7	PC & Data Logger	122
5.1.8	Gas Cylinders.....	122
5.2	Operational Conditions	123
5.3	Operational Procedures	123
5.3.1	Start Up Procedures	123
5.3.2	Shut Down Procedures.....	125
5.4	Sample Preparation.....	126
5.4.1	Preparation of Iron Oxide Particles	126
5.4.2	Preparation of Copper Oxide Supported on Alumina Particles.....	126
5.4.3	Fuel Analysis.....	127
5.5	Experimental Measurement Accuracy	129
5.5.1	Temperature Measurement	129
5.5.2	Gas Measurement.....	129
5.6	Minimum Fluidisation and Pressure Drop Tests.....	130
5.7	Conversion Calculations	131
5.8	Operational Lifetime Analysis	133
5.8.1	Carbon Conversion Analysis	141
5.8.2	Porosimetry Analysis.....	144
5.8.3	X-Ray Diffraction Analysis.....	145
5.8.4	X-Ray Fluorescence Analysis.....	147
5.8.5	Inductive Coupled Plasma Mass Spectrometry Analysis.....	149
5.8.6	Metal Oxide Conversion Analysis	152
5.9	Summary	156
Chapter 6	ATTRITION	158
6.1	Mechanism of Attrition	158
6.2	Attrition of Carbon during Combustion and Gasification.....	160

6.3	Attrition of Oxygen Carriers	160
6.4	Modelling attrition in the Fluidized Bed.....	162
6.4.1	Time Dependence of Attrition.....	162
6.5	Attrition Measurement Methodology.....	165
6.6	Experimental Attrition Measurement	165
Chapter 7	SURFACE ANALYSIS	170
7.1	Carbon Deposition on Oxygen Carriers.....	170
7.2	Scanning Electron Microscopy	173
7.3	X-ray Photoelectron Spectroscopy	174
7.4	Iron Oxide.....	174
7.4.1	Scanning Electron Microscope Analysis	174
7.5	Copper Oxide	180
7.5.1	Cross-Sectional Scanning Electron Microscope Analysis.....	180
7.5.2	Energy Dispersive System Analysis.....	181
7.6	Iron Oxide X-Ray Photoelectron Spectroscopy Experiments	183
7.7	Copper Oxide X-Ray Photoelectron Spectroscopy Experiments	187
7.7.1	Carbon Calibration	187
7.7.2	Copper Oxide Calibration	187
7.7.3	Copper Oxide X-ray Photoelectron Spectroscopy Results.....	187
7.8	Summary.....	193
Chapter 8	CONCLUSIONS & FUTURE WORK	194
8.1	Conclusions	194
8.2	Future Work	197
REFERENCES	199
APPENDIX A	210
APPENDIX B	216
APPENDIX C	218

LIST OF FIGURES

Figure 1.1: World energy consumption from 1985 – 2010 in terms of million tonnes per oil equivalent (BP, 2011)	1
Figure 1.2: Comparison between consumption sources in 1973 and 2009 (BP, 2011)	2
Figure 1.3: Chemical looping combustion flowsheet (Johansson, 2007)	11
Figure 2.1: Amine scrubber flowsheet (Imperial, 2010)	16
Figure 2.2: Calcium looping flowsheet (Imperial, 2010)	18
Figure 2.3: Post combustion capture technology (SCCS, 2008)	19
Figure 2.4: Post combustion capture techniques (SCCS, 2008)	19
Figure 2.5: Hydrogen Production Flowsheet from Integrated Gasification Combined Cycle (IGCC) (Imperial, 2010)	21
Figure 2.6: Pre combustion capture technology (SCCS, 2008)	21
Figure 2.7: Pre combustion capture technique (SCCS, 2008)	22
Figure 2.8: Oxyfuel combustion flowsheet (Imperial, 2010)	22
Figure 2.9: Zero emission coal technology (ZECA) flowsheet (Imperial, 2010)	23
Figure 2.10: Oxyfuel combustion capture technology (SCCS, 2008)	25
Figure 2.11: Oxyfuel combustion capture technique (SCCS, 2008)	25
Figure 2.12: Chemical looping combustion flowsheet (Johansson, 2007)	26
Figure 2.13: Amount of active material for different unsupported oxygen carriers (Johansson, 2007)	36
Figure 2.14: Log K as a function of 1/T in the temperature range of 600-1200°C for different metal oxide systems (Mattisson and Lyngfelt, 2001)	37
Figure 2.15: Conversion of CH ₄ to CO ₂ as a function of temperature for different oxygen carriers (Mattisson and Lyngfelt, 2001)	37
Figure 2.16: System configuration for the pilot-scale chemical looping combustion process of solid fuels (Cao and Pan, 2006; Cao et al., 2006)	40
Figure 2.17: Principal layout of the fuel reactor with the particle circulation directions (Berguerand and Lyngfelt, 2008)	41
Figure 3.1: Pressure drop against gas velocity for a bed of uniformly sized particles (Kunii and Levenspiel, 1977)	45
Figure 3.2: Ellingham diagram for the reduction of iron oxide	58
Figure 3.3: Equilibrium ratio for the reduction of iron oxide in syngas	59
Figure 3.4: Equilibrium constant for the reduction of iron oxide with methane	60
Figure 3.5: Ellingham diagram for the reduction of copper oxide	64
Figure 3.6: Equilibrium ratio for the reduction of copper oxide in syngas	65
Figure 3.7: Equilibrium constant for the reduction of copper oxide with methane	65
Figure 3.8: Mechanism of sintering (Caillet and Harrison, 1982)	75
Figure 3.9: Interparticle neck shape: (1) Diffusion in gas phase; (2) Surface diffusion; (3) Volume diffusion (Bailliez and Nzihou, 2004)	75
Figure 3.10: Reactions during reduction stage	78
Figure 3.11: Initial reduction stage	78
Figure 3.12: Initial oxidation stage	79
Figure 3.13: Complete reoxidation	79

Figure 3.14: Mixing during reduction stage	79
Figure 3.15: Reactions during reduction stage	81
Figure 3.16: Complete reoxidation	81
Figure 3.17: Initial reduction stage and the formation of the quasi-liquid layer	81
Figure 3.18: Initial oxidation stage	81
Figure 4.1: Schematic diagram of the experimental setup.....	82
Figure 4.2: Layout of the system	83
Figure 4.3: Layout of the fluidised bed	84
Figure 4.4: Reacted copper oxide particles' smoothness	96
Figure 4.5: Reacted copper oxide particles' circularity	97
Figure 4.6: Exit gas profile for the 1 st , 10 th and 20 th reaction cycle between iron oxide and lignite char.....	98
Figure 4.7: Exit gas profile for 1 st , 10 th and 20 th reaction cycle between iron oxide and lignite coal	99
Figure 4.8: Exit gas profile for 1 st , 10 th and 20 th reaction cycle between iron oxide and Taldinski bituminous coal	100
Figure 4.9: Exit gas profile for 1 st , 10 th and 20 th reaction cycle between iron oxide and activated carbon.....	101
Figure 4.10: Feeding rates for the different types of fuels for the iron oxide system	106
Figure 4.11: Iron oxide conversion for different fuels system during reduction	108
Figure 4.12: Iron oxide conversion for different fuels system during oxidation	108
Figure 4.13: Exit gas profile for the 1 st , 10 th and 20 th reaction cycle between copper oxide and lignite char.....	110
Figure 4.14: Exit gas profile for the 1 st , 10 th and 20 th reaction cycle between copper oxide and lignite coal	111
Figure 4.15: Exit gas profile for the 1 st , 10 th and 20 th reaction cycle between copper oxide and activated carbon	112
Figure 4.16: Feeding rates for the different types of fuels for the copper oxide system	115
Figure 4.17: Copper oxide conversion for different fuels system during reduction	117
Figure 4.18: Copper oxide conversion for different fuels system during oxidation.....	117
Figure 5.1: Schematic diagram of the experimental setup	118
Figure 5.2: Experimental Setup	119
Figure 5.3: Fluidised bed reactor	120
Figure 5.4: Pressure drop variation in the fluidised bed for setup	130
Figure 5.5: Exit gas profile for the first five reaction cycles between iron oxide and UK bituminous coal.....	134
Figure 5.6: Exit gas profile for cycles 56 to 60 between iron oxide and UK bituminous coal...	134
Figure 5.7: Iron oxide after 30 reaction cycles	135
Figure 5.8: Iron oxide after 60 reaction cycles	135
Figure 5.9: Fresh iron oxide	135
Figure 5.10: Exit gas profile for the first five reaction cycles between copper oxide and UK bituminous coal.....	136
Figure 5.11: Exit gas profile for reaction cycles 206 till 210 between copper oxide and UK bituminous coal.....	136

Figure 5.12: Copper oxide (60 cycles)	137
Figure 5.13: Copper oxide (150 cycles)	137
Figure 5.14: Copper oxide (30 cycles)	137
Figure 5.15: Copper oxide (120 cycles)	137
Figure 5.16: Fresh copper oxide	137
Figure 5.17: Copper oxide (90 cycles)	137
Figure 5.18: Copper oxide (210 cycles)	138
Figure 5.19: Copper oxide (240 cycles)	138
Figure 5.20: Copper oxide (180 cycles)	138
Figure 5.21: Carbon conversion during reduction for iron oxide	143
Figure 5.22: Carbon conversion during reduction for copper oxide	143
Figure 5.23: Iron oxide conversion	153
Figure 5.24: Copper oxide conversion	153
Figure 6.1: Amount of iron oxide in the bed with increasing number of reaction cycle	165
Figure 6.2: Amount of copper oxide in the bed with increasing number of reaction cycle	166
Figure 7.1: SEM image of fresh iron oxide particles	175
Figure 7.2: Magnified SEM image of fresh iron oxide particle	175
Figure 7.3: SEM image of reacted iron oxide particles after 30 cycles	175
Figure 7.4: Magnified SEM image of reacted iron oxide particles after 30 cycles	175
Figure 7.5: SEM image of reacted iron oxide particles after 20 cycles and the location of Spectrum 1	176
Figure 7.6: SEM image of reacted iron oxide particles after 20 cycles and the location of Spectrum 2	176
Figure 7.7: Energy dispersive system for spectrum 1	176
Figure 7.8: Energy dispersive system for spectrum 2	177
Figure 7.9: SEM image of reacted iron oxide particles after 20 cycles and the location of Spectrum 1	178
Figure 7.10: SEM image of reacted iron oxide particles after 20 cycles and the location of Spectrum 2	178
Figure 7.11: Energy dispersive system for spectrum 1	178
Figure 7.12: Energy dispersive system for spectrum 2	179
Figure 7.13: Cross-sectional SEM image of reacted copper oxide particles after 30 cycles	180
Figure 7.14: Magnified cross-sectional SEM image of reacted copper oxide particles after 30 cycles	180
Figure 7.15: Cross-sectional SEM image of reacted copper oxide particles after 30 cycles	180
Figure 7.16: Magnified cross-sectional SEM image of reacted copper oxide particles after 30 cycles	180
Figure 7.17: Cross-sectional SEM image of fresh copper oxide particles	181
Figure 7.18: Oxygen mapping of fresh copper oxide particles	181
Figure 7.19: Aluminium mapping of fresh copper oxide particles	181
Figure 7.20: Copper mapping of fresh copper oxide particles	181
Figure 7.21: Cross-sectional SEM image of reacted copper oxide particles after 30 cycles	182
Figure 7.22: Oxygen mapping of reacted copper oxide particles after 30 cycles	182
Figure 7.23: Aluminium mapping of reacted copper oxide particles after 30 cycles	183

Figure 7.24: Copper mapping of reacted copper oxide particles after 30 cycles	183
Figure 7.25: XPS data for fresh and reacted iron oxide.....	184
Figure 7.26: Carbon calibration for copper oxide	188
Figure 7.27: Copper oxide calibration	189
Figure 7.28: XPS data for fresh and reacted copper oxide.....	190

LIST OF TABLES

Table 2.1: Oxygen carrying capacity for different metal/metal oxide pairs (Hossain and de Lasa, 2008)	36
Table 4.1: Fluidised bed reactor design and operational parameters	85
Table 4.2: ABB EL3020 Detection Range	86
Table 4.3: Operating conditions of the fluidised bed reactor	88
Table 4.4: Proximate and ultimate analyses of fuels	91
Table 4.5: Inductive Coupled Plasma Mass Spectrometry of fuels' ashes	92
Table 4.6: Carbon accumulation in fluidized bed	106
Table 4.7: Feeding rates for iron oxide systems	107
Table 4.8: Feeding rates for copper oxide systems	116
Table 5.1: ADC MGA 3000 Detection Range	122
Table 5.2: Operating conditions of the fluidised bed reactor	123
Table 5.3: Proximate and ultimate analyses of fuels	127
Table 5.4: Inductive Coupled Plasma Mass Spectrometry of fuels' ashes	128
Table 5.5: Porosimetry analysis for fresh and reacted iron oxide particles	144
Table 5.6: Porosimetry analysis for fresh and reacted copper oxide particles	145
Table 5.7: XRD analysis for fresh and reacted iron oxide particles	146
Table 5.8: XRD analysis for fresh and reacted copper oxide particles	146
Table 5.9: XRF analysis of fresh and reacted iron oxide particles	148
Table 5.10: XRF analysis of fresh and reacted copper oxide particles	148
Table 5.11: ICP-MS analysis for fresh and reacted iron oxide particles	150
Table 5.12: ICP-MS analysis of fresh and reacted copper oxide particles	151
Table 6.1: Factors affecting attrition in a fluidized bed (Ray et al. 1987)	159
Table 6.2: Mechanical and redox characteristics of oxygen carriers (Erri and Varma, 2007) ..	161
Table 7.1: Atomic percent of components on the surface of fresh and reacted iron oxide particles	185
Table 7.2: Weight percent of components on the surface of fresh and reacted iron oxide particles	185
Table 7.3: Atomic percent of components on the surface of fresh and reacted copper oxide particles	191
Table 7.4: Weight percent of components on the surface of fresh and reacted copper oxide particles	191

NONCLEMATURES

Symbols

α	=	amount of newly formed debris per unit breaking energy
a_{ij}	=	total number of atoms of element j in species i
A_t	=	cross-sectional area of bed, m^2
C_d	=	orifice coefficient
c_p	=	overall change in the heat capacity
d_p	=	diameter of particle, m
E_b	=	breakage energy, kJ
e_j	=	total number of moles of element j in the mixture, mol
E_k	=	mechanical energy input, kJ
f_i	=	fugacity of species i in the mixture, bar
f_i^0	=	fugacity of pure species i at reference state, bar
$F_{mo,in}$	=	molar flowrate of Me_xO_y in the reducing reactor, $mol\ s^{-1}$
Fr	=	Froude number
g	=	gravity, $m\ s^{-2}$
G	=	total Gibbs free energy of the system, $J\ mol^{-1}$
g_c	=	gravity conversion factor
G_{fi}^0	=	free energy of formation of species i , $J\ mol^{-1}$
G_i	=	molar free energy of species I, J , $J\ mol^{-1}$
G_i^0	=	standard molar Gibbs free energy of the pure species I, J , $J\ mol^{-1}$
G_{rxn}^0	=	standard Gibbs free energy of reaction, $J\ mol^{-1}$
H^{fuel}	=	heat of formation of fuel at 298 K, $J\ mol^{-1}$
H_i	=	molar enthalpy of species I, J , $J\ mol^{-1}$
$H_r(T)$	=	heat of reaction at the reducing reactor temperature calculated per $mol\ Me_xO_y$ reacted, $J\ mol^{-1}$
$H_r(T)$	=	heat of reaction at the reference temperature calculated per $mol\ Me_xO_y$ reacted, $J\ mol^{-1}$
k_a	=	attrition constant
K	=	equilibrium constant

L	=	length of fluidised bed, m
L_{mf}	=	height of bed at minimum fluidisation, m
m_a	=	empirical constant
n_i	=	number of moles of species i, mol
n_{tot}	=	total number of moles in the system, mol
P^0	=	referenced pressure, bar
Q_E	=	heat added or removed from the system, J mol ⁻¹
R	=	universal gas constant, J mol ⁻¹ K ⁻¹
Re_p	=	particle Reynolds number
T_R	=	reference temperature, K
u_0	=	superficial gas velocity, m s ⁻¹
U_E	=	excess gas velocity, m s ⁻¹
u_{mf}	=	superficial gas velocity at minimum fluidising velocity, m s ⁻¹
u_t	=	terminal velocity, m s ⁻¹
U_y	=	threshold velocity, m s ⁻¹
v_i	=	stoichiometric coefficient of species i
W	=	mass of particles in the bed, kg
W_0	=	initial mass of the particles in the bed at time t = 0, kg
x_f	=	weight fraction of the fines
y_i	=	mole fraction of species i
β_a	=	rate of degradation of the material
ϵ_m	=	voidage
ϵ_{mf}	=	voidage at minimum fluidization
η	=	efficiency of energy transformation from kinetic to breakage
θ	=	conversion
μ	=	viscosity of gas, kg m ⁻¹ s ⁻¹
ρ_g	=	gas density, kg m ⁻³
ρ_s	=	solids density, kg m ⁻³
τ_a	=	attrition rate constant
ϕ_a	=	material property of attrition

ϕ_i	=	fugacity coefficient
ϕ_i	=	ratio of the moles of incoming species i to the moles of Me_xO_y entering the reducing reactor
ϕ_s	=	sphericity of a particle

Abbreviations

BET	Theory of Brunauer, Emmett and Teller
BJH	Theory of Barret, Joyner and Halenda
CLC	Chemical looping combustion
EDS/EDX	energy dispersive system
HFC	hydrofluorocarbon
HHV	Higher heating value
ICP-MS	inductive coupled plasma mass spectrometry
IGCC	Integrated gasification combined cycle
MEA	monoethanolamine
SEM	scanning electron microscope
STP	standard temperature and pressure
XPS	X-ray photoelectron spectroscopy
XRD	X-ray diffraction
XRF	X-ray fluorescence
Ag	Silver
Al	Aluminium
Al_2O_3	Alumina
As	Arsenic
B	Boron
Ba	Barium
BaO	Barium oxide
Be	Beryllium
Bi	Bismuth
C	Carbon

Ca	Calcium
CaCO ₃	Calcium carbonate
CaO	Calcium oxide/Quicklime
Cd	Cadmium
CH ₄	Methane
Co	Cobalt
CO	Carbon monoxide
CO ₂	Carbon dioxide
Cr	Chromium
Cu	Copper
CuO	Copper oxide
Fe	Iron
Fe ₂ O ₃	Iron oxide
Ga	Gallium
H ₂	Hydrogen
H ₂ O	Steam
He	Helium
K	Potassium
K ₂ O	Potassium oxide
Li	Lithium
Mg	Magnesium
MgO	Magnesium oxide
Mn	Manganese
MnO	Manganese oxide
Mo	Molybdenum
Na	Sodium
Na ₂ O	Sodium oxide
Ni	Nickel
NiO	Nickel oxide
O	Oxygen atom

O ₂	Oxygen molecule
P ₂ O ₅	Phosphorus pentoxide
Pb	Lead
Rb	Rubidium
Se	Selenium
Si	Silicon
SiO ₂	Silicon dioxide
SO ₂	Sulphur dioxide
SO ₃	Sulphur trioxide
Sr	Strontium
Te	Tellurium
Ti	Titanium
TiO ₂	Titanium dioxide
Tl	Thallium
U	Uranium
V	Vanadium
Zn	Zinc

Chapter 1 INTRODUCTION

1.1 Energy Demand & Supply

It has been projected that about two-thirds of the increase in world primary energy demand between 2002 and 2030 will come from developing countries. Besides that, increasing demand and the shifting geographical location of available reserves will result in significant increases in oil and gas trade. It is projected that oil will continue to dominate international trade and gas imports are expected to rapidly increase. Although this will enhance prosperity and security in the exporting countries, it may adversely affect energy security in importing countries due to increased dependence on imports from a limited, and potentially unstable, supply. In contrast, many countries enjoy sizeable indigenous coal resources while others are able to take advantage of a diverse, rapidly growing and well-supplied international market (ASPI, 2007).

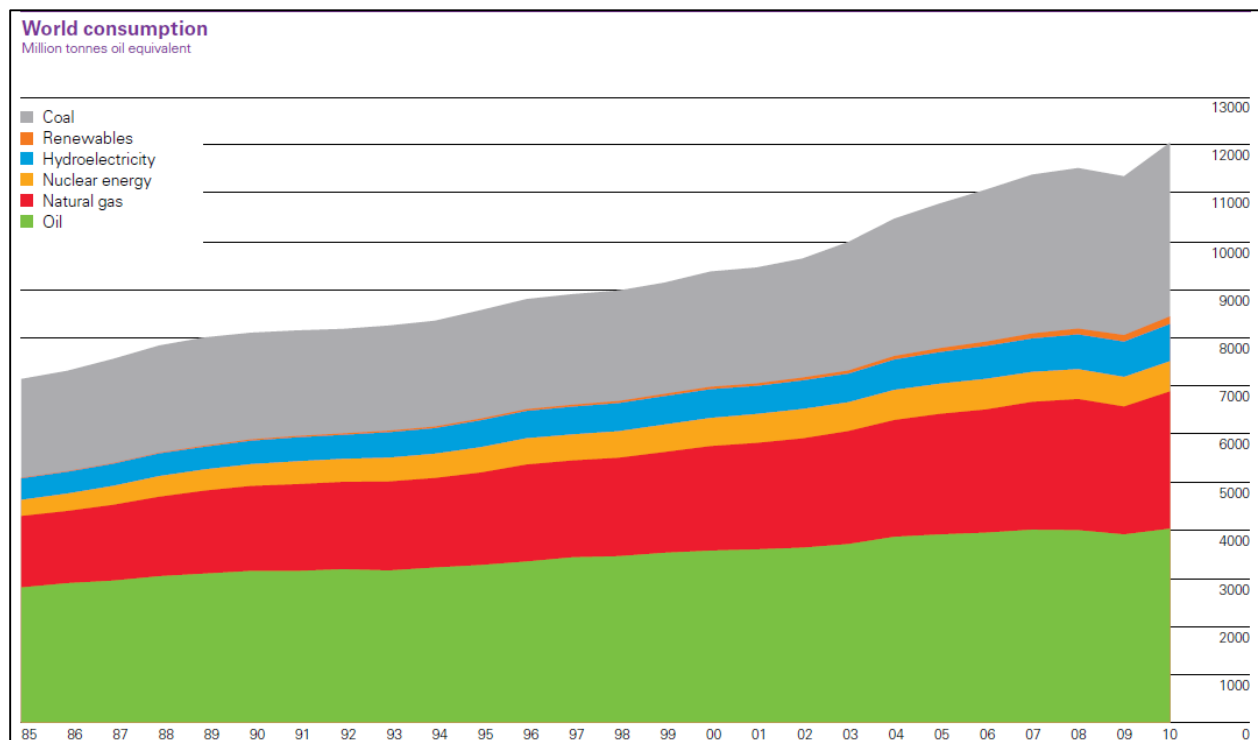


Figure 1.1: World energy consumption from 1985 – 2010 in terms of million tonnes per oil equivalent (BP, 2011)

Figure 1.1 shows that the world primary energy consumption from 1985 to 2010. It can be seen in Figure 1.1 that energy consumption in 2010 grew by 5.6% compared to 2009. Energy consumption through sources such as oil, natural gas, coal, nuclear, hydroelectricity and renewables continue to rise at a rapid pace for power generation. Oil remains the dominant fuel (33.6% of the global total), but has lost its market share over the years and this is exemplified in Figure 1.2. Figures 1.1 and 1.2 also indicate that the share of coal and natural gas in total energy consumption is rising and is projected to continue rising in the near future.

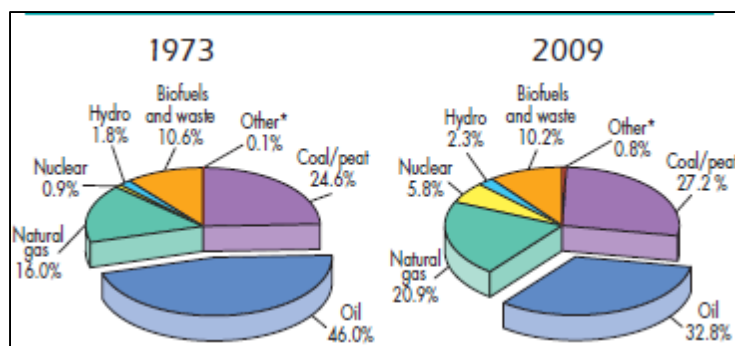


Figure 1.2: Comparison between consumption sources in 1973 and 2009 (BP, 2011)

There are many drivers governing the secure supply of energy. Different sources of energy meet different needs – some are best suited to base load generation, others to peaking, and others to meet environmental considerations. A diverse mix is one way to ensure security of supply. Coal has particular attributes that make a positive contribution to energy security as part of a balanced energy mix. However, coal faces environmental challenges, but through the development and use of clean coal technologies these challenges can be addressed (ASPI, 2007).

The use of a wide range of clean coal technologies enables economies to provide an affordable, reliable and environmentally acceptable supply of electricity as part of a diverse energy mix – reducing energy poverty, providing the means for economic and social development, and enhancing industrial competitiveness (ASPI, 2007).

However, energy demands and the related level of CO₂ emissions are closely linked to population and economic growth. The International Energy Agency has projected that the global population will grow by, on average, 1% per annum, from 6.4 billion in 2005 to 8.2 billion in 2030. At the same time, the world's average Gross Domestic Product (GDP) is expected to grow by, on average, 3.6% per annum. This currently translates to an increase in the total demand for energy of 55% over the same time period.

1.2 Climate Change

Since observation of the planet environment was first recorded about 150 years ago, it has been found that the climate has changed over the course of 150 years in many ways. Some of the evidences include (Imperial, 2010):

- The global average surface temperature has increased by about 0.6°C
- The temperatures in the lowest 8km of the atmosphere has increased
- Snow cover and ice extent have decreased
- Global sea level has increased by about 10 to 20 cm
- Increased precipitation and cloud cover at mid-high latitudes
- More severe and frequent occurrence of droughts
- Increase in occurrence of low temperature events

There are several greenhouse gases proceeding from human activities, each one presenting different global warming potential (GWP). The concept of GWP takes account of the gradual increase in concentration of a trace gas with time, its greenhouse effect whilst in the atmosphere and the time period over which climatic changes occur. The main gases affecting the greenhouse effect are H₂O, CO₂, CH₄, N₂O, CFC's and SF₆. The contribution to the global greenhouse effect of the different gases is related to their GWP and to the concentration in the atmosphere at a given time.

It has been known that carbon dioxide, CO₂, is a greenhouse gas that contributes to the warming of the earth. CO₂ is a naturally occurring gas that helps to regulate the temperature on earth as CO₂ and other greenhouse gases act as a protecting layer in the troposphere that

prevents most of the outgoing long-wave radiation from the earth from leaving the atmosphere. The greenhouse effect is a phenomenon in which water vapour, CO₂, methane and other atmospheric gases absorb outgoing infrared radiation and cause a rise in temperature. However, the amount of CO₂ in the atmosphere has risen to such high levels in the past few decades that the earth's surface and lower atmosphere are warming at a high rate. The temperature increase is believed to be associated with the fact that CO₂ is an anthropogenic gas. The concentration of CO₂ in the atmosphere today has risen to a value of about 380 ppm which is more than 30% higher than the pre-industrial value of about 280 ppm (Benson and Surles, 2006; Socolow, 2005; IPCC, 2007).

It has also been observed that the climate change is affecting biological and physical systems. Some evidences include (Imperial, 2010):

- Thawing of permafrost
- Reduced season of lake surface freezing
- Extension of mid latitude growing seasons
- Earlier flowering of plants
- Pole ward extension of plant and animal ranges
- Loss of some species

Climate models have been used to produce quantitative information about the possible future scenarios if the planet continues to undergo warming at the current rate. These data can be combined with the general information on the consequences of climate change has on the planet in order to predict the possible consequences of climate change (Imperial, 2010). It was deduced that natural and biological systems are vulnerable to the effects of climate change as they lack the ability to adapt quickly. The consequence of continued warming will result in the extinction of many species and damage to some of the planets' key habitats such as coral reefs, tropical forests and glaciers, resulting in the possible collapse of large ecosystems. Besides that, human systems will also be affected by climate change. This is because climate change will decrease water resources, agriculture and energy production (Imperial, 2010).

All the evidence above suggest that the Earth is vulnerable to a sudden and irreversible change and therefore immediate action is required in order to mitigate the effects of climate change. One of the main actions being taken at the moment is that policies and agreements are being implemented in order to mitigate the effects of climate change (Imperial, 2010).

As energy demand is closely associated with gross domestic product (GDP), it is very likely that the demand for energy will continue to increase in the future as an effect of economic growth in developing countries as well as developed countries (Benson and Surles, 2006; IPPC, 2005, 2007; Lindeberg, 1999). In order to meet the increasing energy demand while decreasing the CO₂ emissions, these following general routes were proposed (Yamsaki, 2003; Pacala and Socolow, 2004; IPPC, 2005):

- Increase the efficiency of energy conversion and increase the efficiency in energy usage
- Increase the sequestering of CO₂ from the atmosphere by extending biological sinks such as afforestation
- Switching to fuels with a higher proportion of hydrogen to carbon than coal, e.g. natural gas, nuclear and renewables
- Increasing the use of renewable energy and nuclear energy
- Capturing and storing the CO₂ from the generation of energy
- Movement towards sustainable technologies and renewable energies which produce less carbon dioxide
- Adaptation of lifestyles to reduce waste
- Enhancing carbon sinks such as forests by planting more trees and reducing the scale of deforestation
- Tighter government regulations on areas such as energy production, construction and transportation in order to improve energy efficiency
- Introduction of schemes such as carbon trading
- Imposing stricter conservation guidelines to help as far as possible to preserve and enhance ecosystems and habitats

- Providing support for less economically developed countries to overcome the issues such as poverty, welfare and health that would otherwise leave them vulnerable to the effects of climate change
- Preparing for future scenarios through programmes such as flood defences, stock piling vaccine, city planning and refugee support
- Continuing research into the causes and effects of climate change in order to continuously refine climate change mitigation policy

It was reported that a third of the global anthropogenic CO₂ emissions come from fossil fuel fired power production and about a fifth arises from the transportation sector (Yamasaki, 2003; IEA, 2007). There are major structural differences between these sources of CO₂. In the transport sector, these emissions are divided into numerous mobile sources and each of these releases a relatively small amount of CO₂. It is not feasible to capture CO₂ from each vehicle and hence, to reduce emissions from the transport sector a change to renewable fuels, hydrogen or electricity is necessary. To avoid net emissions of CO₂, hydrogen and electricity as fuels for vehicles need to be produced from non-fossil energy sources, or at large fossil fuel plants where the CO₂ could be captured and stored (Lindeberg, 1999).

Similarly, in the domestic sector it does not seem to be technically and economically feasible to install capture technology on small heating units. As with the transportation sector, a change in energy supply (e.g. to district heating or heat pumps) could improve the possibilities for limiting CO₂ emissions. For the power production sector, the conditions are quite the opposite and therefore a change of fuel does not necessarily need to take place. The sources are stationary and usually very large, which facilitates collection and transport of CO₂. For energy intensive industry such as ammonia production, oil refining, cement or gas processing, a way to sequester and limit CO₂ emissions could be useful (Socolow, 2005; Davidson and Thambimuthu, 2004; Lindeberg, 1999).

Some advances have already been made. For example, currently, coal-fired power stations predominantly employ pulverised fuel boilers. Plants with supercritical steam operating at up to 565°C have been operating for many years. They have higher efficiency than the older

subcritical plants with the same steam temperatures. Materials advances are now permitting steam temperatures to be raised and supercritical plants with steam conditions of about 275 bar, 580 – 600 °C or higher and efficiencies over 45% are now commercially available.

However, it is clear that no single technology option will provide all of the emissions reductions needed. Even, the added efforts for all of the above solutions will probably not allow reaching the desired low levels of CO₂ emissions due to our heavy reliance on fossil fuels. As a result, CO₂ capture and storage may be important and the most viable technique for reducing CO₂ emissions into the atmosphere (IPPC, 2005, 2007; Pacala and Socolow, 2004).

CO₂ capture will be utilized in the combustion industry to reduce CO₂ emission. Separation of CO₂ from the flue gases is required in order to capture CO₂. Many techniques have been developed to perform the separation but most of them require a large amount of energy to obtain a high CO₂ concentration. The separation techniques have a large energy penalty and will decrease the overall power generation efficiency. Besides that, they are expensive to retrofit into power plants and retrofitting will increase the price of energy delivered to consumers (Imperial, 2010).

1.3 Legislation

1.3.1 Kyoto Protocol

The Kyoto Protocol is the United Nations Framework Convention on Climate Change designed as an international response to climate change. The protocol sets that developed countries are required to reduce the emission of long-lived industrial gases such as hydro-fluorocarbons (HFCs), per-fluorocarbons (PFCs) and sulphur hexafluoride and their collective emissions of six key greenhouse gases such as carbon dioxide, methane and nitrous oxide by at least 5% based on their 1990 baseline emission.

Kyoto Protocol introduces a few schemes that allow countries to have a certain degree of flexibility in the way they measure their emissions reductions. The first scheme is known as emissions trading that is established to allow industrialized countries to buy and sell emission credits amongst themselves. The second scheme is known as joint implementation in which industrialised countries will be able to acquire emission reduction units by financing greenhouse gases emission reduction projects in other developed countries. The third scheme is known as the clean development mechanism that is designed to promote sustainable development that will enable industrialised countries to finance greenhouse gases emission reduction projects in developing countries and receiving credit for doing so.

1.3.2 Climate Change Act 2008

One of the main objectives of the Climate Change Act 2008 is to improve the carbon management in the UK to help in the transition towards a low carbon economy in the UK. Besides that, the Act allows the UK government to demonstrate its leadership internationally by signalling that the UK is committed to taking its share of responsibility for reducing global emissions (DECC, 2009).

The UK's Climate Change Act 2008 is a long-term framework by the UK government to reduce greenhouse gas emissions. The Act requires UK to reduce its greenhouse gas emissions by at least 80% of the 1990 level by 2050. Carbon budgets covering a 5-year period have also been set. The first 3 budgets cover the period between 2008-2012, 2013-2017 and 2018-2022. The Committee on Climate Change that was created as part of the Act, recommended that the UK should reduce its greenhouse gas emissions by 34% of the 1990 level in the third carbon period that runs from 2018-2022 and by 42% of the 1990 level, once a global pact to reduce greenhouse gases emission has been achieved (DECC, 2009).

1.3.3 Carbon Budgets

Although a great deal has been achieved in terms of improving power generation efficiency with less carbon dioxide emissions, and reducing emissions from transportation such as trains, more has to be done in maintaining a secure energy supply, seizing opportunities for

new green jobs, and helping to ensure that every home is heated adequately and affordably (DECC, 2009).

1.3.4 Energy Act 2008

This Act covers (DECC, 2009):

- **Offshore Gas Supply Infrastructure:** This regulation allows private sector investments to help maintain the UK's energy supplies as the UK is expected to have to rely on imported gas to meet about 80% of her energy demands by 2020.
- **Carbon Capture and Sequestration (CCS):** This regulation allows private sector investments in CCS projects. This is because CCS has the potential to reduce the carbon dioxide emissions from fossil fuel power plants by about 90%.
- **Renewables:** This regulation strengthens the current Renewables Obligation. It also helps to increase the diversity of the UK electricity generation sources. Besides that, it will also improve the reliability of the energy supplies within the UK and help in reducing the carbon emissions from the electricity generation sector.
- **Feed In Tariffs:** Under this regulation, the UK government will provide financial support for projects related to low-carbon electricity generation plants of up to 5 Megawatts (MW).
- **Renewable Heat Incentive:** Under this regulation, the Secretary of State will be able to provide financial support for renewable heat generated from any sources and from anywhere

1.3.5 Renewables Obligation

Renewables Obligation was established in 2002. It is the UK government's main act to support electricity generation from renewable sources. Electricity generated from renewable sources has doubled and a project pipeline of more than 11 GW has been installed across the UK since the Renewables Obligation came into force in 2002. The UK government has invested more heavily in the fields of offshore wind and biomass in order to generate at least 10% of the UK's electricity demands from renewable sources but there are many constraints to the availability and the use of cheaper forms of renewables (DECC, 2009).

1.3.6 Renewable Energy Strategy

The Renewable Energy Strategy was published by the UK government on the 15th July 2009. One of the articles in the strategy was on expanding and extending the Renewables Obligations to enable the generation of electricity from renewable sources to meet at least 30% of the electricity demand in the UK (DECC, 2009).

The consultation on Renewable Electricity Financial Incentives which was set up as part of the strategy, aims to provide financial incentives for projects related to low carbon electricity generation from renewable sources; renewables obligations and feed in tariffs (DECC, 2009).

1.4 Catalysis

Most industries involved in refining, manufacturing and energy processing uses transition metal oxides as catalysts in their operations. This is because transition metal oxides have the ability to lower the activation energy of an uncatalyst reaction resulting in a higher rate of reaction at the same reaction temperature.

For example, in petrochemical industry, catalysts are used in the processes such as alkylation, catalytic cracking, naphtha reforming and steam reforming. Alkylation uses sulphuric acid or hydrofluoric acid to convert isobutane and low molecular weight alkenes (propene, butene) into a mixture of high-octane, branched-chained paraffinic hydrocarbons (isooheptane, isooctane). Fluid catalytic cracking uses catalysts composed of crystalline zeolite, matrix, binder and filler to convert the higher boiling point, higher molecular weight hydrocarbons fractions in the petroleum crude oils into gasoline and olefinic gases. Steam reforming uses nickel to convert hydrocarbons into syngas. Catalytic converters in petrochemical industries and vehicles use catalysts composed of platinum and rhodium to convert unburned hydrocarbons, carbon monoxide and nitrogen oxides into carbon dioxide, nitrogen and steam.

In chemical looping combustion, a catalyst in the form of a metal oxide or oxygen carrier is used to circulate the two interconnected fluidised bed reactors. The carrier's purpose is to

transfer oxygen from the combustion air to the fuel. During this process, the metal oxide will be oxidised in the riser by taking up oxygen from air or steam. They are then transferred to the downer where they are reduced via combustion of the fuel with the oxygen from the oxygen carrier. This is illustrated in Figure 1.3.

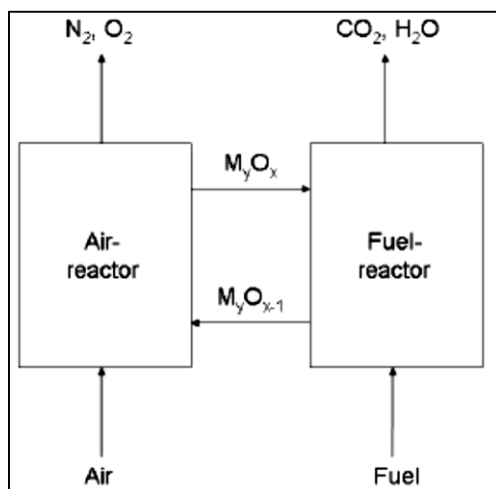


Figure 1.3: Chemical looping combustion flowsheet (Johansson, 2007)

1.5 Statement of Problem Addressed in this Thesis

The increasing threat posed by enhanced global warming as well as the requirement to secure energy supplies around the world have led to the development of several novel technologies to produce clean energy from fuels. Among these new technologies is chemical looping combustion (CLC) that uses a solid metal oxide as the oxygen carrier to react with fuels. This technology has the potential advantage to produce a pure stream of carbon dioxide (CO₂) that can then be utilised or sequestered. This is because the oxygen carrier is reduced by fuels in one reactor, while being reoxidised by air in a separate reactor.

However, as the oxygen carrier circulates the system, it is subjected to morphological and compositional changes such as sintering, attrition and reaction between metal oxides and fuels. These changes might cause the reactivity of the oxygen carrier to decrease over time. These changes have not been studied extensively by other researchers as most of them focused on screening of the oxygen carrier particles and the reactor design.

1.6 Research Objectives

The main objective of this PhD study on chemical looping combustion was to investigate and characterise the morphological and compositional changes in particles such as metal oxides after they have undergone multiple reduction oxidation cycles with solid fuels.

The research study focused on:

- Understand the different analytical techniques used in characterising the metal oxide particles as well as their potential limitations
- Characterise the morphological and compositional changes in the particles after multiple reduction oxidation cycles
- Understand the effects of these changes on the performance of the metal oxide particles

1.7 Layout of Thesis

- Chapter 1: Introduction
 - o Introduces the background of the research study, the problem statements and objectives of this research study.
- Chapter 2: Literature Review
 - o Presents the different types of CO₂ capture and storage technologies, such as pre-combustion, post-combustion and oxy-fuel combustion. It introduces the concept of chemical looping combustion with syngas as well as issues associated with chemical looping combustion with solid fuels. Properties of the commonly used oxygen carriers as well as their preparation methodology are discussed.

- Chapter 3: Theoretical Studies
 - o The concept of fluidisation is discussed. After that the concept of the minimisation of Gibbs free energy used for the thermodynamics calculation is presented. Ellingham diagram as well as the equilibrium constant diagrams for the reactions between pyrolysis gases (CO, H₂ and CH₄) is illustrated. Reaction mechanisms between the pyrolysis gases and the oxygen carriers are described before hypothesis for the interaction between mineral matter and metal oxides are detailed.
- Chapter 4: Experimental Program
 - o Describes the experimental set-up and operating conditions of both experimental setups used in this study. The experimental procedures as well as the measurement accuracy for equipment used in this experimental work are detailed.
- Chapter 5: Experimental and Analytical Results
 - o Describes the results obtained from the experimental work and discusses the analytical work done to characterise the particles using techniques such as X-ray diffraction (XRD), X-ray fluorescence (XRF), porosimetry analysis and inductively coupled plasma mass spectrometry (ICP-MS). The possible metal oxide deactivation mechanisms are presented.
- Chapter 6: Attrition in Chemical Looping Combustion
 - o Presents the results and discusses the rate of elutriation of oxygen carriers used over multiple oxidation and reduction cycles with solid fuels. The possible attrition mechanisms that led to the elutriation of the metal oxide fines as well as the effect of sodium and potassium on the metal oxide particles are discussed.

- Chapter 7: Surface Analysis
 - o Details the results scanning electron microscope with energy dispersive system (SEM/EDS) as well as from the X-ray photoelectron spectroscopy (XPS) analysis. Discusses the possible mechanisms behind the observed trend from these analytical results and how they complement hypothesis presented in Chapter 3.

- Chapter 8: Conclusions & Future Work
 - o Presents the main conclusions from this research and outlines possible future work to be carried out to address issues found in this research.

Chapter 2 LITERATURE REVIEW

2.1 CO₂ Capture & Storage

CO₂ capture is the process of removing CO₂ produced by hydrocarbon combustion (coal, oil and gas) before it enters the atmosphere. The process will be most cost effective when it is used on large point sources of CO₂ such as power stations and industrial plants.

CO₂ capture is an existing industrial technology widely used, on a smaller scale, in the manufacture of fertilisers, the food-processing industry and within the oil and gas sector. The main challenge for any capture process is the low concentration of CO₂ in the flue gas. Depending on the industrial source, CO₂ content can vary from a few percent to over fifty percent. Other contaminant gases such as oxygen, sulphur oxides, water vapour and nitrogen can also be present in flue gases. Due to economic and energy issues, it is impossible to compress and store all of them. As a result, CO₂ must be preferentially separated from the other flue gases by a capturing process.

Currently, there are currently three main methods of capturing CO₂. They are:

- Post-combustion capture
- Pre-combustion capture
- Oxy-fuel combustion capture

2.1.1 Post Combustion Capture

Post combustion capture is a process in which dilute CO_2 is removed from the flue gases after combusting the hydrocarbons. This technology can be retro-fitted onto existing industrial plants and power stations without significant modifications to the existing plants (SCCS, 2008).

There are a number of post combustion capture technologies being investigated at the moment. The first technology is known as solvent capture. An example of solvent capture is the amine scrubber shown in Figure 2.1. An amine scrubber uses a dilute solution of about 30% monoethanolamine in water which will react with CO_2 in the flue gas by 'loading' it. The loaded material will then be transported to a stripper where heat is added to reverse the reaction thereby producing a pure stream of CO_2 while regenerating the sorbent at the same time. The CO_2 will then be compressed and transported to a site where it will be sequestered (Imperial, 2010).

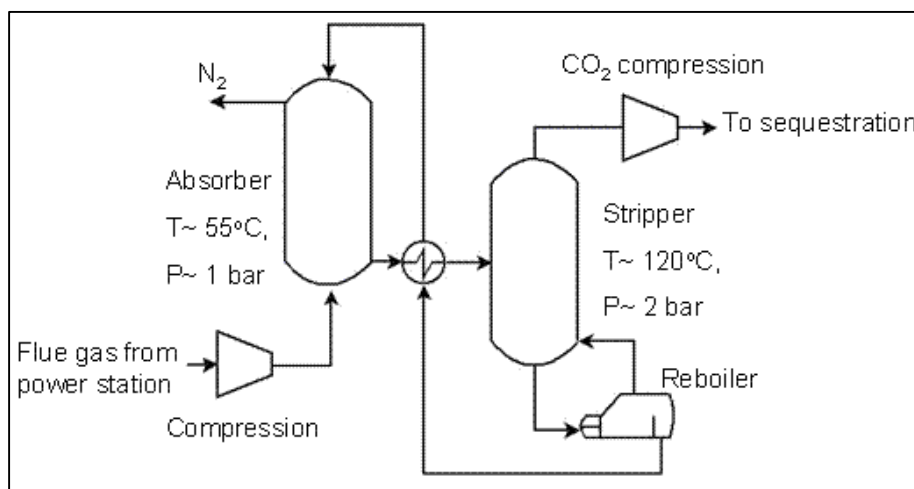


Figure 2.1: Amine scrubber flowsheet (Imperial, 2010)

Current research on solvent capture is focused on the improvement of solvents for CO₂ capture. This includes discovering and testing new solvents. Besides that, investigation of the operation and flexibility of solvent capture plant is being carried out. Other issues with solvent capture that are currently being studied include the degradation in the CO₂ capture ability of the sorbent over repeated cycles. This includes studies to determine the kinetics and the mechanism of degradation of the sorbents. Interactions of sorbent with trace and minor species in the flue gas such as SO₂ and mercury are also being carried out before this technology can be marketable (Imperial, 2010).

The second technology is known as calcium looping. This technology uses the ability of calcium oxide to react with CO₂ to produce limestone, CaCO₃ via carbonation (Imperial, 2010).



Limestone is then heated up to release the CO₂ via calcination and the quicklime is then recycled.

Limestone can be used to enhance the water gas shift reaction. This could be done by adding quicklime to remove CO₂ in reaction. Adding quicklime into the reaction will enhance the production of hydrogen from coal, oil or natural gas (Imperial, 2010).



Besides that, limestone can be added into Reaction 2.1 in order to remove CO₂ from flue gas. An example of this process is shown in Figure 2.2 which shows the mitigation of CO₂ emission from a coal-fired power station (Imperial, 2010).

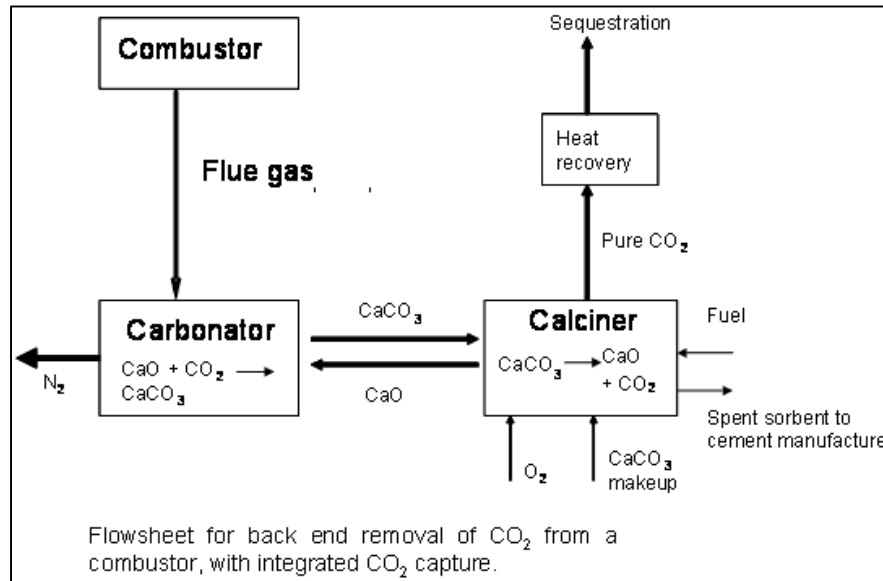


Figure 2.2: Calcium looping flowsheet (Imperial, 2010)

However, the ability of CaO to take up CO₂ reduces with the number of cycles of calcination and carbonation undergone. As a result, various researchers are trying to come up with different pre-activation technologies as well as different methods to reactivate the spent sorbent. It is also possible to integrate this technology with cement manufacturing as it is possible to take the limestone from this process in the calcined form (CaO) with the already sequestered CO₂ to produce cement (Imperial, 2010).

Other forms of post combustion capture are focusing on cryogenically solidifying CO₂ from the flue gases; removing CO₂ with solid adsorbents; and passing CO₂ through a membrane. Post combustion capture requires an additional energy input of about 20–30% compared to plants without the CO₂ capture technology as the additional energy is required released CO₂ from the solvents. Thus, the whole output of 1 plant in 4 plants would be required to provide energy for such carbon capture.

One advantage of this technology is that it is economically feasible to retrofit the technology into existing industrial plants and power stations. The existing technology with amine solvents has existed for about 60 years. This technology is currently being used to capture CO₂ for use in soft drinks plants (SCCS, 2008).

One disadvantage of this technology is that a high operational cost is needed to run this technology. This is because the absorber and the degraded solvents need constant replacement. Besides that, this technology has been used mainly in smaller scale plants and therefore there is limited operational experience in using this technology for larger scale plants (SCCS, 2008).

Figure 2.3 and 2.4 show the layout of a post combustion capture reactor and the schematic diagram of a post combustion capture process respectively (SCCS, 2008).

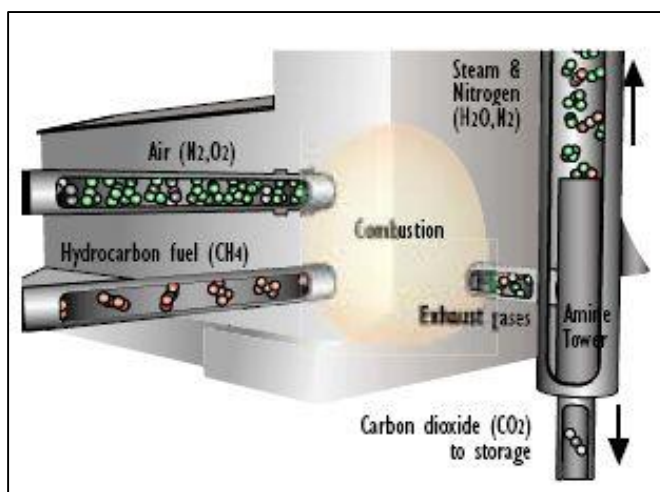


Figure 2.3: Post combustion capture technology (SCCS, 2008)

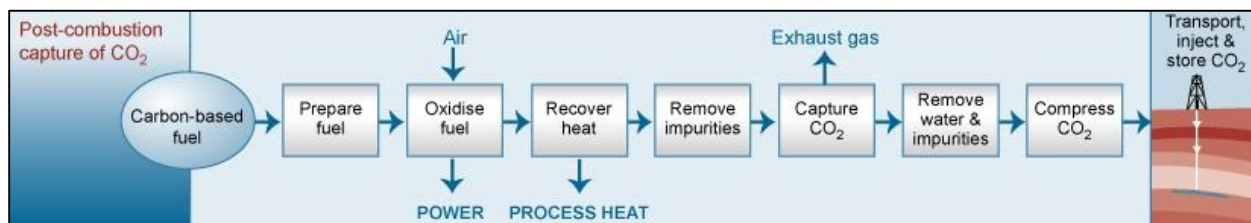


Figure 2.4: Post combustion capture techniques (SCCS, 2008)

2.1.2 Pre-Combustion Capture

Pre-combustion capture is a process in which CO₂ is removed prior to combustion in order to produce hydrogen. Combustion of hydrogen produces no CO₂ emissions as the primary by-product is water vapour. This technology has the potential to provide a CO₂ emission free system if it is integrated with a carbon storage facility (SCCS, 2008).

The CO₂ capture in a process such as the integrated gasification combined cycle (IGCC) process shown in Figure 2.5 consists of 3 stages. During the first stage, fuel is gasified with pure oxygen into H₂ and CO to form syngas. The syngas will then be cleaned up by removing sulphur and the other contaminants before the second stage takes place. During the second stage, a water gas shift reaction (Reaction 2.2) occurs in which the carbon monoxide is reacted with steam to produce more H₂ and convert CO into CO₂ (Imperial, 2010).



In the final stage, the CO₂ will then be separated from H₂ by using a membrane which is permeable only to H₂. The separated H₂ will then be combusted in a gas turbine (or would be used in a fuel cell), while CO₂ will then be compressed into liquid and transported to a storage site (SCCS, 2008).

One advantage of this technology is that it is able to capture 90–95% of the CO₂ emitted to the atmosphere. This technology is applicable generally to oil refineries and natural gas and coal fired IGCC plants. It also has the lowest technology risk. This technology can also be used to produce hydrogen and liquid fuels from coal (SCCS, 2008).

One disadvantage of this technology is that it requires a chemical plant in front of the gas turbine. High investment cost is required in order to build a dedicated new plant. Besides that, this technology produces high nitrogen oxides emissions, and expensive scrubbers will be required to reduce these emissions. The efficiency of hydrogen burning in turbines is also lower than that in conventional turbines. This technology may also be less flexible under a

varying electricity generation market requirement and, as such, base load is normally preferred (SCCS, 2008).

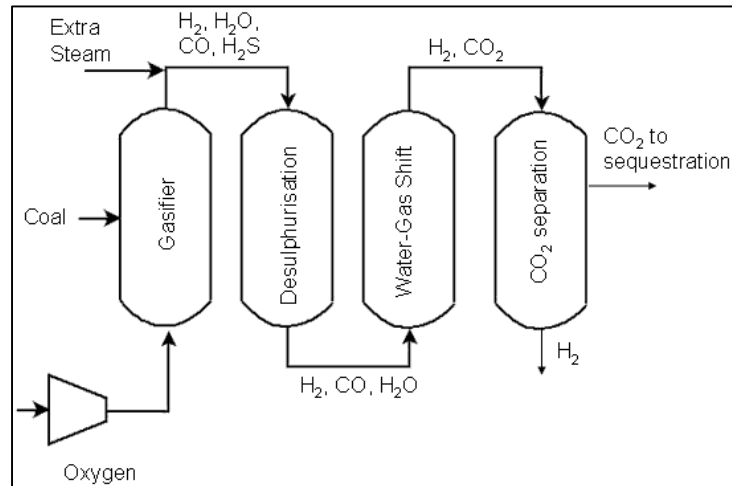


Figure 2.5: Hydrogen Production Flowsheet from Integrated Gasification Combined Cycle (IGCC) (Imperial, 2010)

Figure 2.6 and 2.7 show the layout of a pre-combustion capture reactor and the schematic diagram of a pre-combustion capture process respectively (SCCS, 2008).

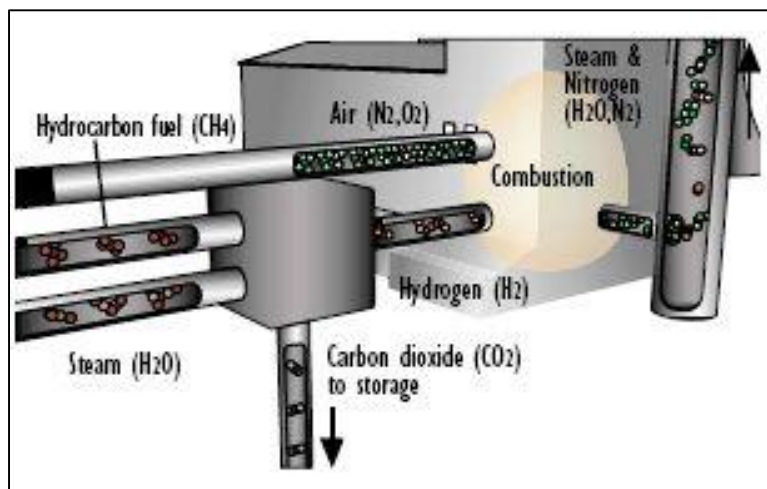


Figure 2.6: Pre combustion capture technology (SCCS, 2008)

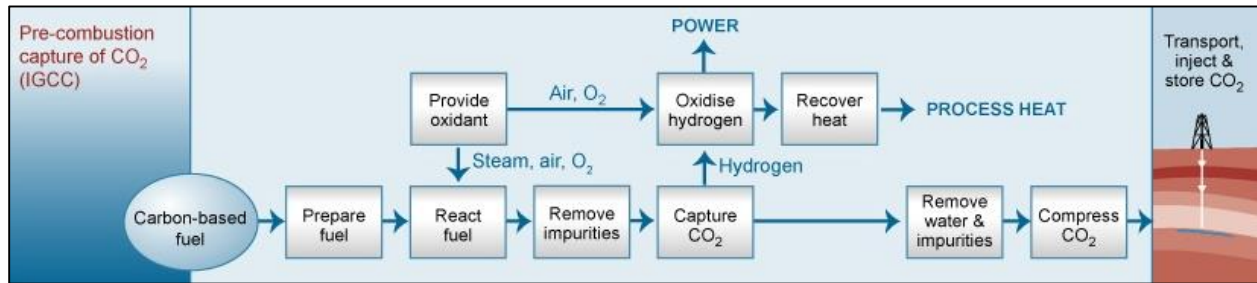


Figure 2.7: Pre combustion capture technique (SCCS, 2008)

2.1.3 Oxyfuel Combustion Capture

Oxy fuel combustion capture is a process in which fuel is combusted in pure oxygen in order to produce water vapour and a pure stream of CO₂. A proportion of the CO₂ will then be recycled to the burner to reduce the temperature of the flame to an acceptable level. The products in the exhaust stream consist of almost pure CO₂ (around 90%) and water vapour. The water vapour can be separated from the CO₂ by condensation (SCCS, 2008). Figure 2.8 illustrates a simple configuration of an oxyfuel combustion system.

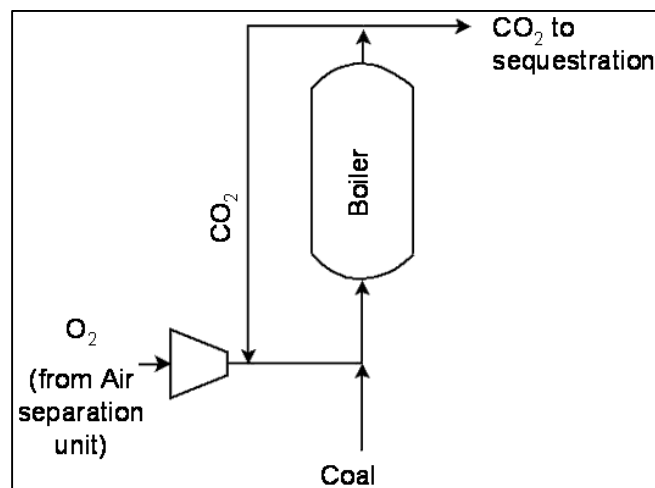


Figure 2.8: Oxyfuel combustion flowsheet (Imperial, 2010)

One of the difficulties with this technology is that it is difficult to separate oxygen from the air. This is because a large amount of energy is required and this is usually carried out cryogenically. A typical 500 MW coal fired power station will require about 15% of its electricity generated to supply pure oxygen. As a result, new technologies such as zero emission coal technology (ZECA) and chemical looping combustion (CLC) are being developed (SCCS, 2008).

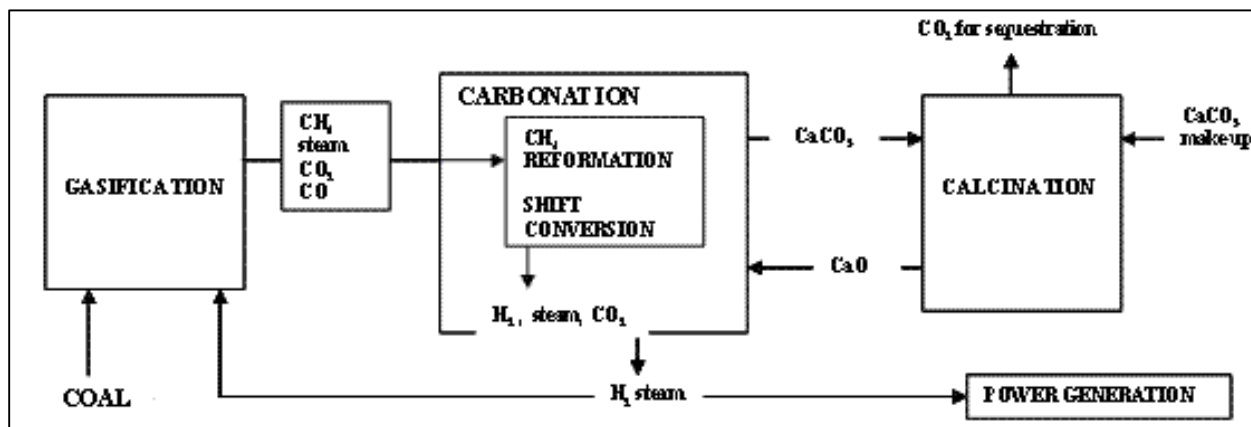
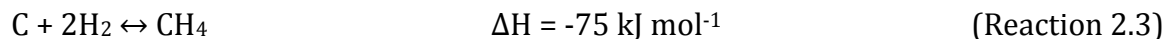


Figure 2.9: Zero emission coal technology (ZECA) flowsheet (Imperial, 2010)

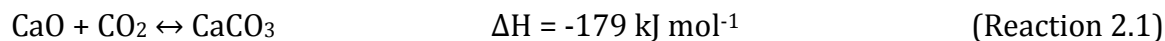
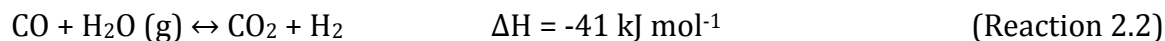
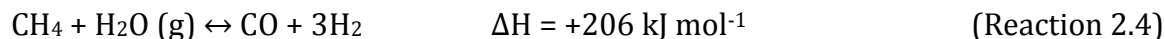
The ZECA concept is shown in the Figure 2.9. The process involves the gasification of coal in hydrogen via hydrogasification and it is designed to avoid using oxygen for combustion. The integrated process route has not been studied experimentally, but different parts of the concept have been studied. They include hydrogasification and CaO driven steam reforming and shifting of CH₄ (Imperial, 2010).

During the first stage of the process, coal is hydrogasified at a pressure of about 70 bars to produce CH₄ (Reaction 2.3) (Imperial, 2010).



Reaction 2.3 is an exothermic reaction and as a result, steam would need to be added into the reactor to moderate the temperature of the reactor to about 900°C. During the second stage, CH₄ undergoes the steam reforming reaction to produce hydrogen (Reaction 2.4).

Besides that, the water gas shift reaction (Reaction 2.2) is used to maximise the hydrogen concentration of the gas (Imperial, 2010).



The overall hydrogen production reactions are endothermic. As a result, the heat required by the reactions will be provided by the hydrogasification reaction (Reaction 2.3) and by the carbonation reaction (Reaction 2.1). The carbonation reaction provides most of the energy required in the production of hydrogen and acts as CO₂ removal from the reaction mixture. The resulting shift in equilibrium of the shift reaction (Reaction 2.2) will ensure that the concentration of H₂ is maximised and provides the means of collecting a concentrated stream of CO₂. Reaction temperatures may be limited by the melting properties of the coal and its mineral matter, the need to avoid the formation of eutectic liquid phases in the solid sorbents used to remove CO₂ and the equilibrium controlled inability of CaO to bind CO₂ at temperatures above 900°C at a CO₂ partial pressure of less than 10 bars. To ensure effective energy utilisation, reactions (2.4, 2.2, 2.1) will need to be conducted in a single reactor (Imperial, 2010).

Overall, the scheme will result in the production of four moles of hydrogen for each two moles of hydrogen used in the hydrogasification stage. Hydrogen required for the hydrogasification stage is taken from the hydrogen stream remaining after the further processing of the gas. The bound CO₂ will then be released as a concentrated stream for sequestration by heating the CaCO₃. Overall, the ZECA process produces the same amount of CO₂ per kg of coal being hydrogasified compared to conventional combustion technologies. However, ZECA process has the potential advantage of producing a higher electrical efficiency of about 65% as energy losses can be avoided via integration of the various process steps. It is also able to isolate CO₂ produced as a nearly pure stream for storage by using the carbonation and calcination cycle (Imperial, 2010).

One of the advantages of this technology is that it has the potential to capture 100% of the CO₂ released during combustion. Besides that complete combustion will produce less harmful emissions. This technology can also be retro-fitted into existing coal power plant (SCCS, 2008).

One of the disadvantages of this technology is that high energy consumption is required if the process is not carried out via the ZECA concept or CLC (SCCS, 2008).

Figure 2.10 and 2.11 show the layout of an oxy-fuel combustion capture reactor and the schematic diagram of an oxy-fuel combustion capture process respectively (SCCS, 2008).

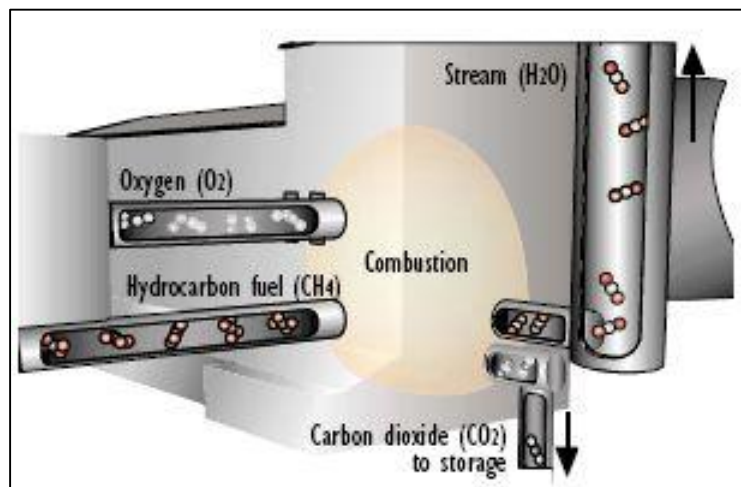


Figure 2.10: Oxyfuel combustion capture technology (SCCS, 2008)

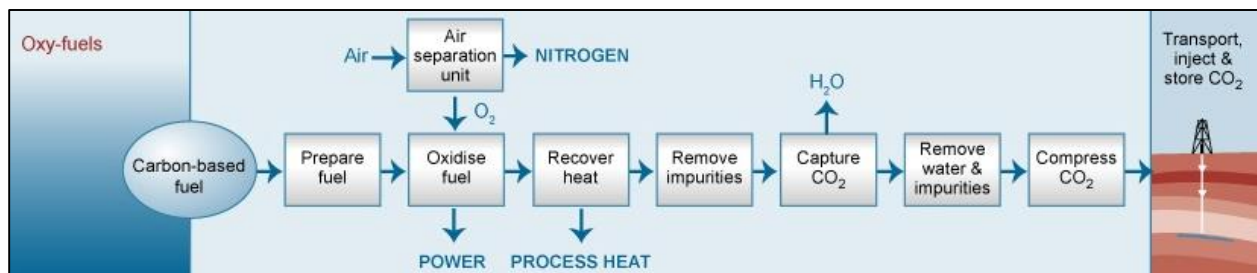


Figure 2.11: Oxyfuel combustion capture technique (SCCS, 2008)

2.2 Chemical Looping Combustion

The concept of chemical looping combustion (CLC) is based on the use of an oxygen carrier material. The carrier's purpose is to transfer oxygen from the combustion air to the fuel. As a result, any costly separation of nitrogen is avoided since the uptake of oxygen from the air is achieved by a simple solid-gas phase reaction. A flowsheet of CLC is shown in Figure 2.12. The combustor consists of two interconnected fluidised bed reactors; an air reactor (riser) or a fuel reactor (downer). The oxygen carrier particles circulate between these two reactors. The oxygen carriers are oxidised in the riser by taking up oxygen from the air. They are then transferred to the downer where they are reduced via combustion of the fuel with the oxygen from the oxygen carrier. Hence, in both reactors, the reactions proceed through solid-gas phase reactions shown below:

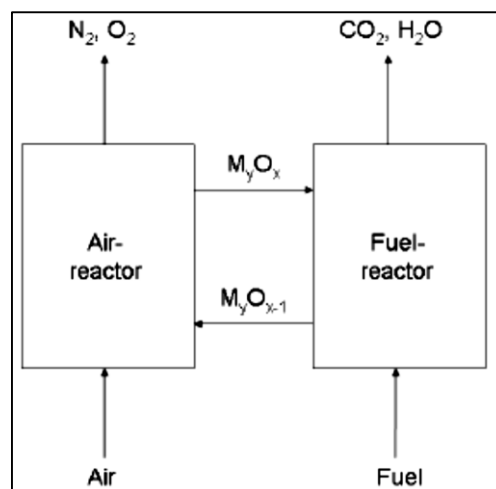
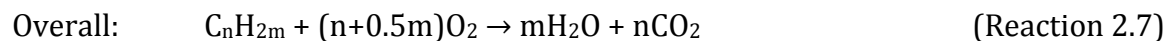
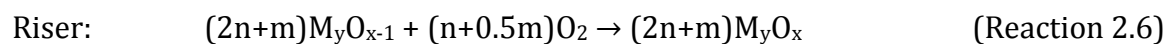
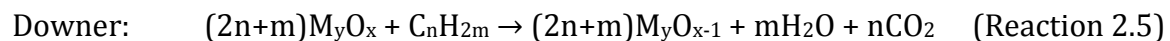


Figure 2.12: Chemical looping combustion flowsheet (Johansson, 2007)



The overall result of the two separate reactions is the same as for normal combustion. Reaction 2.5 is either endothermic or exothermic, depending on the type of oxygen carrier and fuel whereas Reaction 2.6 is always exothermic. The advantage of CLC is that the mixture

of CO₂ and steam can be condensed such that CO₂ is obtained in a separate stream. The temperature range of a CLC system is 800-1200°C and the combustor can either be pressurised or atmospheric.

Besides that, a CLC system does not generate thermal NO_x in the riser due to the low reaction temperature. The absence of thermal NO_x in the exit gases was verified experimentally by Ishida and Jin (1996) and Son and Kim (2006). The existence of fuel NO_x has not been verified, but the conditions in the downer is expected to be unfavourable for NO_x formation.

2.3 Oxygen Carriers

2.3.1 General Particle Characteristics

Listed below are some of the desired oxygen carrier characteristics for usage in a chemical looping combustion system adapted from Fan (2010).

Good Oxygen Carrying Capacity

Higher oxygen carrying capacity will allow lower particle circulation rate in a dual fluidised bed system. The maximum oxygen carrying capacity of the particle is determined by the property of the primary metal oxide and support used in preparing the particle. The effective oxygen carrying capacity is defined as the amount of transferable oxygen in the particle during the looping operation, reflects the extent of the solid conversion that is affected by the gas and solid residence time in the looping reactor. For oxygen carrier particles with multiple oxidation states, the type of the looping reactors and their gas solid contact patterns can influence the effective oxygen carrying capacity of the particles.

Good Gas Conversions during Reduction and Oxidation

Higher gas conversions will increase the energy conversion efficiencies. This can be achieved during oxidation and reduction by using properly selected primary metal oxide materials, reactor type and gas-solid contact mode. Thermodynamic relationships among the various oxidation states of the metal oxide with the reactant as well as the product gas concentrations play an important role in the metal oxide selection process.

High Rate of Reaction

Higher rate of reaction will enable smaller reactor to be used in order to achieve the same reactant conversion. The rate of reaction is influenced by the properties of the primary metal oxides, supports, promoters, particle synthesis techniques and reaction conditions.

Satisfactory Long Term Recyclability and Durability

Improving the recyclability and durability of the particle will lead to the reduction in the spent particle purging rate and the fresh particle makeup rate required for continuous operation. The particle recyclability and durability is influenced by the properties of the support used with the primary metal oxides as well as the particle synthesis procedures.

Good Mechanical Strength

Good mechanical strength can lower the rate of attrition. The mechanical strength of the particle is influenced by the properties of the support or binder materials, additives, overall particle's composition and preparation methodologies.

High Heat Capacity and High Melting Point

Particle with a high heat capacity can be used as a heat transfer medium in the reactor. This will benefit the reactor design in that the particle can be used to moderate the temperature changes in the reactor as a result of the endothermic or exothermic reactions. This will thus reduce the requirement of constructing heat exchangers to moderate the temperature in the reactor. The heat capacity of the particle is influenced by the properties of the inert support. High melting point for the metal oxides and their reduced forms as well as for the support materials is preferred to maintain the integrity and reactivity of the particles.

Ability to Change the Heat of Reaction

Minimising the heat duty requirement in the reactor is essential when designing the heat integration scheme for the process. This is usually done by adding a secondary reactive metal oxide into the particle that will participate in at least one of the redox reactions. The chosen secondary metal oxide usually has an opposite sign for its heat of reaction when compared to the primary metal oxide.

Low Cost and Ease in Scaling Up of the Synthesis Procedures

The cost of the raw material and the cost required to synthesise the oxygen carrier play a major role when it comes to choosing the preferred metal oxide, support material and the synthesis methodology. Besides that, the synthesis methodology should be easily scaled up for industrial application.

Suitable Particle Size

Particle size can influence the rate of reaction and the flow properties in the reactor.

Resistance to Contaminant and Inhibition of Carbon Formations

Various contaminants may be present in the fuels used for chemical looping combustion processes. As a result, the interaction between the contaminants and the oxygen carrier particles in the reducing reactor should be minimised because the formation of metal carbide and/or metal sulphide will lead to the deactivation of the oxygen carrier particle. This is usually done by reducing the gas concentration into the reducing reactor or by adding a suitable doping agent onto the particle.

Pore Structure

A porous particle is desirable for low temperature operations as the rates of reaction in this regime is influenced by the diffusivity of the gaseous reactants and products. High temperature operations will result in particle sintering which will alter the pore structure and hence the reactivity of the particle. As such it is desirable to synthesise particles with a stable pore structure for usage in a chemical looping combustion system.

Health and Environmental Impacts

Due to the large particle circulation rate in a chemical looping combustion system, a large quantity of purged particles will need to be disposed. As a result, metal oxides and supports chosen during the synthesis process will need to have low health and environment impacts so that they can be disposed easily.

2.3.2 Oxygen Carriers Preparation Methodologies

Listed below are some of the most commonly used oxygen carrier preparation methodologies found in literature.

Mechanical Mixing

Mechanical mixing is the simplest and most economical preparation method that can yield a satisfactory result. The preparation procedure involves the direct mixing of the metal oxide and the support in a certain ratio to form the composite looping medium. The powders for both materials are first dried before the dried powders are mechanically mixed. Binding agents are sometimes added in the mixing step to strengthen the composite matrix. After the formation of the metal-support matrix, the powder is processed into the desired size and shape. This can be done by using the extrusion or compression process to produce pellets or granulation to produce powders. Calcination is often performed after obtaining particles in a desirable morphology. When bulk pores are desirable, graphite can be mixed into the matrix initially and can then be combusted during calcination to form pores (de Diego et al., 2004).

Although mechanical mixing is cheap and effective for most applications, it yields a less homogeneous medium compared to other preparation methodologies. The particles obtained by mechanical mixing have been observed to have a metal oxide-rich phase and a support-rich phase. However, mechanical mixing was found to be unsuitable for metal oxides such as copper oxide as copper oxide sinters at low temperatures. De Diego et al. (2004) found that copper based oxygen carriers prepared by mechanical mixing lose activity because of sintering of the metal-rich phase.

Freeze Granulation

Freeze granulation is the preferred methodology to synthesise small spherical particles with well-defined morphology. In order to prepare freeze granulation type of particles, the metal oxide and the support are mixed in distilled water with a small amount of dispersant such as polyacrylic acid. The dispersant is used to improve the homogeneity of the mixture. The mixture will then be grounded in a ball mill for an extended period of time to obtain a fine powder slurry. The slurry is then treated with a small amount of binder to achieve improved particle strength. The resulting product is then dried using the freeze-drying technique. Finally, the particles are sintered at elevated temperatures before sieving them to yield desired particle sizes. After being treated at certain sintering temperatures, the spherical shape particles obtained using this method can have a very smooth surface (Johansson et al., 2004).

Freeze granulation is not suitable for the synthesis of copper-based oxygen carriers due to the sintering of the copper-rich phase (Cho et al., 2004). The chemical reactivity of the particles prepared by this method is highly dependent on the metal oxide and binder interaction. The crushing strength of the particles was found to improve with increasing number of redox cycles. This is believed to be due to the adjustment of the structure of the particle to the best suited form (Johansson et al., 2003, 2004).

Dry Impregnation

A support medium with well-defined pore volume in its powder form is essential for the preparation of dry impregnation particles. The support is first exposed to a metal salt solution with volume equal to the total pore volume. Solutions of metal nitrate salts are often used because of their high solubility and availability. After being doped on the support, the oxygen carrier is then calcined. The calcination step will cause the metal nitrates to decompose into metal oxides. This process is repeated until the desired metal oxide percentage is achieved. Finally, high temperature calcination is carried out to obtain the desired physical stability. It is difficult to predict the exact amount of metal loading because of the inherent nature of the technique. As a result, two parameters are used to quantify the metal oxide percentage. They are theoretical percentage of metal loading and actual

percentage of metal loading. The theoretical metal loading is determined based on the amount of the metal salt solution used, whereas the actual metal loading is determined from reduction/oxidation experiments (Mattisson et al., 2003).

This methodology is suitable for the synthesis of all types of oxygen carriers. However, due to the tedious synthesis procedure and the high synthesis cost, the method is predominantly used for a copper-based looping medium to reduce the effect of copper sintering. It is believed that the reduced sintering effect is due to the limited metal loading in the pores of the support (de Diego et al., 2005). The particles synthesized using this method showed a crushing strength similar to that of the support, thus highlighting the importance of the support selection (Mattisson et al., 2003). The metal loading of the particle obtained using this methodology is limited by the pore volume of the support.

Wet Impregnation

The wet impregnation technique is an empirical preparation methodology. The difference between wet and dry impregnation lies in the amount of metal nitrate solution used. Wet impregnation required the support to be soaked in the metal nitrate solution followed by low-temperature calcination to decompose the nitrates into insoluble oxides. This procedure is repeated until the desired metal loading is achieved. The amount of solution used in wet impregnation in each soaking step is higher than that for dry impregnation. A high-temperature sintering step is then used to improve the properties of the particles.

Particles prepared via wet impregnation have properties similar to that prepared via dry impregnation technique. De Diego et al. (2004) found that copper based particles generated using this method have very good chemical stability and reactivity coupled with mechanical resistance when compared with other preparation methodologies. However, wet impregnation preparation technique will form an outer shell of metal oxide that has a weak bond with the support and tends to attrite after initial cycles.

Co-Precipitation and Dissolution

Co-precipitation and dissolution are the preferred preparation methodologies to obtain oxygen carriers that are homogeneous. This method can also be used when the support material is less porous causing the impregnation approach to be unfeasible. Three precursors, that is, the metal salt solution, the support solution, and the precipitating agent, are required for this preparation methodology.

Co-precipitation particles are prepared by mixing the metal salt solution and the support solution together in liquid form. The precipitating agent, usually alcohol, is then added to the mixed solution to initiate the precipitation of metal and support in powder form (de Diego et al., 2004).

Dissolution particles are prepared by adding the metal salt solution and the support solution to the alcohol (precipitating agent) and water simultaneously (Jin et al., 1998, 1999; Ishida et al., 1998, 2002; Jin & Ishida 2001, 2002, 2004). Powders that contain metal and support are obtained in a similar manner as the co-precipitation method. Although the methodologies followed by co-precipitation and dissolution are different, the particles obtained from these two methods are similar (Haber et al., 1995).

Multiple drying steps will then be carried out in order to remove the water, alcohol and acid, and to improve the interaction between the metal and the support. Jin et al. (1998) used a four-step drying and calcining path whereby the sample was initially dried at 100°C for 12 hours to remove the water content completely. This is then followed by drying at 150°C and 200°C for 24 hours and 5 hours respectively to heat-treat the particles, to initiate interactions between support and metal and to remove the alcohol. Finally, calcination at 500°C for 3 hours in the presence of air removes the acid formed and induces physical stability by sintering (Jin et al., 1999). The resulting powder is then formed to the final product.

The occurrence of simultaneous precipitation of metal and support is essential for the dissolution and co-precipitation method. Some governing factors for such a simultaneous precipitation include the pH of the solution and reaction rates of the individual precipitation reactions.

Sol-Gel Synthesis

The sol-gel synthesis is the preferred methodology when a highly homogeneous particles are desired as this methodology allows for excellent control over the physical parameters of the particles. However, this increases the difficulty and the cost in preparing sol-gel based particles.

This method was originally defined as 'the preparation of ceramic materials by preparation of a sol, gelation of the sol, and removal of the solvent' (Brinker et al., 1990). The process begins with the selection of the dissolved or solution precursors of the intended metal oxide and support. The precursors can be metal alkoxides, metal salt solutions, and/or other solutions containing metal complexes. Metal alkoxides are commonly employed because of the high purity observed in the final product. These precursors are then mixed together and undergo a series of hydrolysis and condensation reactions with water to form amorphous metal oxide or oxy-hydroxide gels. These gels contain colloidal particles of metal, metal oxide, metal oxy-hydroxides, and/or other insoluble compounds that is subsequently molded to the required shape and rigidified using dehydration, chemical cross-linking, or freezing. This rigid mass is then cured by calcinations. In some cases, the calcination step is essential for obtaining the desirable metal oxide (Sakka et al., 1995).

The sol-gel method produces a homogeneous mixture and provides good control over the microstructure. The degree of aggregation or flocculation of the colloidal precursor can control the pore size of the yield. The drawback of the sol-gel method is the high raw materials cost and the elaborate synthesis procedures.

Solution Combustion

Solution combustion based particles is prepared by mixing metal nitrates and the support in the desired ratio in water solution with glycine (combustible agent). The solution is then heated to vaporise the water. Once most of the water is driven out, the solution is ignited when the temperature is beyond the critical self-ignition temperature. The metal-oxide-based oxygen carrier is obtained after combustion is then ground in a mill and processed to the desired shape and calcined.

This method avoids the time consuming drying steps required for the other preparation methods. The particles obtained from this method showed good reactivity for multiple cycles and high crushing strength. However, they were found to have high rates of attrition (10%) and that the performance of the extruded particles deteriorate quite rapidly (13% reduction in activity after 10 cycles) (Erri & Varma, 2007).

2.4 Oxygen Carrying Capacity

Table 2.1 shows the oxygen carrying capacity (moles of oxygen per mole of metal) for different metal oxide configurations (Hossain and de Lasa, 2008). The oxygen transfer capacity, i.e. the ratio of mass of active oxygen in the carrier to the mass of the fully oxidised oxygen carrier for different metal oxides is illustrated in Figure 2.13 (Johansson, 2007). Figure 2.14 highlights the equilibrium constant, K (logarithmic scale) against $1/T$ plots for the reduction of the different metal oxides with methane as the reducing agent. A high $\log K$ value indicates that the metal oxide has a high potential to react with methane. Finally, Figure 2.15 provides the degree of CH_4 conversion to CO_2 calculated via the minimisation of Gibbs free energy (Mattisson and Lyngfelt, 2001).

Table 2.1: Oxygen carrying capacity for different metal/metal oxide pairs (Hossain and de Lasa, 2008)

Metal Oxide	Moles of O ₂ /mole metal
NiO/Ni	0.5
CuO/Cu	0.5
Cu ₂ O/Cu	0.25
Fe ₂ O ₃ /Fe ₃ O ₄	0.083
Mn ₂ O ₃ /MnO	0.25
Mn ₃ O ₄ /MnO	0.17
Co ₃ O ₄ /Co	0.67
CoO/Co	0.5

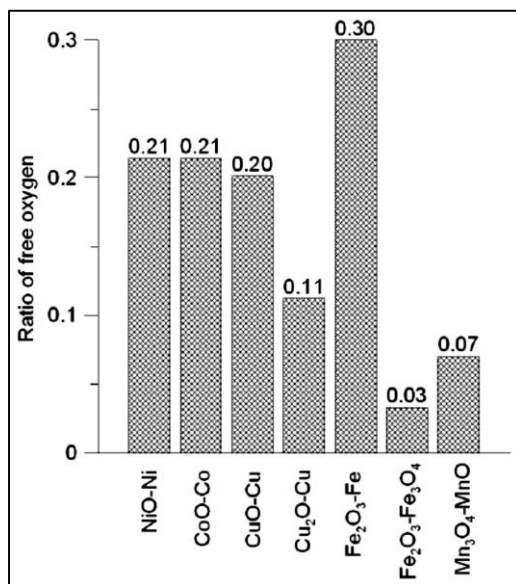


Figure 2.13: Amount of active material for different unsupported oxygen carriers (Johansson, 2007)

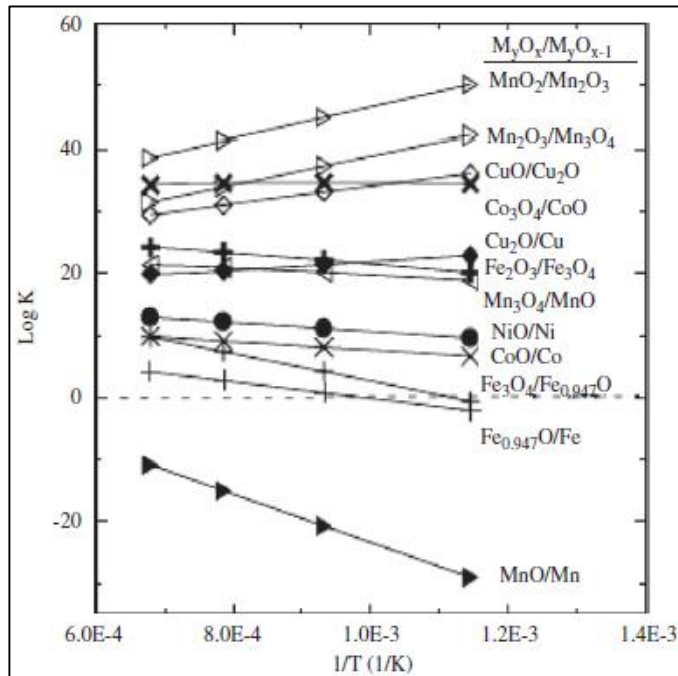


Figure 2.14: Log K as a function of 1/T in the temperature range of 600-1200°C for different metal oxide systems (Mattisson and Lyngfelt, 2001)

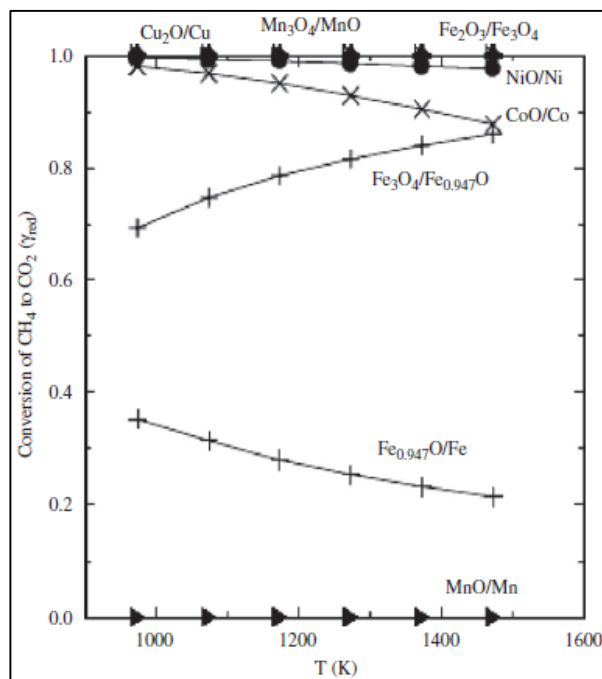


Figure 2.15: Conversion of CH₄ to CO₂ as a function of temperature for different oxygen carriers (Mattisson and Lyngfelt, 2001)

2.5 Chemical Looping Combustion with Solid Fuels

There are plenty of research studies on chemical looping focusing on gaseous fuels, but there is only limited research conducted on chemical looping with solid fuels, as the oxygen carrier particles are not easily separable from the fuel or the ash particles. Without separation, the solid fuels would enter the air reactor along with the oxygen carrier and give CO₂ in the off-gas. As a result, a few techniques have been developed (Dennis, 2009).

The first technique is to gasify the solid fuel separately and burn the syngas using a conventional chemical looping arrangement for gaseous fuels. The advantages of this technique are that it allows better combustion efficiencies, reduced coking, and syngas as input for the chemical looping system as opposed to natural gas. One of the disadvantages of this technique is that the gasifying agent would need to be pure O₂ or a mixture of O₂ and CO₂, to ensure that the syngas is mainly CO and H₂, without N₂. This, however, would require an air separation unit that will defeat the purpose of using chemical looping (Dennis, 2009).

Alternatively, the gasification could be performed in pure CO₂ or mixtures of CO₂ and steam. However, in order to balance the endothermic gasification reactions, heat will have to be supplied to the gasifier from the air reactor. This method will complicate the reactor design. One possibility would be to use a packed bed configuration or to design a concentric fluid bed arrangement whereby heat transfer can take place from the air reactor to the gasifier, both fluidised, via a shared vessel wall (Dennis, 2009).

The second technique is in situ gasification in a cyclic batch operation. This technique involves the in situ gasification and combustion of solid fuel with one fluidised bed. The reactor operated in a cycle of three consecutive periods: t₁, t₂ and t₃. During t₁, solid fuel is fed continuously to a bed of oxygen carrier, fluidized by steam or CO₂, or a mixture of both. During the reaction, the fuel loses its volatile matter that will be oxidised. After that, the fluidising gas gasifies the resulting char, producing syngas, which immediately reacts with the oxygen carrier to form CO₂ and steam (Dennis, 2009).

At the end of t_1 , the feed of coal is stopped and the remaining inventory of carbon is allowed to gasify and combust for a further time period of t_2 , until the inventory of char is sufficiently small. At the end of t_2 , the bed is fluidised with air instead of steam or CO_2 for a time period of t_3 , when the depleted oxygen carrier is regenerated. A new cycle will then begin. Ideally several reactors would be used to operate the various phases in the cycle to even the load to the downstream power cycle. If the solid fuel produces a very reactive char, the second phase may be omitted as the inventory of fixed carbon in the bed would be low (Dennis, 2009).

The third technique is in situ gasification of the solid fuel in the presence of the metal oxide in pure CO_2 or steam or a mixture of both. The unburned fuel will then be separated from the spent oxide before the solids are passed to the oxidation reactor. Lyngfelt and colleagues developed a fuel reactor designed to separate the unburned fuel from the spent metal oxide before the carrier is recycled to the air reactor. The overall plant design consists of an air reactor operating as a fast fluidised bed connected to a riser that leads to a cyclone where the elutriated particles are separated. The fuel reactor is designed so that gasification and reaction occur, and that the solids pass to a downstream section, where a separation can be effected between the fuel particles and the carrier on the basis of different elutriability of the carrier and the fuel particles, the latter being of lower density and smaller in size (Dennis, 2009).

Figure 2.16 shows a CLC layout for solid fuels proposed by Cao and Pan (2006) and Cao et al. (2006). The riser and cyclone are used to oxidise the reduced metal oxide particles and recycle them back into the downer. Steam or recycled CO_2 is used as the fluidisation media and gasification agent in the downer. Metal oxide particles are reduced during their reaction with volatiles and carbons in the downer. The reduced particles will enter the riser via a small loop seal. A bubbling bed and a turbulent fluidised bed are designed in the downer to react and separate the metal oxide particles. A bubbling bed is designed for the downflow section as the residence time for the reaction between the oxygen carriers and the solid fuel is relatively long. The oxygen carrier is separated from the fly ash by controlling the operating velocity at bubbling or turbulent flow regimes as the ash and unburned carbon are lighter due to the smaller density of 800-1200 (kg/m^3) compared with the oxygen carrier

particles (density $>5000 \text{ kg/m}^3$). The fly ash and unburned carbon are entrained out of the separation section as 'flue gas 2' and enter 'cyclone 2' for clean-up. The flue gas after separation by cyclone is a nitrogen-free gas with CO_2 , H_2O , CO and H_2 .

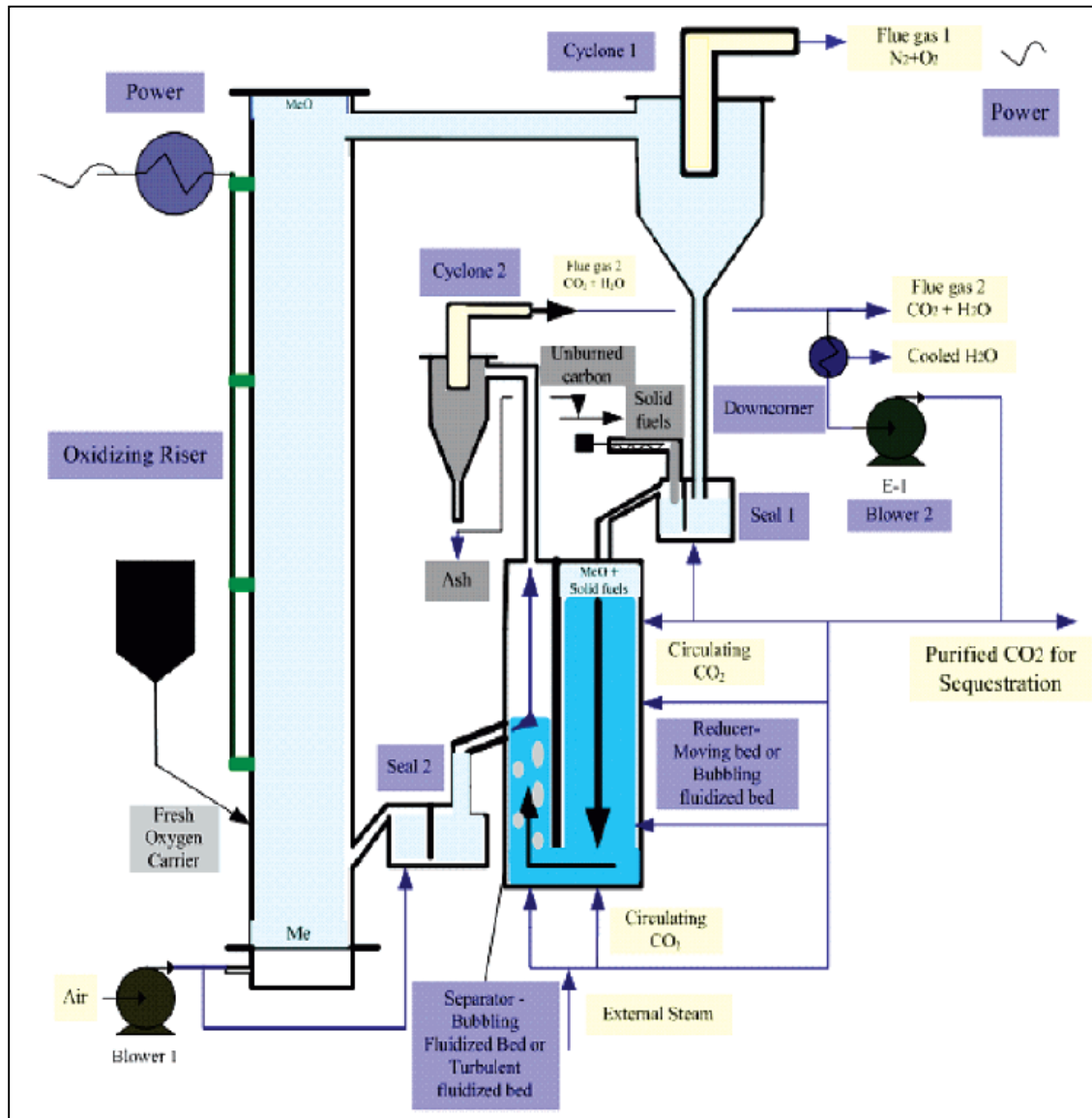


Figure 2.16: System configuration for the pilot-scale chemical looping combustion process of solid fuels (Cao and Pan, 2006; Cao et al., 2006)

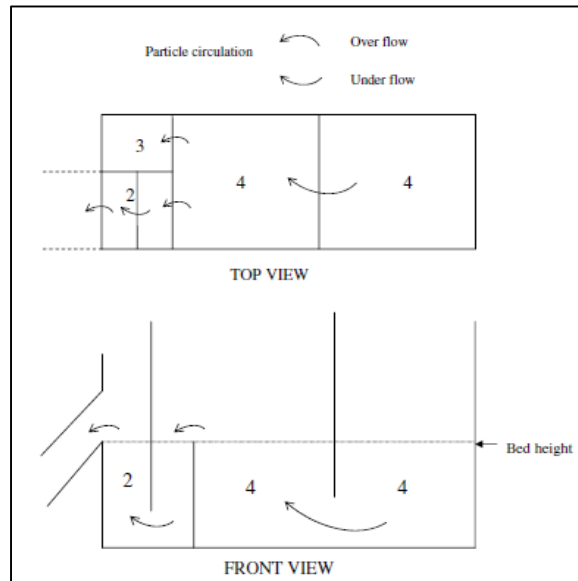


Figure 2.17: Principal layout of the fuel reactor with the particle circulation directions (Berguerand and Lyngfelt, 2008)

Legend: (2) carbon stripper, (3) high velocity part, (4) low velocity part

Berguerand and Lyngfelt (2008) operated a 10 kW CLC for 22 hours, 12 hours of which were under stable conditions, with South African coal and ilmenite as oxygen carrier. The experimental design was quite similar to the one above except the downer was divided into three chambers; low velocity chamber, carbon stripper and high velocity chamber, as shown in Figure 2.17. The solid fuels are gasified, while the oxygen carrier particles are reduced by the volatiles in the low velocity chamber. This chamber is further divided into two parts separated by a wall with an opening at the bottom through which the particles are forced to pass. The unburned carbon is separated from the metal oxide particles in the carbon stripper. The unburned carbon is recovered with a cyclone while the metal oxide particles enter the riser. In the high velocity chamber, a certain proportion of both unburned carbon and metal oxide particles are entrained upwards in order to provide particle recirculation and re-collection back into the downer. Steam is used as the fluidising agent instead of the fuel gas flow. Ilmenite was found to be a suitable oxygen carrier as it has good mechanical properties, low fragmentation/attrition, and good reactivity.

Their experiments detect some key issues with the application of solid fuels in chemical looping combustion. Firstly, they found that the conversion of the fuel in the reactor system is mostly dependent on the residence time of the fuel particles in the fuel reactor and the separation efficiency of the fuel reactor cyclone that recirculates unburned particles. The low conversion rates obtained during their experiments were attributed to the poor efficiency of the cyclone as well as the low reactivity of the fuel (Berguerand and Lynfelt, 2008).

Besides that, they found that the carbon capture is dependent on the loss of unconverted carbon to the air reactor. This was attributed to the low efficiency of the separation in the carbon stripper and the low reactivity of the fuels used. The low reactivity causes the residence time in the fuel reactor to be too short to achieve high conversion for the fuels (Berguerand and Lynfelt, 2008).

Lastly, they found that the degree of gas conversion shows that even with sufficient circulation, unconverted gases are present in the stream from the fuel reactor. The low oxygen demand was attributed to the inadequate contact between the reducing gases released from the particles and the oxygen carrier. They suggested a possibility to deal with the reducing gases in the exhaust from the fuel reactor is by adding an 'oxygen polishing' step downstream where, after the fuel reactor cyclone, pure oxygen is injected into the gas flow to fully oxidize the combustibles to CO₂ and H₂O (Berguerand and Lynfelt, 2008).

Chapter 3 THEORETICAL STUDY

3.1 Fluidisation

Principle of Fluidisation

Fluidisation occurs when the drag force by upward moving gas equals to the weight of the particles or:

Pressure drop across the bed x Cross-sectional area of tube = Volume of bed x Fraction of solids x Specific weight of solids (Kunii & Levenspiel, 1977).

$$\Delta p \cdot A_t = W = (A_t L_{mf})(1 - \varepsilon_{mf}) \left[(\rho_s - \rho_g) \frac{g}{g_c} \right] \quad \text{(Equation 3.1)}$$

$$\frac{\Delta p}{L_{mf}} = (1 - \varepsilon_{mf}) (\rho_s - \rho_g) \frac{g}{g_c} \quad \text{(Equation 3.2)}$$

This phenomenon is caused by the resistance between the particles and the fluid passing through them (Botterill, 1983). As the gas passes through the bed, it is able to convert the bed particles into a suspended and expanded mass. This will cause the bed particles to exhibit liquid like properties and as a result, this will reduce the resistance as the particles will be able to move more freely (van Swaaij and Prins, 1986; Pell and Dunson, 1997). If the air flow rates are below the critical value for the system, complete fluidization will not occur, whereas if the air flow rates are above the threshold, bubbles will form within the sand bed (Pell and Dunson, 1997). Bed expansion is often not uniform when a gas is used and consequently instabilities (bubbles) will form in the bed (Howard, 1989). If expansion and fluidization are more uniform, the mixing is will be more even and will result in a more constant heat transfer during combustion (Valk, 1986).

Minimum and Maximum Fluidising Velocities and Pressure Drop

The fluidising velocity is the speed at which the gas, or liquid, flows through the packed bed to initiate fluidisation. There are five key stages in the behaviour of the bed as the fluidizing velocity is increased. They are: (i) when the bed remains packed; (ii) the occurrence of incipient fluidization; (iii) bubbling of the bed starts; (iv) slugging of the bed ensues; and (v)

entrainment of the bed begins (Botterill, 1983; Howard, 1989). In the first phase, the bed does not change a great deal as the gas initially flows through it. A pressure drop, ΔP , caused by the loss of mechanical energy due to the friction between the particles and gas can be observed (van Swaaij and Prins, 1986). As the gas velocity, the ΔP across the system rises, the magnitude of which depends on the gas and particle properties. Pressure drop through fixed beds of uniformly sized solids can be calculated by using Equation 3.3 correlated by Ergun (Kunii & Levenspiel, 1977):

$$\frac{\Delta p}{L} g_c = 150 \frac{(1 - \varepsilon_m)^2}{\varepsilon_m^3} \frac{\mu u_0}{(\phi_s d_p)^2} + 1.75 \frac{1 - \varepsilon_m}{\varepsilon_m^3} \frac{\rho_g u_0^2}{\phi_s d_p} \quad (\text{Equation 3.3})$$

As the gas flow rate increases further, the second behavioural phase is achieved, as the incipient fluidization of the particles occurs once the minimum fluidization condition is reached. U_{mf} , the superficial velocity at minimum fluidizing condition can be calculated by combining Equations 3.2 and 3.3 (Kunii & Levenspiel, 1977).

$$\frac{1.75}{\phi_s \varepsilon_{mf}^3} \left(\frac{d_p u_{mf} \rho_g}{\mu} \right)^2 + \frac{150(1 - \varepsilon_{mf})}{\phi_s^2 \varepsilon_{mf}^3} \left(\frac{d_p u_{mf} \rho_g}{\mu} \right) = \frac{d_p^3 \rho_g (\rho_s - \rho_g) g}{\mu^2} \quad (\text{Equation 3.4})$$

The distributor plate and the rest of the system are usually designed for a specific ΔP (van Swaaij and Prins, 1986). Once incipient fluidization is achieved, however, the ΔP does not increase further as shown in Figure 3.1, but the bed expands as particles are rearranged to increase bed voidage. As the gas velocity increases, phase three occurs whereby the temperature and composition of the bed become somewhat more homogeneous and this is usually accompanied by the presence of sufficient but non-uniform bubbles. By increasing the fluidizing gas velocity further, phases four and five can be achieved whereby slugging of the bed and subsequent particle entrainment occur respectively. Both cause severe pressure fluctuations across the bed, until so much of the bed has been entrained that the pressure drop decreases. The behaviour of particles fluidised using a liquid instead of a gas is somewhat different, particularly when fluidizing velocities above those inducing incipient fluidization are used (Howard, 1989).

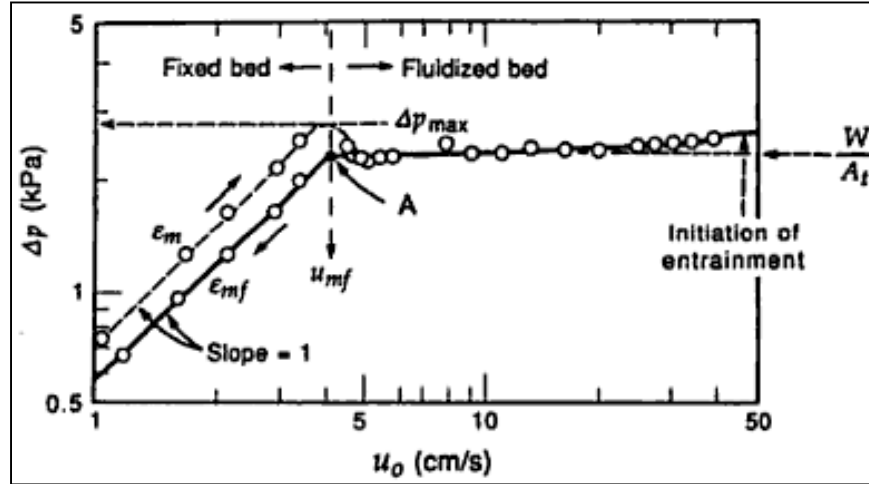


Figure 3.1: Pressure drop against gas velocity for a bed of uniformly sized particles (Kunii and Levenspiel, 1977)

Terminal Velocity, Transport Disengagement Height and Elutriation

The gas flow rate through a fluidized bed is limited on one hand by u_{mf} and on the other by entrainment of solids by the gas. When entrainment occurs these solids must be recycled or replaced by fresh material to maintain steady state operations. This upper limit to gas flow rate is approximated by the terminal or free fall velocity of the particles (Kunii & Levenspiel, 1977), which can be estimated from fluid mechanics by:

$$u_t = \left[\frac{4gd_p(\rho_s - \rho_g)}{3\rho_g C_d} \right]^{\frac{1}{2}} \quad \text{(Equation 3.5)}$$

For both spherical and nonspherical particles the terminal velocity u_t can be obtained from Figure 3.2, an experimental correlation of dimensionless groups $C_d Re_p^2$ versus Re_p (Kunii & Levenspiel, 1977), where:

$$Re_p = \frac{d_p \rho_g u_t}{\mu} \quad \text{(Equation 3.6)}$$

And the velocity independent group (Kunii & Levenspiel, 1977):

$$C_d Re_p^2 = \frac{4gd_p^3 \rho_g (\rho_s - \rho_g)}{3\mu^2} \quad \text{(Equation 3.7)}$$

An alternate way of finding u_t for spherical particles uses analytic expressions for the drag coefficient C_d (Kunii & Levenspiel, 1977).

$$C_{d,spherical} = \frac{24}{Re_p} \quad Re_p < 0.4$$

$$C_{d,spherical} = \frac{10}{Re_p^{1/2}} \quad 0.4 < Re_p < 500$$

$$C_{d,spherical} = 0.43 \quad 500 < Re_p < 200000$$

Replacing the values of C_d obtained into Equation 3.7 gives analytic expressions for u_t (Kunii & Levenspiel, 1977):

$$u_{t,spherical} = \frac{g(\rho_s - \rho_g)d_p^2}{18\mu} \quad Re_p < 0.4$$

$$u_{t,spherical} = \left[\frac{4(\rho_s - \rho_g)^2 g^2}{225 \rho_g \mu} \right]^{1/3} d_p \quad 0.4 < Re_p < 500$$

$$u_{t,spherical} = \left[\frac{3.1g(\rho_s - \rho_g)d_p}{\rho_g} \right] \quad 500 < Re_p < 200000$$

To avoid carry-over of solids from a bed, the gas velocity for fluidized bed operations should be kept somewhere between u_{mf} and u_t . In calculating u_{mf} , the mean diameter for the size distribution present in the bed is used whereas in calculating u_t , the smallest size of solid present in appreciable quantity is used (Kunii & Levenspiel, 1977).

Pinchbeck and Popper (1956) derived an equation to estimate the ratio u_t/u_{mf} for spherical particles, considering the total force holding a particle in suspension as the sum of viscous resistance and fluid impact. Both the upper and lower limits of u_t/u_{mf} may be calculated directly via:

For fine solids, $Re_p < 0.4$: $u_t/u_{mf} = 91.6$

For large, solids, $Re_p > 1000$: $u_t/u_{mf} = 9.16$

The ratio u_t/u_{mf} is usually between 10:1 and 90:1 and is one indication of the flexibility of possible operations. The ratio u_t/u_{mf} is smaller for large sized particles, indicating less flexibility than for smaller particles. It is also an indication of the maximum possible height of the fluidized bed. This is because the pressure drop through the bed results in an increase in gas velocity through the bed. Thus the maximum height of bed is where the bed is just fluidized at the bottom and where u_t is just reached at the top. These considerations of maximum height of bed and narrowed range of operations do not apply to liquid fluidized bed because the density of fluid remains essentially unchanged (Kunii & Levenspiel, 1977).

The range of satisfactory operations of a gas fluidized bed may be considerably narrowed by channelling and slugging. This is especially serious with large, uniformed sized particles where it is often difficult to fluidize the bed. With proper use of baffles or in tapered vessels, this undesirable behaviour can be reduced (Kunii & Levenspiel, 1977).

Violently bubbling fluidized bed can be made to operate at gas velocities in excess of the terminal velocity of practically all the solids, with some entrainment, which may not be severe. This is possible because the major portion of the gas flows through the bed as large, practically solid free gas bubbles while the bed solids are suspended by a relatively slow moving gas. In addition, by using cyclone separators to return the entrained solids, even higher gas velocities can be used (Kunii & Levenspiel, 1977).

A related concept to u_t is the transport disengagement height (TDH), which is the distance above the bed at which particle entrainment and elutriation become constant, also known as the transport disengagement zone (Pell and Dunson, 1997). This TDH is also the term used to describe the sufficient height of the freeboard to limit the amount of particles that are lost; these two different definitions are sometimes referred to as the TDH_C and TDH_F, respectively for coarse (C) and fine (F) particles (Howard, 1989). It is therefore vital that enough freeboard height is provided to ensure that any disengaged particles above the surface of the bed will fall back to the bed from the gas stream (Howard, 1989). This ensures that particles are not lost from the system and carried out with the gas emissions. Elutriation occurs at extreme velocities as it is caused particularly by bubbles bursting at the surface (Botterill,

1983). Providing a sufficient TDH is necessary for appropriate solid loading and size distribution within the fluid; it is also important that heights which dramatically exceed the TDH are not used, as this not only increases the cost of construction, but also the height needed to house the vessel (Howard, 1989).

Types of fluidisation

On increasing the fluid velocity up to the point of fluidisation, flow patterns are usually well described by Darcy's law. However, after the fluidisation point, two very distinct types of fluid flow are observed: particulate and aggregative fluidization. In the former case the bed behaves in a uniform manner: as the flow rate is increased the bed height increases; hence, the increasing fluid flow simply goes to expand the bed as shown in Figure. The overall pressure drop remains constant, and equal to the bed height per unit area, until entrained particles are elutriated out by the fluid flow.

In aggregating, or bubbling, fluidisation aggregates (of fluid) may be observed within the fluidized bed that move rapidly to the surface. This type of fluidization is often associated with the fluidization of solids using gases.

In an aggregative fluidised bed the fluid can pass through the bed in a similar fashion to particulate fluidization and bubbles of fluid form. The bubbles may travel very quickly through the bed – hence in the case of catalytic of hydrocarbons this provides a way in which some hydrocarbon vapour can by-pass the catalyst and, therefore, reaction. So, a bubbling bed has an emulsion phase surrounding the bubble and a lean phase where the bubble is lean of solids.

Froude number:

$$Fr = \frac{u_{mf}^2}{xg} \quad (\text{Equation 3.8})$$

For high (>1) values bubbling is more likely. Other correlations include the use of Reynolds number, density ratio and bed ratio:

$$\text{Re}' = \frac{xu_{mf}\rho_g}{\mu}; \frac{\rho_s - \rho_g}{\rho_g}; \frac{L_{mf}}{d_b} \quad (\text{Equation 3.9})$$

$$\text{Fr Re}' = \left(\frac{\rho_s - \rho_g}{\rho_g} \right) \left(\frac{L_{mf}}{d_b} \right) < 100 \quad \text{Particulate fluidisation}$$

$$\text{Fr Re}' = \left(\frac{\rho_s - \rho_g}{\rho_g} \right) \left(\frac{L_{mf}}{d_b} \right) > 100 \quad \text{Bubbling fluidisation}$$

3.2 Minimisation of Gibbs Free Energy

Two methods of equilibrium analysis can be employed. They are minimisation of Gibbs free energy and method of independent reactions. Minimisation of Gibbs free energy was preferred due to its flexibility. This is because the method of independent reactions has the disadvantage in that an extra reaction must be added for every component added into the system.

The following section was adapted from Brown (2010). In order to establish the basis of the minimisation of Gibbs free energy, consider an isothermal, isobaric system. At equilibrium the total Gibbs free energy of the system, G , is at minimum i.e.

$$dG = 0 \quad (\text{Equation 3.10})$$

where the total Gibbs free energy is given by:

$$G = \sum_i \bar{G}_i n_i \quad (\text{Equation 3.11})$$

That is, total Gibbs free energy is equal to the sum of the product of the partial molar free energy of species i , \bar{G}_i , and the number of moles of species i , n_i . At a given temperature, T , and pressure, P , the partial molar free energy of species i can be expressed as follows:

$$\bar{G}_i = G_i^0 + RT \ln \left(\frac{f_i}{f_i^0} \right) \quad (\text{Equation 3.12})$$

where G_i^0 is the standard molar Gibbs free energy of the pure species i and f_i/f_i^0 is the ratio of the fugacity of species i in the mixture to the fugacity of the pure species at the reference state. This ratio can be further simplified since the gas is considered to be 'ideal' at the reference state, so f_i^0 can be replaced with P^0 (the referenced pressure). Furthermore, $f_i = y_i P \phi_i$, where y_i is the mole fraction of species i and ϕ_i , the fugacity coefficient, is equal to unity for ideal gases. The ideal gas assumption is valid for high temperatures and low pressures, both of which are consistent with the proposed system. Thus,

$$G = \sum_i \left(G_i^0 + RT \ln \left(\frac{n_i P}{n_{tot} P^0} \right) \right) \cdot n_i \quad (\text{Equation 3.13})$$

where n_i is the number of moles of species i and n_{tot} the total number of moles in the system. Differentiating Equation 3.13 results in:

$$dG = \sum_i n_i d\bar{G}_i + \sum_i \bar{G}_i dn_i = 0 \quad (\text{Equation 3.14})$$

The first term is zero at constant temperature and pressure, in accordance with the Gibbs Duhem equation.

Two constraints must be imposed on the system. Firstly, that mass is conserved according to the following elemental balance:

$$\sum_i \alpha_{ij} n_i - e_j = 0 \quad (\text{Equation 3.15})$$

where α_{ij} is the total number of atoms of element j in species i , and e_j is the total number of moles of element j in the mixture. Secondly, to avoid negative concentrations of species, a non-negativity constraint is imposed on the solid species, i.e.:

$$n_i \geq 0 \quad (\text{Equation 3.16})$$

Combining Equations 3.11, 3.15 and 3.16 results in a constrained minimisation problem. Using Lagrange's method of undetermined multipliers, the following objective function, Θ , is obtained:

$$\Theta = \sum_i \bar{G}_i n_i + \sum_j \lambda_j \left(e_j - \sum_i \alpha_{ij} n_i \right) + \sum_i \gamma_i n_i \quad (\text{Equation 3.17})$$

where λ_i and γ_i are Lagrange multipliers. The minimum of this new function must now be obtained. Thus the objective function is partially differentiated with respect to the independent variables (n_i , λ_i and γ_i) and set equal to zero, resulting in the following:

$$\frac{\partial \Theta}{\partial n_i} = 0 \Rightarrow \bar{G}_i - \sum_j \lambda_j \alpha_{ij} + \gamma_i = 0 \quad (\text{Equation 3.18})$$

$$\frac{\partial \Theta}{\partial \lambda_j} = 0 \Rightarrow e_j - \sum_i \lambda_i n_{ij} = 0 \quad (\text{Equation 3.19})$$

$$n_i > 0 \Leftrightarrow \gamma_i = 0 \quad (\text{inactive}) \quad (\text{Equation 3.20})$$

$$n_i = 0 \Leftrightarrow \gamma_i < 0 \quad (\text{active}) \quad (\text{Equation 3.21})$$

Equations 3.18 to 3.21 were solved at a given pressure and temperature using a reduced step Newton method. For all components the free energy of formation, $\Delta \underline{G}_{fi}^\circ$, at 1 bara and at the temperature of interest was used. For gases, ideal behaviour was assumed and \bar{G}_i was calculated from

$$\bar{G}_i = \underline{G}_{fi}^\circ(T) + RT \cdot \ln \left(\frac{P}{1 \text{ bara}} \right) + RT \cdot \ln \left(\frac{n_i}{\sum_{i \in \text{gas phase}} n_i} \right) \quad (\text{Equation 3.22})$$

while solid species were assumed to have a fixed chemical potential at a given T and P , thus

$$\bar{G}_i = \underline{G}_{fi}^\circ(T) \quad (\text{Equation 3.23})$$

$\Delta G_{fi}^{\circ}(T)$ was calculated from:

$$\Delta G_{fi}^{\circ}(T) = \Delta H_{fi}^{\circ}(T) - T \cdot \Delta S_{fi}^{\circ}(T) \quad (\text{Equation 3.24})$$

where the partial molar enthalpies and entropies were calculated from the enthalpies of formation at a reference temperature of 298 K.

$$\bar{H}_i(T) = \Delta H_{fi}(T_{ref}) - \int_{T_{ref}}^T C_{p_i}(T) dT \quad (\text{Equation 3.25})$$

and

$$C_{p_i}(T) = a_i + b_i \cdot T + c_i \cdot T^2 + d_i \cdot T^3 \quad (\text{Equation 3.26})$$

Equilibrium Constant

The relationship between Gibbs free energy and the equilibrium constant is as follows:

$$K_a(T) = \exp\left(-\frac{\Delta G_{rxn}^{\circ}}{RT}\right) \quad (\text{Equation 3.27})$$

where K_a is the equilibrium constant in terms of activity, ΔG_{rxn}° is the standard Gibbs free energy of reaction and R is the universal gas constant. K_a is related to the species' activities at equilibrium,

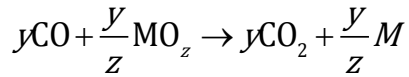
$$K_a(T) = \prod_{i=1}^c a_i^{v_i} = \frac{a_R^{\rho} \dots}{a_A^{\alpha} a_B^{\beta} \dots} \quad (\text{Equation 3.28})$$

where a_i is the activity and v_i is the stoichiometric coefficient of species i , respectively. For a species in a gaseous mixture at low or moderate pressure the activity of the species can be simplified to

$$a_i = \frac{y_i P}{1 \text{ bar}} = \frac{P_i}{1 \text{ bar}} \quad (\text{Equation 3.29})$$

For pure solids the activity is equal to unity.

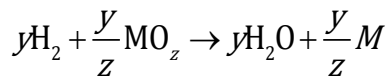
Coal-derived syngas, which is composed of CO, H₂ and CH₄ is a frequently used fuel in chemical looping combustion processes. In these processes, metal oxide is first reduced with syngas and then regenerated with steam and/or air. Specifically, the reduction of metal oxide with CO can be written as:



The equilibrium constant is then defined as:

$$K_{eq1} = \frac{P_{CO_2}^y}{P_{CO}^y} \quad (\text{Equation 3.30})$$

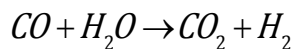
where P is the total pressure or the partial pressure of a gaseous species. Similarly, the reduction reaction between metal oxide and H₂ is:



The equilibrium constant is

$$K_{eq2} = \frac{P_{H_2O}^y}{P_{H_2}^y} \quad (\text{Equation 3.31})$$

It is noted that when the reducing gas is a mixture of CO and H₂, the reaction among CO, H₂, H₂O and CO₂ also will take place:



The above water gas shift (WGS) reaction has the equilibrium constant of:

$$K_{eq3} = \frac{P_{CO_2} P_{H_2}}{P_{CO} P_{H_2O}} \quad (\text{Equation 3.32})$$

K_{eq3} can be expressed in terms of K_{eq1} and K_{eq2} by combining equations to form:

$$K_{eq3} = \left(\frac{K_{eq1}}{K_{eq2}} \right)^{\frac{1}{y}} \quad (\text{Equation 3.33})$$

Therefore, the overall thermodynamic equilibrium condition for a system composed of metal oxide, CO, H₂ and their reaction products is determined by K_{eq1} and K_{eq2} . It can also be shown that the molar fractions of CO and H₂ exiting from the reducer, x , can be expressed by:

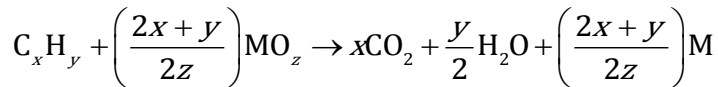
$$x = \frac{P_{CO} + P_{H_2}}{P_{CO} + P_{H_2} + P_{CO_2} + P_{H_2O}} \quad (\text{Equation 3.34})$$

The initial CO fraction in the syngas f_{CO}^0 can be derived as:

$$x = \frac{f_{CO}^0}{1 + K_{eq1}^{\frac{1}{y}}} + \frac{(1 - f_{CO}^0)}{1 + K_{eq2}^{\frac{1}{y}}} \quad (\text{Equation 3.35})$$

where x represents the minimum amount of CO and H₂ exiting from the reducing step and is an important parameter for the selection of particles as oxygen carriers. An ideal oxygen carrier particle should have a very small value of x .

The general equation for the reduction of hydrocarbon can be written as:



The equilibrium constant is defined as:

$$K_{eq} = \frac{P_{CO_2}^x P_{H_2O}^{\frac{y}{2}}}{P_{C_xH_y}} \quad (\text{Equation 3.36})$$

Without considering other reactions such as the Boudouard's reaction and reforming reactions, the maximum equilibrium hydrocarbon conversion θ at a given total pressure P_0 can be expressed by the following equation:

$$K = \frac{x^x \left(\frac{y}{2}\right)^{\frac{y}{2}} \theta^{x+\frac{y}{2}} P_0^{x+\frac{y}{2}-1}}{(1-\theta) \left[1 + \theta \left(x + \frac{y}{2} - 1\right)\right]^{x+\frac{y}{2}-1}} \quad (\text{Equation 3.37})$$

Heat Balance

The heat balance for a steady flow system is given by:

$$Q_E = H_f^{fuel} + \sum_i (n_i \bar{H}_i)_{feed} - \sum_i (n_i \bar{H}_i)_{product} \quad (\text{Equation 3.38})$$

where \bar{H}_i is the partial molar enthalpy of species i and H_f^{fuel} is the heat of formation of the fuel at 298 K. It should be noted that Q_E is defined with respect to the surroundings such that a negative value implies that heat must be supplied from the surroundings. H_f^{fuel} was calculated from the equation given by Li et al. (2001) as follows:

$$H_f^{fuel} = HHV - (327.63C + 1417.94H) \quad (\text{Equation 3.39})$$

where HHV is the higher heating value of the fuel calculated from the equation given by Cordero et al. (2001):

$$HHV = 357.8C + 1135.6H + 54.9N + 119.5S - 85.4O - 974 \quad (\text{Equation 3.40})$$

where C, H, N, S and O are the mass fractions of carbon, hydrogen, nitrogen, sulphur and oxygen in the fuel. The reactor was assumed to be isothermal, the outlet temperature of the product species was set and the model calculated the heat load required to maintain that temperature. The inlet temperature for all cases was assumed to be the same as the

temperature of the reactor. Thus, the energy required to heat the reactants was not considered.

3.3 Oxygen Carrier Chemistry and Thermodynamics

3.3.1 Iron Oxide

The following are the reaction schemes for the reduction of iron oxide in syngas and pyrolysis gas at 800°C and for the oxidation of iron oxide in air at 800°C were calculated based on data found in NASA Glenn Thermodynamics Properties (McBride et al., 2002).



$$\Delta G = -33.9 \text{ kJ mol}^{-1}, \Delta H = -12.5 \text{ kJ mol}^{-1}, \Delta S = 19.9 \text{ J K}^{-1} \text{ mol}^{-1}$$



$$\Delta G = -33.8 \text{ kJ mol}^{-1}, \Delta H = -1.25 \text{ kJ mol}^{-1}, \Delta S = 30.4 \text{ J K}^{-1} \text{ mol}^{-1}$$



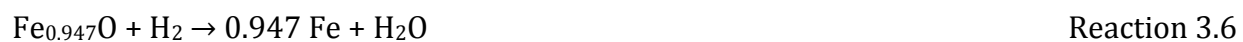
$$\Delta G = -3.7 \text{ kJ mol}^{-1}, \Delta H = 17.6 \text{ kJ mol}^{-1}, \Delta S = 19.9 \text{ J K}^{-1} \text{ mol}^{-1}$$



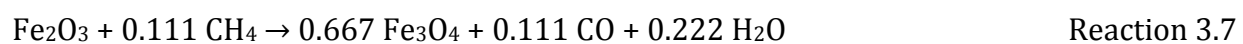
$$\Delta G = -3.19 \text{ kJ mol}^{-1}, \Delta H = 45.9 \text{ kJ mol}^{-1}, \Delta S = 45.8 \text{ J K}^{-1} \text{ mol}^{-1}$$



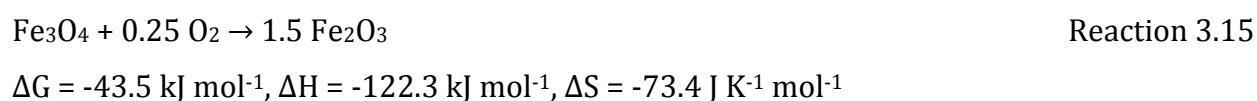
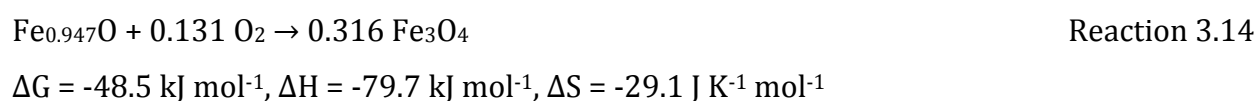
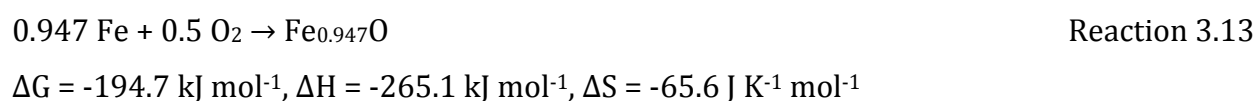
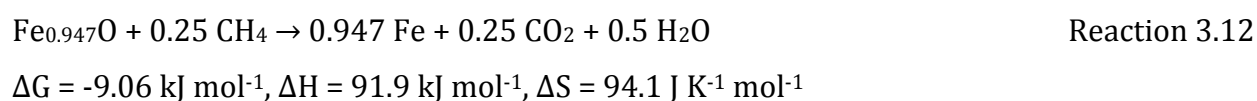
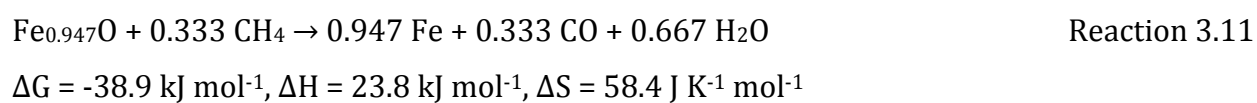
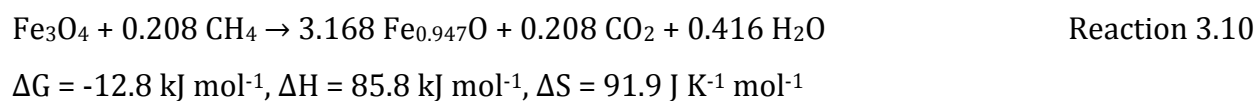
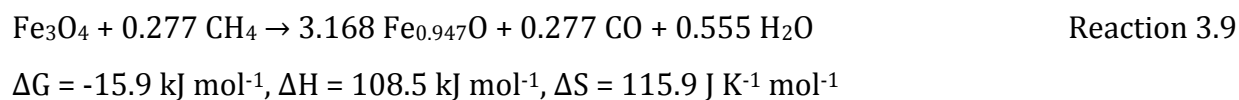
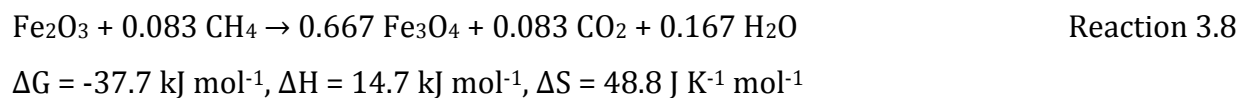
$$\Delta G = 5.44 \text{ kJ mol}^{-1}, \Delta H = -17.3 \text{ kJ mol}^{-1}, \Delta S = -21.2 \text{ J K}^{-1} \text{ mol}^{-1}$$



$$\Delta G = 6.15 \text{ kJ mol}^{-1}, \Delta H = 16.8 \text{ kJ mol}^{-1}, \Delta S = 9.91 \text{ J K}^{-1} \text{ mol}^{-1}$$



$$\Delta G = -38.9 \text{ kJ mol}^{-1}, \Delta H = 23.8 \text{ kJ mol}^{-1}, \Delta S = 58.4 \text{ J K}^{-1} \text{ mol}^{-1}$$



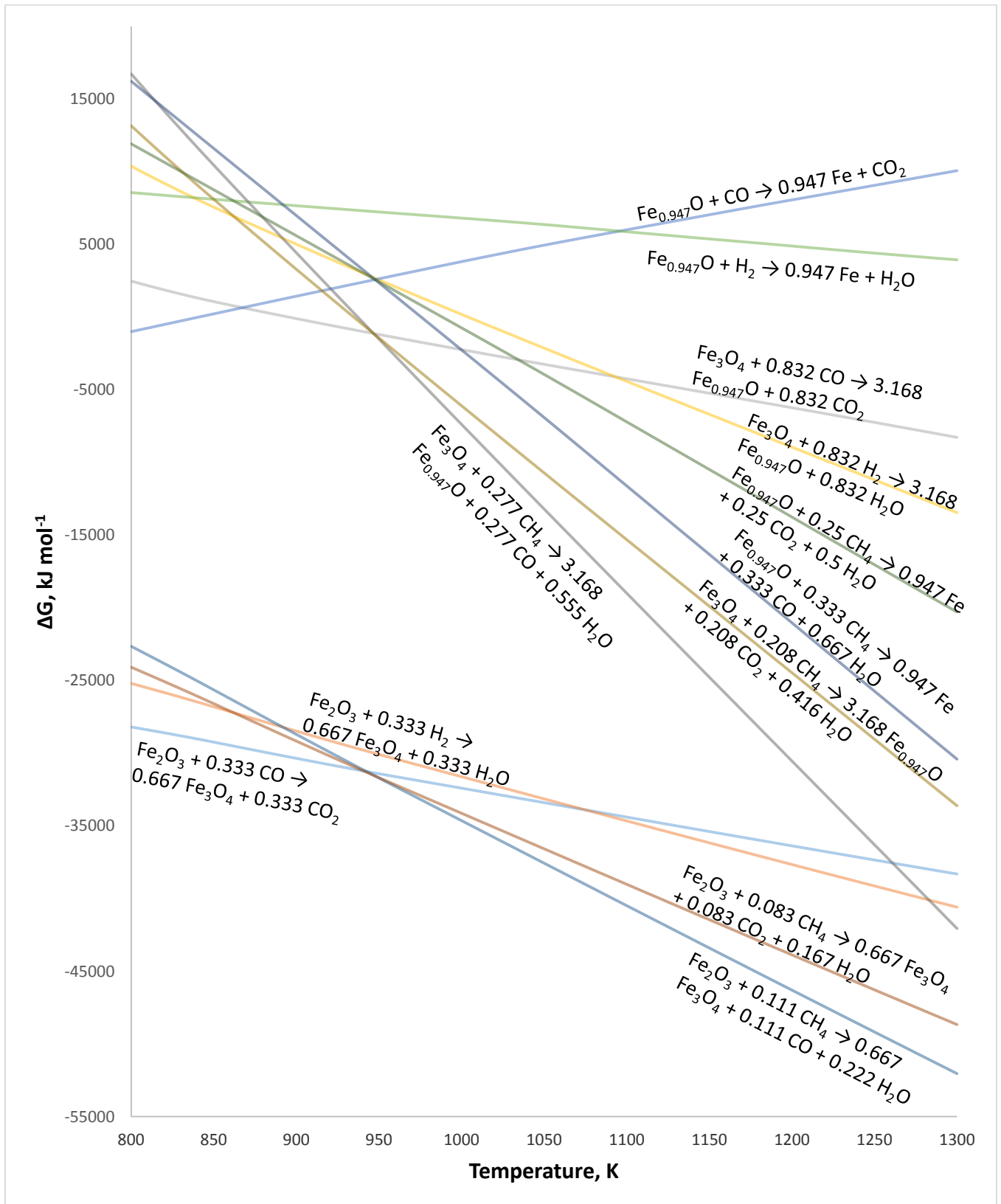


Figure 3.2: Ellingham diagram for the reduction of iron oxide

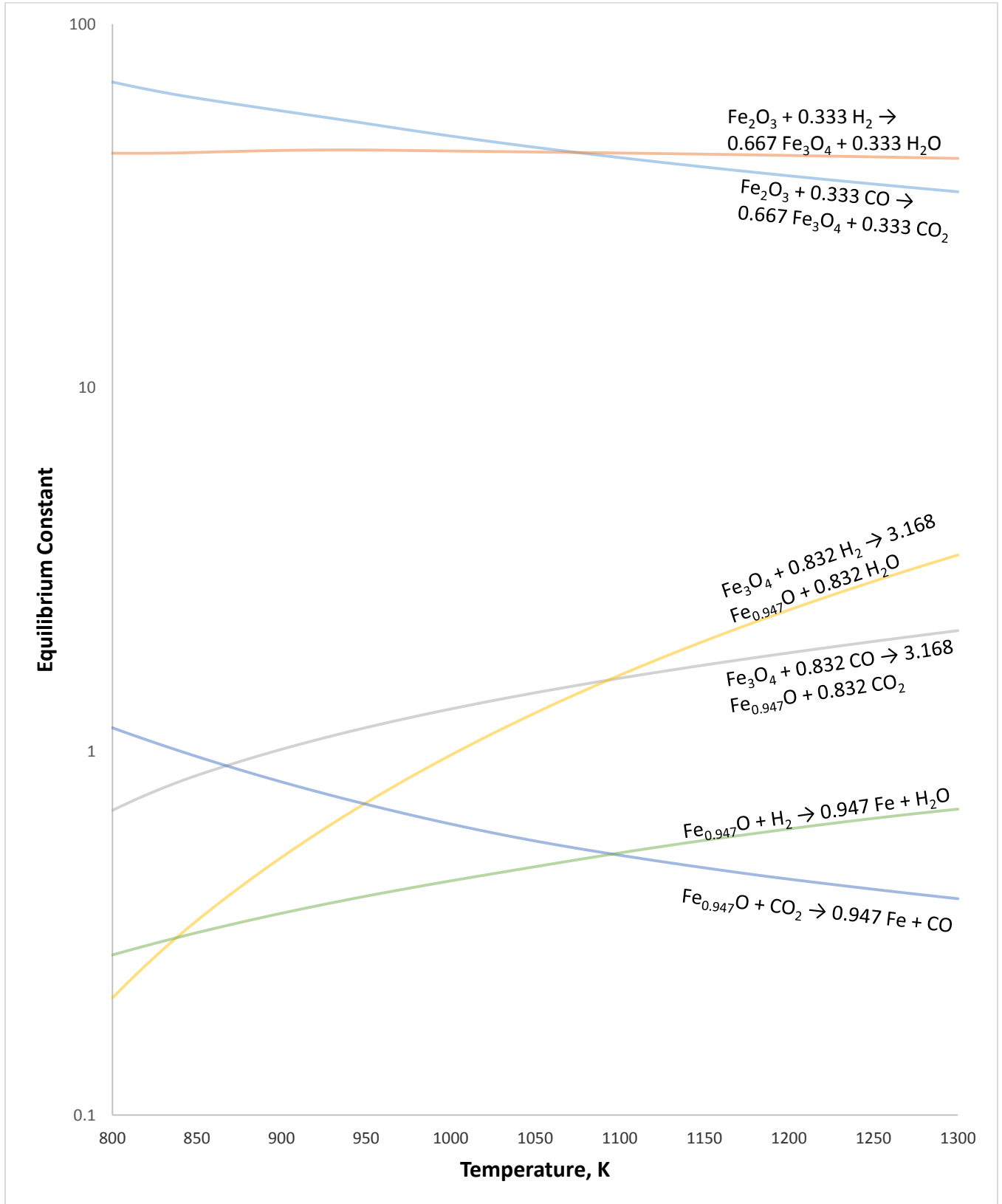


Figure 3.3: Equilibrium ratio for the reduction of iron oxide in syngas

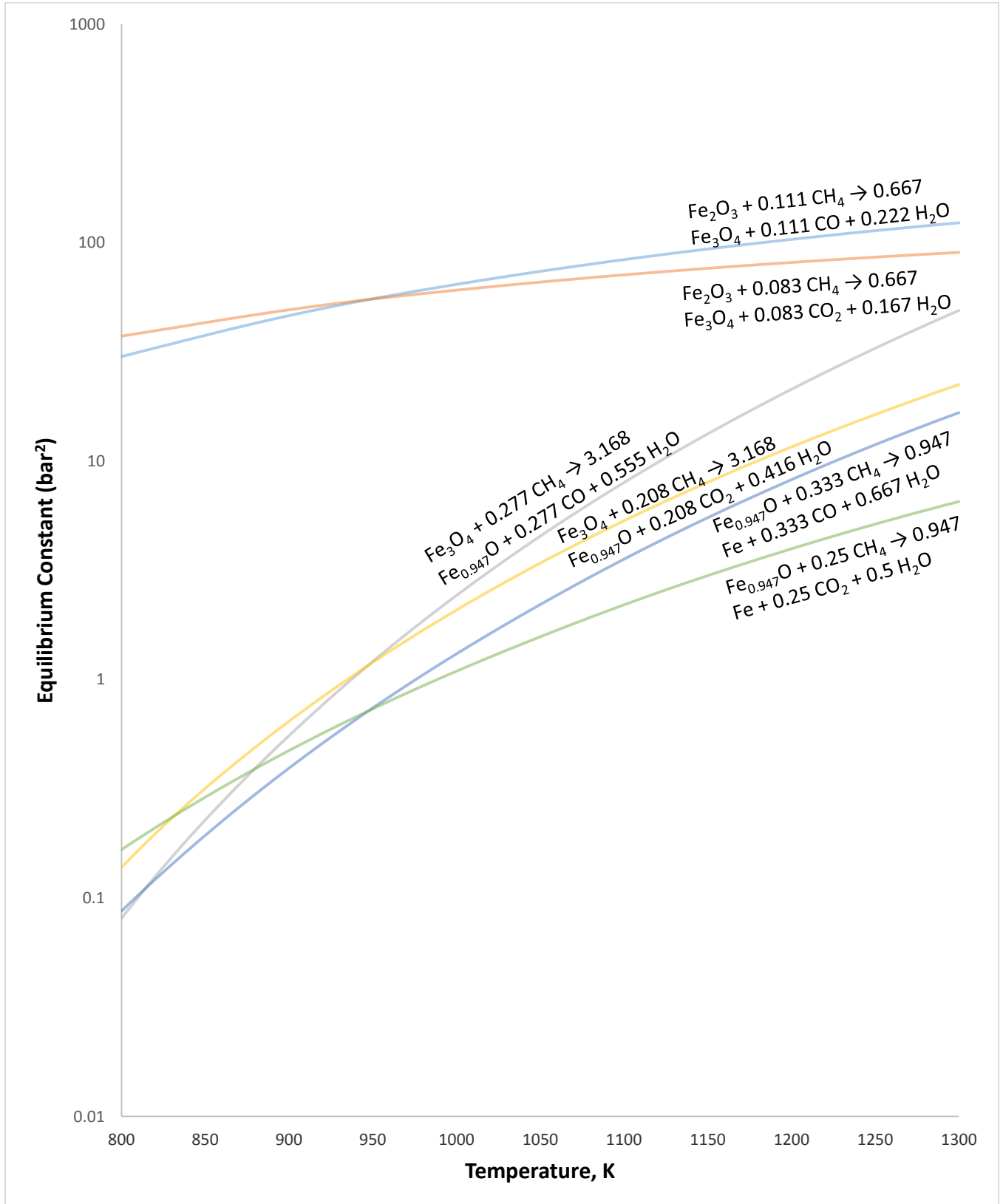


Figure 3.4: Equilibrium constant for the reduction of iron oxide with methane

Figure 3.2 shows the Ellingham diagram for the reduction of iron oxide with syngas and methane. Figure 3.2 illustrates the feasibility for the reaction to occur at a particular reaction temperature used in the reactor as a particular reaction is feasible if it has a $\Delta G < 0$. The reduction of iron oxide in syngas can be seen in Figures 3.2 and 3.3. It can be seen from both figures that Fe_2O_3 can be easily reduced to Fe_3O_4 in the presence of syngas. Besides that, Fe_3O_4 can be sustained in the reactor if the equilibrium ratio of $P_{\text{CO}_2}/P_{\text{CO}}$ is above 1. Being able to sustain the reduction of Fe_2O_3 to Fe_3O_4 reduces the undesirable effects such as particle agglomeration, particle unable to regenerate back to its original oxidation form, enhanced rate of attrition due to the fragmented nature of the reduced iron oxide especially at its lowest oxidation form (Fe) and carbon deposition on iron oxide if Fe_2O_3 is reduced to $\text{Fe}_{0.947}\text{O}$ or Fe. However, this will increase Fe_2O_3 loading in the reactor in order to achieve similar amount of reduction. Figure 3.3 also highlights the fact that Fe_3O_4 and $\text{Fe}_{0.947}\text{O}$ can be sustained in their particular state without undergoing further reduction that will reduce them to a lower oxidation form if desired. This is because Fe_2O_3 , Fe_3O_4 , $\text{Fe}_{0.947}\text{O}$ and Fe have their own equilibrium ratio of $P_{\text{CO}_2}/P_{\text{CO}}$ regions which can be easily distinguish from one another.

The reduction of iron oxide in methane can be seen in Figures 3.2 and 3.4. It can be seen from both figures that Fe_2O_3 can be easily reduced to Fe_3O_4 in methane. However, at low reaction temperatures, Fe_3O_4 does not further reduce into $\text{Fe}_{0.947}\text{O}$ or Fe due to the positive ΔG values. At higher temperatures, Fe_2O_3 can be easily reduced to $\text{Fe}_{0.947}\text{O}$ or Fe due to the close proximity of the ΔG values of these reactions as well as the equilibrium constant regions of Fe_2O_3 , Fe_3O_4 , $\text{Fe}_{0.947}\text{O}$ and Fe at high temperatures. It was calculated from Equation 3.37 that a 90% conversion of CH_4 at 1 bar requires an equilibrium constant of 3.7 bar² whereas a 98% conversion of CH_4 at 1 bar requires an equilibrium constant of 49 bar². From Figure 3.3, it can thus be deduced that Fe_2O_3 can be reduced easily to $\text{Fe}_{0.947}\text{O}$ at operating conditions used in chemical looping combustion. This has a major influence in the reduction of iron oxide with solid fuels as the pyrolysis of solid fuel produces CO, H₂ and CH₄ thereby causing Fe_2O_3 to be reduced to a lower oxidation form than intended.

3.3.2 Copper Oxide

The following are the reaction schemes for the reduction of copper oxide in syngas and pyrolysis gas at 800°C and for the oxidation of copper oxide in air at 800°C were calculated based on data found in NASA Glenn Thermodynamics Properties (McBride et al., 2002).



$$\Delta G = -79.9 \text{ kJ mol}^{-1}, \Delta H = -75.4 \text{ kJ mol}^{-1}, \Delta S = 4.16 \text{ J K}^{-1} \text{ mol}^{-1}$$



$$\Delta G = -79.5 \text{ kJ mol}^{-1}, \Delta H = -58.4 \text{ kJ mol}^{-1}, \Delta S = 19.7 \text{ J K}^{-1} \text{ mol}^{-1}$$



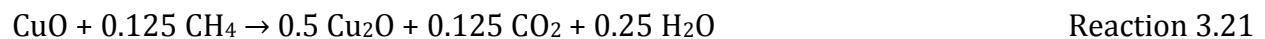
$$\Delta G = -98.9 \text{ kJ mol}^{-1}, \Delta H = -115 \text{ kJ mol}^{-1}, \Delta S = -15 \text{ J K}^{-1} \text{ mol}^{-1}$$



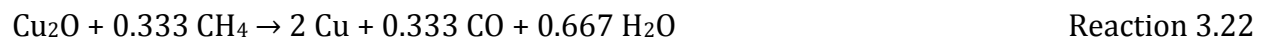
$$\Delta G = -98.2 \text{ kJ mol}^{-1}, \Delta H = -81 \text{ kJ mol}^{-1}, \Delta S = 16.1 \text{ J K}^{-1} \text{ mol}^{-1}$$



$$\Delta G = -87.1 \text{ kJ mol}^{-1}, \Delta H = -20.8 \text{ kJ mol}^{-1}, \Delta S = 61.8 \text{ J K}^{-1} \text{ mol}^{-1}$$



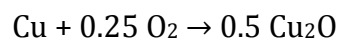
$$\Delta G = -85.3 \text{ kJ mol}^{-1}, \Delta H = -34.5 \text{ kJ mol}^{-1}, \Delta S = 47.4 \text{ J K}^{-1} \text{ mol}^{-1}$$



$$\Delta G = -113.4 \text{ kJ mol}^{-1}, \Delta H = -5.79 \text{ kJ mol}^{-1}, \Delta S = 100.3 \text{ J K}^{-1} \text{ mol}^{-1}$$



$$\Delta G = -109.8 \text{ kJ mol}^{-1}, \Delta H = -33.1 \text{ kJ mol}^{-1}, \Delta S = 71.5 \text{ J K}^{-1} \text{ mol}^{-1}$$



Reaction 3.24

$$\Delta G = -45.2 \text{ kJ mol}^{-1}, \Delta H = -83.7 \text{ kJ mol}^{-1}, \Delta S = -35.9 \text{ J K}^{-1} \text{ mol}^{-1}$$



Reaction 3.25

$$\Delta G = -29.5 \text{ kJ mol}^{-1}, \Delta H = -131.5 \text{ kJ mol}^{-1}, \Delta S = -95.1 \text{ J K}^{-1} \text{ mol}^{-1}$$

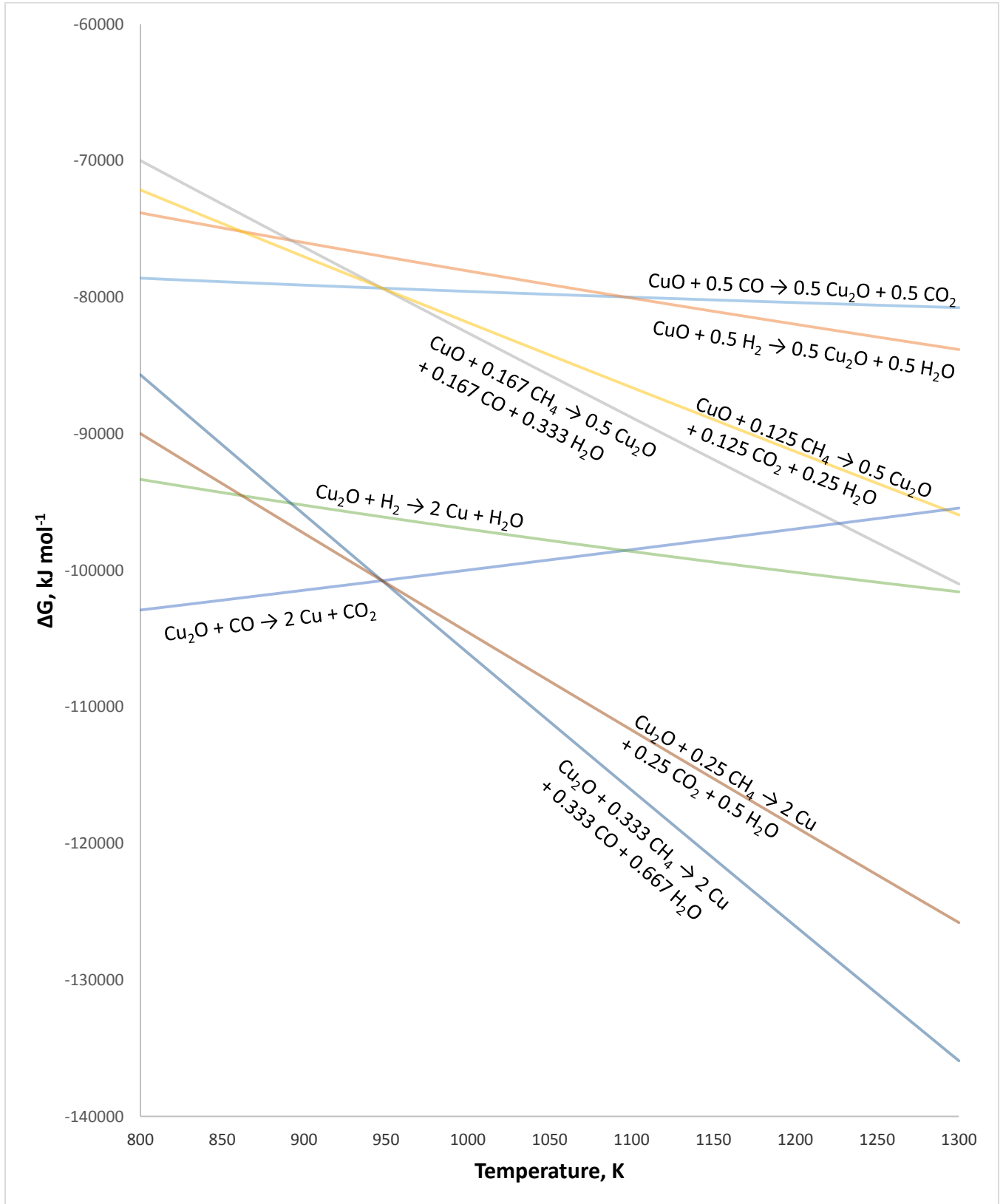


Figure 3.5: Ellingham diagram for the reduction of copper oxide

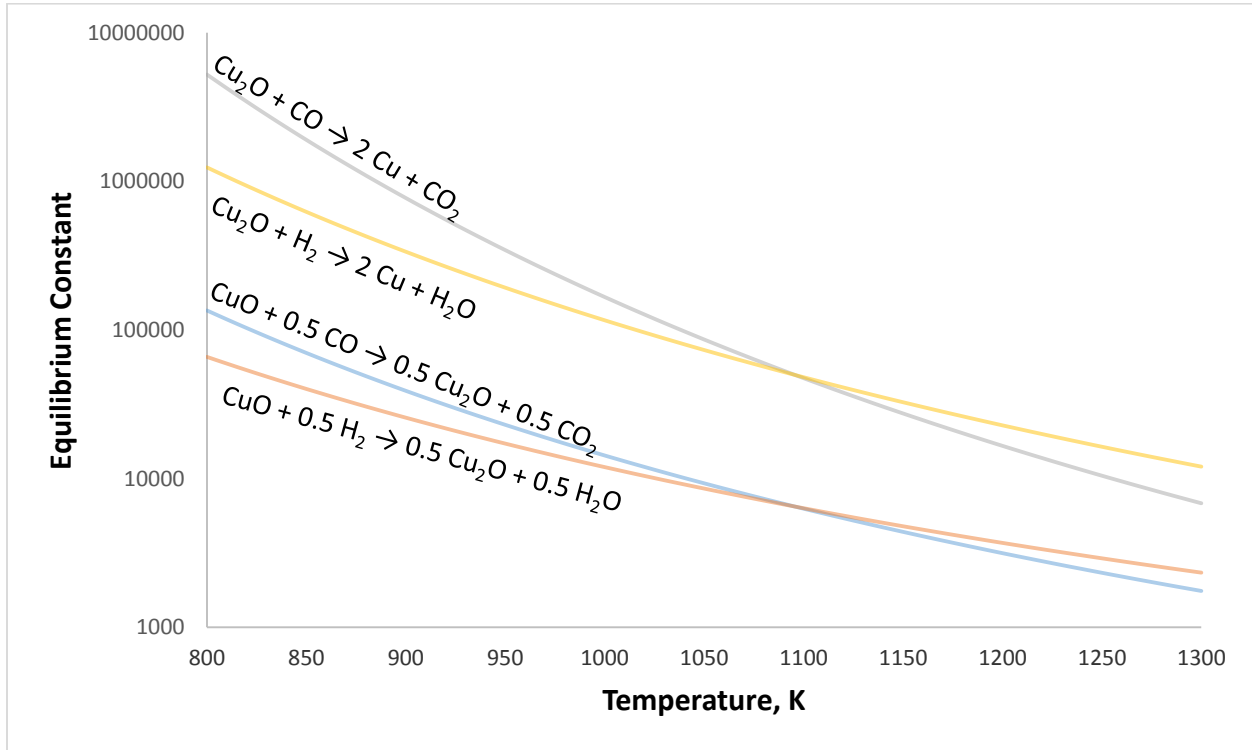


Figure 3.6: Equilibrium ratio for the reduction of copper oxide in syngas

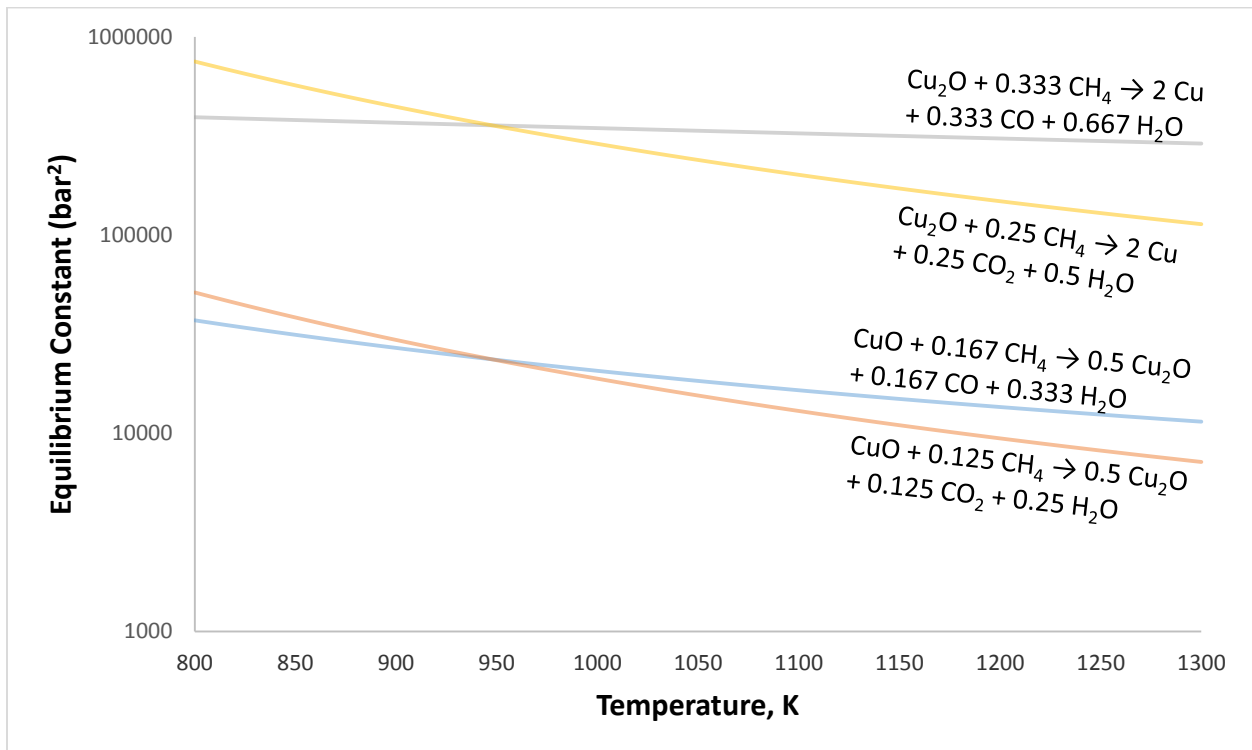


Figure 3.7: Equilibrium constant for the reduction of copper oxide with methane

Figure 3.5 shows the Ellingham diagram for the reduction of copper oxide with syngas and methane. Figure 3.5 illustrates the feasibility for the reaction to occur at a particular reaction temperature used in the reactor as a particular reaction is feasible if it has a $\Delta G < 0$. The reduction of copper oxide in syngas can be seen in Figures 3.5 and 3.6. It can be seen from both figures that CuO can be easily reduced to Cu₂O and Cu in the presence of syngas. Besides that, Figure 3.6 also highlights the difficulty to sustain the reduction of CuO in a way that it will only reduce to Cu₂O due to the highly negative ΔG value as well as the high equilibrium ratio of P_{CO_2}/P_{CO} required to sustain Cu₂O at its oxidation form. As a result, it is difficult to verify if the reduction of CuO will go through the intermediate step to Cu₂O before Cu₂O is further reduced to Cu. However, without being able to sustain the reduction of CuO to Cu₂O increases the undesirable effects such as particle agglomeration, particle unable to regenerate back to its original oxidation form, enhanced rate of attrition due to the fragmented nature of the reduced copper oxide especially at its lowest oxidation form (Cu) and carbon deposition on copper oxide if CuO is reduced Cu.

Some of these issues can be solved by introducing a support such as alumina into the metal oxide during the preparation of the metal oxide. This is due to the fact that support does not react with the reducing or oxidising agents. As a result, they help maintain the form or integrity of the metal oxide during reduction and oxidation.

Figures 3.6 and 3.7 depict the strength in using copper oxide as oxygen carrier for chemical looping combustion. This is due to the relative ease for copper oxide to convert syngas and hydrocarbons into carbon dioxide and steam at relatively low temperatures. It was calculated from Equation 3.37 that a 90% conversion of CH₄ at 1 bar requires an equilibrium constant of 3.7 bar² whereas a 98% conversion of CH₄ at 1 bar requires an equilibrium constant of 49 bar². From Figure 3.7, it can be seen that nearly all CH₄ present in the pyrolysis gas will reduce CuO to Cu at relatively low operating temperatures.

3.4 Particle Reaction Mechanism

In most studies of the reduction and oxidation of metal oxides, it is assumed that the gas-solid reaction is carried out in the following steps:

Step 1: Diffusion and/or convection of gaseous reactant across the gas film to the surface of the particle

Step 2: Diffusion of gaseous reactant through the pores of the particle

Step 3: Adsorption of the gaseous reactant onto the reactive pore surface

Step 4: Chemical reaction on the pore surface

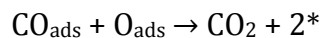
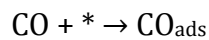
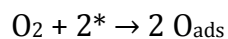
Step 5: Desorption of gaseous product from the pore surface

Step 6: Diffusion of gaseous product out of the particle

Step 7: Diffusion and/or convection of gaseous product across the gas film to the bulk gas phase.

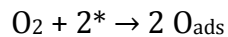
Oxidation of Carbon Monoxide with Metal and Metal Oxides

The oxidation of carbon monoxide over metals is thought to follow either the Langmuir – Hinshelwood mechanism or the Eley – Ridel mechanism whereas the oxidation of carbon monoxide over metal oxides is thought to follow the Mars and van Krevelen mechanism. When the reaction mechanism follows the Langmuir – Hinshelwood route, the reaction pathway is as follows (Iablokov, 2011):

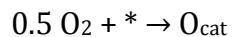
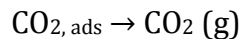
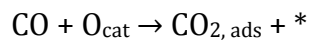


where * depicts a free site on the metal surface. Carbon dioxide formed is only weakly adsorbed and as a result, it will not affect the rate substantially as it is quickly desorbed into the gas phase. Langmuir – Hinshelwood mechanism does not involve the formation of surface carbonate species as intermediates. The rate of reaction will then be proportional to the surface coverage of O_{ads} and CO_{ads} (Iablokov, 2011).

Eley-Rideal mechanism is the preferred route when the gas phase carbon monoxide reacts directly with the adsorbed oxygen (Iablokov, 2011).



Mars and van Krevelen (1954) suggested that the oxidation of carbon monoxide with metal oxides follows a stepwise mechanism. In the first stage, the reactant is oxidized by surface lattice oxygen in the metal oxide. This will create an oxygen vacancy that will reduce the neighbouring metal ions into a lower oxidation state. In the second stage, the surface metal atoms are reoxidised by gas-phase oxygen.



where * depicts an oxygen vacancy and O_{cat} is a surface lattice oxygen. The oxidation of carbon monoxide with metal oxides will thus occur via a redox mechanism whereby the metal ion will undergo changes in its oxidation state. Surface carbonates may form as intermediate products on the surface of the metal oxide particles during the carbon monoxide oxidation process. Holmgren (1998) reported the formation of unidentate carbonate, bidentate carbonate, inorganic carboxylate and bridged carbonate when CeO_2 was exposed to carbon monoxide at room temperature. It is possible to detect these surface carbonates via an infrared spectroscopy (Davydov, 1990).

However, some studies have shown that the Mars and van Krevelen mechanism does not account for the entire reduction process and suggested that the mechanism for the reduction of metal oxide is due to a combination of a few mechanisms (Kromer, 2008; Vannice, 2007; Soto, 2007).

Jansson (2000) found in his isotope exchange study on the oxidation of CO with Co_3O_4 supported on $\gamma\text{-Al}_2\text{O}_3$ at room temperature that oxygen participating in the reaction comes from oxygen bound onto the cobalt oxide surface. He suggested the following mechanism for the redox process:

- CO(g) is adsorbed on an oxidised cobalt site (Co^{3+}).
- The adsorbed CO reacts with an oxygen linked to the active Co^{3+} . CO_2 is formed and desorbs quickly resulting in a partially reduced site. The partially reduced site may consist of two Co^{2+} ions or may be regarded as an oxygen vacancy.
- The partially reduced site can either be reoxidised by gas-phase oxygen to an active Co^{3+} site or a CO can adsorb to the site and thus deactivate it. It is possible that the adsorbed CO thereafter undergoes dissociation or reacts with another CO to form CO_2 and C (CO disproportionation).
- Gas-phase CO_2 can react with the oxidised surface to form a carbonate species. The carbonate may exchange oxygen with the surface and desorb as CO_2 again.

Fan and his colleagues (2010) found that there is a significant decrease in pore volume after the first redox cycle and that this does not affect the reactivity of the iron oxide supported on titanium oxide particle thereby suggesting a different gas-solid reaction mechanism and that the pore structure and pore volume of the particles does not affect the reactivity of the particle in a significant factor.

Fan and his colleagues (2010) championed the idea of ionic diffusion as the main mechanism for the reduction of supported metal oxide particles in a chemical looping combustion system. Ionic diffusion occurs due to the defects formed in the support crystal structure in the presence of metallic ions. The introduction of metal oxide into its support can cause either lattice substitution defects or interstitial addition defects in the support crystal structure. In their study with iron oxide supported on titanium oxide, they found that the particle forms a close packing structure of the lattice. Besides that, they found that the atomic radius of the metallic ion and ionic form of the support are quite similar and as a result, it can be assumed that lattice substitution is preferred over interstitial addition. During this

mechanism, oxygen ion is vacated in order to achieve electrical neutrality in the crystal structure. The resulting oxygen ion vacancies will create point defects in the crystal structure, if the vacancy concentration is lower than a critical concentration. When the vacancy concentration is higher than the critical concentration other defects such as shear planes will occur. These vacancies will improved ionic diffusivity as oxygen ions will be able to diffuse through the crystal structure via the oxygen vacancies.

Such diffusion will be limited severely in pure metal oxide where such vacancies in the crystal lattice are absent. In pure metal oxides, alternative mechanisms for oxygen to diffuse out of the particle include anionic substitution and interstitial migration have been suggested. The activation energy for these diffusion mechanisms however will always be higher compared with supported metal oxide whereby an oxygen diffusion path may readily exist (Fan, 2010).

Surface melting is another possible reaction mechanism between metal oxide and pyrolysis gases. Criteria for surface melting include (van der Veen, 1999):

- For metals and metal oxides, complete surface melting (i.e. wetting by a diverging melt thickness) occurs on crystal faces with open atom packing. Densely packed crystal faces are generally non-melting, i.e. remain completely dry. Metallic surfaces with intermediate atom packing density tend to exhibit incomplete melting (i.e. wetting by a melt of microscopic thickness that does not diverge as T_m is approached).
- Crystal faces vicinal to a non-melting orientation may exhibit faceting into a dry surface orientation and a wet surface orientation.
- The melted layer is a quasi-liquid; it always retains some of the order of the crystal underneath.
- Surfaces of covalently bonded crystal are more likely to exhibit incomplete surface melting than surfaces of metallic crystals. Noble-gas crystals and other weakly bonded crystals also show complete surface melting for dense packing of atoms.

This mechanism is championed by Siriwardane and his colleagues (2010) for use in chemical looping combustion. They observed from their studies that metal oxide sinters at low operating temperatures and that the surface of the metal oxide appears to be progressively smoother as the operating temperature is increased. As a result, they suggested that when carbonaceous comes in contact with the surface of the metal oxide particles, the surface of the metal oxide structure is optimized for the reaction to occur. This is done by reducing the bond length between the metal atom and the oxygen atom. The increase in bond length on the surface of the metal oxide reduces the bond strength between the atoms on the surface of the metal oxide thereby reducing the melting point on the surface due to the lower activation energy required for the reaction to occur. When this happens, the surface of the metal oxide will transform into a quasi-liquid layer structure which will allow oxygen atoms to diffuse to the surface of the metal oxide much more easily and that the reaction will take place through the quasi-liquid layer formed.

3.5 Metal Oxide Deactivation

The activity and selectivity of metal oxides may change during the course of multiple reduction and oxidation cycles due to either chemical or physical reasons or a combination of both factors. However, sometimes a loss in the activity of the metal oxide will improve its selectivity. For example, when zeolitic and acid catalysts such as Al_2O_3 undergo hydrocarbon cracking, there is a possibility that they will lose some of their activity in the process. However, this is counteract by an improvement in their ability to facilitate isomerisation when they are exposed to nitrogenous bases such as pyridine or quinolone (Maldonado Hodar, 2009).

Catalyst deactivation can be caused by:

- A decrease in the number of active sites
- A decrease in the quality of the active sites
- Degradation of accessibility of the pore space

Poisoning

Poisoning occurs when the active sites on the metal oxide particle adsorb impurities from the surroundings leading to the active sites becoming inactive. This is a common appearance when carbonaceous, sulphurous and lead species are present in the feed streams. This is because metal oxides have the tendency to react with the carbon and sulphur species to form metal carbide and/or metal sulphide.

Even though carbon, sulphur and lead are potential poisons, there is a possibility that the poisoning effect is temporary rather than permanent. Permanent poisoning occurs when the poison is strong and the process is not readily reversible whereas temporary poisoning occurs when the adsorption of the poison is relatively weak and the process is reversible such that the removal of the poison will restore the original catalytic activity of the metal oxide.

Temporary poisoning might occur in chemical looping combustion whereby metal oxide and its reduced form might react with the carbonaceous and sulphurous species present in the bed to form metal carbide and/or metal sulphide. However, when the oxidation process is conducted at a high temperature, there is the possibility that the metal carbide and/or metal sulphide formed during the reduction stage will react with oxygen to form metal oxide and carbon dioxide and/or sulphur dioxide.

Formation of Deposits

Deposits can form on the metal oxide surface physically or chemically. An example of physical fouling is metal oxide fouling. Fouling occurs due to the nature of transition metal oxide that causes the formation of undesired by-products during the reduction process. These by-products might deposit on the surface of the metal oxide and block the active sites and/or pores on the particle. An example of chemical fouling is coking. Coke is formed during the chemical reactions of hydrocarbons at high temperatures. When large amounts of coke are deposited on the surface of the metal oxide, this will result in the narrowing or blocking of the metal oxide pores. This will reduce the ability of oxygen to diffuse to the surface of the metal oxide (Maldonado Hodar, 2009).

Thermal Degradation

Thermal degradation is a physical process caused by the high operating temperature in the bed that will induced sintering, chemical transformation and evaporation. This will lead to the deactivation of the metal oxide.

Sintering

Sintering is defined as the consolidation on heating of a loose mass of particles to a denser mass. Sintering causes both the specific surface area and the porosity to decrease and the density to increase. The Tammann temperature of the solid is about half its melting point below which sintering does not occur to any appreciable extent.

Sintering occurs in three stages as shown in Figure 3.8. During the initial stage, growing necks form and grow. In the intermediate stage, growing necks merge and the large numbers of small particles are replaced by a smaller number of large particles. This stage produces interparticle porosity whose surface may be inaccessible both to reactant gas during the reaction and to the nitrogen used to measure the specific surface area. In the final stage of sintering, the pore spaces become broken up with isolated closed pores remaining which shrink in size as densification proceeds.

German and Munir (1976) proposed a model of the interparticle neck shape during sintering. They used this model to establish the kinetic dependence for the rate of surface area reduction on the operative sintering mechanism. As a result, the mass transport process can be identified via the kinetics of the specific surface area reduction. The neck-growth model is in the form of:

$$\left(\frac{x}{a}\right)^n = Bt \quad \text{(Equation 3.41)}$$

$\frac{x}{a}$ = ratio of interparticle neck radius to the particle radius

B = constant (includes particle size, temperature and geometric term)

t = sintering time

n = mechanism-characteristic exponent dependent on the mass transport process

It was assumed that the interparticle neck shape was formed via a torus of radius r as shown in Figure 3.9. For small neck sizes such an approximate neck shape has little influence on the result. The significant point of Equation 3.41 represents sintering driven by the curvature gradient in the neck region. Thus initial sintering does not result from excess energy but rather from the chemical potential gradient produced by the varying mean curvature.

Equation 3.41 can be recast to give surface area reduction for the case of a small neck where surface area loss with necking growth can be approximated as:

$$\Delta S = S_0 - S \approx \pi r^2 \quad (\text{Equation 3.42})$$

S = Surface area at a neck size of x

S_0 = Initial surface area

For compact of spherical powder, the initial surface area per interparticle contact is given by:

$$S_0 = \frac{4\pi a^2}{N_c} \quad (\text{Equation 3.43})$$

N_c = Particle packing coordination number which is related to the density

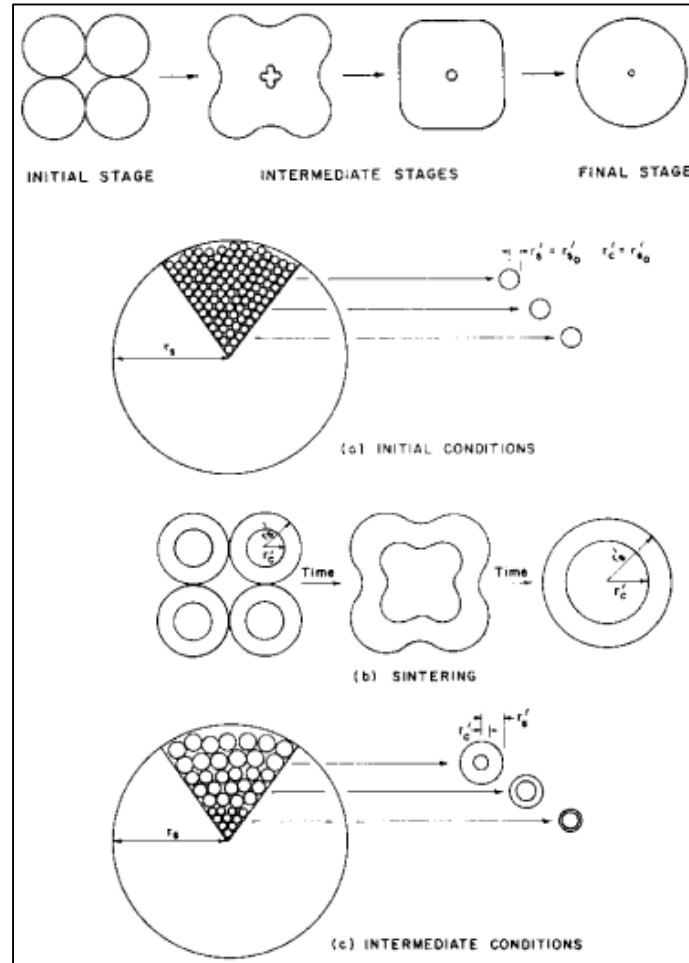


Figure 3.8: Mechanism of sintering (Caillet and Harrison, 1982)

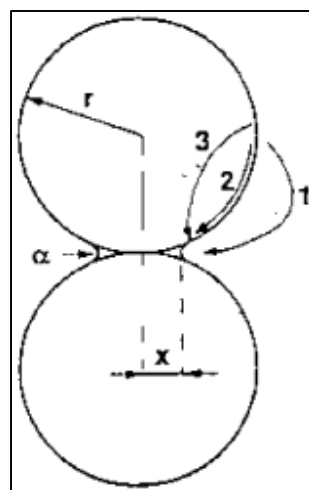


Figure 3.9: Interparticle neck shape: (1) Diffusion in gas phase; (2) Surface diffusion; (3) Volume diffusion (Bailliez and Nzihou, 2004)

Chemical transformations

Chemical transformations occur when metal oxide reacts with its support. This was observed in this research study with copper oxide supported on alumina whereby copper aluminate complexes were detected for the fresh and reacted copper oxide particles. This is because at high temperatures, solid state diffusion occurs whereby the copper ion can diffuse easily into the alumina support to form a spinel form of copper aluminate complexes. The spinel form of the complexes will reduce the ability of oxygen to diffuse through the spinel structure to react with the pyrolysis gases.

Evaporation

High temperature processes can also cause evaporation which will lead to the progressive loss of the active phase of the metal oxide. This usually occurs in steam reforming and catalytic combustion processes when platinum is used as a catalyst. This is because platinum can react with oxygen at high temperatures in an oxygen containing environment to form platinum oxide that will decompose at high temperatures.

The effect of evaporation in a chemical looping combustion process is minimal as the metal oxides used in the process do not decompose easily.

Mechanical Deactivation

Mechanical strength in a metal oxide particle is important to provide it with some resistance against attrition. In a fluidised bed reactor, attrition will always occur and fines generated are easily carried away with the product flow. The mechanical strength of a metal oxide particle is influenced by its shape and porosity. Even though a spherical shape metal oxide particle is favourable due to its high porosity, it has a lower mechanical strength. Besides that, the existence of macropores in the metal oxide particle will reduce its mechanical strength as well.

Based on these observations and results obtained from the experimental results found in this research study, the following hypotheses for the mechanism of interaction between supported and non-supported metal oxide and ash were derived.

3.6 Mechanism of Interaction between Metal Oxide with Coal and Ash

When metal oxide comes into contact with coal during the reduction stage, carbon and hydrogen from coal will react with oxygen from the metal oxide to form carbon monoxide and/or carbon dioxide and steam. When this occurs, carbon monoxide and/or carbon dioxide and steam formed during the reaction will be liberated from the fluidised bed leaving behind char, fly ash and mineral matters. Fly ash will elutriate from the fluidised bed due to its low density. Mineral matters will remain in the bed as a result of their high density. As for the metal oxide, reaction with carbon and hydrogen causes it to lose its oxygen content. When this occurs, the reduced form of the metal oxide will have voids caused by the missing oxygen atoms. Surface with voids requires large amount of surface energy in order to maintain its form and is therefore highly unsustainable. In order to reduce its surface energy, it will undergo surface reconstruction and/or adsorb impurities from the surrounding environment. During the process, it is possible that the char and mineral matter will deposit on the surface of the reduced metal oxide and block some of its pores.

During the oxidation stage, when steam or air is introduced into the fluidised bed, char formed during the reduction stage will also react with oxygen from steam or air to form carbon dioxide and steam. Besides that, the reduced metal oxide will react with oxygen from steam or air to regenerate itself back to its highest oxidation form. During this process, the metal oxide will undergo surface restructuring to return to its original form. However, as the mineral matter will neither react with steam nor air, they will continue to be held in the pores of the metal oxide. During the surface restructuring process, it is possible that some of the mineral matter will be trapped within the metal oxide. The mechanism for this interaction is illustrated in Figures 3.10 to 3.14.

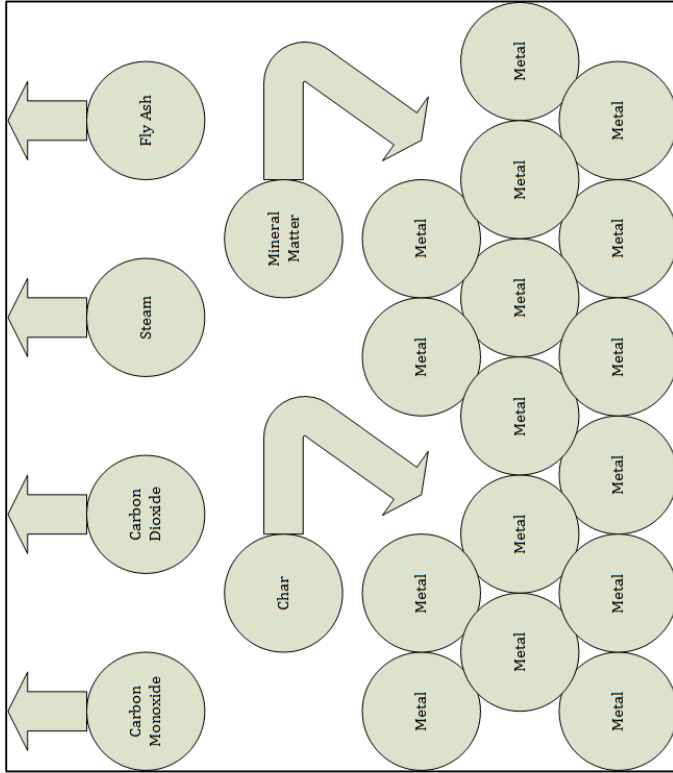


Figure 3.10: Reactions during reduction stage

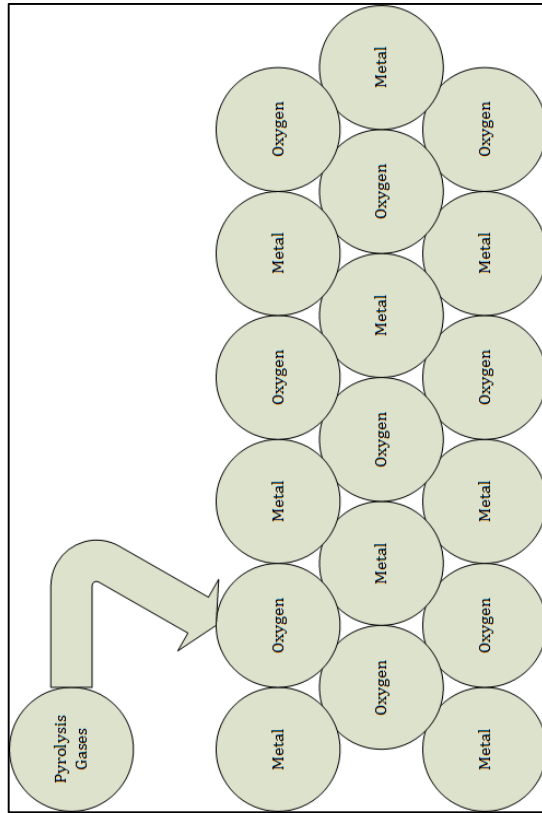


Figure 3.11: Initial reduction stage

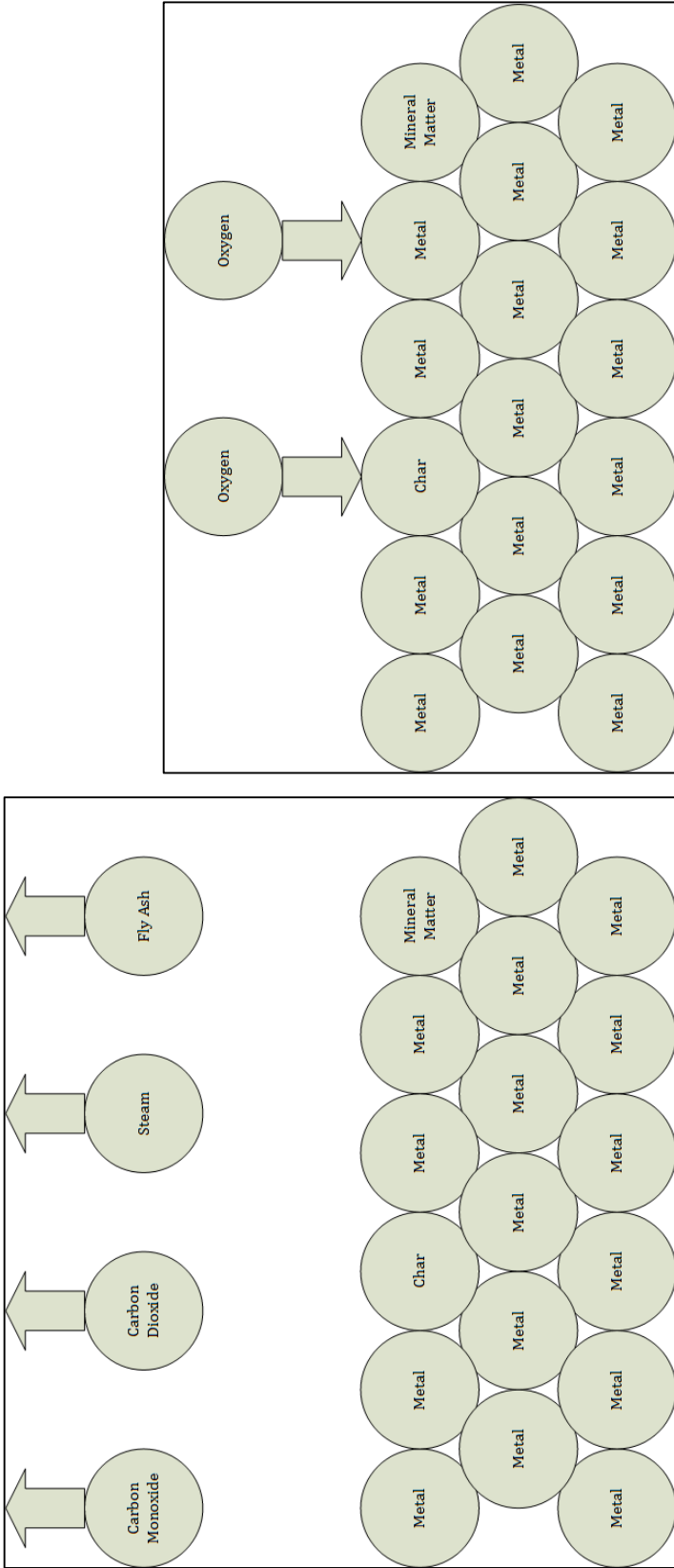


Figure 3.12: Initial oxidation stage

Figure 3.14: Mixing during reduction stage

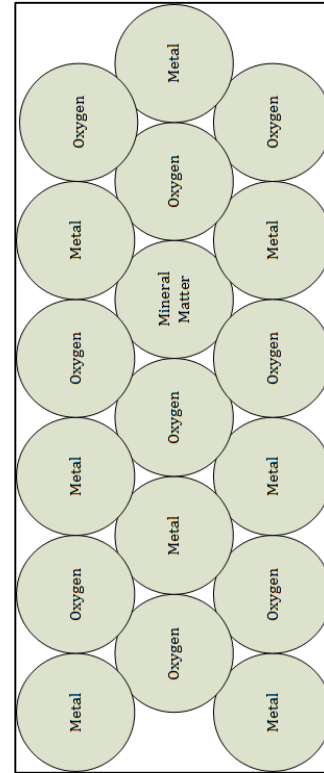


Figure 3.13: Complete reoxidation

3.7 Mechanism of Interaction between Metal Oxide with Coal and Ash via Surface Melting

When metal oxide is operated at high temperatures or when it comes in contact with carbonaceous species, there is a possibility that planes with specific Miller Indices will undergo surface melting. This is because the metal oxide particle will optimised its surface structure to reduce its surface energy as well as to reduce the activation energy required for the reaction to occur. When this happens, the surface of the metal oxide will transform into a quasi-liquid layer structure which will allow oxygen atoms to diffuse to the surface of the metal oxide much more easily. It is possible the existence of the quasi-liquid layer will allow the gaseous reactants will react with the metal oxide on the surface via a liquid-gas reaction. This will have a huge implication on the evaluation of the thermodynamics of the rate of reaction of a liquid-gas reaction is much quicker than that of a solid-gas reaction. The mechanism for this interaction is illustrated in Figures 3.15 to 3.18.

The existence of the quasi-liquid layer can also be used to justify the sudden drop in the BET surface area and pore volume of the supported metal oxide. This is due to the fact that when the reactor is cooled down in order to replace or collect the particles for analysis, the quasi-liquid layer cools down to form a solid layer surrounding the metal oxide. When this occurs, it is possible that the solid layer formed will block the pores on the surface of the particles thereby creating a large number of close pores which could not be detected via the porosimetry analysis leading to a fall in BET surface area and pore volume even though the metal oxide particle is able to maintain its reactivity through a large number of reduction and oxidation cycles.

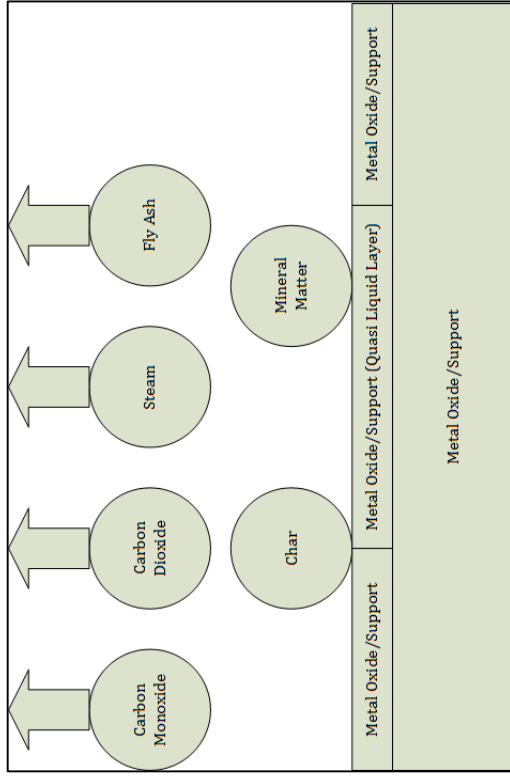


Figure 3.15: Reactions during reduction stage

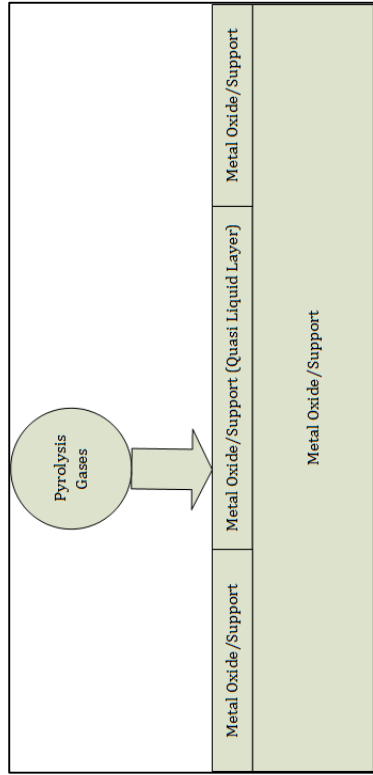


Figure 3.17: Initial reduction stage and the formation of the quasi-liquid layer

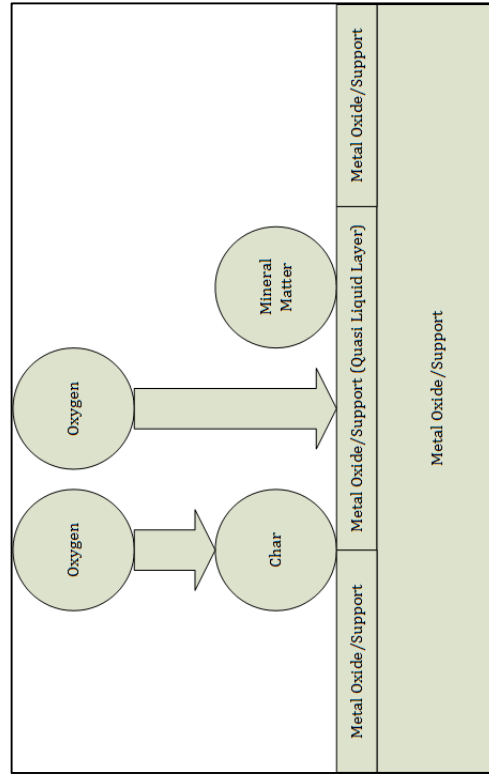


Figure 3.18: Initial oxidation stage

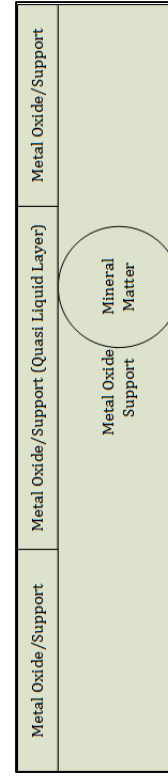


Figure 3.16: Complete reoxidation

Chapter 4 EXPERIMENTAL SETUP 1

Two fluidised beds were used in this research study. The first fluidised bed used in this research study was designed by Chuang (2009) and operated by Chuang (2009) and Brown et al. (2010) at the University of Cambridge. Brown et al. (2010) studied the kinetics and attrition of mechanically mixed iron oxide and copper oxide impregnated on alumina with a number of different fuels over multiple reduction and oxidation cycles with this experimental setup. This setup was used as a proof of concept for further studies on chemical looping combustion. The first setup was used by the author to study the morphological changes on the iron oxide and copper oxide/alumina particles after they have undergone 20 reduction oxidation cycles with 5 different fuels under the reduction condition of 50% CO₂ in N₂ and oxidation condition of 50% air in N₂.

4.1 Experimental Setup 1

The experimental configuration was designed to emulate chemical looping combustion for solid fuels in a fluidised bed in a batch process. The schematic diagram of the setup is shown in Figure 4.1. The system consists of a fluidised bed, furnace, screw feeder and other supporting instruments. Some of these instruments are featured in Figures 4.2 and 4.3.

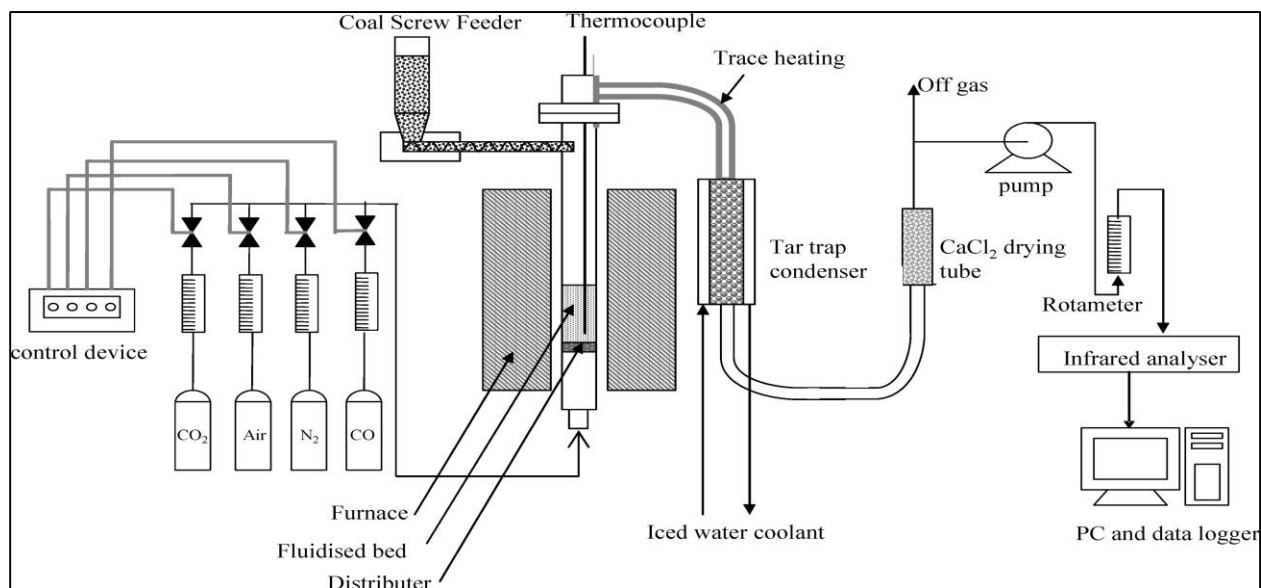


Figure 4.1: Schematic diagram of the experimental setup



Figure 4.2: Layout of the system

Legend: (1) Thermocouple, (2) Fluidised bed, (3) Screw feeder inlet, (4) External heater, (5) Tar trap condenser, (6) Rotameter

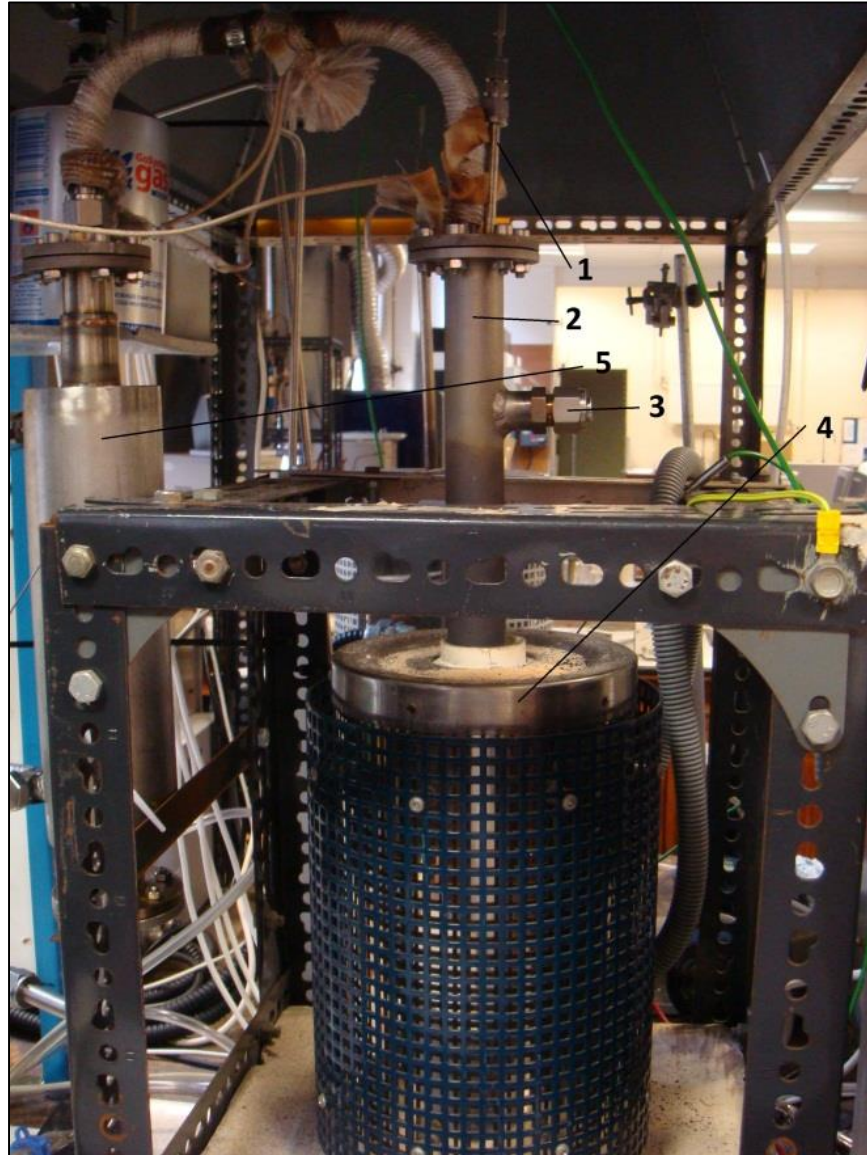


Figure 4.3: Layout of the fluidised bed

Legend: (1) Thermocouple, (2) Fluidised bed, (3) Screw feeder inlet, (4) External heater,
(5) Tar trap condenser

The objective of this investigation was to study the morphology and compositional changes in mechanically mixed iron oxide and copper oxide impregnated on alumina after 20 reaction cycles with 5 different fuels under the reduction condition of 50% CO₂ in N₂ and the oxidation condition of 50% air in N₂.

Table 4.1 shows the design and operation data for the experimental rig. A separate externally heated fluidised bed reactor was used to produce lignite char from lignite coal. It has an internal diameter of 78 mm and has a perforated plate acting as a distributor with 37 holes and each hole has an internal diameter of 0.4 mm. A plenum chamber is placed below the distributor.

Table 4.1: Fluidised bed reactor design and operational parameters

Parameter	Value
Reactor diameter, d_r (mm)	25
Cross-sectional area of the bed, A_r (m ²)	4.9×10^{-4}
Initial superficial gas velocity at 1073 K and 1 bar, U_0 (m/s)	0.32
Minimum fluidising velocity for Fe ₂ O ₃ at 1073 K, U_{mf} (m/s)	0.05
Voidage at minimum fluidisation, ϵ_{mf}	0.4
Volume of the bed (unfluidised), V_{bed} (m ³)	2.8×10^{-5}
Height of bed at minimum fluidisation, H_{mf} (mm)	41
Mean bubble diameter, D_b (mm)	16.2
Mean bubble volume, V_b (m ³)	2.2×10^{-6}
Volumetric rate of interphase transfer, Q (m ³ /s)	3.1×10^{-5}
Fluidised bed height, H (mm)	88
Cross-flow factor, X_f	2.2
Bubble rise velocity, U_b (m/s)	0.56

4.1.1 Tar Trap Condenser

The gas sample was passed to knock-out pots, immersed in ice, to remove moisture, volatile matter and ash and was then pumped at a known rate through a bed of CaCl₂ drying agent, a fine filter and rotameter to the FTIR.

4.1.2 External Heater

The external heater has a diameter of 38mm and is used to heat the fluidised bed reactor.

4.1.3 Screw Feeder

The screw feeder is used to supply fuel into the fluidised bed. The rate of feeding is adjustable by the user.

4.1.4 Thermocouples

The temperature of the bed was measured by a K-type thermocouple inserted from the top of the bed so that the tip was about 100 mm above the distributor. This thermocouple is used to measure the temperature of the bed. A second K-type thermocouple was inserted between the fluidised bed reactor and the furnace to measure the temperature of the fluidised bed.

4.1.5 Gas Analyser

The concentrations of CO, CO₂ and O₂ in the gases leaving the fluidised bed were continuously monitored with an ABB EL3020 instrument, which is a non-dispersive infra-red analyser, coupled with a paramagnetic one for O₂. The measurement range of the ABB EL3020 is shown in Table 4.2.

Table 4.2: ABB EL3020 Detection Range

Analyser	Type	Range
CO	Infrared	0-100 volume %
CO ₂	Infrared	0-100 volume %
SO ₂	Infrared	0-10000 ppm
O ₂	Paramagnetic	0-100 volume %

4.1.5.1 Interference of CH₄ with SO₂ Analyser

Methane interferes with the SO₂ infrared analyser. This is owing to the overlapping of a wide absorption peak of methane at 1200 to 1400 cm⁻¹ with only significant peak for SO₂ at about 1380 cm⁻¹ (NIST Chemistry Webbook). By calibrating the analyser with 10 volume percent CH₄, the SO₂ analyser could be used to estimate the amount of CH₄ present. However, this method assumes that when there is SO₂ present there is no CH₄ present and vice versa. If both are present at the same time the relative contribution of each cannot be determined. The presence of oxygen carrier creates an oxidizing environment that could result in the formation of SO₂. Thus, this measurement is more qualitative than quantitative and must be approached with caution.

4.1.6 PC & Data Logger

The program used to record data from the thermocouples and exit gas concentrations for CO₂, CO, O₂, H₂ and SO₂ was designed using Visual Basics by the University of Cambridge.

4.1.7 Gas Cylinders

The CO₂, N₂ and air cylinders were used in these experiments and they were supplied by BOC. Nitrogen was used to fluidise the bed while oxygen was used to reoxidise the reduced oxygen carriers and to burn off char formed during the process. Nitrogen and air were also used to cool the reactor at the end of the experiment. Carbon dioxide was used to generate a condition whereby the reaction rate was close to maximum.

4.2 Operating Conditions

The experiments were conducted at about 1198 K and 1 atmospheric pressure. The temperatures were chosen such that during the initial oxidation period when char reacts with oxygen to produce carbon dioxide, the temperature of the bed does not exceed the melting point of copper that might cause agglomeration of copper and incomplete re-oxidation of the oxygen carrier. Table 4.3 shows the operating conditions of the experimental run.

Table 4.3: Operating conditions of the fluidised bed reactor

Parameter	Value
Temperature, T (K)	1198
Pressure, P (bar)	1
Total volumetric flowrate at 1 bar and 298 K, q (mL/s)	45
Inlet mole fraction of CO ₂ , $y_{CO_2,i}$	0.5
Superficial gas velocity at 1073 K and 1 bar, U_0 (m/s)	0.32
Fe ₂ O ₃ particle size (μm)	300 – 425
CuO/Al ₂ O ₃ particle size (μm)	300 – 425
Fuel particle size (μm)	600 – 1400
Fuel feeding rate (g/min)	0.18
Initial mass of Fe ₂ O ₃ (g)	20
Initial mass of CuO/Al ₂ O ₃ (g)	20

4.3 Procedures

4.3.1 Start Up Procedure

1. Clean the internal surface of the fluidised bed to remove any dusts or leftovers from previous experiments.
2. Switch on the digital weighing scale and tare it to zero.
3. Weigh 20 grams of iron oxide particles and load them through the top of the fluidised bed.
4. Assemble the fluidised bed back into the furnace.
5. Switch on the gas analyser, pumps, tap water and extractor fan.
6. Check all the connections.
7. Heat the fluidised bed to 1198 K.
8. Switch on the computer and the data acquisition software.
9. Switch on the nitrogen, air and CO₂ gas cylinders.
10. Adjust the valve settings such that nitrogen, carbon dioxide, and air flowrate will each be 20 mL/s to when the valves are switched on.
11. Switch on the nitrogen valve to the fluidised the bed.
12. Clean the screw feeder with a vacuum cleaner to remove any dusts of leftovers from previous experiments.
13. Pour the lignite coal into the screw feeder.

14. Switch on the screw feeder and allow it to run continuously for 10 minutes in order to achieve a steady state feeding.
15. Calibrate the screw feeder by measuring the amount of fuel fed into a plastic container during 5 minutes.
16. Repeat step 15 for a few times to achieve a steady state feeding.
17. Install the screw feeder back into the system. (Warning: Use a glove as the fluidised bed is hot).
18. Once the temperature of the fluidised bed has reached a constant temperature of 1198 K, switch on the carbon dioxide valve.
19. After 1 minute, switch on the screw feeder at a rate of 0.18 g/min.
20. Note the time required to achieve carbon monoxide breakthrough and record this time as t_1 .
21. Once the breakthrough is achieved, switch off the carbon dioxide valve to purge the bed with nitrogen.
22. After 1 minute, switch on the air valve to burn off chars and unreacted fuel, as well as to reoxidised the reduced iron oxide particles.
23. Note the maximum temperature achieved during the initial reoxidation period and the time required to achieve complete oxidation and record this time as t_2 .
24. Repeat the cycle on automatic mode for 19 times by setting the software to achieve the following:
 - i. Switch on the carbon dioxide and nitrogen valve for one minute.
 - ii. Switch on the screw feeder and allow the feed to run for t_1 minutes (to the nearest 0.5 minutes) while leaving the carbon dioxide and nitrogen valve open.
 - iii. Switch off the carbon dioxide valve to purge the bed for one minute.
 - iv. Switch on the air valve for t_2 minutes (to the nearest upper 0.5 minutes).
 - v. Repeat step I to step iv.

4.3.2 Shut Down Procedure

1. After the last cycle, switch off the automatic running mode and stop the data collection on the computer, but leave the nitrogen and oxygen valve open.
2. Switch off the external heating system.
3. Switch off the gas analyser.
4. Switch off the pump.
5. Switch off the screw feeder.
6. Switch off the digital weighing scale.
7. Once the fluidized bed has cooled to room temperature, switch off the nitrogen and air valve.
8. Switch off the extractor fan.
9. Dismantle the fluidised bed and the screw feeder.
10. Pour the remaining fuel in the feeder back to its appropriate bottle.
11. Collect the bed particles in a container.

4.3.3 Fuels Preparation

Five fuels were used: Hambach lignite coal and a char prepared from the lignite; activated carbon, Taldinski bituminous coal and US bituminous coal. The coals were used after drying to constant weight in an electrically-heated oven at 353 K. Fuels used in this experiment had a size range of the following: Lignite coal, 600-1000 μm ; US bituminous coal and Taldinski bituminous coal, 1000-1700 μm (Brown et al., 2010).

4.3.4 Char Preparation

The char was prepared by feeding dried lignite, sieved to 1190-1700 μm , continuously to the 78 mm fluidized bed at 4 g/min. The reactor was maintained at 1073 K and contained 1500 g of pure alumina sand (sieved to 425-500 μm , Boud Mineral, purity > 99.9 wt.%): it was fluidized with N_2 (BOC plc.) at a flowrate of 500 cm^3/s , as measured at 293 K and atmospheric pressure. The off-gases left the top of the reactor via a 10 mm (i.d.) pipe, 300 mm long. After 60 minutes all of the charge of coal had been fed and the reactor was allowed to cool to room temperature under the flow of N_2 . The resulting char was then sieved from

the alumina. After the char was cooled, it was recovered from the bed and sieved to a range of size fractions of 355-600, 600-850, 850-1000, and 1000-1400 μm . The full range of sizes for char was used in this study (Brown et al., 2010).

4.4 Fuel Analysis

Proximate and ultimate analyses of the fuels are given in Table 4.4. Procedures involved in the proximate and ultimate analyses are shown in Appendix A. Table 4.5 shows the inductive coupled plasma mass spectrometry for the ash content for these fuels.

Table 4.4: Proximate and ultimate analyses of fuels

	Hambach Lignite Coal	Hambach Lignite Char	Activated Carbon	Taldinski Bituminous Coal	US Bituminous Coal
Moisture Content %	7.15	4.69	6.43	4.59	4.44
Volatiles %	57.75	13.17	12.02	30.77	37.23
Ash %	3.70	8.62	12.72	15.87	13.06
N (dry %)	0.90	0.62	0.62	1.72	1.41
C (dry %)	61.80	65.66	70.34	71.92	75.73
H (dry %)	4.80	0.90	0.74	3.99	4.48
S (dry %)	0.00	0.00	0.00	0.01	2.03
O ₂ (dry %)	32.51	32.82	28.30	22.37	16.35

Table 4.5: Inductive Coupled Plasma Mass Spectrometry of fuels' ashes

Element	Lignite Coal (mg/kg)	Lignite Char (mg/kg)	Activated Carbon (mg/kg)	US Bituminous Coal (mg/kg)	Taldinsky Bituminous Coal (mg/kg)
Ag	0.10	0.05	0.09	0.09	0.09
Al	11024.89	11668.12	6510.35	22323.72	32688.48
As	5.59	67.13	36.48	54.15	20.87
B	1404.96	1525.00	33.73	181.14	154.44
Ba	5148.89	3105.10	6342.84	2252.99	1594.61
Be	0.38	0.35	0.76	3.10	3.61
Bi	0.00	0.00	0.04	0.12	0.37
Ca	318649.50	336504.48	9304.65	39475.11	30496.69
Cd	0.65	0.03	0.94	0.27	2.83
Co	6.02	3.95	10.05	15.84	14.11
Cr	14.98	42.12	39.92	48.61	71.83
Cu	624.77	736.83	10706.13	288.10	232.72
Fe	123506.58	124612.91	1743.40	26381.17	14863.23
Ga	192.05	128.97	247.52	92.39	75.67
Li	86.64	33.94	6.71	37.29	51.84
Mg	98566.83	103210.01	2263.44	7154.95	4406.77
Mn	2391.25	2628.63	63.18	829.55	365.05
Mo	2.13	10.99	16.80	18.40	7.29
Ni	20.60	80.16	54.72	59.68	40.88
Pb	5.49	1.84	4.89	21.68	15.74
Rb	10.32	1.08	1.95	10.63	10.02
Se	15.77	4.64	0.86	2.23	1.61
Sr	3249.34	3276.97	701.47	660.34	2139.99
Te	5.20	3.45	6.83	1.10	0.06
Tl	0.00	0.00	0.00	0.04	0.43
U	0.58	0.66	3.87	1.88	5.47
V	24.61	30.16	67.55	95.93	105.06
Zn	6.03	11.08	29.37	46.45	67.83
K	3884.02	176.85	622.22	1888.81	1561.72
Na	9909.24	797.74	4221.08	2978.50	1110.01

4.5 Conversion Calculation Methodology

Conversion of iron oxide during reduction was calculated by Equation 4.1 while conversion during oxidation can be calculated by Equation 4.2.

$$X_{I,r} = \frac{(2 \times CO_{2,r}) + CO_r + H_2O_r + (2 \times SO_{2,r}) - O_F}{O_{I,r}} \quad (\text{Equation 4.1})$$

$X_{I,r}$ = Fe_2O_3 conversion during reduction (%)

$CO_{2,r}$ = Number of moles of CO_2 released during reduction (*mol*)

CO_r = Number of moles of CO released during reduction (*mol*)

H_2O_r = Number of moles of H_2O released during reduction (*mol*)

$SO_{2,r}$ = Number of moles of SO_2 released during reduction (*mol*)

O_F = Number of moles of oxygen in fuel (*mol*)

$O_{I,r}$ = Number of moles of oxygen released when Fe_2O_3 is converted to Fe_3O_4 (*mol*)

$$X_{I,o} = \frac{(2 \times O_{2,o}) - [(2 \times CO_{2,o}) + CO_o + H_2O_o + (2 \times SO_{2,o})]}{O_{I,o}} \quad (\text{Equation 4.2})$$

$X_{I,o}$ = Iron oxide conversion during oxidation (%)

$CO_{2,o}$ = Number of moles of CO_2 released during oxidation (*mol*)

CO_o = Number of moles of CO released during oxidation (*mol*)

H_2O_o = Number of moles of H_2O released during oxidation (*mol*)

$SO_{2,o}$ = Number of moles of SO_2 released during oxidation (*mol*)

$O_{2,o}$ = Number of moles of oxygen in air used during oxidation (*mol*)

$O_{I,o}$ = Number of moles of oxygen used when Fe_3O_4 is converted to Fe_2O_3 (*mol*)

Conversion of copper oxide during reduction was calculated by Equation 4.3 while conversion during oxidation can be calculated by Equation 4.4.

$$X_{CuO,r} = \frac{(2 \times CO_{2,r}) + CO_r + H_2O_r + (2 \times SO_{2,r}) + (2 \times O_{2,CuO,r}) - O_F}{O_{CuO,r}} \quad (\text{Equation 4.3})$$

$X_{CuO,r}$ = *CuO* conversion during reduction (%)

$CO_{2,r}$ = Number of moles of CO_2 released during reduction (*mol*)

CO_r = Number of moles of CO released during reduction (*mol*)

H_2O_r = Number of moles of H_2O released during reduction (*mol*)

$SO_{2,r}$ = Number of moles of SO_2 released during reduction (*mol*)

$O_{2,CuO,r}$ = Number of moles of oxygen released via decomposition of *CuO* (*mol*)

O_F = Number of moles of oxygen in fuel (*mol*)

$O_{CuO,r}$ = Number of moles of oxygen released when *CuO* is converted to *Cu* (*mol*)

$$X_{Cu,o} = \frac{(2 \times O_{2,o}) - [(2 \times CO_{2,o}) + CO_o + H_2O_o + (2 \times SO_{2,o})]}{O_{Cu,o}} \quad (\text{Equation 4.4})$$

$X_{Cu,o}$ = Copper conversion during oxidation (%)

$CO_{2,o}$ = Number of moles of CO_2 released during oxidation (*mol*)

CO_o = Number of moles of CO released during oxidation (*mol*)

H_2O_o = Number of moles of H_2O released during oxidation (*mol*)

$SO_{2,o}$ = Number of moles of SO_2 released during oxidation (*mol*)

$O_{2,o}$ = Number of moles of oxygen in air used during oxidation (*mol*)

$O_{Cu,o}$ = Number of moles of oxygen used when *Cu* is converted to *CuO* (*mol*)

4.6 Separation of Oxygen Carriers from Ash

After the experiments, the particles collected were sieved into different sizes to separate fines, reactor scaling material and unburned fuel from the oxygen carrier. After that, attempts were made to try to separate the oxygen carrier particles from the ash particles to determine the recoverability of oxygen carriers after multiple cycle tests.

The iron oxide particles can be separated from the ash particles by using a strong magnet as the iron oxide particles are attracted to the magnet because of their magnetic properties compared to ash particles that have little or no magnetic properties. Besides that, the iron oxide particles have a distinctive colour that allows for easier identification, thereby allowing the possibility of a manual separation to be carried out. However, it was soon discovered that some of the particles were coated with an unknown layer that could be peeled off by applying a slight pressure on the particles but making it difficult to sort the particles appropriately for analysis. As a result, further separation was temporarily suspended until a clearer idea on the morphology of the particles was obtained.

Attempts were made to separate the copper oxide from the ash particles as well. However, attempts were futile as it was discovered that it was very difficult to perform the separation test. One of the reasons is due to the fact that copper oxide has very weak magnetic properties, hence a magnet could not be used to identify or separate them. Besides that, the copper oxide particles have quite similar colour as the ash particles, so manual separation was not possible. An attempt was made to try to separate the particles via density difference. This was done by filling a burette with carbon tetrachloride that has a density of 1594 kg m^{-3} . This method was successful in separating the fly ash particles from copper oxide and bottom ash particles, but it was difficult to separate the copper oxide from the bottom ash. A final attempt to separate the particles was carried out by using Particulate Systems' Particle Insight Dynamic Image Analyser. The image analyser was able to provide information regarding the equivalent circular area diameter (ECAD), equivalent circular perimeter diameter (ECPD), bounding circle diameter (BCD), circularity, and smoothness as well as bounding rectangle length, width and aspect ratio.

Figures 4.4 and 4.5 show the smoothness and the circularity of the copper oxide and ash particles. The donut-like images captured by the image analyser are water bubbles. The figures indicate that the copper oxide particles appear in different shapes and sizes and that there is no definite shape for either the copper oxide or the ash particles such that they can be singled out. This is because the copper oxide particles appeared to have fused with ash in the fluidised bed. As a result, analytical analysis of the metal oxide particles were conducted without any prior separation between metal oxide and ash.

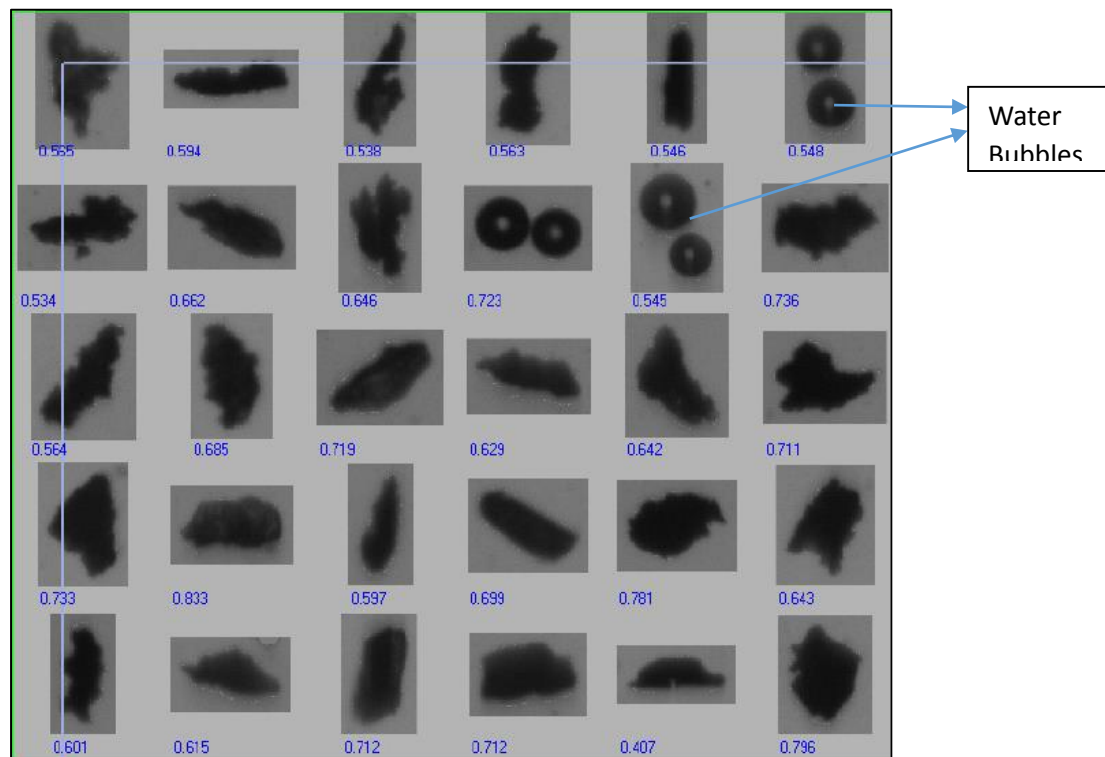


Figure 4.4: Reacted copper oxide particles' smoothness

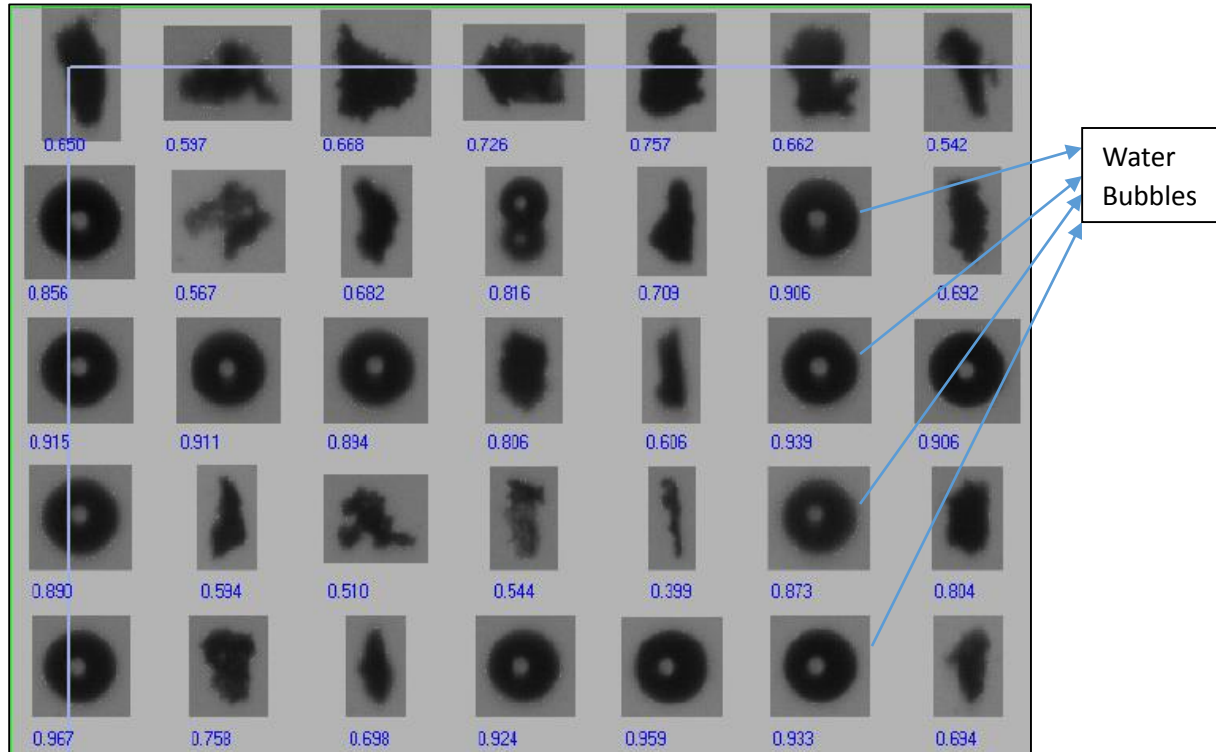


Figure 4.5: Reacted copper oxide particles' circularity

4.7 Iron Oxide

4.7.1 Exit Gas Profiles Analysis

Figure 4.6 shows a typical cycle obtained when feeding lignite char into a bed of 20 g of iron oxide at 950°C. During the initially feeding period, the amount of CO₂ and CO released from the fluidised bed appears to be low. This is because the high concentration of CO₂ in the bed is extremely high and it inhibits the gasification of coal. This is more pronounced for cases with lignite char and lignite coal (Figures 4.6 and 4.7). The sharp rise in the concentration of CO₂ indicates the point at which the gasification and combustion process begins. During this stage, syngas produced from the gasification of coal will react with iron oxide to produce carbon dioxide and steam. As more iron oxide is reduced, there is less iron oxide available to react with the syngas. As a result, the concentration of CO and H₂ rises rapidly towards the end of the reduction stage.

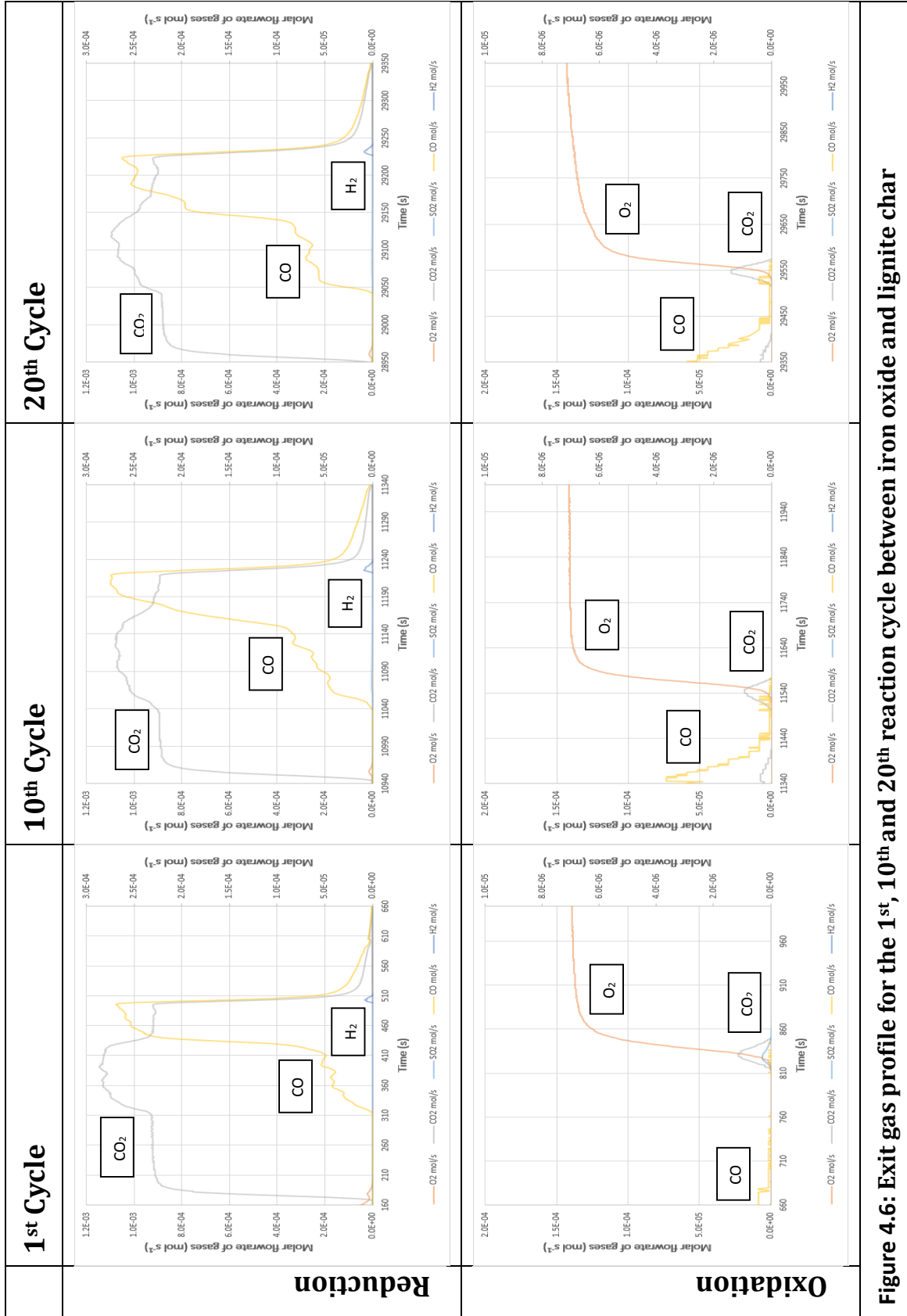


Figure 4.6: Exit gas profile for the 1st, 10th and 20th reaction cycle between iron oxide and lignite char

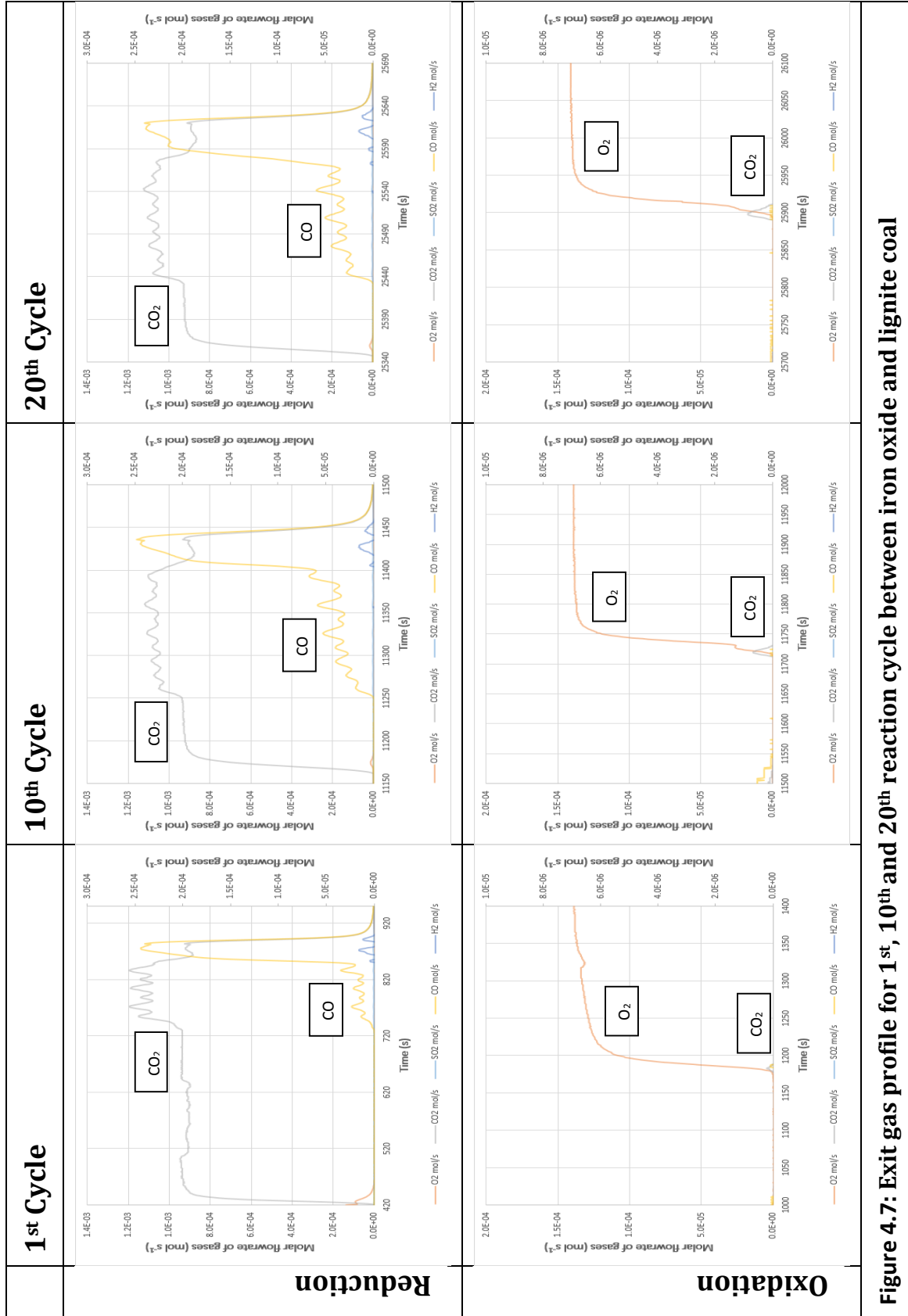


Figure 4.7: Exit gas profile for 1st, 10th and 20th reaction cycle between iron oxide and lignite coal

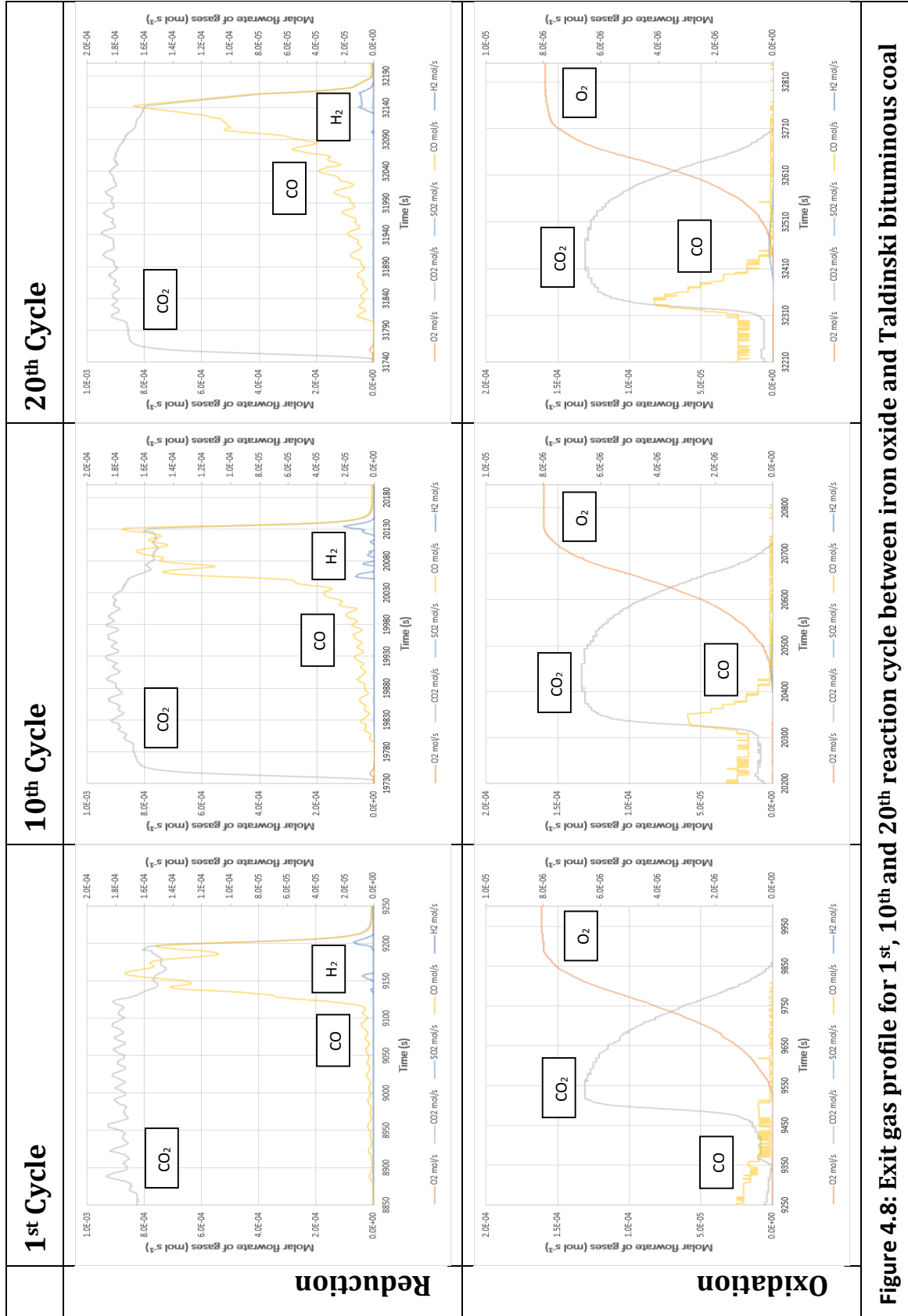


Figure 4.8: Exit gas profile for 1st, 10th and 20th reaction cycle between iron oxide and Taldinski bituminous coal

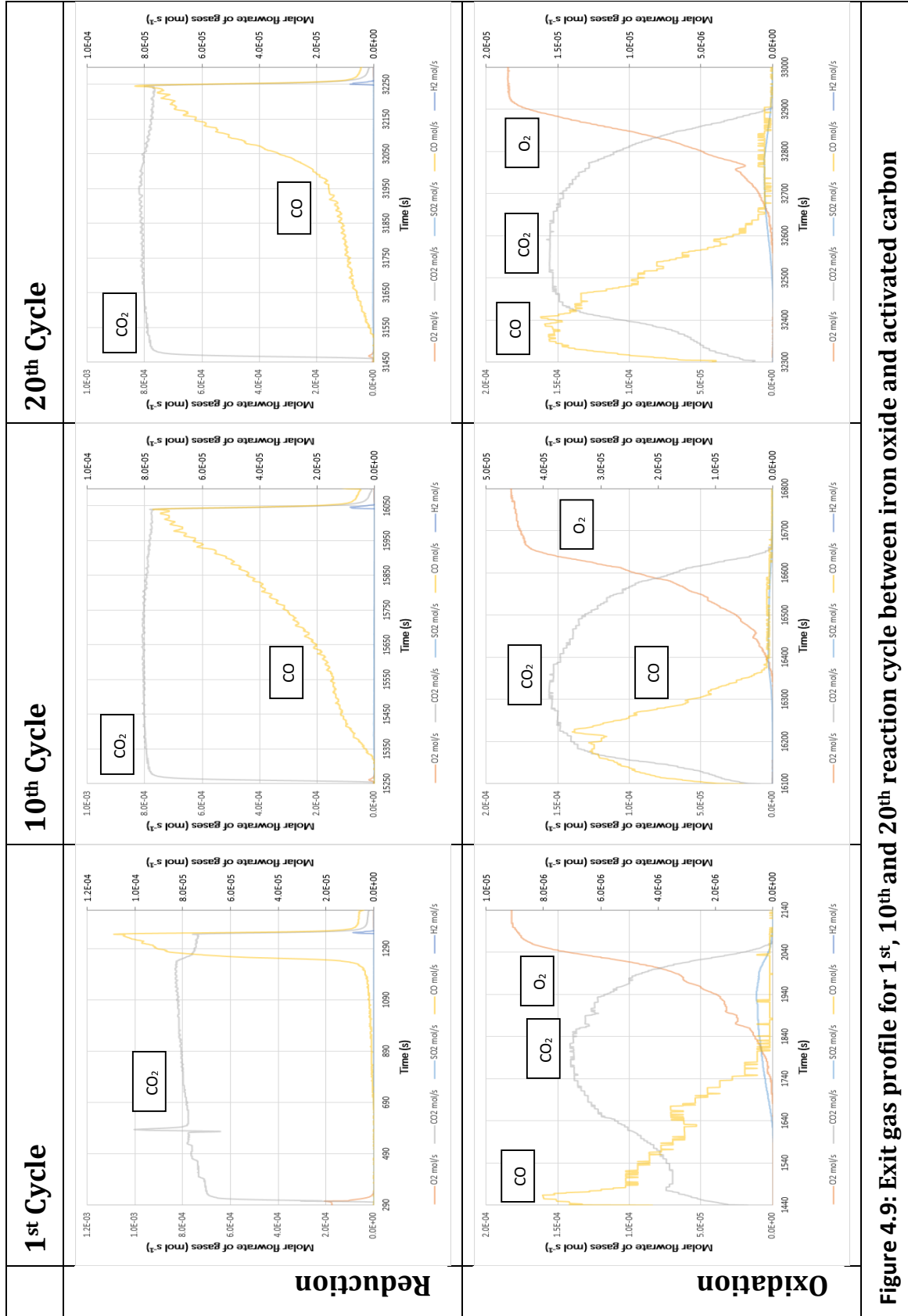


Figure 4.9: Exit gas profile for 1st, 10th and 20th reaction cycle between iron oxide and activated carbon

Figures 4.6 to 4.9 show the mole fraction of gases exiting the reactor during the 1st, 10th and 20th cycles for experiments with Hambach lignite char, Hambach lignite, Taldinsky bituminous coal and activated carbon respectively. The results for experiment conducted with US bituminous coal was not shown due to experimental file corruption issue. The cycle is broken up into the reduction stage, given in the first row, and the oxidation stage in the second row. Comparison of the 4 figures shows that the four different fuels behaved very differently. The Hambach lignite char and activated carbon (Figures 4.6 and 4.9 respectively) both produced relatively smooth curves during feeding, because neither fuel contains volatile matter so that there are no sharp peaks arising from rapid devolatilisation. Sharp spikes were however observed with Hambach lignite and Taldinsky bituminous coal (Figures 4.7 and 4.8 respectively). This is to be expected since both these fuels are raw coals and so underwent devolatilisation when batches of fuel were added to the reactor by the screw feeder, resulting in a sudden peak of CO₂ and CO. The point at which the Fe₂O₃ was completely converted to Fe₃O₄ was signified by the sudden decrease in CO₂ and rise in CO. For all fuels, this was very clear in the first cycle and became slightly less defined as the cycles progressed.

Figure 4.6 illustrates that at the beginning of the reduction period, only a small amount of lignite coal is being converted to carbon dioxide due to the small feed amount. However, after a few minutes of continuous feeding, a sharp increase in the concentration of carbon dioxide is observed. This increase coincides with the formation of carbon monoxide and this observation continues until a carbon monoxide breakthrough (sharp increase in the concentration of carbon monoxide) is observed that sharply decreases the concentration of carbon dioxide from the bed. Carbon monoxide was initially produced due to the formation of char in the bed as a result of the incomplete oxidation of fuel via pyrolysis. This is because the screw feeder is placed above the fluidized bed and as a result, when the fuel first enters the reactor it undergoes pyrolysis to produce CO and CH₄ that were liberated before it had the chance to react with the iron oxide in the bed.

A similar reduction stage phenomenon was observed for lignite char (Figure 4.6) and Taldinski bituminous coal (Figure 4.8). However, for the case with Taldinski bituminous coal (Figure 4.8), the sharp increase in the concentration of carbon dioxide occurred much earlier compared to cases with lignite coal and lignite char. For the case with activated carbon (Figure 4.9), it was found that the increase in the concentration of carbon dioxide occurred rather gradually. This is in contrast to the sudden increase in the concentration of carbon dioxide seen in cases with lignite coal and lignite char. This is then followed by a sharp decrease in the concentration of carbon dioxide when carbon monoxide breakthrough is observed. The variation in the concentration of carbon dioxide and carbon monoxide seen in cases with lignite coal and Taldinski bituminous coal is attributed to the uneven feeding rate provided by the screw feeder. The gradient of the slope for the increase in the concentration of carbon dioxide indicated that lignite coal is the most reactive fuel followed by lignite char, Taldinski bituminous coal, and activated carbon.

Carbon monoxide breakthrough is believed to be due to fact that the reverse Boudouard reaction, i.e. $\text{CO}_2 + \text{C} \rightarrow 2\text{CO}$, became the dominant reaction towards the end of the reduction period. This is believed to occur when all the Fe_2O_3 in the bed has been converted into Fe_3O_4 . However, the conversion of Fe_3O_4 to FeO is believed to be thermodynamically non-feasible unless the ratio between the partial pressure of carbon dioxide and the partial pressure of carbon monoxide, $\frac{p_{\text{CO}_2}}{p_{\text{CO}}}$, in the bed falls below 2 (Bohn et al., 2008). As a result, it is believed carbon dioxide fed into the bed might have reacted with the fuel to form carbon monoxide via the reaction stated above.

It was observed that ‘tails’ of CO_2 and CO were formed at the end of the feeding period. Importantly, this tail accounts for the small amount of CO_2 present at the start of the oxidation stage that can be seen in later figures. For more than 4 minutes after the oxygen is switched on, no oxygen appears in the outlet indicating that all of the oxygen is being used to reoxidise the oxygen carrier. Additionally, apart from the small amount of CO_2 visible at the start of oxidation from the end of the ‘tail’, it appears as though the char combustion only occurs at the end of the oxidation period when the second CO_2 increase is observed.

SO₂ or CH₄ was produced during the feeding stage for all fuels; however, there was a difference in the way that it was produced. For lignite char and activated carbon, the SO₂ or CH₄ was produced as a peak, which was released whilst the iron oxide was still active. Since lignite char and activated carbon contain negligible volatile matter, the SO₂ or CH₄ signal most likely arose from SO₂.

During the initial oxidation stage, a very small amount of oxygen or carbon dioxide was detected for the case with lignite coal (Figure 4.7). This was then followed by a sharp increase in the concentration of oxygen till it reached equilibrium. This observation indicates that most of the fuels fed into the bed as well as the char which was formed during the reduction period were combusted to form carbon dioxide and carbon monoxide. As a result, there was very little fuel or char left in the bed during oxidation period. Besides that, it can also be deduced that most of the oxygen supplied during the initial oxidation is spent to reoxidise the reduced iron oxide from FeO to Fe₃O₄ and finally to Fe₂O₃. It shows that iron oxide in the reduced form (FeO and Fe₃O₄) has high affinity to react with oxygen in air.

A similar oxidation stage phenomenon was observed for lignite char (Figure 4.6). During the oxidation period for the case with activated carbon (Figure 4.9), carbon dioxide and carbon monoxide were liberated when air was introduced into the system. This shows that there is quite a large amount of unreacted fuel and leftover char in the bed that has not been reacted and will compete with iron oxide for oxygen during the oxidation period. It can also be deduced that activated carbon and its char have a higher affinity for oxygen in air compared to iron oxide due to the fact that a sharp increase in the concentration of carbon dioxide and small releases of carbon monoxide was observed when air was introduced into the bed. Carbon monoxide release indicated that the amount of oxygen supplied to the bed was still insufficient in order to achieve complete combustion, thereby causing some of the fuel and char to be partially oxidised. For the case with bituminous coal (Figure 4.8) however, a sharp increase in the concentration of carbon dioxide was observed after about 1 minute when air was introduced into the bed. This phenomena indicates that iron oxide has a higher affinity for oxygen compared to bituminous coal and its char.

As mentioned earlier, during the first part of the oxidation stage there is no oxygen seen in the off gases. This was observed for all fuels with iron oxide. This indicates that the rate of supply of oxygen was limiting. For the cases where there were small inventories of carbon in the bed, i.e. with Hambach lignite and its char, the carbon inventory was only burnt – as signified by the appearance of CO₂ in the off gases – once there was a breakthrough of oxygen, indicating that up until that point the oxygen carrier was reacting with oxygen at a much higher rate than the char. Note that the small amount of CO₂ observed at the start of oxidation with the lignite char (Figure 4.6) is actually the end of the ‘tail’ which was observed during the purge stage. A similar ‘tail’ was observed with the lignite coal, but is much smaller since the inventory of carbon for the lignite coal was smaller than that of the lignite char. For Taldinsky bituminous coal and the activated carbon, which gave larger carbon inventories, CO₂ was seen at the onset of oxidation as there was a large amount of char being accumulated in the bed. The rate of emission of CO₂ increased as the iron oxide reached complete conversion.

SO₂ was produced during the oxidation stage with Hambach lignite char, Taldinsky bituminous coal and activated carbon, it being assumed that methane would not be present in conditions of oxidation. The SO₂ is produced as a batch at the same time as the carbon inventory is burnt off, rather than during the initial oxidation of the iron oxide.

There is also a strong contrast in the reactivities of the different fuels as evidenced by the different amounts of carbon that were accumulated during the feeding stage. A comparison of the carbon inventory is made in Table 4.6. The Hambach lignite and its char are both highly reactive and so the inventory of carbon was small. The Taldinsky bituminous coal and activated carbon have a much lower reactivity by comparison, resulting in inventories an order of magnitude larger.

Table 4.6: Carbon accumulation in fluidized bed

Fuel	Moles of Carbon Accumulation Per Mole of Carbon Fed
Hambach Lignite Char	0.038 ± 0.008
Hambach Lignite Coal	0.010 ± 0.006
Taldinsky Bituminous Coal	0.630 ± 0.038
Activated Carbon	0.722 ± 0.049

Figure 4.10 shows the feeding rates for the different cycles and the different fuels used in the study with iron oxide whereas Table 4.7 details the average feeding rate throughout the experimental run as well as the errors involved due to the screw feeder. It is important to note that it was assumed throughout the experimental work that fuels introduced into the bed were fully converted into carbon dioxide due to the difficulty involved in obtaining a specific value of the amount of fuel fed into the bed in every cycle. Errors derived from the screw feeder are due to two reasons. The first reason is due to the fact that the screw feeder is placed horizontally during the feeding period thereby limiting the effect of gravity on the feeding. The other reason is due to the fact that the fuels used in these experiments are in different sizes, thereby increasing the probability that some of the fuel particles are larger than the outlet of the screw feeder. This will cause the screw feeder to have to grind the fuel to a slightly smaller size which will cause a slight inconsistency in the feeding.

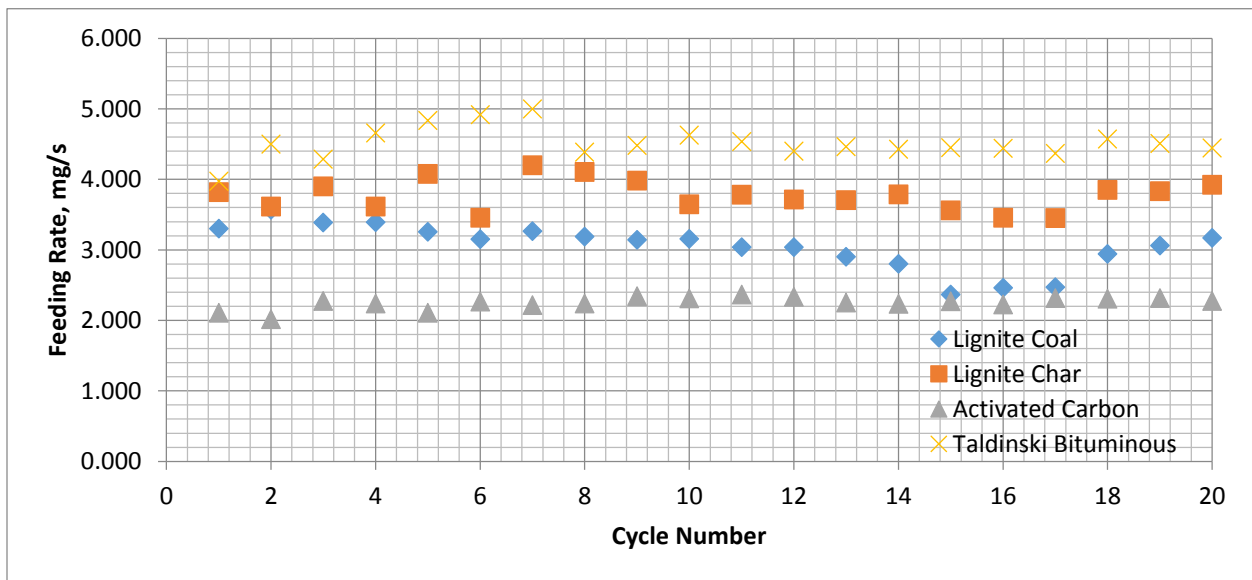


Figure 4.10: Feeding rates for the different types of fuels for the iron oxide system

Table 4.7: Feeding rates for iron oxide systems

	Lignite Coal	Lignite Char	Activated Carbon	Taldinski Bituminous Coal
Average (mg/s)	3.054	3.775	2.252	4.515
Standard Deviation (mg/s)	0.321	0.218	0.087	0.225
95% Confidence Interval (mg/s)	0.141	0.096	0.038	0.098

4.7.2 Iron Oxide Conversion Analysis

Figure 4.11 shows the percentage of Fe_2O_3 converted Fe_3O_4 during the reduction period whereas Figure 4.12 details the percentage of Fe_3O_4 oxidised back into Fe_2O_3 . It can be deduced from both figures that the percentage of iron oxide being converted during reduction and oxidation follows a similar pattern as the fuel feeding rate (Figure 4.10) where a higher feeding rate produces a higher iron oxide conversion ratio and vice versa. This is true for all cases except for the case with activated carbon. For the case with activated carbon, iron oxide conversion oscillates till it reaches a stable value towards the end of the experimental run.

The conversion of Fe_3O_4 to FeO was initially believed to be thermodynamically non-feasible in these experiments. As a result, it was believed that the apparent conversion of over 100% of Fe_2O_3 to Fe_3O_4 could have been caused by the reverse Boudouard reaction but was instead being attributed to the conversion of Fe_3O_4 to FeO . However, pyrolysis of coal produces CH_4 as well as CO and H_2 . From the thermodynamic analysis conducted in Chapter 3, it is highly possible that the conversion of more than 120% seen for cases with lignite coal and lignite char is due to the higher percentage of CH_4 in the pyrolysis gas. This will cause a higher percentage of Fe_2O_3 being converted into FeO during the reduction stage.

However, as these initial sets of experiments were conducted as a proof of concept, one main inaccuracy occurred whereby the bed materials were sieved at the end of the experiment without measuring the weight of the bed materials. As a result, the percentages of iron oxide converted were calculated based on the assumption that there was no loss of iron oxide from

the bed. However, ICP-MS analysis carried out on the bed materials indicated that there were some losses in the amount of iron oxide at the end of the experiment. As a result, the true iron oxide conversion is believed to be increasing as the number of reaction cycle increases rather than being stable throughout the entire study. This issue was addressed in the calculations conducted for experimental setup 2.

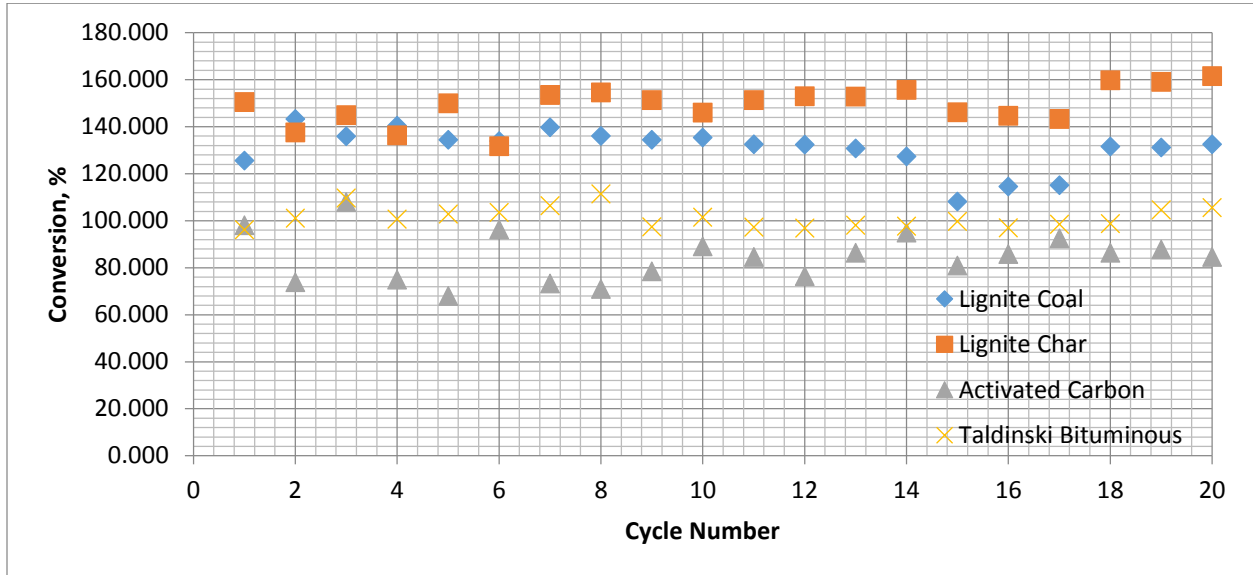


Figure 4.11: Iron oxide conversion for different fuels system during reduction

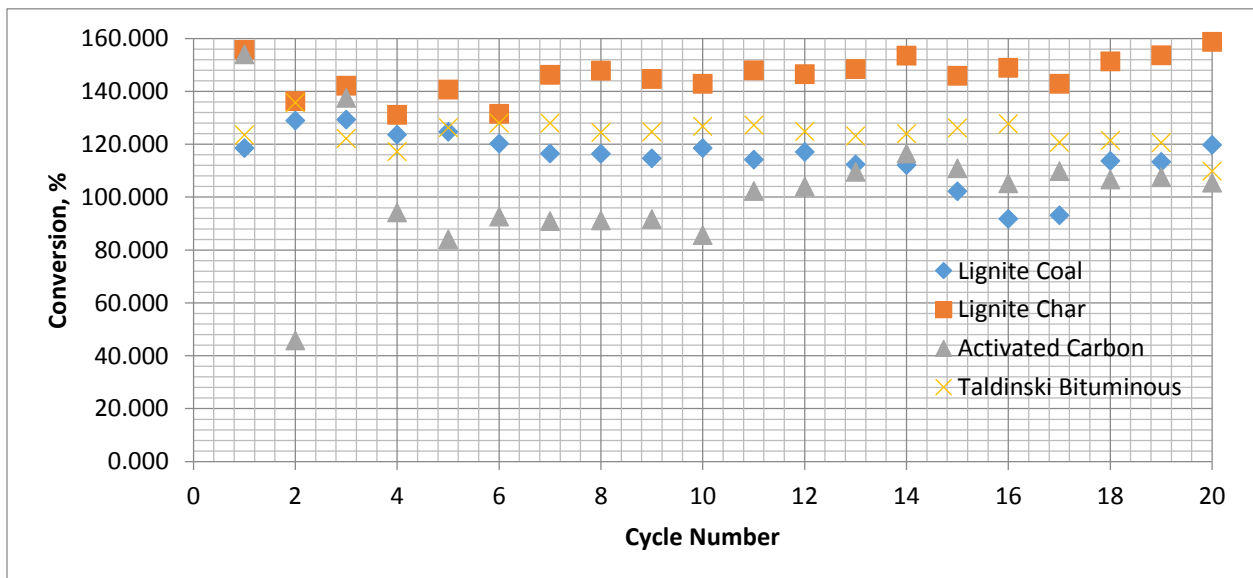


Figure 4.12: Iron oxide conversion for different fuels system during oxidation

4.8 Copper Oxide

4.8.1 Exit Gas Profiles

Figure 4.13 shows a typical cycle obtained when feeding lignite char into a bed of 20g of copper oxide at 925°C. At the start of the experiment, the bed is fluidized with 9 mol percent oxygen in nitrogen. The gas supply was switched over to 50 mol percent CO₂ in N₂. During this transition, it can be seen that the oxygen level does not fall directly to zero. The insert shows that oxygen was released during the 60s transition period before feeding was commenced. This oxygen is due to the decomposition of CuO to Cu₂O which occurs rapidly at temperatures above 900°C. Previous experiments by Chuang (2009) indicated that at 925°C, the copper oxide took approximately 130s to completely decompose to Cu₂O. Thus it was assumed that at the start of feeding, the copper oxide was 50% decomposed to Cu₂O. Lignite char was fed to the bed for 5.5 minutes; the breakthrough occurred much earlier than in the experiments with the iron oxide, because the amount of active oxygen carrier present for the experiments with the copper oxide is much less than for those with iron oxide. Since the copper oxide was partially converted to Cu₂O, the copper oxide carrier becomes depleted sooner than with the iron oxide carrier. After the feeding period, the CO₂ and fuel feeding were discontinued and the bed was purged with nitrogen for 60s. Thereafter, a mixture of 9 mol percent oxygen in nitrogen was supplied to the bed; the copper oxide was regenerated and the char in the bed was combusted for around 12 minutes.

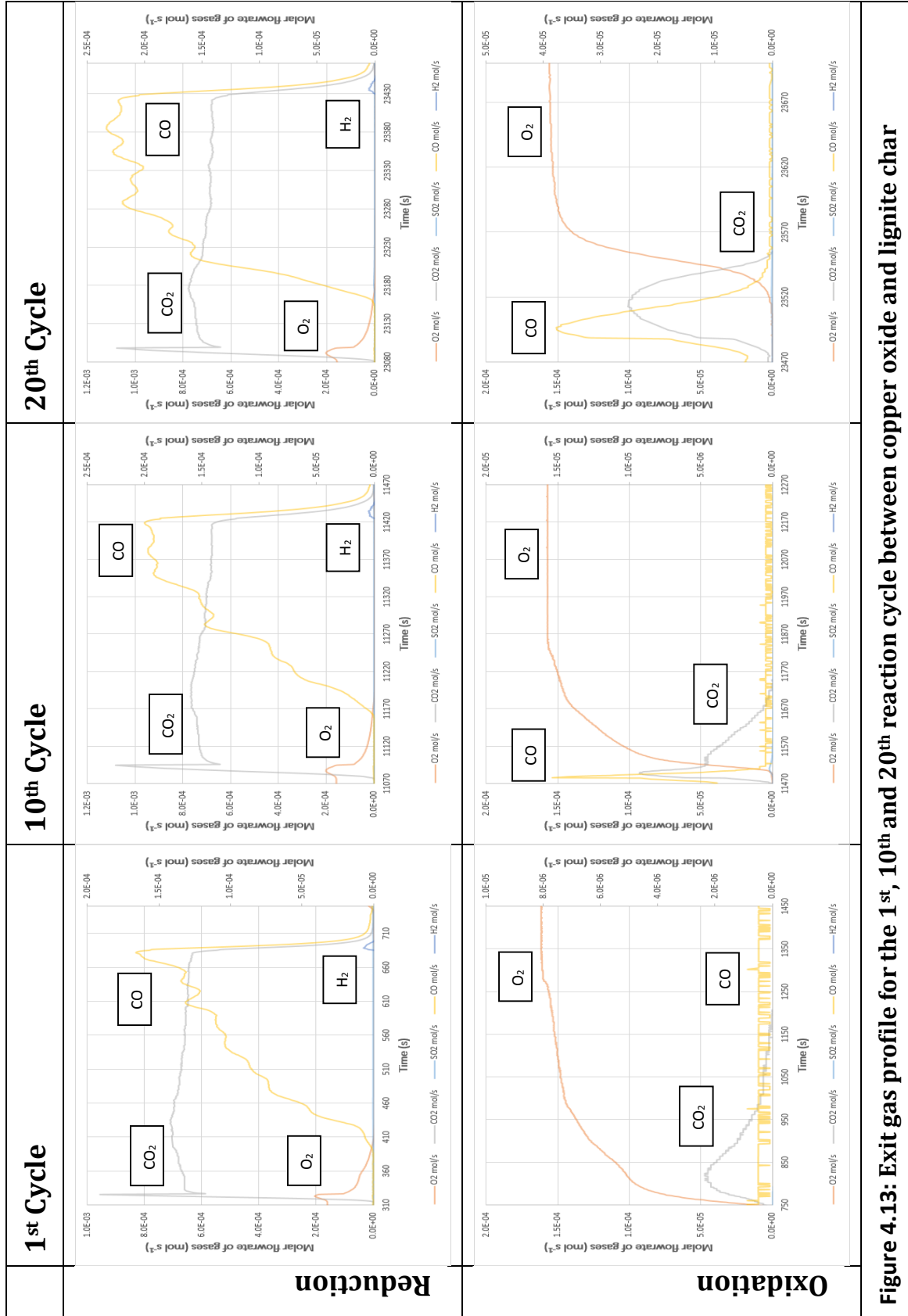


Figure 4.13: Exit gas profile for the 1st, 10th and 20th reaction cycle between copper oxide and lignite char

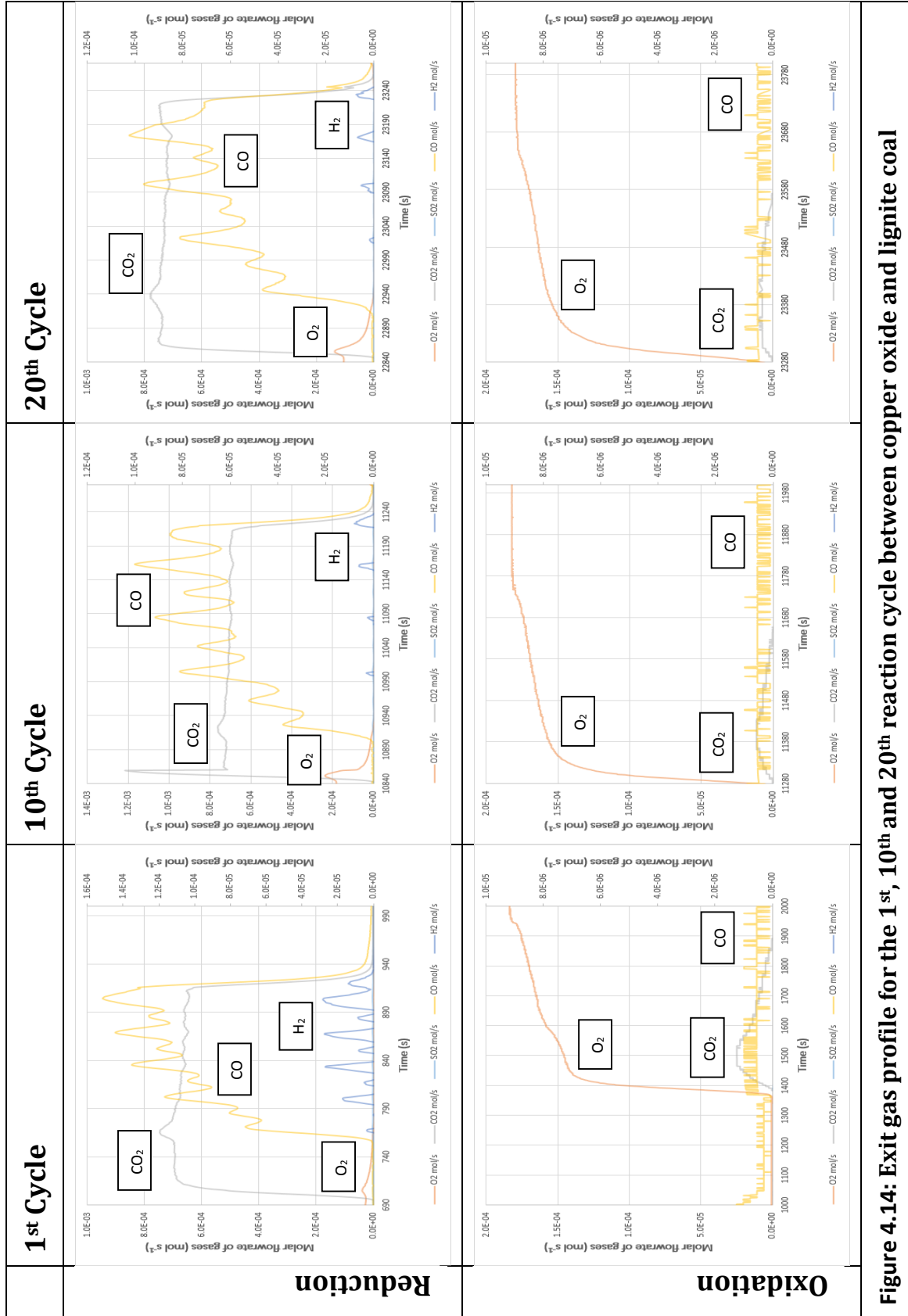


Figure 4.14: Exit gas profile for the 1st, 10th and 20th reaction cycle between copper oxide and lignite coal

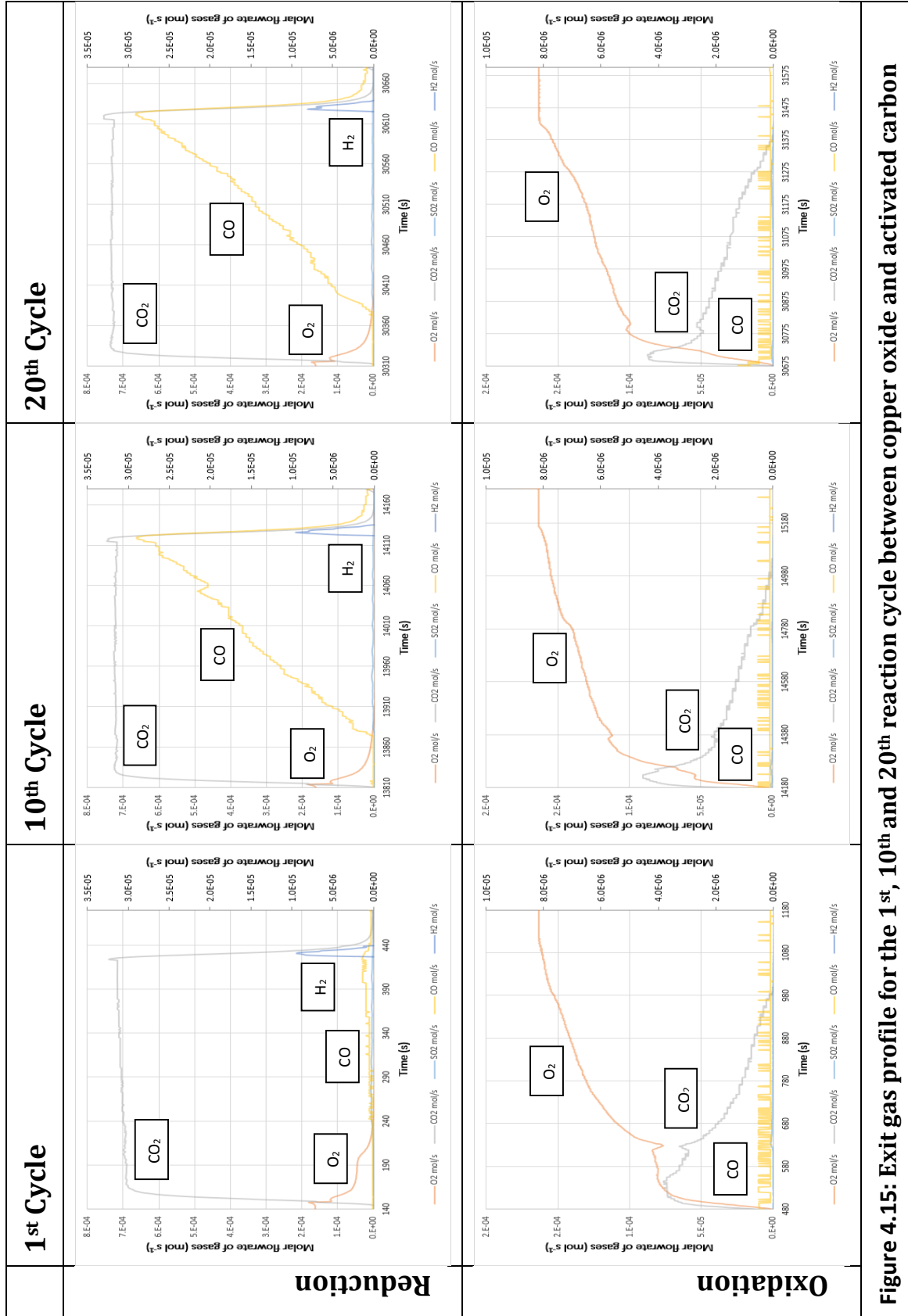


Figure 4.15: Exit gas profile for the 1st, 10th and 20th reaction cycle between copper oxide and activated carbon

Figures 4.13 to 4.15 show the mole fraction of gases exiting the reactor during the 1st, 10th and 20th cycles for experiments with Hambach lignite char, Hambach lignite, coal and activated carbon respectively. The results for experiment conducted with Taldinski bituminous coal and US bituminous coal were not shown due to experimental file corruption issue. The cycle is broken down into the reduction stage, which is given in the first row and the oxidation stage in the second row. Figures 4.13 to 4.15 describe the oxygen is released during the initial stage of feeding. This occurs due to the low partial pressure of oxygen in the bed, thereby allowing copper (II) oxide to decompose into copper (I) oxide and possibly to copper during that initial period of time. Calculations indicated that between 10 to 14% of the oxygen from copper oxide is released during this period. Figure 4.13 illustrates that the concentration of carbon dioxide released from the bed increases gradually. This is in contrast to the case of iron oxide with lignite coal, where a sudden increase in the concentration of carbon dioxide was seen.

This indicates that there are two possible reaction mechanisms occurring in the bed during the feeding period. The first mechanism is via the gas-solid interaction. This is due to the fact that the decomposition of copper (II) oxide to copper (I) oxide occurs till all copper (II) oxide has been converted to its lower oxidation form due to the low partial pressure of oxygen in the bed. As a result, the oxygen released via the decomposition of copper oxide reacts with lignite coal that is fed into the bed. The second mechanism is via direct reaction between copper oxide and lignite coal. As a result, the initial carbon dioxide released is due to the faster first mechanism while carbon dioxide and carbon monoxide released in the later stages are due to the second mechanism.

Figure 4.14 also shows that carbon monoxide is formed as soon as the concentration of oxygen falls to zero indicating that the amount of oxygen available in the bed is insufficient to achieve complete combustion. As a result, some of the fuel fed into the bed will only be partially oxidised via pyrolysis. Carbon monoxide was initially produced due to the formation of char in the bed as a result of the incomplete oxidation of fuel via pyrolysis. This is because the screw feeder is placed above the fluidized bed and as a result, when the fuel first enters the reactor, it undergoes pyrolysis to produce CO and CH₄ which were liberated

before it had the chance to react with the copper oxide in the bed. Similar reduction stage phenomenon was observed for lignite char (Figure 4.13). However for the case with activated carbon (Figure 4.15), the concentration of carbon dioxide released from the reaction is constant throughout the cycle indicating that activated carbon is not as reactive when compared to lignite coal and lignite char.

During the oxidation stage for all cases, a sharp increase in oxygen was observed during the initial oxidation period followed by a gradual increase in the concentration of oxygen till equilibrium was reached. This is in sharp contrast to cases with iron oxide whereby a sharp increase is observed a few minutes after air is introduced into the bed and reaches equilibrium within a short period of time after that. The sharp increase in the concentration of oxygen during the initial oxidation stage can be attributed to 3 factors. The first is due to the fact that most of the fuel fed into the bed has been fully combusted or partially oxidised via pyrolysis. Pyrolysis of fuel creates char which is less reactive thereby requiring a longer period of time for the combustion to proceed to completion. As a result, the initial sharp increase in the concentration of carbon dioxide seen in cases with lignite char (Figure 4.13) and activated carbon (Figure 4.15) can be attributed to the unreacted fuel. Carbon dioxide released during the latter stages of the oxidation period can be attributed to the unreacted char. The second factor is due to the fact that an equilibrium oxygen partial pressure would need to be achieved before copper and copper (I) oxide react with oxygen in air to form copper (II) oxide. Finally, alumina which is present as a support in copper oxide causes the copper oxide particles to be more stable and have a lower affinity for oxygen. The second and third factor is believed to be the cause for the longer time required for complete oxidation.

Sharp spikes in the concentration of CO₂ observed by Scott and Dennis (2010) during the initial oxidation periods were not observed in these experiments due to the fact that the carbon dioxide valve was switched off at the end of the feeding period. However, a sharp spike in the concentration of CO₂ during the initial period of feeding was observed for cases with lignite char (Figure 4.13) and lignite coal (Figure 4.14). This could be due to rapid decomposition of the copper oxide particles to balance the sudden drop in the partial

pressure of oxygen in the reactor. The rapid increase in the concentration of oxygen released during this time could have reacted with the lignite coal. This is believed to occur until equilibrium in the partial pressure of oxygen in the reactor is achieved. It was noted that there was an increase in the temperature of the bed during the initial oxidation period and this is associated with the burning off of the carbon inventory in the bed. Fluctuations in mole fractions of CO₂ and CO during the feeding period are attributed to the unsteady state feeding of the coal screw feeder.

Figure 4.16 shows the feeding rates for the different cycles and the different fuels used in the study with copper oxide whereas Table 4.8 details the average feeding rate throughout the experimental run as well as the errors involved due to the screw feeder.

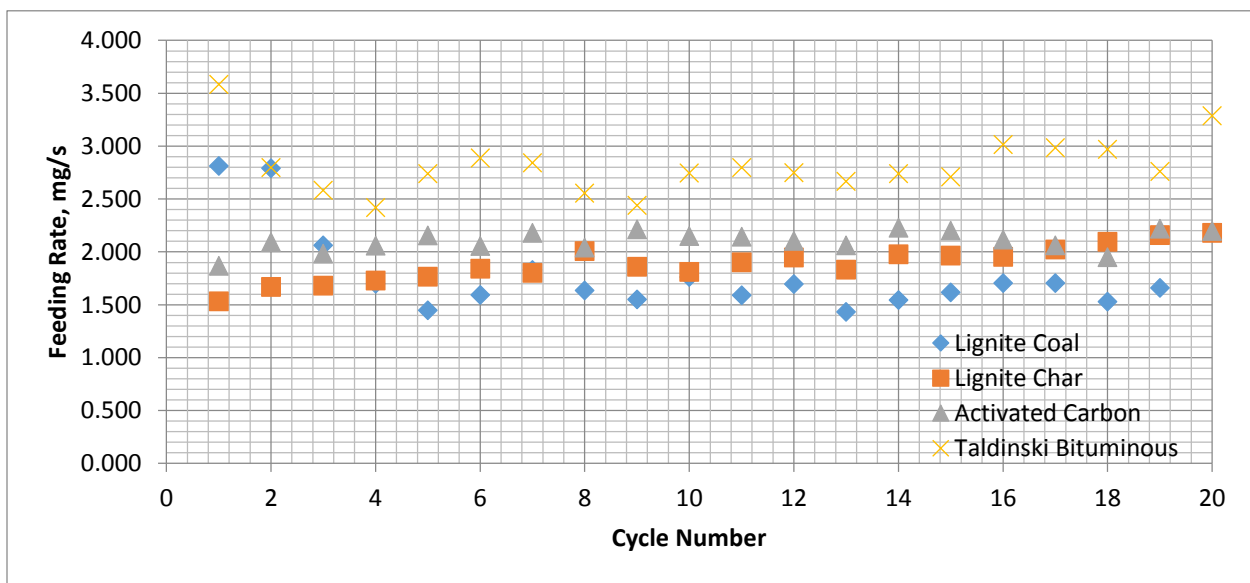


Figure 4.16: Feeding rates for the different types of fuels for the copper oxide system

Table 4.8: Feeding rates for copper oxide systems

	Lignite Coal	Lignite Char	Activated Carbon	Taldinski Bituminous
Average (mg/s)	1.771	1.886	2.104	2.813
Standard Deviation (mg/s)	0.389	0.168	0.097	0.271
95% Confidence Interval (mg/s)	0.171	0.074	0.042	0.119

4.8.2 Copper Oxide Conversion Analysis

Figure 4.17 shows the percentage of CuO which is converted to Cu during the reduction period whereas Figure 4.18 describes the percentage of Cu which is oxidised back into CuO. It can be deduced from both figures that the percentage of copper oxide being converted during reduction and oxidation follows a similar pattern as the fuel feeding rate (Figure 4.16), where a higher feeding rate produces a higher copper oxide conversion ratio and vice versa. This is true for all cases except for the case with lignite coal. It is also noted that the amount of copper oxide converted during oxidation is quite similar for the case with activated carbon, but differs significantly for cases with lignite coal and lignite char.

As alumina is an inert compound that does not react with fuel and is very difficult to decompose (Hossain and de Lasa, 2008), it is believed that the difference is mainly due to the error involved in the gas analysers. This error is believed to have occurred during the initial feeding period as a sharp increase in the concentration of oxygen was observed for cases with lignite coal and lignite char, but not observed in the case with activated carbon. This will then increase the estimated amount of copper oxide decomposition during the initial feeding period. Since the conversion of copper oxide during reduction is calculated based on the sum of amount of copper oxide that is decomposed during the initial feeding period and the amount of copper oxide that reacts with fuel fed into the bed. This phenomenon will thereby increase the estimated conversion of copper oxide during reduction.

However, as these initial sets of experiments were conducted as a proof of concept, it encountered the same inaccuracy described in the iron oxide section whereby the final bed material was not weighed. As a result, the percentage of copper oxide converted during the reduction stage is lower than expected.

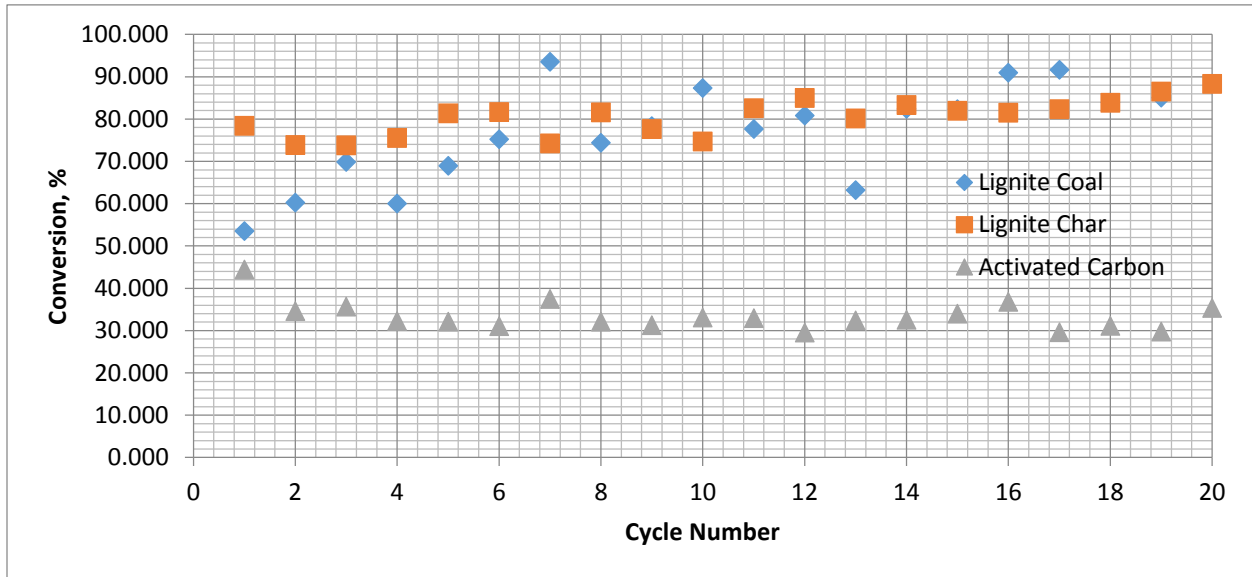


Figure 4.17: Copper oxide conversion for different fuels system during reduction

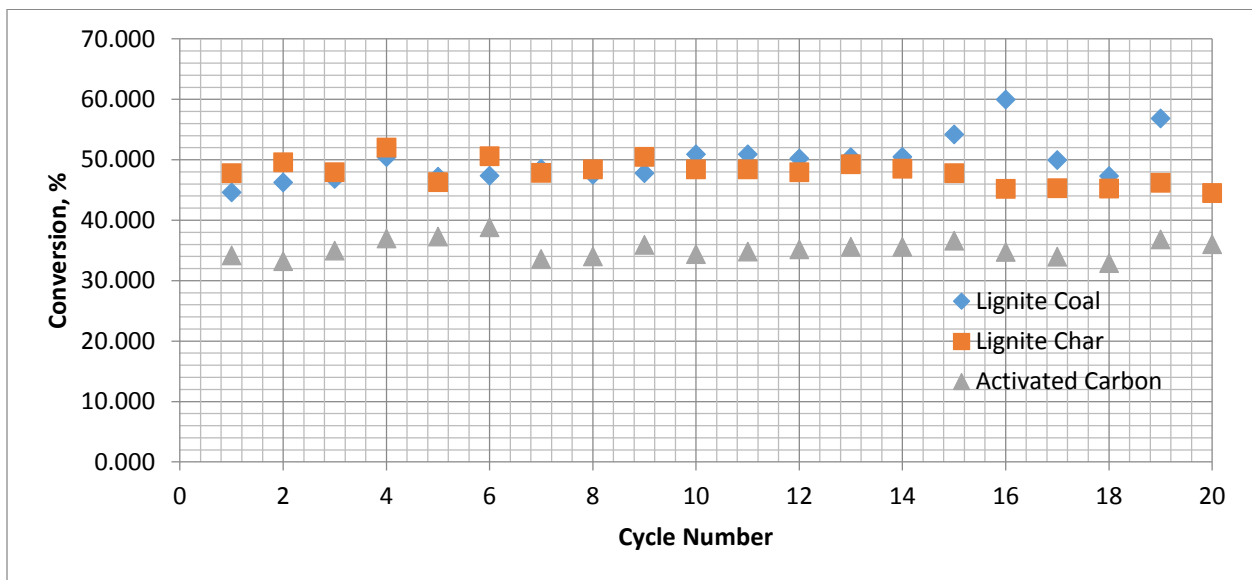


Figure 4.18: Copper oxide conversion for different fuels system during oxidation

Chapter 5 EXPERIMENTAL SETUP 2

A second fluidised bed was constructed at the University of Sheffield under a different specification. The objective of the study using experimental setup 2 was to study the morphology and compositional changes in mechanically mixed iron oxide and copper oxide impregnated on alumina during a long operational period with 3 different fuels under the reduction condition of coal particles and pure N₂ and the oxidation condition of air. The result from this study would then give a good approximation of the operating lifetime of these particles in a chemical looping combustion system.

5.1 Experimental Setup 2

Figure 5.1 shows the experimental setup for this chemical looping combustion system. The system consists of 5 main components. They are; the reactor system that consists of the fluidized bed reactor, feeding system consisting of the screw feeder, cooling and clean-up section consisting of 2 condensers, gas analyser and data logger system, and external heater components. They are shown in Figures 5.2 and 5.3.

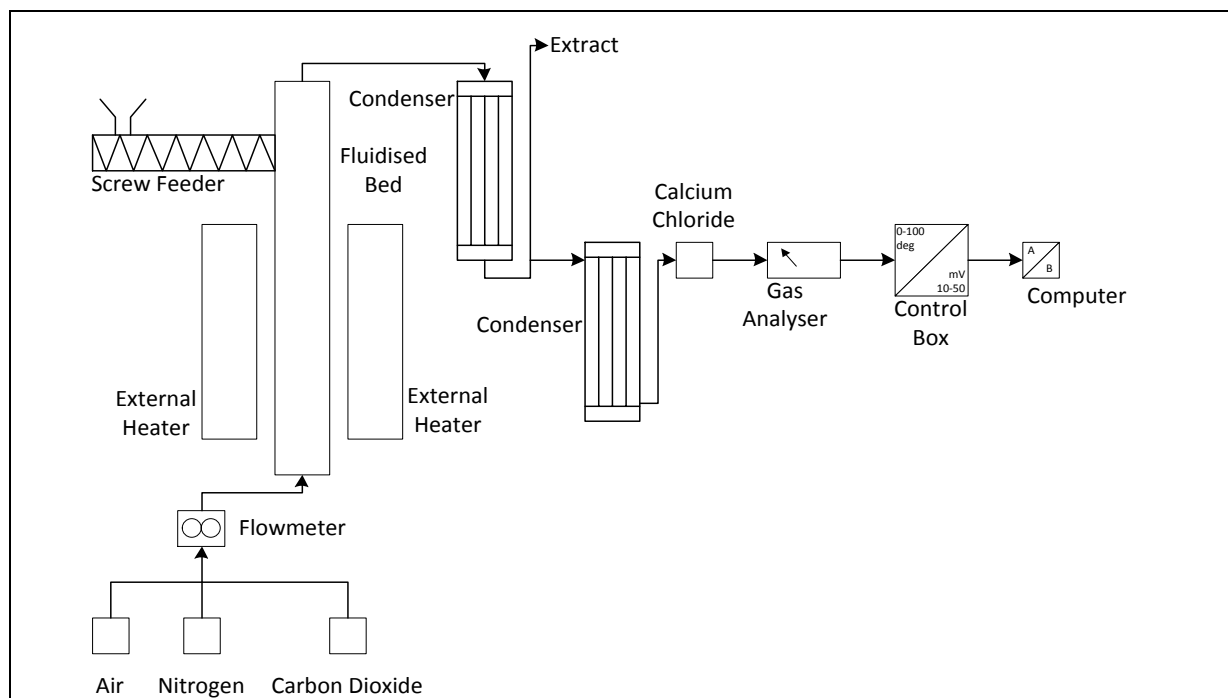


Figure 5.1: Schematic diagram of the experimental setup



Figure 5.2: Experimental Setup

Legend: (1) Screw feeder, (2) External heaters, (3) Fluidised bed, (4) Condenser, (5) Trace heater

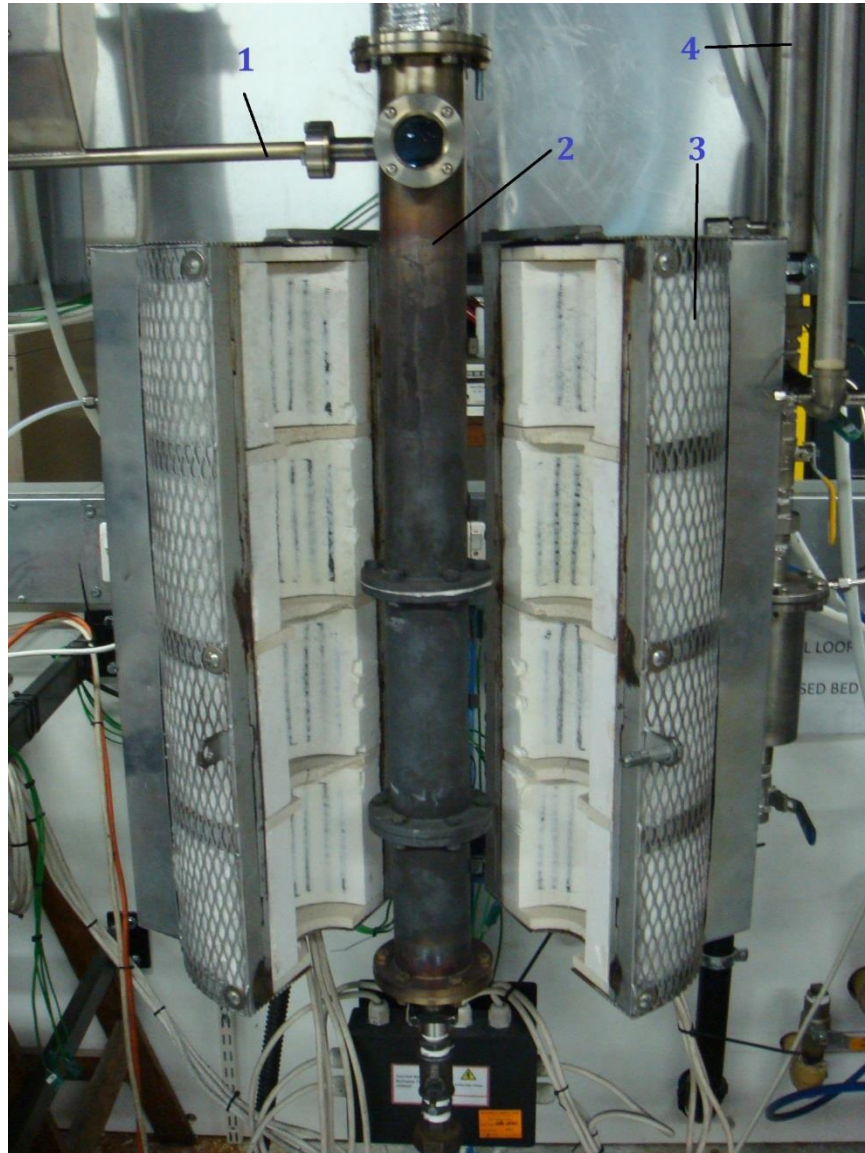


Figure 5.3: Fluidised bed reactor

Legend: (1) Screw feeder, (2) Fluidised bed, (3) External heater, (4) Condenser

5.1.1 Fluidised Bed Reactor

The fluidized bed used for this study has an inner diameter of 75 mm. The height of the fluidized bed is height 1000 mm. It is constructed from 316 stainless steel. A perforated plate made from sintered material is used to support the material in the fluidised bed. Perforated plate was chosen as it is cheap and easy to fabricate. However, this type of plate design has an issue in that fines created during experiments are susceptible to get trapped within the plate itself reducing the homogeneity of the flow into the fluidised bed.

5.1.2 External Heaters

Eight external electrical heaters were used to heat up the fluidized bed. The heaters are made from ceramic fiber and they use iron – chrome – aluminium wire as the heating element. Each heater has a specification of 650 watts and 120 volts.

5.1.3 Screw Feeder

The screw feeder is used to supply fuel into the fluidized bed. The feeding rate is adjustable by the user.

5.1.4 Condensers

The gas sample was passed through a traced heater line before being fed into the first cold finger. The first cold finger cools down the gas to collect any particulates and fines or condensed tar before the gas is sent to the gas analyser or the extract. The second cold finger cools down the gas to collect any leftover particulates before the gas enters the gas analyser.

5.1.5 Thermocouples

Six thermocouples were used to measure the temperature of the gases throughout the system. Four of the thermocouples are placed inside the bed. The first thermocouple is placed just above the perforated plate, the second thermocouple in the middle of the bed, the third thermocouple just on above the bed and the fourth thermocouple one and a half times the height of the bed above the perforated plate. The fifth thermocouple is placed in the

middle of the traced heated line while the sixth thermocouple is placed on the gas line to the gas analyser.

5.1.6 Gas Analyser

An ADC MGA 3000 multi-gas analyser was used to measure the volume concentration of oxygen, carbon dioxide and carbon monoxide. The concentration of oxygen is measured via a chemical oxygen sensor; while the concentration of carbon dioxide and carbon monoxide is measured via infrared absorption. The measurement range of ADC MGA 3000 is shown in Table 5.1.

Table 5.1: ADC MGA 3000 Detection Range

Analyser	Type	Range
CO	Infrared	0-30 volume %
CO ₂	Infrared	0-20 volume %
O ₂	Paramagnetic	0-25 volume %

5.1.7 PC & Data Logger

Data logging software from Azeo Tech, Inc-DAQ Factory Lite Release 5.11 was used to record data from the thermocouples and the exit gas concentrations of oxygen, carbon dioxide and carbon monoxide.

5.1.8 Gas Cylinders

The pure nitrogen gas cylinder was purchased from BOC; 15% carbon dioxide and nitrogen, and 50% carbon dioxide in nitrogen gas cylinder were from BOC special gases.

5.2 Operational Conditions

The experiments were conducted at about 1198 K and 1 atmospheric pressure. The temperatures were chosen such that during the initial oxidation period when char reacts with oxygen to produce carbon dioxide, the temperature of the bed does not exceed the melting point of copper that might cause agglomeration of copper and incomplete reoxidation of the oxygen carrier. Table 5.2 shows the operating conditions of the experimental run.

Table 5.2: Operating conditions of the fluidised bed reactor

Parameter	Value
Pressure (bar)	1
Temperature (°C)	800
Fluidising Gas Flowrate (L/min)	50 ± 2
Iron Oxide Particle Size:	500 – 800 μm
Copper Oxide/Alumina Particle Size:	500 – 800 μm
Fuel Particle Size:	$1000 \mu\text{m} \pm 200 \mu\text{m}$
Fuel Mass Per Cycle:	$5 \text{ g} \pm 1 \text{ g}$
Initial Mass of Iron Oxide:	$200 \text{ g} \pm 1 \text{ g}$
Initial Mass of Copper Oxide:	$200 \text{ g} \pm 1 \text{ g}$

5.3 Operational Procedures

5.3.1 Start Up Procedures

1. Clean the inside of the fluidised bed to remove any dust or leftovers from previous experiments.
2. Switch on the digital weighing scale and tare it to zero.
3. Weigh 200 grams of iron oxide particles and load them through the top of the fluidised bed.
4. Assemble the fluidised bed back into the heater system.
5. Switch on the gas analyser, pumps, tap water and extractor fan.
6. Check all the connections.
7. Heat the fluidised bed to 800°C.
8. Switch on the computer and the data acquisition software.

9. Switch on the air valve.
10. Switch on the nitrogen and CO₂ gas cylinders.
11. Adjust the valves such that nitrogen, carbon dioxide, and air flowrate will each be 50 litres per minute when the valves are switched on.
12. Switch on the nitrogen valve to fluidise the bed.
13. Clean the screw feeder with a vacuum cleaner to remove any dust or leftover from previous experiments.
14. Pour the bituminous coal into the screw feeder.
15. Switch on the screw feeder and allow it to run continuously for 10 minutes in order to achieve steady state feeding rate.
16. Calibrate the screw feeder by measuring the amount of fuel fed into a plastic container after 5 minutes.
17. Repeat step 15 for a few times to achieve a steady state feeding.
18. Install the screw feeder back into the system. (Warning: Use a glove as the fluidized bed is hot).
19. Once the temperature of the fluidised bed has reached a constant temperature of 800°C, switch on the carbon dioxide valve.
20. After 1 minute, switch on the screw feeder for 30 seconds to feed approximately 5 g of bituminous coal into the system.
21. Allow the reaction to proceed for 10 minutes.
22. After 10 minutes, switch off the carbon dioxide valve to purge the bed with nitrogen.
23. After 1 minute, switch on the air valve to burn off chars and unreacted fuel as well as to reoxidise the reduced iron oxide particles.
24. Note the maximum temperature achieved during the initial reoxidation period and the time required to achieve complete oxidation and record this time as t_1 .

25. Repeat the cycle on automatic mode for 29 times by setting the software to achieve the following:
- Switch on the carbon dioxide and nitrogen valve for one minute.
 - Switch on the screw feeder and allow the feed to run for 30 seconds while leaving the carbon dioxide and nitrogen valve open.
 - Switch off the carbon dioxide valve to purge the bed for one minute.
 - Switch on the air valve for t_1 minutes (to the nearest upper 0.5 minutes).
 - Repeat step a to step e.

5.3.2 Shut Down Procedures

- After the last cycle, switch off the automatic running mode and stop the data collection on the computer, but leave the nitrogen and oxygen valve open.
- Switch off the external heating system.
- Switch off the gas analyser.
- Switch off the pump.
- Switch off the screw feeder.
- Switch off the digital weighing scale.
- Once the fluidized bed has cooled to room temperature, switch off the nitrogen and air valve.
- Dismantle the fluidised bed and the screw feeder.
- Pour the remaining fuel in the feeder back to its appropriate bottle.
- Collect the bed particles in a container.

The procedures were then repeated with different fuels with iron oxide or copper oxide as the oxygen carrier.

5.4 Sample Preparation

5.4.1 Preparation of Iron Oxide Particles

The iron oxide particles were prepared by using the mechanical mixing method. This method consists of spraying high-purity powdered hematite (Fe_2O_3) (>99 wt %, sized to <10 μm , Fisher Scientific Ltd.) with a fine mist of water. The water caused the fine particles to form agglomerates, which were then sieved to the size range of 400 – 700 μm , and then roasted at 1023 K for 3 hours, after which, the particles were sieved again to the size range of 400 – 700 μm .

5.4.2 Preparation of Copper Oxide Supported on Alumina Particles

A solution containing 762 g $\text{Cu}(\text{NO}_3)_2 \cdot 2.5\text{H}_2\text{O}$ and 400 g $\text{Al}(\text{NO}_3)_3 \cdot 9\text{H}_2\text{O}$ was made up in 200 cm^3 of deionized water at 318 K, at which temperature the whole of the copper nitrate was just soluble. This solution was added, with stirring, to 1400 cm^3 alumina extrudates (1.5 mm diameter, 150 m^2/g surface area from Sasol Germany). It was then sieved to a size range of 600-1190 μm by maintaining the temperature above 313 K throughout the sieving process to avoid crystallization of the copper nitrate from the solution. The slurry was then allowed to stand for 18 hours at 335 K, with care being taken to prevent evaporative losses. At the end of this period, it was found that the alumina extrudates had absorbed all of the solution without any excess liquid remaining. The resulting material was transferred to a large evaporating basin and dried for 19 hours at 423 K. This temperature was chosen such that copper nitrate did not decompose. Finally, the solids were calcined at 1023 K in an oven. This mode of preparation gave a robust carrier containing 21 weight percent CuO , based on the quantitative masses of materials used in its preparation.

Both of these methods are chosen as they are simple and can be produced at a large quantity in a short amount of time. Besides that, the materials chosen for the oxygen carrier preparation are fairly cheap.

5.4.3 Fuel Analysis

Proximate and ultimate analyses of the fuels are given in Table 5.3. Procedures involved in the proximate and ultimate analyses are shown in Appendix A. Table 5.4 shows the inductive coupled plasma mass spectrometry for the ash content for these fuels.

Table 5.3: Proximate and ultimate analyses of fuels

	Hambach Lignite Coal	Russian Bituminous Coal	UK Bituminous Coal
Moisture Content %	7.15	4.59	4.44
Volatiles %	57.75	30.77	37.23
Ash %	3.70	15.87	13.06
N (dry %)	0.90	1.72	1.41
C (dry %)	61.80	71.92	75.73
H (dry %)	4.80	3.99	4.48
S (dry %)	0.00	0.01	2.03
O₂ (dry %)	32.51	22.37	16.35
Calorific Value (Mj/kg)	25.52	31.58	34.50

Table 5.4: Inductive Coupled Plasma Mass Spectrometry of fuels' ashes

Element	Hambach Lignite Coal (mg/kg)	Russian Bituminous Coal (mg/kg)	UK Bituminous Coal (mg/kg)
Ag	0.32	1.20	0.00
Al	14126.40	292517.07	71853.88
As	5.84	29.73	16.27
B	613.02	0.00	373.49
Ba	3332.10	989.49	1768.52
Be	0.11	16.37	2.89
Bi	0.00	0.59	0.00
Ca	263051.94	9709.29	31963.92
Cd	0.00	2.25	0.12
Co	3.83	24.33	22.76
Cr	19.20	163.38	37.75
Cu	250.59	314.32	147.71
Fe	120311.30	16782.21	22297.98
Ga	78.08	41.67	54.32
Li	647.51	372.14	37.89
Mg	123750.87	6477.07	15109.55
Mn	854.91	295.70	227.35
Mo	1.43	7.01	5.56
Ni	33.06	128.49	55.38
Pb	6.95	181.03	25.09
Rb	23.25	71.33	39.96
Se	8.59	1.30	0.95
Sr	2868.43	456.19	1815.52
Te	0.00	0.00	0.37
Tl	0.00	6.49	0.61
U	1.23	3.73	4.23
V	17.48	175.47	67.04
Zn	38.20	2661.06	105.84

5.5 Experimental Measurement Accuracy

5.5.1 Temperature Measurement

Temperatures inside the bed and between the furnace and the bed were measured with K type thermocouples. They are able to measure the continuous temperature range of 0°C to 1350°C. The accuracy of the thermocouples used in the experiments was about $\pm 0.75\%$ of the measured temperature.

5.5.2 Gas Measurement

The gas emitted from the reactor passed through piping, joints and filters before reaching the gas analyser. This caused a delay of about 1 minute in the time for the passage of gas from the reactor into the gas analyser.

The accuracy of the ADC MGA 3000 was dependent on the reading errors of the 1565 AV span gas supplied by BOC, which was less than 5% for the maximum ranges of 20% volume of CO and 16% volume of CO₂. Therefore, with ranges of 30% volume CO and 20% CO₂, the error readings for cases of both CO and CO₂ were less than $\pm 4\%$. O₂ was calibrated by using atmospheric air (21% volume) and nitrogen for zero calibration gases. The maximum reading error for O₂ was $\pm 1.5\%$ volume.

5.6 Minimum Fluidisation and Pressure Drop Tests

Figure 5.4 shows the pressure drop in the bed against fluidising velocity for setup 2's fluidised bed. The minimum fluidising velocity was calculated to be about 0.16 m s^{-1} based on the model described in Chapter 3. The value corresponded to a $3.84 \times 10^{-2} \text{ m}^3 \text{ s}^{-1}$ or 38.4 L min^{-1} . This is in agreement with the minimum fluidising velocity point seen in the Figure 4.7. However, Figure 4.7 also highlights the tight working conditions during the commissioning of the fluidised bed in that the point at which initiation of entrainment occurs lies somewhere between 2.5 and $3u_{mf}$. This is believed to be due to the slightly larger range of particles sizes being used in this study. The net effect of this is that fines created during the experiments are more susceptible to elutriate from the fluidised bed.

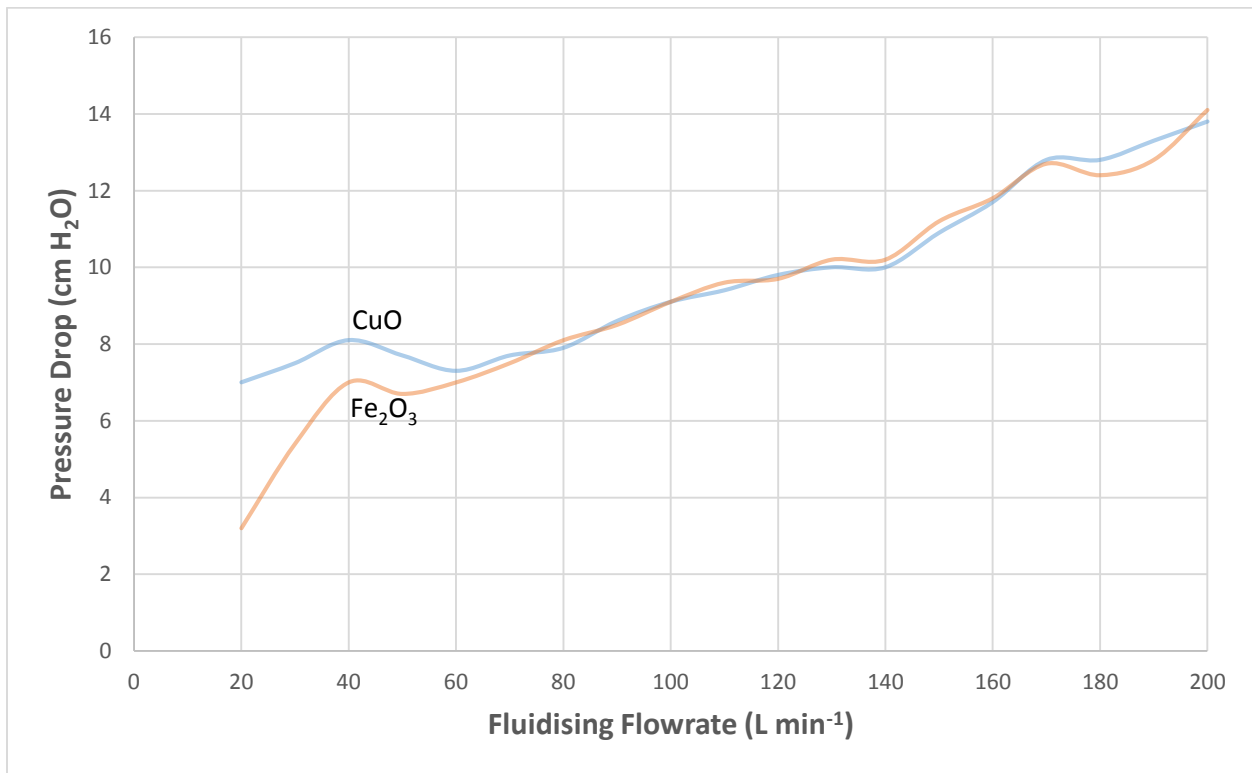


Figure 5.4: Pressure drop variation in the fluidised bed for setup

5.7 Conversion Calculations

Conversion of iron oxide during reduction was calculated by Equation 4.1 while conversion during oxidation can be calculated by Equation 4.2.

$$X_{I,r} = \frac{(2 \times CO_{2,r}) + CO_r + H_2O_r + (2 \times SO_{2,r}) - O_F}{O_{I,r}} \quad (\text{Equation 4.1})$$

$X_{I,r}$ = Fe_2O_3 conversion during reduction (%)

$CO_{2,r}$ = Number of moles of CO_2 released during reduction (*mol*)

CO_r = Number of moles of CO released during reduction (*mol*)

H_2O_r = Number of moles of H_2O released during reduction (*mol*)

$SO_{2,r}$ = Number of moles of SO_2 released during reduction (*mol*)

O_F = Number of moles of oxygen in fuel (*mol*)

$O_{I,r}$ = Number of moles of oxygen released when Fe_2O_3 is converted to Fe_3O_4 (*mol*)

$$X_{I,o} = \frac{(2 \times O_{2,o}) - [(2 \times CO_{2,o}) + CO_o + H_2O_o + (2 \times SO_{2,o})]}{O_{I,o}} \quad (\text{Equation 4.2})$$

$X_{I,o}$ = Iron oxide conversion during oxidation (%)

$CO_{2,o}$ = Number of moles of CO_2 released during oxidation (*mol*)

CO_o = Number of moles of CO released during oxidation (*mol*)

H_2O_o = Number of moles of H_2O released during oxidation (*mol*)

$SO_{2,o}$ = Number of moles of SO_2 released during oxidation (*mol*)

$O_{2,o}$ = Number of moles of oxygen in air used during oxidation (*mol*)

$O_{I,o}$ = Number of moles of oxygen used when Fe_3O_4 is converted to Fe_2O_3 (*mol*)

Conversion of copper oxide during reduction was calculated by Equation 4.3 while conversion during oxidation can be calculated by Equation 4.4.

$$X_{CuO,r} = \frac{(2 \times CO_{2,r}) + CO_r + H_2O_r + (2 \times SO_{2,r}) + (2 \times O_{2,CuO,r}) - O_F}{O_{CuO,r}} \quad (\text{Equation 4.3})$$

$X_{CuO,r}$ = *CuO* conversion during reduction (%)

$CO_{2,r}$ = Number of moles of CO_2 released during reduction (*mol*)

CO_r = Number of moles of CO released during reduction (*mol*)

H_2O_r = Number of moles of H_2O released during reduction (*mol*)

$SO_{2,r}$ = Number of moles of SO_2 released during reduction (*mol*)

$O_{2,CuO,r}$ = Number of moles of oxygen released via decomposition of *CuO* (*mol*)

O_F = Number of moles of oxygen in fuel (*mol*)

$O_{CuO,r}$ = Number of moles of oxygen released when *CuO* is converted to *Cu* (*mol*)

$$X_{Cu,o} = \frac{(2 \times O_{2,o}) - [(2 \times CO_{2,o}) + CO_o + H_2O_o + (2 \times SO_{2,o})]}{O_{Cu,o}} \quad (\text{Equation 4.4})$$

$X_{Cu,o}$ = Copper conversion during oxidation (%)

$CO_{2,o}$ = Number of moles of CO_2 released during oxidation (*mol*)

CO_o = Number of moles of CO released during oxidation (*mol*)

H_2O_o = Number of moles of H_2O released during oxidation (*mol*)

$SO_{2,o}$ = Number of moles of SO_2 released during oxidation (*mol*)

$O_{2,o}$ = Number of moles of oxygen in air used during oxidation (*mol*)

$O_{Cu,o}$ = Number of moles of oxygen used when *Cu* is converted to *CuO* (*mol*)

5.8 Operational Lifetime Analysis

Figures 5.5 and 5.6 show 5 cyclic reduction oxidation cycles for iron oxide as the bed material, while Figures 5.7 to 5.9 show the stereo-microscope images of the fresh and reacted iron oxide particles after 30 and 60 reaction cycles respectively.

Figures 5.10 and 5.11 show 5 cyclic reduction oxidation cycles for copper oxide as the bed material while Figures 5.12 to 5.20 show the stereo microscope images of the fresh and reacted copper oxide particles after 30, 60, 120, 150, 180, 210 and 240 reaction cycles respectively.

The fresh particles for the copper oxide (Figure 5.16) appears greener compared to the reacted particles. This could be due to the fact that the fresh particles were not completely calcined during the preparation stage. Besides that, even though the fresh copper oxide particles were sieved into the range desired for these experiments, it was found that there were still a lot of copper oxide fines sticking onto the surface of the larger particles.

Figures 5.8 to 5.9 and Figures 5.13 to 5.20 show that the reacted particle size for both iron oxide and copper oxide has increased quite significantly compared to the fresh particles. Besides that, the reacted particle appears to be darker red compared to the bright red of the fresh particles.

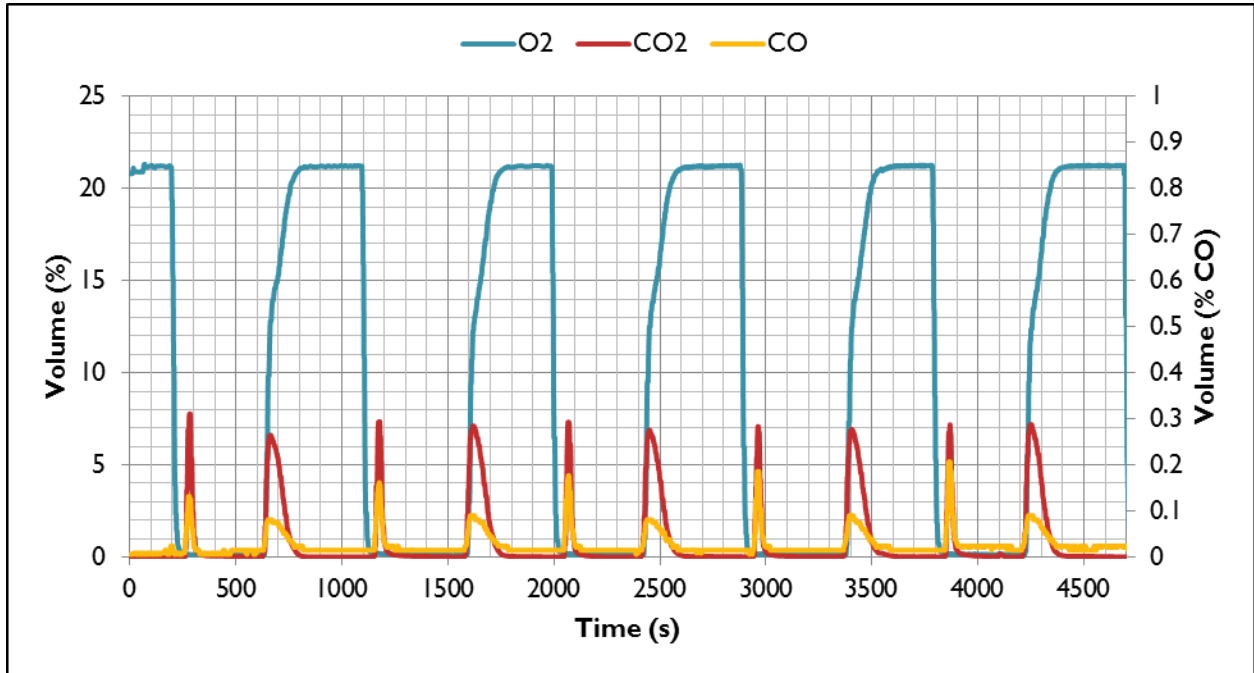


Figure 5.5: Exit gas profile for the first five reaction cycles between iron oxide and UK bituminous coal

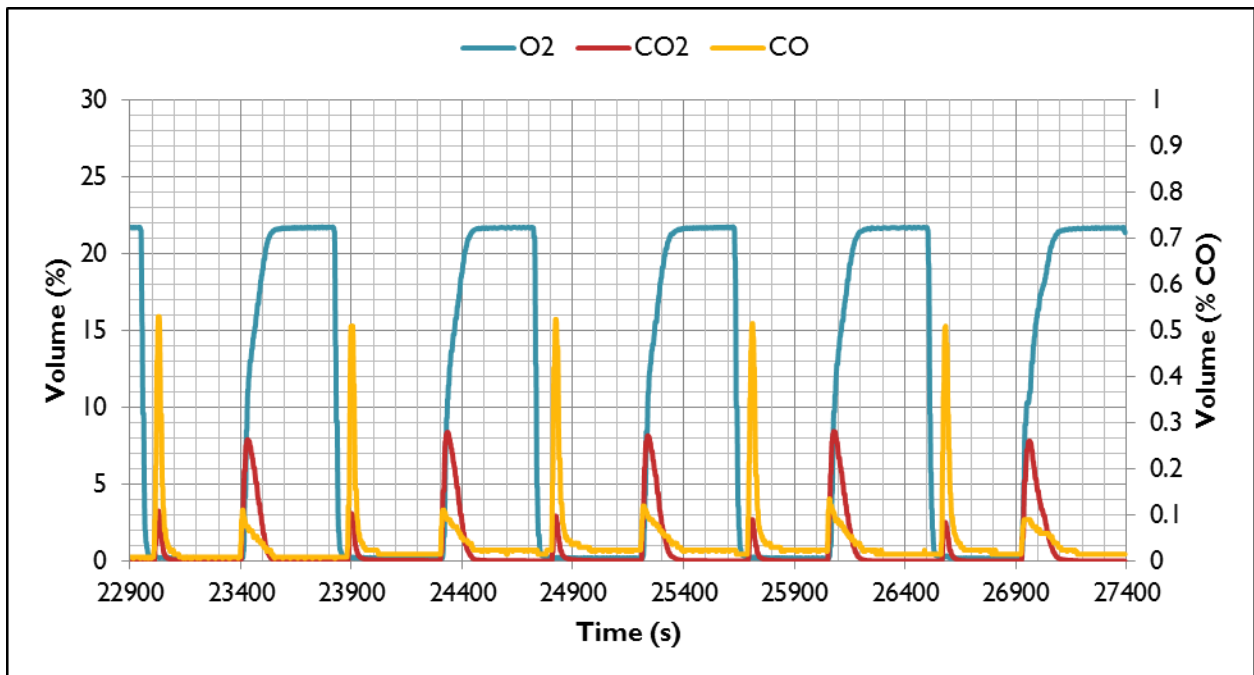


Figure 5.6: Exit gas profile for cycles 56 to 60 between iron oxide and UK bituminous coal

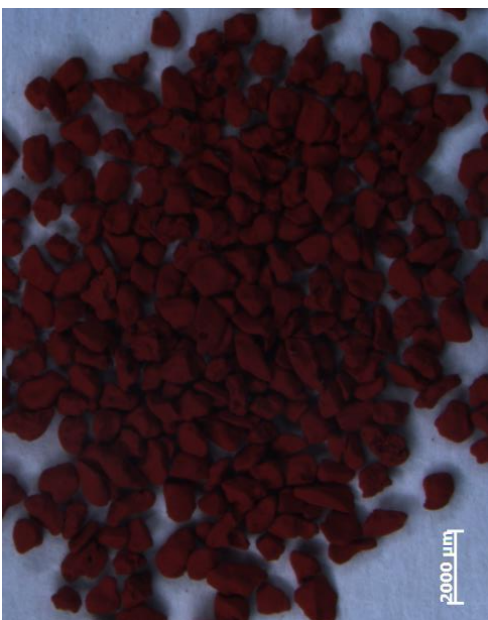


Figure 5.9: Fresh iron oxide

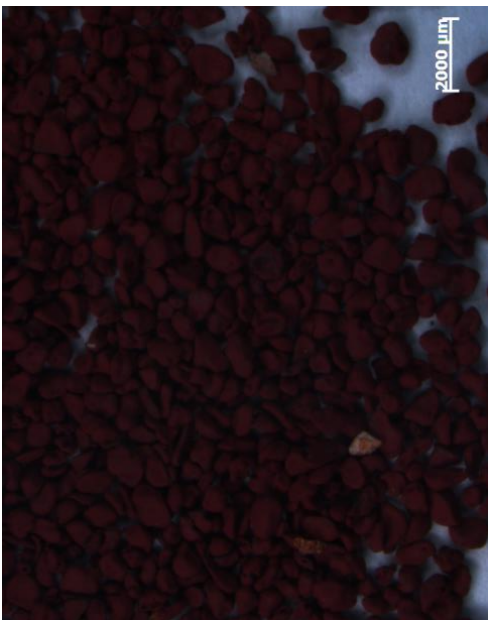


Figure 5.7: Iron oxide after 30 reaction cycles

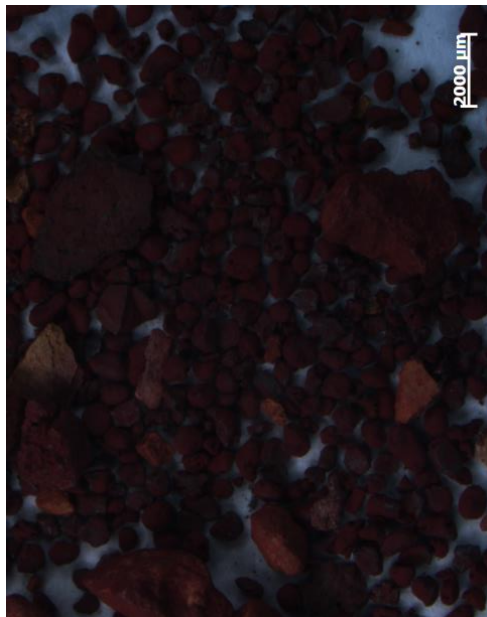


Figure 5.8: Iron oxide after 60 reaction cycles

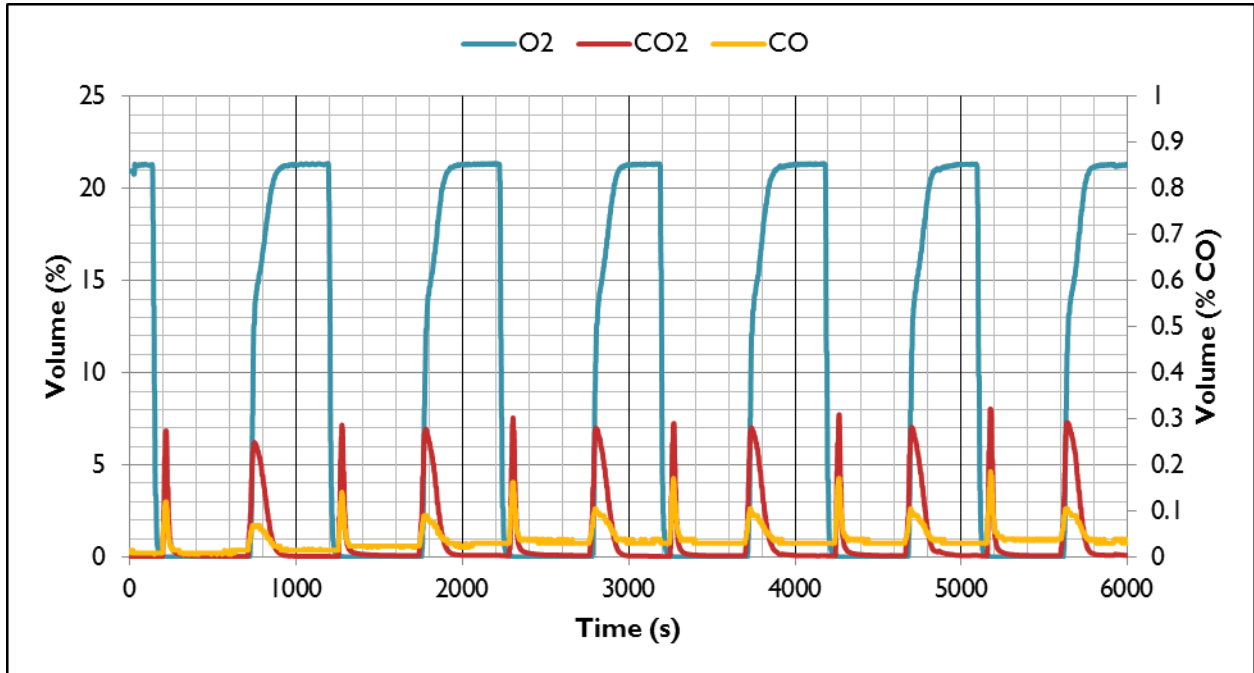


Figure 5.10: Exit gas profile for the first five reaction cycles between copper oxide and UK bituminous coal

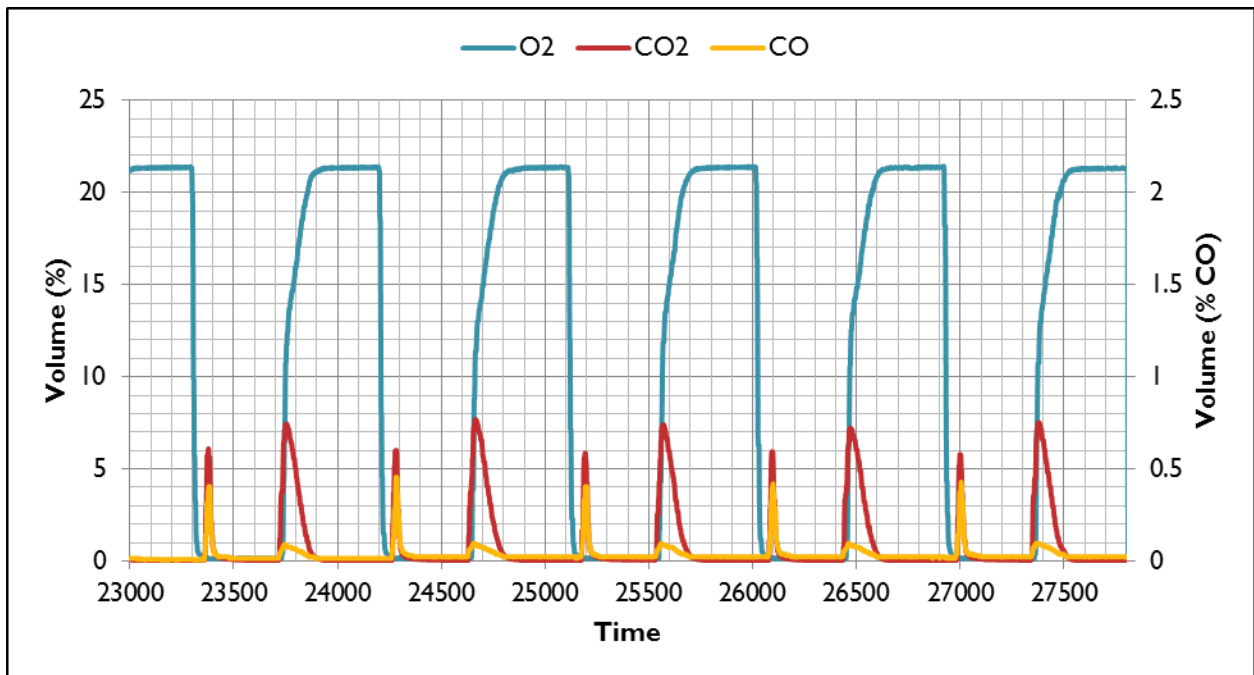


Figure 5.11: Exit gas profile for reaction cycles 206 till 210 between copper oxide and UK bituminous coal



Figure 5.16: Fresh copper oxide



Figure 5.14: Copper oxide (30 cycles)



Figure 5.12: Copper oxide (60 cycles)

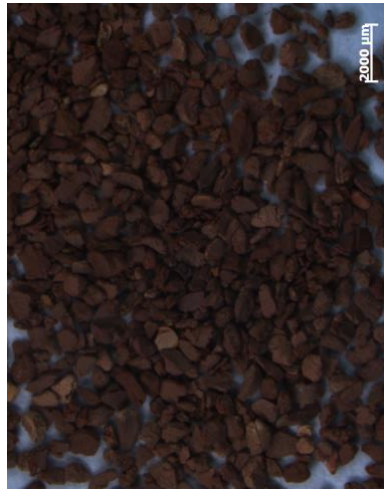


Figure 5.17: Copper oxide (90 cycles)

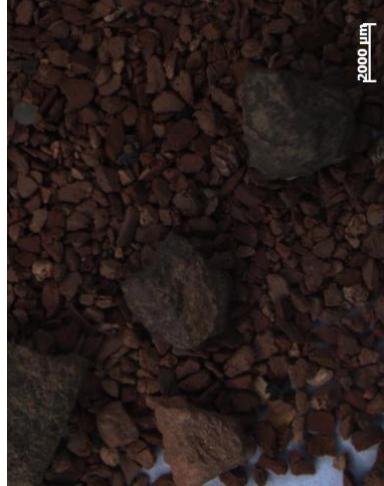


Figure 5.15: Copper oxide (120 cycles)

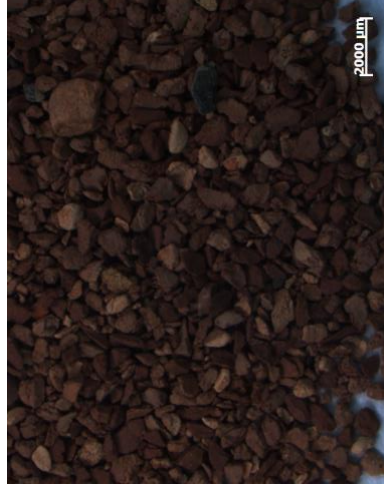


Figure 5.13: Copper oxide (150 cycles)

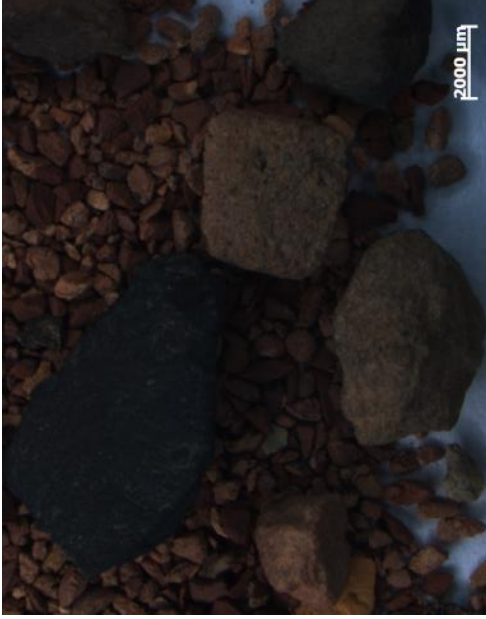


Figure 5.18: Copper oxide (210 cycles)

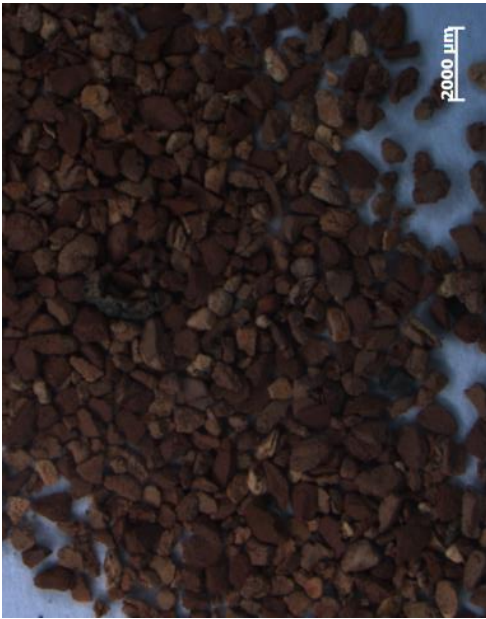


Figure 5.20: Copper oxide (180 cycles)

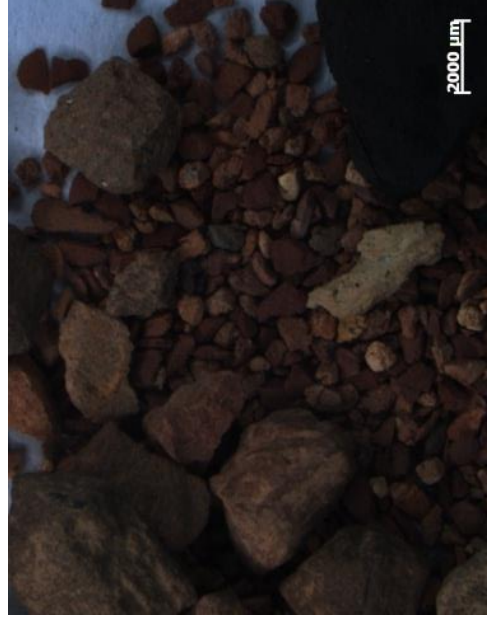


Figure 5.19: Copper oxide (240 cycles)

These changes are believed to be caused by ash elements depositing onto the surface of the particles causing the reacted particle to have a larger particle size range. There are two forms of agglomeration that can occur in the fluidised bed. The first type is via molten material in the bed fusing particles together during the reaction. This phenomenon occurs when the molten phase of ash deposits on the surface of the metal oxide particle. The molten ash is transferred onto the surface of the metal oxide particle by collision between burning char particles and bed particles. It is highly probable that the ash layer coating on the surface of the metal oxide particle will remain molten at the operating conditions used in the fluidised bed, particularly for low rank coals with a low melting point ash. The metal oxide particles will thus become sticky over prolonged periods of operation. As a result, in order to achieve the desired carbon conversion levels, fluidised beds are usually operated at temperatures above the melting point of ash. Besides that, agglomerates will form if the kinetic energy of metal oxide particles cannot overcome the sticky forces between particles (Manzoori, 1990). Besides that, interaction between the particles and the atmosphere can cause agglomeration. The fluidised bed reactor was cooled down to room temperature with compressed air. During this period, water vapour in the compressed air might condense and mix with the particles causing solid lumps to be formed after cooling down and drying.

Figures 5.5 to 5.6 and Figures 5.10 to 5.11 illustrates that when fuel is introduced into the bed, it is pyrolysed into form carbon monoxide (CO), methane (CH₄) and hydrogen (H₂). Hematite (Fe₂O₃) in the bed will then react with these pyrolysis gases to form magnetite (Fe₃O₄) and wustite (Fe_{0.947}O) while copper oxide will react with these pyrolysis gases to form copper (Cu) via reactions shown in Chapter 3.

It was also noted that the metal oxide particles will only react with the pyrolysis gases and that they do not react with the char formed via the pyrolysis process. As a result, there is a large amount of carbon inventory being accumulated in the bed. This has an implication in the commercialisation of chemical looping combustion as the accumulation of char will decrease the carbon capture efficiency of the process. This will also lead to a decrease in the combustion efficiency of the process. The major implication of this phenomena is that chemical looping combustion with solid fuels is best carried out with fuels with high

volatilities to minimise the building up of char in the bed or that solid fuels will have to be gasified in a separate reactor before channelling the syngas produced via the gasification process into the chemical looping combustion system.

Continuous feeding throughout the reduction stage was not preferred in this study due to the highly exothermic reaction during the oxidation stage for both iron oxide and copper oxide. Besides that, there is a large inventory of iron oxide and copper oxide in the bed. As the metal oxide particles have undergone substantial reduction when they react with the pyrolysis gases, the large inventory of reduced metal oxide particles will react vigorously with oxygen to return to its original oxidation state. This will cause the temperature of the fluidised bed to rise substantially and it might cause the metal oxide particles to melt if the temperature in the fluidised bed exceeds the metal oxides melting point. As a result, less fuel is introduced into the fluidised bed to control the amount of metal oxide being reduced during the reduction stage.

It was also noted that the carbon monoxide peak seemed to be increasing slightly over successive cycles. This is believed to be due to the fact that some of the active sites are starting to deactivate or that impurities are starting to deposit onto the surface of the particles and this will reduce the amount of oxygen available for reaction. Attrition also affects the amount of oxygen available for reaction. Attrition is caused by the collision between the metal oxide particles with mineral matter from ash as well as with themselves and the wall of the fluidised bed. Attrition will cause metal oxide fines to be generated. These fines are easily elutriable from the fluidised bed due to their relatively low terminal velocity. Elutriation of the bed material causes the bed depth to decrease over successive cycles and this will result in less metal oxide available for the reaction to take place. Rubel et al. (2011) also found that high ash concentration in a fluidized bed will limit the contact between the oxide particles and the carbon molecules in coal thereby reducing the combustion efficiency of the system.

5.8.1 Carbon Conversion Analysis

Figure 5.21 and 5.22 show the fraction of carbon fed into the bed being converted into carbon monoxide and carbon dioxide during the reduction cycle for iron oxide and copper oxide respectively.

The variation in the amount of carbon converted during the reduction period is due to the variation in the amount of fuel fed into the bed. However, it does show a general trend in which the amount of carbon converted during the reduction period decreases with increasing number of reaction cycles.

A sharp drop in the conversion of carbon was noted during the last 3 reaction cycles for the case with iron oxide before the experiment was discontinued. The slight increase in the amount of carbon converted after cycle 30 was due to the new iron oxide particles added into the bed to replace some of the iron oxide lost during the 30 reaction cycles as well as to replace the iron oxide collected for analysis. Besides that, it was believed that the iron oxide particles achieve slightly better regeneration during the oxidation stage prior to the next reduction stage during cycles 31 to 39. As the particle is able to undergo better regeneration, this might have unblocked some of the active sites, thereby allowing a higher percentage of carbon fed into the bed to be converted into carbon monoxide and carbon dioxide.

The rapid decrease in the amount of carbon converted during the reduction period towards the end of the experiment is believed to be due to the combination of a few factors. The first factor is due to the elutriation of metal oxide from the bed. Collision between the metal oxide particles with mineral matter from ash as well as with themselves and the wall of the fluidised bed will cause metal oxide fines to be generated. These fines are easily elutriable from the fluidised bed due to their relatively low terminal velocity. Elutriation of the bed material causes the bed depth to decrease over successive cycles and this will result in less metal oxide available for the reaction to take place as described in the previous section.

Besides that, there's a possibility that metal oxide in the bed will react with carbon and/or sulphur from coal will to form metal carbide and/or metal sulphide. When this occurs, the amount of oxygen available for reaction to occur will decrease due to there being less metal molecules to take up oxygen as it is believed that the strength of the metal carbide and metal sulphide bonds are greater than that of metal oxide. The effect of carbon and sulphur on iron oxide and copper oxide used in this study is believed to be minimal as carbide and sulphide compounds were not detected during X-ray diffraction (XRD) analysis.

Interaction between ash and metal oxide might also limit the contact between the oxide particles and the gaseous reactants thereby reducing the combustion efficiency of the system. This is due to the fact that the deposition of ash on the surface of the metal oxide particles will reduce the number of active sites available for reaction to occur. Besides that, the mechanism of interaction between ash and metal oxides described in Chapter 3 might also lead to the deactivation of metal oxide. This is because as more mineral matter diffuse into the core of the metal oxide particle, it is possible that some form of segregation will occur within the oxide particles. When this occurs, it is possible that the segregated sections will reduce the ability of oxygen molecules located at the core of the metal oxide particles to diffuse to the surface for reaction to occur.

The low carbon conversion achieved during the reduction stage is due to the low temperature of operation used in this study and that the metal oxide particles will only react with volatiles released during the gasification of coal as observed in both sets of experimental setups. This is a concern in the commercialization of chemical looping combustion, since a carbon conversion of less than 30% of the fuel introduced into the bed is not desirable in industrial applications. This is because the building up of char in the bed will decrease the carbon capture efficiency of the system.

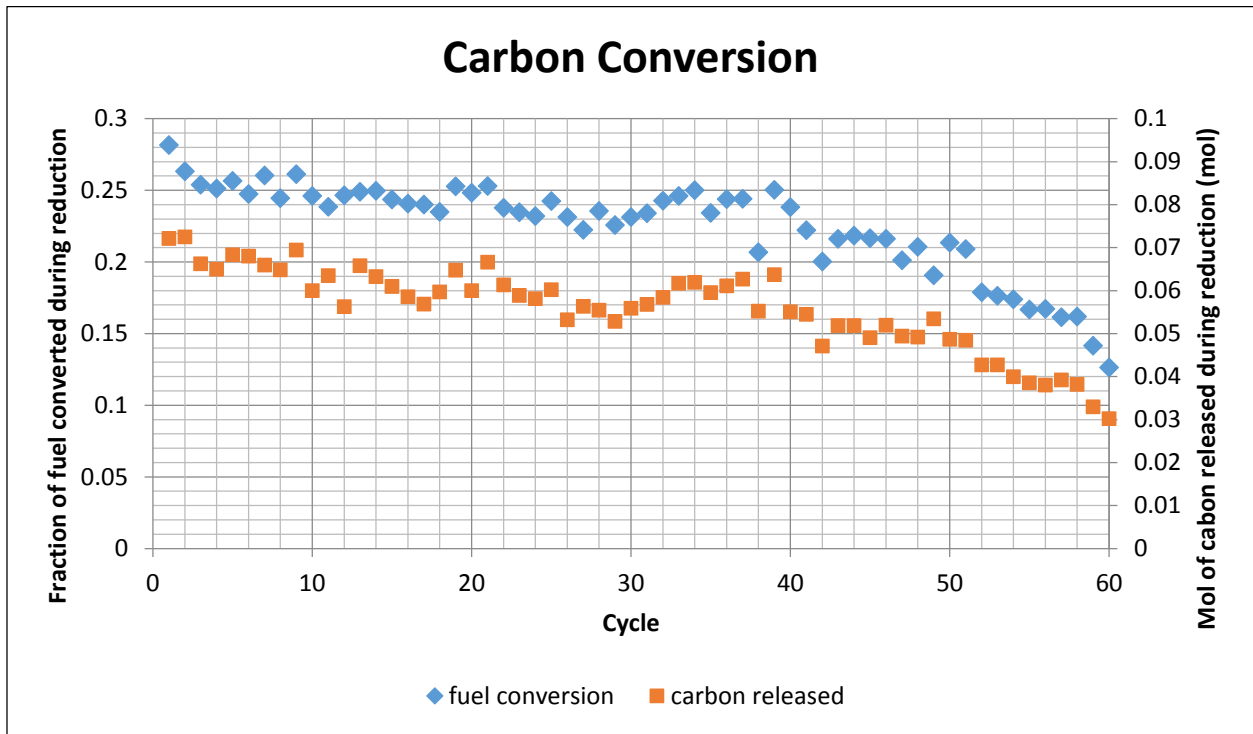


Figure 5.21: Carbon conversion during reduction for iron oxide

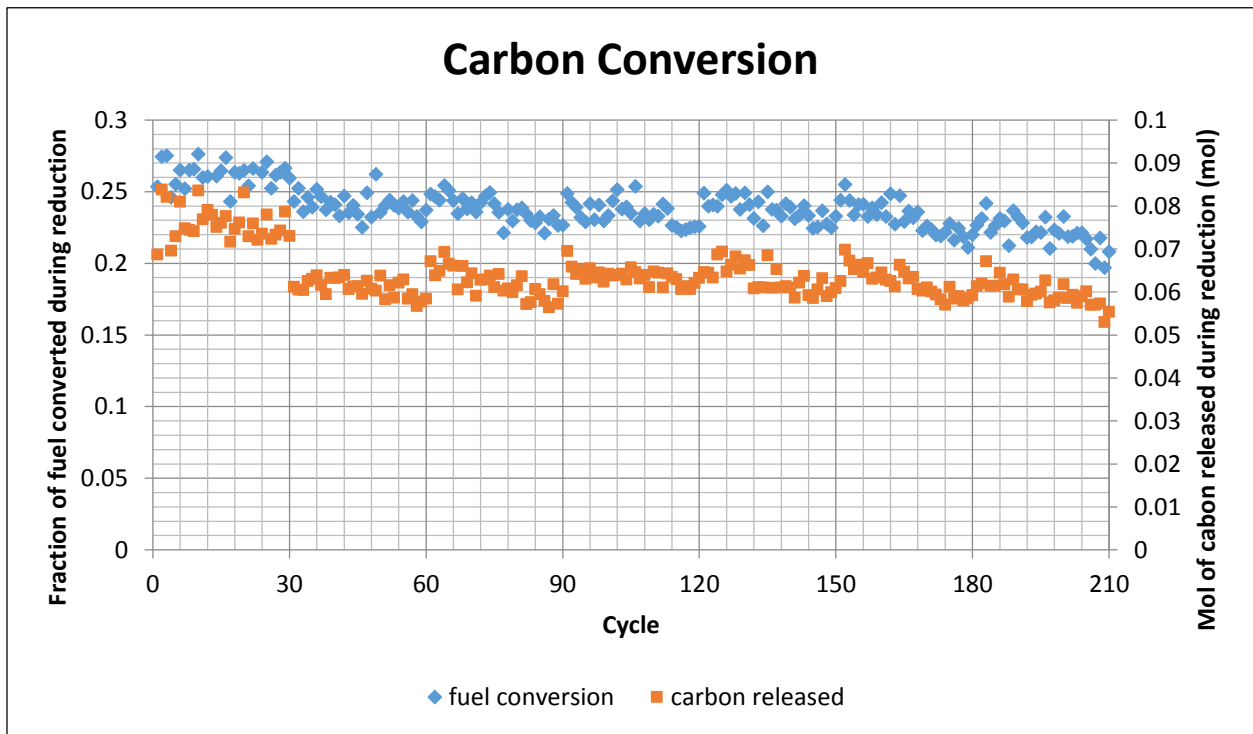


Figure 5.22: Carbon conversion during reduction for copper oxide

5.8.2 Porosimetry Analysis

Table 5.5 shows the porosimetry analysis conducted for the fresh and reacted iron oxide particles. It was found that the BET surface area decreased rapidly during the initial 30 reaction cycles as the BET surface area of the particles decreased by more than half of its initial value. After that, the BET surface area decreased much more slowly. A similar trend can be seen for the pore volume of the particles. The pore size of the particles appears to increase from its initial value of about 16 μm to 18 μm after 60 reaction cycles.

Table 5.5: Porosimetry analysis for fresh and reacted iron oxide particles

	Surface Area, (m^2/g)	Pore Volume, (cc/g)	Pore Radius $D_v[r]$, (\AA)
Fresh	3.3287	0.0100	16.0555
30 Cycles	1.1717	0.0030	16.1025
60 Cycles	0.9153	0.0030	18.0130

Table 5.6 describes the porosimetry analysis for the fresh and reacted copper oxide particles after 30 successive reaction cycles. It was found that the BET surface area decreased rapidly during the initial 30 reaction cycles whereby the BET surface area of the particles decreased by more than half of its initial value. After that, the BET surface area decreased much more slowly till it reaches a minimum value. A similar trend can be seen for the pore volume of the particles. The pore size of the particles appears to increase from its initial value of about 54 μm to 124 μm after 90 reaction cycles and it appears to stabilise at that maximum value.

The rapid reduction in the BET surface area as well as the pore volume of the oxide particles while the particles were able to achieve fairly consistent conversion ratio can both be explain by the ionic diffusivity and surface melting model.

Under the ionic diffusivity model, it is believed that when the oxygen ions diffuse to the surface of the metal oxide, it is possible some of the mineral matter to replace the space vacated by the oxygen ions. As mineral matter has low porosity, they are susceptible to block off the pores on the surface of the metal oxide particles thereby reducing the particles surface area as well as its pore volume. However, this will not prevent oxygen ions to diffuse to the

surface of the metal oxide in subsequent reduction stages due to the small amount of mineral matter present in the coal used in this study.

Under the surface melting model, it is believed that oxygen atom will diffuse to the quasi-liquid layer on the surface of the oxide particles to react with the pyrolysis gas. It is believed that the oxide particles will regenerate during the oxidation stage by taking up oxygen atoms through this quasi-liquid layer as well. As a result, when the reactor is cooled down after the reduction stage or oxidation stage, the quasi-liquid layer will solidify. During this process, it is possible that the pores in the original particles are blocked by the solidified surface thereby reducing the particles surface area as well as its pore volume.

Table 5.6: Porosimetry analysis for fresh and reacted copper oxide particles

	Surface Area, (m ² /g)	Pore Volume, (cc/g)	Pore Radius Dv[r], (Å)
Fresh	119.3073	0.3095	54.4170
30 Cycles	49.7873	0.2325	74.1970
60 Cycles	35.4753	0.1970	101.9645
90 Cycles	27.5590	0.1605	123.8965
120 Cycles	21.3153	0.1250	123.9245
150 Cycles	23.1200	0.1395	104.0755
180 Cycles	21.4550	0.1275	103.3320
210 Cycles	17.7880	0.1105	124.6085
240 Cycles	16.1670	0.0990	124.4630

5.8.3 X-Ray Diffraction Analysis

Table 5.7 shows the X-ray diffraction (XRD) analysis for both the fresh and reacted iron oxide particles. XRD analysis showed that iron oxide that was reduced during the continuous feeding stage, was reoxidised back to its original form during the oxidation stage. However, minor traces of impurities such as silicon dioxide (SiO₂) were found on some of these particles indicating that SiO₂ from the ash or fuel interacted with the iron oxide particles. It was also found that SiO₂ reacted with the iron oxide particles to form FeSiO₄ as seen in the case with lignite coal. The impurities were found to have no effect on the reactivity of the iron oxide particles as only a very small amount of them were detected.

Table 5.7: XRD analysis for fresh and reacted iron oxide particles

Sample	Compounds
Fresh iron oxide particles	Fe ₂ O ₃
Iron oxide with Hambach lignite coal after 20 redox cycles	Fe ₂ O ₃ , FeSiO ₄
Iron oxide with Hambach lignite char after 20 redox cycles	Fe ₂ O ₃
Iron oxide with activated carbon after 20 redox cycles	Fe ₂ O ₃ , SiO ₂
Iron oxide with Taldinski bituminous after 20 redox cycles	Fe ₂ O ₃ , SiO ₂
Iron oxide with US bituminous coal after 20 redox cycles	Fe ₂ O ₃
Iron oxide with UK bituminous coal after 30 redox cycles	Fe ₂ O ₃
Iron oxide with UK bituminous coal after 60 redox cycles	Fe ₂ O ₃

Table 5.8 describes the X-ray diffraction (XRD) analysis for the fresh and reacted copper oxide particles. XRD analysis on the fresh particles show that most dominant compound found in these particles is CuAl₂O₄ which is consistent with other studies found in the literature. XRD analysis on the reacted particles indicated that most dominant compound is still CuAl₂O₄. However, it was also found that there was CuAlO₂ present in these particles.

Table 5.8: XRD analysis for fresh and reacted copper oxide particles

Samples	Compounds
Fresh	CuAl ₂ O ₄ , CuO, Al ₂ O ₃
30 Cycles	CuAl ₂ O ₄ , CuO, Al ₂ O ₃ , CuAlO ₂
60 Cycles	CuAl ₂ O ₄ , CuO, Al ₂ O ₃ , CuAlO ₂
90 Cycles	CuAl ₂ O ₄ , CuO, Al ₂ O ₃ , CuAlO ₂
120 Cycles	CuAl ₂ O ₄ , CuO, Al ₂ O ₃ , CuAlO ₂
150 Cycles	CuAl ₂ O ₄ , CuO, Al ₂ O ₃ , CuAlO ₂
180 Cycles	CuAl ₂ O ₄ , CuO, Al ₂ O ₃ , CuAlO ₂
210 Cycles	CuAl ₂ O ₄ , CuO, Al ₂ O ₃ , CuAlO ₂
240 Cycles	CuAl ₂ O ₄ , CuO, Al ₂ O ₃ , CuAlO ₂

The presence of CuAlO₂ shows that the reduction of CuAl₂O₄ occurs through the intermediates CuAlO₂ and Cu₂O as shown in the study by Patrick and Gavalas (1990) on the reduction of mixed – copper aluminium oxide. However, the presence of CuAlO₂ also indicates that the oxidation of CuAlO₂ to CuAl₂O₄ is difficult. If that is the case, the amount of oxygen available for the gasification reactor will reduce if the amount of CuAlO₂ increases.

The absence of SiO₂ in the reacted copper oxide samples indicate that SiO₂ is present in the amorphous form which could not be detected via XRD. The XRD analysis also show that there is very little presence of impurities in the reacted samples or that if they are present, they are present in very small amount or in the amorphous form.

5.8.4 X-Ray Fluorescence Analysis

Tables 5.9 and 5.10 show the X-Ray Fluorescence (XRF) analysis of both the fresh and the reacted iron oxide and copper oxide particles over successive 30 reaction cycles respectively. It can be seen from these tables that the amount of SiO₂ increases whereas the amount of the core components (Fe₂O₃, CuO and Al₂O₃) decrease as the number of reaction cycles increases. This is because SiO₂ is hard and abrasive such that it is able to displace the core components by means of attrition. This causes fines to be generated and elutriated from the bed. The table also shows that as the number of reaction cycles increase, the amount of impurities in the form of MgO, CaO, TiO₂, MnO, NiO, and CaO increases slightly. These impurities have the ability to replace the elutriated core components as the oxygen carrier or as the oxygen carrier support for the reaction to occur. However, they are present in very small amounts such that they have very little significance in terms of oxygen availability in the bed.

However, the increasing presence of sodium and potassium in the sample will cause an operating issue over time as their compounds have low melting points and will act as a binder which will cause the particles in the bed to agglomerate over time. This will cause the particles in the bed to increase in size and might cause the bed to defluidise or that a higher fluidising velocity will be required to sustain the fluidisation condition.

Table 5.9: XRF analysis of fresh and reacted iron oxide particles

Oxides	Fresh (mass percent)	30 Cycle (mass percent)	60 Cycle (mass percent)
Fe ₂ O ₃	99.04	93.85	64.99
SiO ₂	0.126	2.20	22.56
Al ₂ O ₃	0.143	2.92	8.85
K ₂ O	-	0.144	1.16
MgO	-	0.0801	0.612
CaO	-	0.0742	0.521
TiO ₂	-	-	0.381
Na ₂ O	-	-	0.284
SO ₃	0.366	-	0.115
CuO	-	0.286	0.0823

Table 5.10: XRF analysis of fresh and reacted copper oxide particles

Oxides	Fresh (Mass %)	30 Cycles (Mass %)	60 Cycles (Mass %)	90 Cycles (Mass %)	120 Cycles (Mass %)	150 Cycles (Mass %)	180 Cycles (Mass %)	210 Cycles (Mass %)	240 Cycles (Mass %)
Al ₂ O ₃	76.63	72.98	75.36	66.74	63.44	62.36	48.99	54.27	45.89
CuO	20.90	19.46	18.15	16.01	14.24	14.35	9.93	12.54	9.87
SiO ₂	0.292	4.30	3.76	12.83	17.30	17.58	32.83	26.39	34.19
K ₂ O	-	0.211	0.237	0.648	0.889	0.895	1.77	1.37	2.02
Na ₂ O	-	-	-	0.099	0.112	0.146	0.248	0.195	0.242
Fe ₂ O ₃	1.64	2.20	1.73	2.30	2.56	2.87	4.05	3.29	5.05
NiO	0.165	0.158	0.156	0.141	0.120	0.121	0.0872	0.107	0.0823
MgO	0.0563	0.123	0.129	0.293	0.361	0.359	0.637	0.533	0.868
CaO	-	0.0575	0.0559	0.245	0.294	0.558	0.433	0.283	0.500
TiO ₂	-	0.0821	0.0769	0.215	0.299	0.291	0.570	0.442	0.618
SO ₃	-	0.145	0.133	0.205	0.173	0.154	0.160	0.168	0.220
MnO	-	-	-	-	-	-	0.0517	-	0.0628
BaO	-	-	-	-	-	-	-	-	0.077
P ₂ O ₅	-	-	-	-	-	-	-	-	0.0575

5.8.5 Inductive Coupled Plasma Mass Spectrometry Analysis

Tables 5.11 and 5.12 show the inductive coupled plasma mass spectrometry (ICP-MS) analysis of both the fresh and the reacted iron oxide and copper oxide particles over successive 30 reaction cycles respectively. The concentration of silicon in the particles were not included due to the fact that the ICP-MS analysis to obtain the concentration for silicon is unreliable. It can also be seen from these tables that as the number of reaction cycles increase, the amount of impurities in the form of calcium, magnesium, and nickel increases slightly. These impurities have the ability to replace the elutriated core components as the oxygen carrier or as the oxygen carrier support for the reaction to occur. However, they are present in very small amounts such that they have very little significance in terms of oxygen availability in the bed.

It was also noted that the total metallic concentration of the sample decreases after every 30 reaction cycles. This suggests that the concentration of non-metal impurities such as carbon, silicon, fluorine, chlorine and oxygen have increased and that they could not be detected with the ICP-MS.

XRD analysis showed that the fuel and ash particles had very minor effects on the oxygen carriers. As a result of that, it can be deduced that some of these impurities deposited onto the surface of the metal oxide particles but they did not react with the metal oxides to form complexes.

Table 5.11: ICP-MS analysis for fresh and reacted iron oxide particles

Element	Iron Fresh (mg/kg)	Iron 30 cycles (mg/kg)	Iron 60 cycles (mg/kg)
Ag	0.32	0.0	0.0
Al	170.16	3528.6	1792.1
As	0.40	2.5	3.7
B	546.75	0.0	0.0
Ba	1.00	0.0	0.0
Be	3.84	0.1	0.1
Bi	0.00	0.0	0.0
Ca	21.74	667.9	563.4
Cd	1.40	0.0	0.0
Co	17.07	2.2	1.6
Cr	13.16	25.3	19.5
Cu	387.37	161.8	352.4
Fe	573910.27	200523	119727.6
Ga	0.13	0.0	0.0
Li	0.29	3.1	2.1
Mg	19.81	407.0	228.5
Mn	68.53	40.9	41.9
Mo	2.69	0.1	0.4
Ni	24.82	23.1	27.6
Pb	1.79	0.0	0.0
Rb	0.07	5.7	3.3
Se	2.39	0.0	0.0
Sr	0.39	17.5	20.4
Te	0.06	0.1	0.2
Tl	0.23	0.1	0.0
U	0.00	0.0	0.1
V	0.00	6.2	5.3
Zn	90.18	64.2	66.6

Table 5.12: ICP-MS analysis of fresh and reacted copper oxide particles

Element	Fresh (mg/kg)	30 Cycles (mg/kg)	60 Cycles (mg/kg)	90 Cycles (mg/kg)	120 Cycles (mg/kg)	150 Cycles (mg/kg)	180 Cycles (mg/kg)	210 Cycles (mg/kg)	240 Cycles (mg/kg)
Ag	0.27	0.2	0.2	0.2	0.1	0.1	0.1	0.1	0.0
Al	344654	239534	175931	178610	145642	144779	115708	116548	110080
As	0.00	0.7	0.4	0.6	1.5	2.1	2.1	2.7	3.4
B	0.00	0.0	0.0	0.0	0.0	0.0	0.0	0.0	0.0
Ba	0.54	0.0	0.0	0.0	34.0	63.4	43.7	24.4	67.4
Be	0.00	0.6	0.4	0.5	0.9	1.3	1.1	1.0	1.0
Bi	0.00	0.0	0.0	0.0	0.0	0.3	0.0	0.0	0.0
Ca	156.65	871.0	608.5	547.4	1866.4	2242.0	2547.2	3256.7	5518.3
Cd	0.00	0.0	0.0	0.0	0.0	0.0	0.0	0.1	0.0
Co	0.14	4.2	3.9	3.8	6.9	8.9	10.6	8.2	8.1
Cr	0.65	30.7	27.0	26.1	33.9	42.6	41.9	39.9	45.8
Cu	116270	62236	59938	65690	47648	45844	33891	39037	33404
Fe	450.66	22466.2	18136.2	14617.8	32929.1	38961.5	54537.5	53938.7	33099.1
Ga	19.24	17.1	12.4	11.3	15.2	17.7	15.0	13.4	15.6
Li	0.38	11.4	8.4	9.2	15.6	23.4	20.5	16.8	19.6
Mg	22.67	2337.5	1943.4	1613.5	3653.4	5293.7	6459.5	4332.9	4644.2
Mn	7.41	232.0	132.4	94.5	309.5	422.3	687.5	882.1	318.9
Mo	0.43	2.2	2.8	3.3	4.5	5.6	6.7	14.4	16.7
Ni	4.79	493.6	408.2	409.4	315.0	295.2	246.8	299.3	273.0
Pb	0.45	0.0	0.0	0.0	0.0	0.0	0.0	0.0	0.0
Rb	0.01	26.7	21.3	19.4	35.5	46.6	44.6	36.9	44.0
Se	1.77	0.0	0.1	0.5	1.1	0.8	0.3	0.8	0.1
Sr	0.18	28.1	22.6	22.9	42.8	55.4	52.3	59.6	58.8
Te	0.00	0.0	0.1	0.1	0.0	0.0	0.0	0.0	0.0
Tl	0.06	0.3	0.2	0.2	0.2	0.2	0.2	0.1	0.2
U	0.00	0.1	0.1	0.1	0.2	0.3	0.3	0.3	0.3
V	0.00	23.0	20.2	19.8	36.1	44.7	48.6	42.5	46.2
Zn	30.35	33.9	33.1	31.9	34.6	45.9	40.5	37.5	61.6

5.8.6 Metal Oxide Conversion Analysis

Figures 5.23 and 5.24 show the amount and percentage of Fe_2O_3 and CuO being converted during the reduction stage as the number of reaction cycles increases respectively. The main assumption used in the calculation of the weight percentage of both Fe_2O_3 and CuO obtained via the X-Ray Fluorescence (XRF) analysis was representative of the actual composition in the fluidised bed. This will then represent the amount of Fe_2O_3 and CuO available for the reaction to take place during the reduction stage. It was also assumed that the rate of elutriation of Fe_2O_3 and CuO in the bed occurs linearly during each 30 successive reaction cycles. The first assumption is prone to errors arising from random errors during the collection of the bed sample for analysis and this can be seen in the case for copper oxide whereby the number of moles of CuO converted during cycles 180 to 210 remained fairly constant and similar to the previous 30 reaction cycles but the percentage of CuO converted decreased. Better regeneration of the reduced CuO particles is possibility that will reduce the amount of CuO converted during the next reduction stage but this is not the case for this phenomenon.

Figure 5.23 indicates that during the initial 30 reaction cycles, the number of moles of Fe_2O_3 converted decreases slightly, whereas the percentage of Fe_2O_3 converted into Fe_3O_4 remains fairly constant. This illustrates that the amount of Fe_2O_3 in the bed is decreasing as the number of reaction cycles increase. This is highly evident in the next 30 reaction cycles, whereby the amount of Fe_2O_3 converted decreases much more rapidly from cycle 40 till 60 and this is accompanied by a sharp increase in the percentage of Fe_2O_3 converted into Fe_3O_4 from cycle 40 till 60.

The study was discontinued after 60 cycles due to the fact that about half of the bed material at the beginning of cycle 31 was elutriated. Besides that, the carbon conversion during the last 2 cycles of the study had dropped to less than 15% of the carbon introduced into the bed causing a significant amount of char to be accumulated in the bed. Addition of new iron oxide material at such a significant amount is projected to cause the conversion profile to have a similar behaviour shown in Figure 5.23.

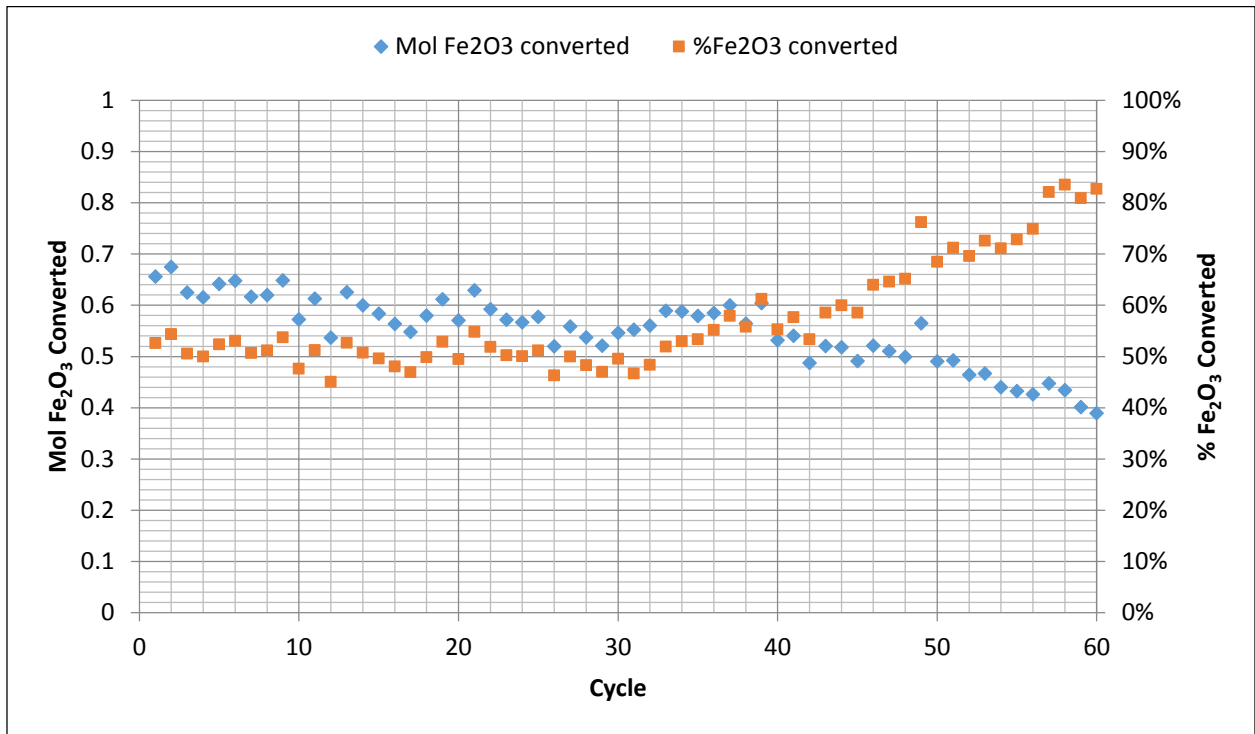


Figure 5.23: Iron oxide conversion

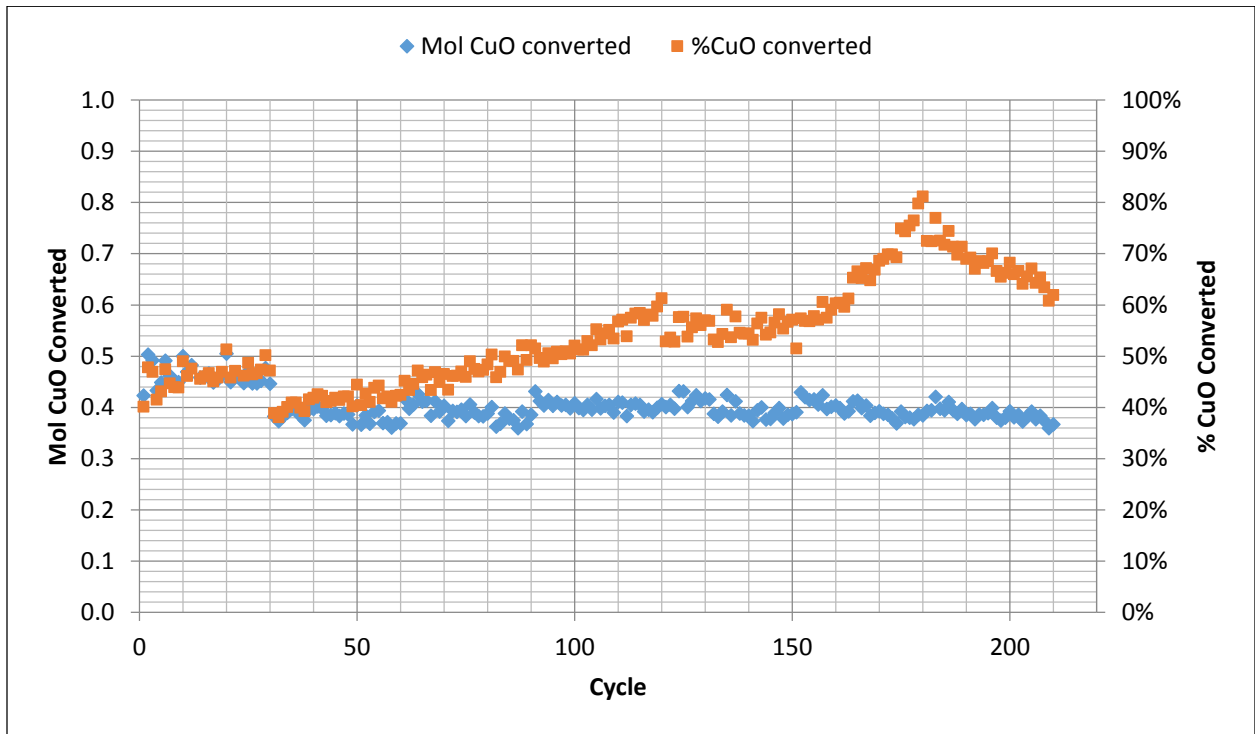


Figure 5.24: Copper oxide conversion

This is largely due to the fact that the mechanically mixed iron oxide particle is not strong and robust to withstand a high rate of attrition. As a result, after the particle has undergone multiple reduction and oxidation cycle, the structure and strength of the particle is significantly reduced. This will cause iron oxide fines to be generated at a much higher rate when it undergoes the reduction reaction as well as collisions with other particles in the bed and with the wall of the fluidised bed. These fines are easily elutriable from the fluidised bed due to their low terminal velocity.

Figure 5.24 shows that during the initial 30 reaction cycles, the number of moles of $\text{CuO}/\text{CuAl}_2\text{O}_4$ converted decreases slightly whereas the percentage of $\text{CuO}/\text{CuAl}_2\text{O}_4$ converted increases slightly. This shows that the amount of $\text{CuO}/\text{CuAl}_2\text{O}_4$ in the bed is decreasing as the number of reaction cycle increase.

Patrick and Gavalas (1990) studied the reduction of mixed copper – aluminium oxide and found that the reduction of CuAl_2O_4 in H_2 to Cu occurred through the intermediates in the form of CuAlO_2 and Cu_2O before the intermediates are further reduced into Cu.

The presence of CuAlO_2 detected via X-ray diffraction (XRD) shows that there is a possibility that the reduced copper oxide particles are not fully regenerated during the oxidation stage or that CuAlO_2 is quite a stable compounds such that it is difficult to reoxidised it back to its original state, CuAl_2O_4 . This has a major implication in that there will be fewer oxygen molecules available for the reaction to occur during subsequent reduction stages.

The decrease in the amount of oxygen carrier being converted during the reduction period towards the end of the experiment is believed to be due to the combination of a few factors. The first factor is due to the elutriation of metal oxide from the bed. Collision between the metal oxide particles with mineral matter from ash as well as with themselves and the wall of the fluidised bed will cause metal oxide fines to be generated. These fines are easily elutriable from the fluidised bed due to their relatively low terminal velocity. Elutriation of the bed material causes the bed depth to decrease over successive cycles and this will result

in less metal oxide available for the reaction to take place as described in the previous section.

Besides that, there's a possibility that metal oxide in the bed will react with carbon and/or sulphur from coal will to form metal carbide and/or metal sulphide. When this occurs, the amount of oxygen available for reaction to occur will decrease due to there being less metal molecules to take up oxygen as it is believed that the strength of the metal carbide and metal sulphide bonds are greater than that of metal oxide. The effect of carbon and sulphur on iron oxide and copper oxide used in this study is believed to be minimal as carbide and sulphide compounds were not detected during X-ray diffraction (XRD) analysis.

Interaction between ash and metal oxide might also limit the contact between the oxide particles and the gaseous reactants thereby reducing the combustion efficiency of the system. This is due to the fact that the deposition of ash on the surface of the metal oxide particles will reduce the number of active sites available for reaction to occur. Besides that, the mechanism of interaction between ash and metal oxides described in Chapter 3 might also lead to the deactivation of metal oxide. This is because as more mineral matter diffuse into the core of the metal oxide particle, it is possible that some form of segregation will occur within the oxide particles. When this occurs, it is possible that the segregated sections will reduce the ability of oxygen molecules located at the core of the metal oxide particles to diffuse to the surface for reaction to occur.

5.9 Summary

In chapter 4, the performance of mechanically mixed iron oxide and copper oxide impregnated on alumina were initially assessed over the course of 20 reduction oxidation cycles with five different fuels. The fuels used in the investigation include Hambach lignite coal, Hambach lignite char, Taldinsky bituminous coal, US bituminous coal and activated carbon.

The rate of gasification for the fuels were found to vary considerably. Hambach lignite coal and Hambach lignite char were found to be much more reactive compared to Taldinsky bituminous coal, US bituminous coal and activated carbon. These unreactive fuels resulted in a large accumulation of char in the bed. This is an operational issue for a semi-batch chemical looping combustion process since char present during oxidation is combusted and the CO₂ released cannot be captured. If this accumulation cannot be avoided, this would mean that the semi-batch process is only suitable for used with highly reactive fuels which can be easily gasified.

Results from the second experimental setup detailed in chapter 5 was used to determine the effects of large number of reaction cycles on the iron oxide and copper oxide particles. Gas released profiles show that the amount of carbon converted during reduction decreases gradually as the experiments proceed.

Porosimetry analysis on both iron oxide and copper oxide particles indicated that the BET surface area of these particles decreased by more than 50% of their original values. However, this decrease does not seem to affect the reactivity of the metal oxide particles as the conversion of the pyrolysis gases was found to decrease gradually throughout the experimental study. The shrinking core model was disregarded as a result of this observation as this phenomena shows that pores on the metal oxides particles appear to play a minor part in the combustion processes. Instead, it is believed that the reactions will occur either via the ionic diffusivity or the surface melting mechanisms described in Chapter 3.

Results from the XRD analysis on the iron oxide particles highlighted that the reduced iron oxide after reacting with coal was reoxidised back to its original form with trace amounts of impurities such as silicon dioxide (SiO_2). XRD analysis on the copper oxide particles showed that copper oxide reacted with its impregnated support (alumina, Al_2O_3) to form copper aluminate complexes (CuAl_2O_4 and CuAlO_2). The intermediate reduction product of CuAl_2O_4 , CuAlO_2 , was detected during the XRD analysis which shows that the reduced copper oxide particles were not fully regenerated and that CuAlO_2 is a fairly stable compound. The immediate impact of the detection of CuAlO_2 is that it will reduce the amount of oxygen available for reaction to occur during subsequent reduction stages. XRD on these particles did not reveal the presence of SiO_2 and other forms of impurities indicating that most of these impurities are either present in a small amount or that they are present in the amorphous form which could not be detected via XRD.

XRF and ICP-MS analysis on the reacted metal oxide particles revealed that the concentration of core components of the metal oxide particles (iron, copper and alumina) decreased over successive reaction cycles. The attrition and subsequent elutriation of these components is believed to be due to the interactions between the metal oxides themselves as well as their interaction with mineral matter from ash and the wall of the fluidised bed. These interactions will cause metal oxide fines to be generated. These fines are easily elutriable from the fluidised bed due to their relatively low terminal velocity.

The number of moles of iron oxide and copper oxide converted during reduction were found to decrease with increasing number of cycles. This is believed to be due to the combination of two factors. The major factor is the elutriation of the oxide fines leading to less oxide being available for subsequent reduction to occur. The other factor is that the oxide particles are starting to deactivate. Even though the number of moles of oxygen carrier converted during the reduction stage is decreasing, the extent to which the oxygen carrier are converted appears to be increasing. This is due to the fact that as the amount of metal oxide in the bed is decreasing, the metal oxide is converted at a higher degree in order to achieve the observed amount of oxygen carrier converted during the reduction stage.

Chapter 6 ATTRITION

The attrition of particles in fluidized beds is defined as the breakdown of particles within a process, including both abrasion and fragmentation. The study of attrition of solids in fluidized beds is of considerable importance since

- The generation of fines which are elutriated from the bed, places stresses on the downstream filtration systems (i.e. collection system must be larger)
- The loss of valuable material is expensive and can decrease the efficiency of the process
- Attrition influences the particle size distribution and in the bed in turn will affect the performance of the process in areas such as heat transfer and the fluidized bed hydrodynamics

6.1 Mechanism of Attrition

The attrition of particulate solids is a complicated process dependent on many variables. Both the particle properties (e.g. size, shape, surface structure, porosity and hardness) as well as the environment (e.g. temperature, pressure, hydrodynamics and time of exposure) will influence the rate of attrition. In fluidized beds, the source of attrition largely stems from:

- Bubbling within the bed
- The jets present at holes in the distributor
- Splashing of ejected particles
- Thermal shock on injection of particles
- Collision between the bed and collection systems

It is generally accepted that, in the absence of any chemical or thermal effects, there are two primary modes of attrition:

- Surface wear due to abrasion
- Fragmentation due to collisions of particles with each other and with the walls of the container

Table 6.1: Factors affecting attrition in a fluidized bed (Ray et al. 1987)

Group	Factor	Description	Duration	Region of occurrence
1	Screw feeder	Mechanical crushing	Feeding period	Screw & feeding tube
	Pneumatic conveyer; Transfer line	High-velocity impact	Feeding period	Transfer line
	Impact plate	Inertial impaction; High-velocity impact	Feeding period	Plate surface
	Grid jets	High-velocity impact; Abrasion	Continuous	Grid region
	Bubbling bed	Low-velocity impact & abrasion from stirring by bubbles	Continuous	Volume of bed between grid & freeboard
	Freeboard splashing	Low-velocity impact	Continuous	Freeboard
	Cyclone	High-velocity impact	Continuous	Cyclone Walls
2	Thermal shock	Heat-induced stress	Once (after feeding)	Inside fluidized bed
	Calcination	Stress caused by change in crystal	Once (after feeding)	Inside fluidized bed
	Chemical reaction	Stress caused by change in crystal lattice	Once or continuous	Inside fluidized bed
	Internal gas pressure	Explosion	Once (after feeding)	Inside fluidized bed

Abrasive wear or abrasion is typically associated with low velocities such as those experienced in the particulate phase of the fluidized bed. Fragmentation, by comparison, occurs in the regions of high velocity of gas and solids, such as the jetting region and at entry to cyclones. Within a fluidized bed, both modes of attrition will take place and it is difficult to separate the effects and study them individually. Table 6.1 shows the factors affecting particles attrition in a combustion system.

6.2 Attrition of Carbon during Combustion and Gasification

Chirone et al. (1991) and Salatino (2007) studied the attrition of carbon during combustion and gasification. They found that there are 3 forms of carbon attrition. The first form is primary fragmentation associated with the rapid release of gases from solids during processes such as pyrolysis. It was found that an increase in pressure within the particle can lead to particle failure. The second form of fragmentation is due to the loss of particle connectivity. This was associated with percolation theory. Percolation theory is a mathematical theory of connectivity and transport in geometrically complex systems. By applying the percolation theory to oxidation of carbon, it was deduced that as the oxidation process proceeds, the porosity of char increases until the point in which the integrity of the char matrix collapses. The third form of attrition is due to combustion. It was found that combustion restores the roughness of the surface of the coal particles that will then be susceptible to abrasion.

6.3 Attrition of Oxygen Carriers

There have not been many studies conducted to properly characterise the attrition of oxygen carriers. Most studies have been focused on basic attrition tests to screen and eliminate unsuitable oxygen carriers. Gayan et al. (2008) studied the performance of different nickel-based oxygen carriers prepared via dry impregnation of alumina in a fluidised bed over 120 oxidation-reduction cycles. They found that after the first few cycles, the attrition rate of all of the particles fell to a steady rate of less than 0.05% loss in weight per cycle. Berguerand and Lyngfelt (2008) studied the performance of ilmenite as oxygen carrier for chemical looping combustion. They found that the rate of attrition of ilmenite was 0.01–0.03% per

hour based on the particle size distribution of particles recovered from the bed at the end of their experiments.

Erri and Varma (2007) studied the performance of nickel-based oxygen carriers. They then used a modified ASTM test in which particles were placed in a glass cylinder with 4 mm baffles and were rotated on a ball mill roller for 30 minutes at a rate of 60 rpm. They found that all of the carriers except one (40% NiO/60% NiAl₂O₄) showed a loss of less than 4% by weight due to attrition over 100 oxidation-reduction cycles at 1000°C. Results from their studies are shown in Table 6.2.

Table 6.2: Mechanical and redox characteristics of oxygen carriers (Erri and Varma, 2007)

NiO-support weight ratio	Composition (Mg:Ni)	Oxygen capacity	Attrition (%)
40:60	NiO/NiAl ₂ O ₄	0.086	5.6
30:70	NiO/NiAl ₂ O ₄	0.064	1.2
20:80	NiO/NiAl ₂ O ₄	0.043	1.2
32:68	(NiO) _{0.79} (MgO) _{0.21} /Ni _{0.62} Mg _{0.38} Al ₂ O ₄ (0.4; 1 step)	0.068	1.7
35:65	(NiO) _{0.88} (MgO) _{0.12} /Ni _{0.49} Mg _{0.51} Al ₂ O ₄ (0.4; 2 step)	0.076	2.7
34:66	(NiO) _{0.79} (MgO) _{0.21} /Ni _{0.65} Mg _{0.35} Al ₂ O ₄ (0.3; 1 step)	0.073	2.0
36:34	(NiO) _{0.79} (MgO) _{0.21} /Ni _{0.75} Mg _{0.25} Al ₂ O ₄ (0.2; 1 step)	0.078	2.4
-	Fe ₂ O ₃	0.03	3.9

Adanez et al. (2006) studied the performance of a dry impregnated copper oxide alumina oxygen carrier in a circulating fluidised bed. They concluded from their studies that most of the fines are generated from the air reactor and that elutriation from the fuel reactor was minimal based on the fines collected in cyclones and filters downstream of the fuel reactor and air reactor. They also found that the initial rate of attrition was 1.2% in weight per hour and that the rate of attrition fell to 0.04% in weight per hour after 100 hours of operation.

Most studies on attrition and fragmentation have been conducted with limestone for one cycle calcination and sulphation. It was found that the particles break up (decrepitate) during calcination due to thermal shock. It was found that calcination and sulphation have opposite effects on the attrition rate in that a more friable solid is formed from the porous calcium oxide created during calcination. Besides that, it was found that the sorbent strength increase upon sulphation was possibly due to surface hardening or filling of surface cracks. The mechanism of sulphation is found to be slower due to the formation of a product layer that plugs pores and hinders the diffusion of SO₂ into the particle. As a result, smaller particles were found to have higher SO₂ capture capacities than larger particles. However usage of smaller particle size to increase SO₂ capture capacity reduces the residence time of particles in the system.

Studies conducted on attrition of limestone during carbonation and calcination cycles for CO₂ capture concluded that limestone exhibits a high rate of attrition rate during initial calcination, with reduction of attrition rate upon cycling. However it was found that the continuous attrition of limestone particles during repeated carbonation and calcination will pose a serious issue in scaling up of this technology. Lu et al. (2008) found that approximately 30-60% of limestone sized between 0.4–0.8 mm used in a pilot-scale dual fluidized bed system was captured as fines with size < 0.1 mm in the cyclones after 3 and 25 carbonation and calcination cycles.

6.4 Modelling attrition in the Fluidized Bed

6.4.1 Time Dependence of Attrition

Studies on attrition have continuously shown that the rate of attrition for a fresh batch of particles in a fluidised bed starts off at a higher rate and that it decreases with time until a constant rate is achieved (Forsythe & Hertwig 1949; Chraibi & Flamant 1989; Patel et al. 1986; Wolff et al. 1993). This is due to the fact that fresh particles may have a rough surface with friable defects or asperities that are worn off during the initial time spent in the bed. Thereafter, abrasion occurs on a relatively smooth surface and fines are generated at a constant rate.

By assuming a first order approach to describe the time dependence of attrition, the rate of loss of material in a certain size interval is proportional to the amount of material in that size interval. This expression is described in Equation 6.1 (Brown, 2010).

$$\frac{dW}{dt} = -\frac{1}{\tau_a} W \quad (\text{Equation 6.1})$$

where W is the mass of particles in the bed and τ_a is the attrition rate constant. Integrating Equation 6.1 gives:

$$\frac{W}{W_0} = \exp\left(-\frac{t}{\tau_a}\right) \quad (\text{Equation 6.2})$$

where W_0 is the initial mass of the particles in the bed at time $t=0$. One would expect this to be dependent on the initial particle size distribution; however, studies carried out to address this issue has found that this approach can offer a reasonable approximation for some systems irrespective of the initial particle size distribution (Neil & Bridgewater, 1994; Gardner & Austin, 1962; Sedlatschek & Bass, 1953). Alternatively, the process can also be described as a second order process which is proportional to the square of the number of particles, thus:

$$\frac{W}{W_0} = \frac{1}{1 + \frac{t}{\tau_a}} \quad (\text{Equation 6.3})$$

Gwyn (1969) studied the attrition of particles of silica-alumina catalyst in a fluidized bed. The following power law relationship was proposed for describing the attrition of initially mono-sized particles:

$$x_f = k_a t^{m_a} \quad (\text{Equation 6.4})$$

where x_f is the weight fraction of the fines, k_a is a constant dependent on the initial particle size and m_a is an empirical constant which accounts for the change in propensity of the material to abrade with time and is independent of time and particle size. Differentiating,

$$R_a = \frac{dx_f}{dt} = k_a m_a t^{m_a - 1} \quad (\text{Equation 6.5})$$

As a result, a plot of $\ln(R_a)$ vs $\ln(t)$ should yield a straight line and can be used to obtain parameters k_a and m_a since:

$$\ln(R_a) = \ln(k_a m_a) + (m_a - 1)\ln(t) \quad (\text{Equation 6.6})$$

Neil & Bridgwater (1994) found that m_a is often constant for a given material and k_a is related to the normal stress. The parameter m_a can be further split into $m_a = \phi_a \beta_a$ where ϕ_a is a material property of attrition and β_a describes the rate of degradation of the material.

6.5 Attrition Measurement Methodology

Attrition in this study is measured based on the results obtained from the mass of the bed at the end of every 30 reaction cycles as well as the results from the X-ray fluorescence (XRF) results. Measuring attrition this way will provide a good indication on how the oxygen carriers used will interact with mineral matter from ash. It is believed that silicon dioxide found in mineral matter will cause the expected attrition rate to be higher than those calculated from models described in this chapter due to its highly abrasive nature.

6.6 Experimental Attrition Measurement

Figure 6.1 shows the results of measurement of the variation in the amount of Fe_2O_3 and the number of moles of Fe_2O_3 whereas Figure 6.2 shows the variation in the amount of CuO and the number of moles of CuO in the fluidised bed with increasing number of reduction oxidation cycles.

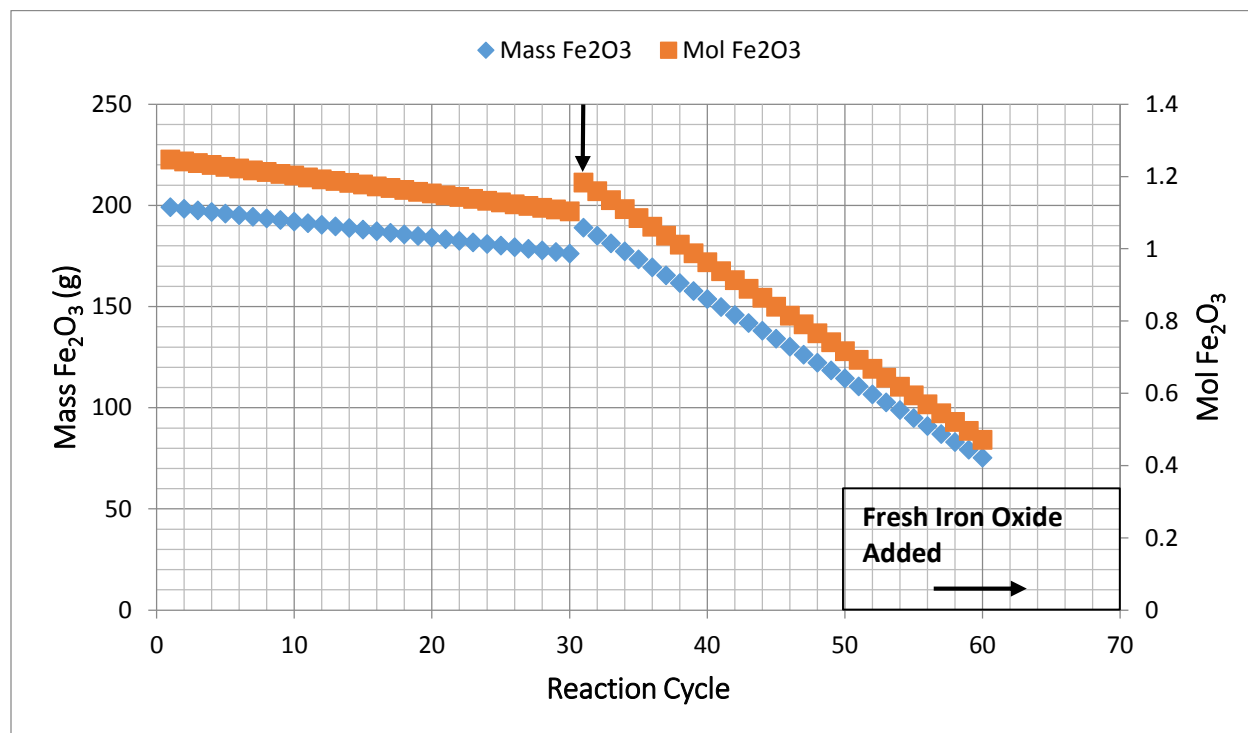


Figure 6.1: Amount of iron oxide in the bed with increasing number of reaction cycle

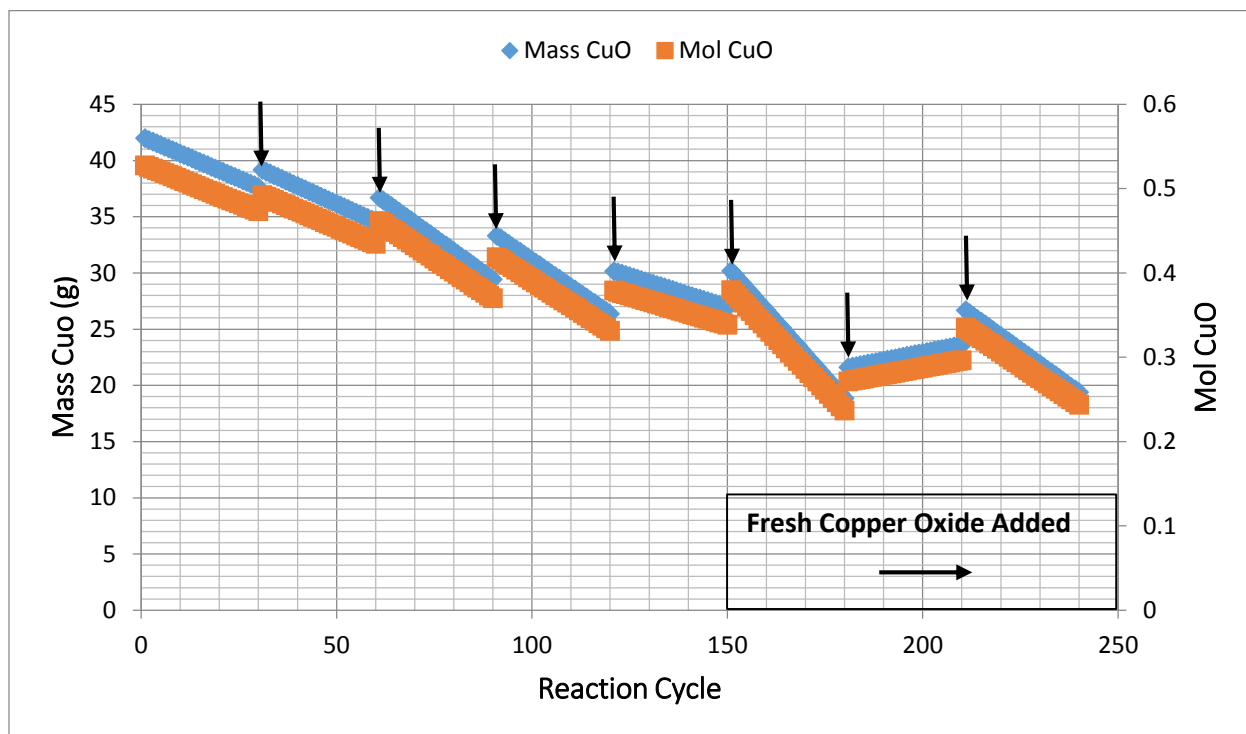


Figure 6.2: Amount of copper oxide in the bed with increasing number of reaction cycle

The gradient of the slopes in Figures 6.1 and 6.2 represent the rate of elutriation of Fe_2O_3 and CuO from the fluidised bed. The steeper the gradient the higher rate of elutriation of Fe_2O_3 and CuO from the fluidised bed over 30 reaction cycles.

The main assumption used in the calculation of the weight percentage of Fe_2O_3 and CuO obtained from the X-Ray Fluorescence (XRF) analysis was taken to be representative of the actual composition in the fluidised bed at the end of the particular reaction cycle. Besides that, it was also assumed that the elutriation of Fe_2O_3 and CuO in the fluidised bed occurs linearly during each of the 30 successive reaction cycles. The first assumption is prone to errors arising from random errors during the collection of the bed sample for analysis and this can be seen in the case for copper oxide whereby the amount of copper oxide in the bed appears to increase over time during cycles 180 till 210 that is not possible as the amount of copper in the fuels used are not significant enough to cause this increase.

A possible solution to mitigate this issue is to use a fresh batch of copper oxide after 30 reaction cycles and perform the experiment for 60 cycles without replacing any lost bed material at the end of the 30th reaction cycle.

Figure 6.1 shows that during the initial 30 reaction cycles, the number of moles of Fe_2O_3 converted decreases slightly whereas the percentage of Fe_2O_3 is fairly low at about 11.5%. However, the percentage of Fe_2O_3 attrited increases much more rapidly over the next 30 reaction cycles when about 60% of the iron oxide in the bed was elutriated.

Figure 6.2 indicates that the rate at which CuO is elutriated from the bed increases during every subsequent 30 reaction cycles until a maximum value is achieved before the elutriation rate starts to fall off. This can be attributed to two main phenomena.

The attrition models described earlier in this chapter projected that the rate of attrition of the particles should fall with time and with that, the rate of elutriation should fall with time as well. However, this was not observed in this study as the rate of elutriation was observed to be higher after the initial 30 reaction cycles for both cases with iron oxide and copper oxide. The higher than expected rate of elutriation is believed to be due to the combinations of these factors.

The first factor is due to the fact that the mechanically mixed metal oxides are not as strong and robust to withstand high rate of attrition compared to supported metal oxides. As a result, after the particle has undergone multiple reduction and oxidation cycles, the structure and strength of the particles is significantly weaker. This will cause oxide fines to be generated at a much higher rate when it undergoes the reduction reaction as well as collisions with other particles in the bed and with the wall of the fluidised bed. These fines are easily elutriable from the fluidized bed due to their relatively low terminal velocity.

Besides that, during the reduction of Fe_2O_3 to its intermediate form of Fe_3O_4 and/or its final reduction form, $\text{Fe}_{0.947}\text{O}$, it is believed that the intermediate and/or the final reduction product has a smaller molecular size compared to Fe_2O_3 . This is believed to be true as well for the reduction of CuO and CuAl_2O_4 to their intermediate forms, Cu_2O and CuAlO_2 , and/or to their final form, Cu , whereby the intermediate and/or the final reduction product is believed to have a smaller molecular size compared to CuO and CuAl_2O_4 . When this occur, it is believed that some of these molecules will dislodge from the bulk of the molecules and as they have a small particle size, they are prone to be elutriated from the bed as a result of their low terminal velocity.

The other factor is believed to be due the mixing between the metal oxide particles and mineral matter from coal ash. When mineral matter diffuses into the oxide particles, it is possible that they will cause the oxide structure to deform thereby reducing the strength of the particles making them more susceptible to breakage when they collide with one another or with the walls of the fluidised bed.

The final reason is due to the presence of SiO_2 in the mineral matter as detected via X-Ray Fluorescence (XRF) analysis. As SiO_2 is a hard and abrasive particle, it has a large tendency to collide with the softer metal oxides and its support. The collision will cause fines to be generated which can be easily elutriated from the bed due to their low terminal velocity.

The iron oxide study was discontinued after 60 cycles due to the fact that about half of the bed material at the beginning of cycle 31 had been elutriated. Besides that, the carbon conversion during the last 2 cycles of the study has dropped to less than 15% of the carbon introduced into the bed causing a significant amount of char being accumulated in the bed which was discussed in Chapter 5. Addition of new iron oxide material at such significant amount is projected to cause the profile to have a similar behaviour shown in Figure 6.1.

The fall in the rate of elutriation for copper oxide towards the end of the study is believed to be due to the fact that agglomeration of the particles in the bed is getting more severe. This is because as the length of the study increases, the amount of coal introduced into the bed increases as well. The immediate result is that the presence of potassium and sodium in the bed will increase with time. Potassium and sodium low melting point and as a result, they will melt and stick onto the surface of the ash or copper oxide particles binding them with other particles in the fluidized bed. When this happens, the particles in the fluidised bed will grow in size and over time, this will cause the bed to defluidise.

Chapter 7 SURFACE ANALYSIS

7.1 Carbon Deposition on Oxygen Carriers

Carbon formation is a possible side reaction in chemical looping combustion. It has been found that carbon deposition is dependent on metal oxide, inert material and H₂O/fuel ratio. The main ways for carbon formation are pyrolysis and decomposition of hydrocarbons, e.g. CH₄, or disproportionation of CO to C and CO₂, i.e. Boudouard reaction (Mattisson et al., 2006).

Pyrolysis is an endothermic reaction, thermodynamically favoured at high temperatures. The exothermic Boudouard reaction is more likely to take place at lower temperatures. Kinetically, both pyrolysis and Boudouard reactions are known to have a limited importance in the absence of a catalyst. However, transition metals such as nickel and iron can catalyse carbon formation. Carbon formation also depends on reaction conditions, such as the availability of oxygen, fuel conversion, reaction temperature and pressure. It has been observed that carbon deposition appears to be more prominent towards the end of the reduction period when more than 80% of the available oxygen was consumed. As a result, rapid carbon formation happens when fuel gas combustion cannot take place, at least substantially (Cho et al., 2005; Ryu et al., 2003; Corbella et al., 2005a,b).

In chemical looping combustion, the carbon deposition on the solid carrier in the fuel-reactor can flow with the particles to the air-reactor and be burnt by air. This will reduce the efficiency of the total CO₂ capture in the process (Corbella et al., 2005a,b). Carbon deposition can also lead to the deactivation of oxygen carriers or catalysts used in the process. As a result, it is important not only to understand the possible carbon formation mechanisms but also to investigate the operating strategies that need to be implemented to minimize and/or avoid carbon formation.

Most of the reported data on carbon deposition has been obtained in TGA units at high concentration of fuel gas. Ishida and co-workers (1998) reported carbon deposition on nickel and iron supported YSZ oxygen carriers. Their study shows that carbon formation is mainly caused by the Boudouard reaction, with the amount of carbon deposited on the nickel-based oxygen carriers being greater than that found on iron-based materials under the same conditions. In addition, it is shown that an increase in temperature decreases the amount of carbon deposited on a NiO/YSZ particle with carbon deposition being almost completely phased out at 900°C.

Ryu et al. (2003) reported using a nickel-based oxygen carrier material with exactly the opposite temperature trends suggesting that carbon formation decreased while temperature was increased.

Cho and co-researchers (2005) reported a comprehensive investigation on carbon formation on chemical looping combustion oxygen carriers using a laboratory scale fluidized bed. Their study reveals that carbon formation on a nickel-based carrier is strongly dependent on the oxygen availability. During the initial reduction stage when there is sufficient oxygen, no carbon formation is observed. Rapid carbon formation starts, however, when more than 80% of the available oxygen is consumed.

It has been suggested that pyrolysis is the main reaction by which carbon deposition occurs on nickel supported on YSZ or NiAl₂O₃ carriers. Carbon deposition by pyrolysis can be controlled by the addition of steam (Jin et al., 1999; Jin and Ishida, 2004; Villa et al., 2003; Ryu et al., 2003). One should however notice that no excess steam is needed and process produced steam from the reduction reaction should be included in the required steam calculations (Jin et al., 1998).

Temperature was found to be an important variable that can be adjusted to suppress carbon deposition (Ryu et al., 2003). Usually, an increased temperature is favourable for both increasing methane conversion and decreasing carbon formation. However care should be taken when selecting the maximum operating temperatures, since higher temperatures also cause metal sintering and phase transformation.

The introduction of a second metal can also reduce the carbon deposition on the catalyst materials. For example, trace amounts of noble metal are beneficial in a naphtha reforming catalyst to reduce carbon deposition.

Jin et al. (1998) studied a bimetallic CoO–NiO/YSZ system for a chemical looping combustion study. Their study suggest that carbon deposition can be completely eliminated by employing cobalt as a promoter along with NiO being the main active species on the YSZ support. It was speculated that formation of a solid solution between nickel and cobalt might change the free energy of the carbon formation reactions, giving rise to reduced coke deposition.

As there have not been that many studies on the deposition of carbon on iron oxide and carbon oxide, it was therefore desirable to detect the presence of carbon and other forms of impurity on these particles (if any) and study their effect on the reactivity of the oxygen carriers over a large number of reduction and oxidation cycles.

Two techniques were employed to study the surfaces of these particles. They are scanning electron microscopy with electron dispersive system and x-ray photoelectron spectroscopy.

7.2 Scanning Electron Microscopy

Scanning electron microscopy (SEM) is commonly used to study the surface morphology of metal oxides. This technique involves the use of a primary beam of electrons that will interact with the sample of interest in a vacuum environment that will result in different types of electrons and electromagnetic waves to be emitted. The secondary electrons ejected from the surface of the metal oxide are then collected and displayed to provide a high resolution micrograph.

SEM sample preparation involves the fixation of the metal oxide particles by attaching them to a metallic stub and then coating them with a thin metallic coating. The metallic coating is usually applied via a sputter coating. Gold is the most common conductive metal used for the metallic coating process. SEM can also be combined with other analysis methods such as energy dispersive X-ray (EDX) system in order to determine the elemental distribution in the sample. However, in order to perform the EDX analysis, carbon coating is used instead of gold coating.

In the scanning electron microscope analysis conducted for this study, the cross-sectional images and mapping were done for the copper oxide particles. These were done using resins made from a mixture of 50% CY212 (Araldite) and 50% DDSA (Dodecyl Succinic Anhydride) with added BDMA (Benzyl dimethylamine) hardener to form 'Araldite' epoxy resin whereby the copper oxide samples were placed onto this mixture and casted into 'coffin' molds before they were placed into an oven at 60°C for 3 days. The samples were then cut with a non-ferrous cutting wheel (MetPrep Type 5, maximum speed 5460 rpm). The cutting speed used in cutting these samples was 3000 rpm. This technique was chosen to determine if there is any form of segregation occurring within the particles.

7.3 X-ray Photoelectron Spectroscopy

X-ray photoelectron spectroscopy (XPS) is often used to determine the elemental composition of solid surfaces. The principle of XPS revolves around the emission of electrons from matter in response to the irradiation of the surface by a beam of monochromatic X-rays. This kinetic energy of the emitted photoelectrons (K_E) is unique for the different elements as well as being sensitive to the chemical state of the atoms.

The most commonly used X-rays energies are 1253.6 eV (MgK_{α}) and 1486.6 eV (AlK_{α}). However, since the emitted electrons have little ability to penetrate the matter, only those electrons emitted from the outermost 100 Å of a sample can escape from the surface and be quantified. All elements except hydrogen and helium can be detected by their characteristic binding energies of the electrons with a sensitivity of about 0.1 atom percent. In addition, angle resolved XPS can be used to examine layers that may not be uniform, to investigate a surface whereby its coverage is believed to be patchy or to examine the change or transition between the bulk and surface of a 'surface modified' material. Destructive XPS can be used by applying argon etching in order to obtain information of several thousand angstroms into the sample (Merrett et al. 2002).

7.4 Iron Oxide

7.4.1 Scanning Electron Microscope Analysis

Figures 7.1 to 7.4 show the SEM images of the fresh iron oxide particles. Figure 7.1 indicates that even though the iron oxide particles have been sieved to the range desired for this experimental work, there are still some forms of fines attached onto the surface of the particles. The magnified fresh iron oxide particles (Figure 7.2) also highlights that the iron oxide molecules appear in the form of small agglomerates distributed randomly throughout the particle. Figure 7.3 describes the iron oxide particles after it has undergone 30 reduction oxidation cycles. The image shows some cracks on the surface of the particles due to attrition. The magnified reacted iron oxide particles seen in Figure 7.4 highlights that even though the iron oxide molecules are still appear in the form of agglomerates, the agglomerates are larger in size due to the fact that the particles have undergone sintering during the combustion

process. Besides that, it is also believed that the iron oxide particles might have undergone slight melting during the combustion proves resulting in the smoother appearance of the molecules at the surface of the particles.

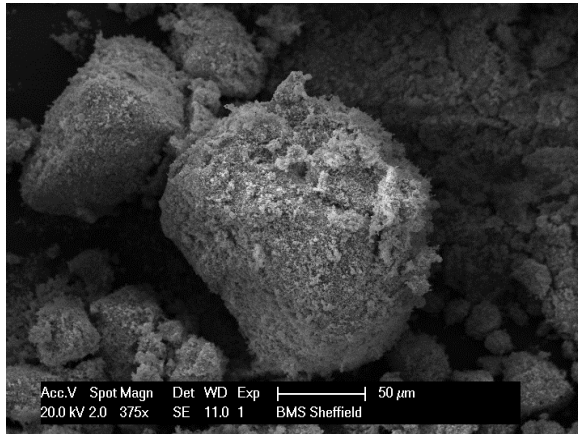


Figure 7.1: SEM image of fresh iron oxide particles

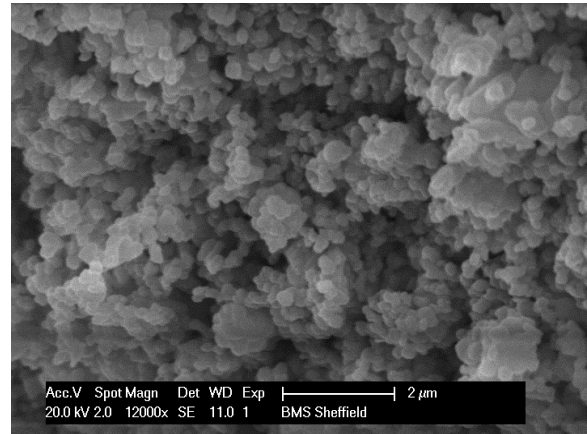


Figure 7.2: Magnified SEM image of fresh iron oxide particle

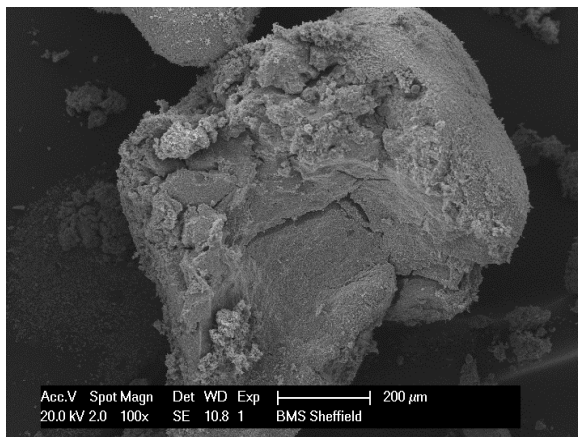


Figure 7.3: SEM image of reacted iron oxide particles after 30 cycles

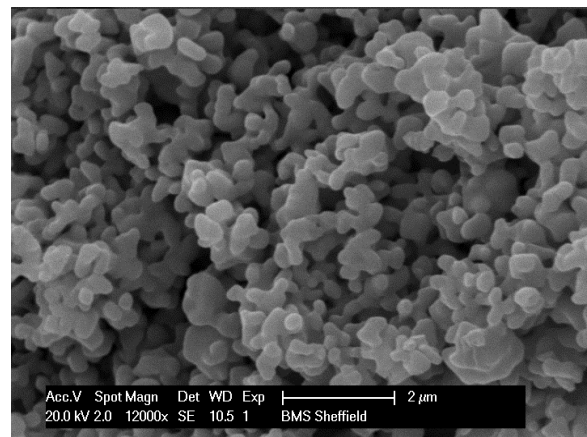


Figure 7.4: Magnified SEM image of reacted iron oxide particles after 30 cycles

Figures 7.5 and 7.6 show the scanning electron microscopy images of the reacted iron oxide particles after 20 reduction and oxidation cycles whereas Figures 7.7 and 7.8 describe the energy dispersive system analysis for these 2 spectra.

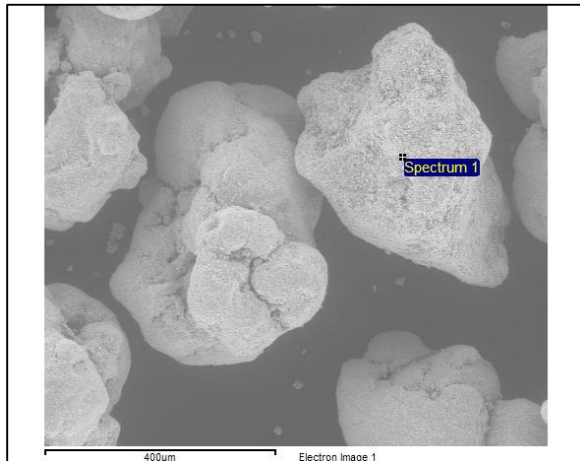


Figure 7.5: SEM image of reacted iron oxide particles after 20 cycles and the location of Spectrum 1

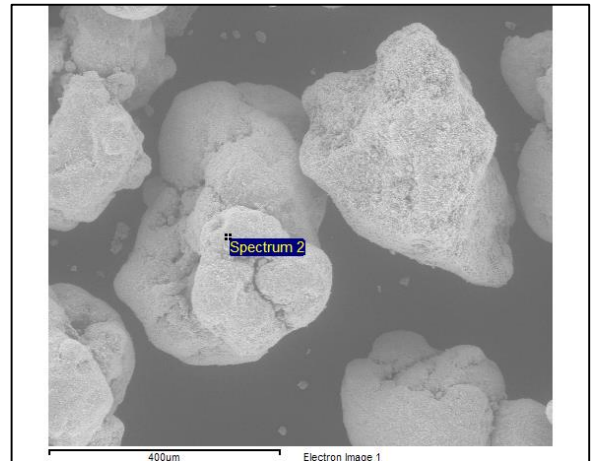


Figure 7.6: SEM image of reacted iron oxide particles after 20 cycles and the location of Spectrum 2

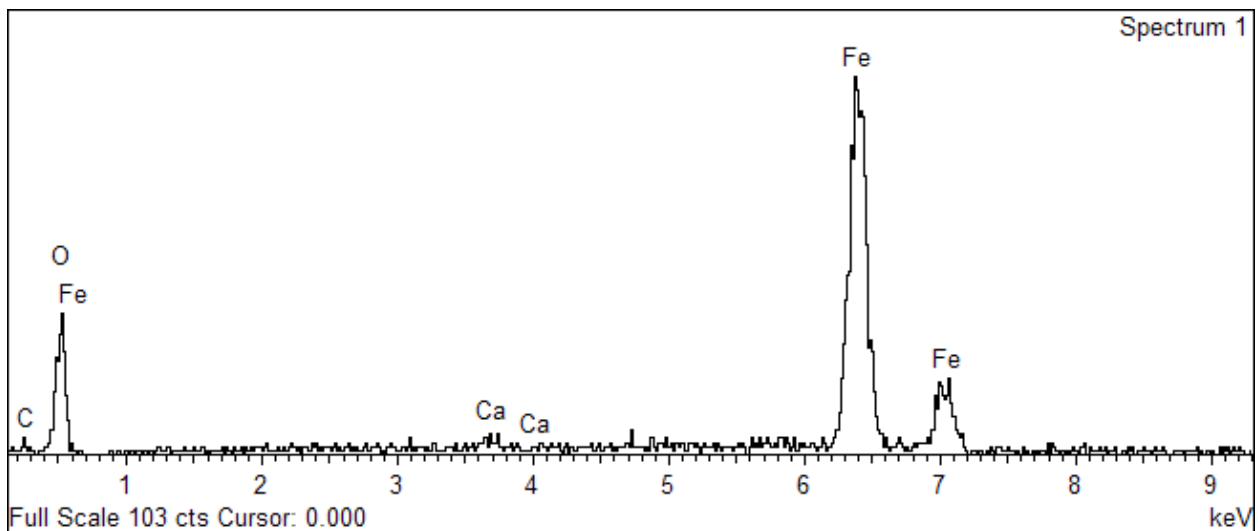


Figure 7.7: Energy dispersive system for spectrum 1

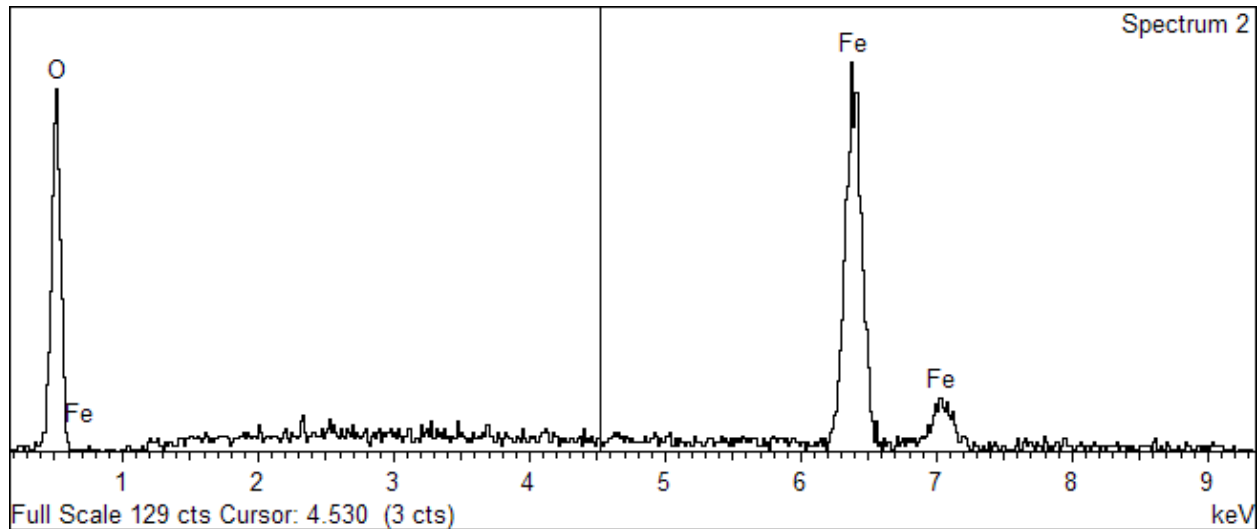


Figure 7.8: Energy dispersive system for spectrum 2

Figures 7.7 and 7.8 show that the iron peaks are situated at 6404, 6391, 7058, 705, 705 and 719 corresponding to $K\alpha_1$, $K\alpha_2$, $K\beta_1$, $L\alpha_1$, $L\alpha_2$ and $L\beta_1$ respectively.

Figure 7.7 shows the presence of calcium on the surface of the reacted iron oxide particle after 20 oxidation and reduction cycles. However, they were not observed in the energy dispersive system analysis for spectrum 2. This indicates that there is some form of impurities such as calcium depositing onto the surfaces of the reacted iron oxide particles. However, their exact location is difficult to pin-point as seen in the result for spectrum 2. Nevertheless, spectrum 2 seems to indicate the presence of impurities. However, as there is no significant peaks that could be detected due to the high background noise, some of these impurities might have been discarded as background noise.

Besides that, spectrum 1 seems to indicate some form of carbon deposition on the surface of the reacted iron oxide particle that was not observed in spectrum 2. As the iron oxide samples analysed were coated with a silver paint lining on the stub rather than the commonly used carbon coating method, this indicates that there is some unburned carbon from the reduction stage that was not completely burnt off during the oxidation stage. However, it is believed that the occurrence of this phenomena is quite small as the peak does

not seem significant enough to truly indicate the presence of carbon on the surface of the iron oxide particles due to the high background noise.

Figures 7.9 and 7.10 show scanning electron microscopy images of the magnified surface of the iron oxide particles after 20 reduction and oxidation cycles whereas Figures 7.11 and 7.12 describe the energy dispersive system analysis for these 2 spectra.

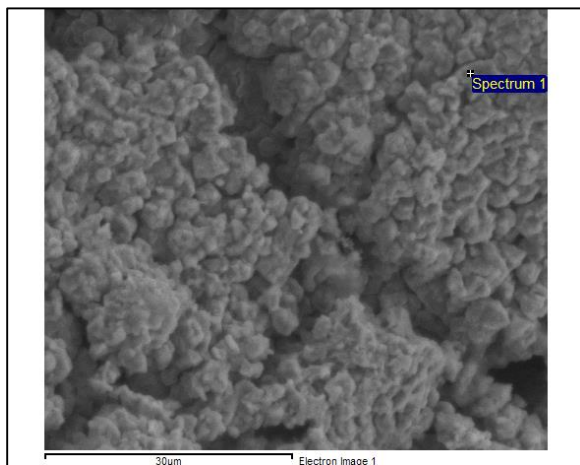


Figure 7.9: SEM image of reacted iron oxide particles after 20 cycles and the location of Spectrum 1

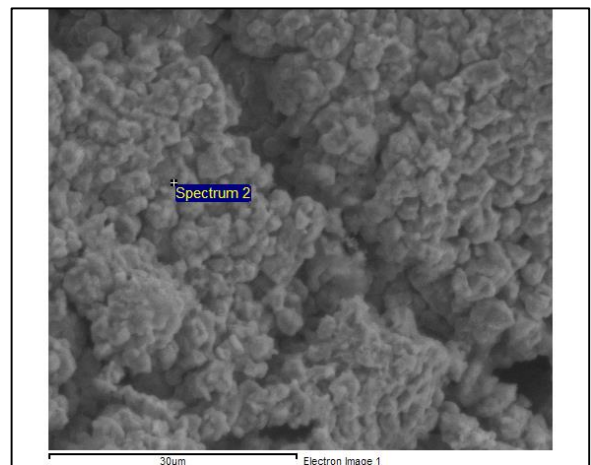


Figure 7.10: SEM image of reacted iron oxide particles after 20 cycles and the location of Spectrum 2

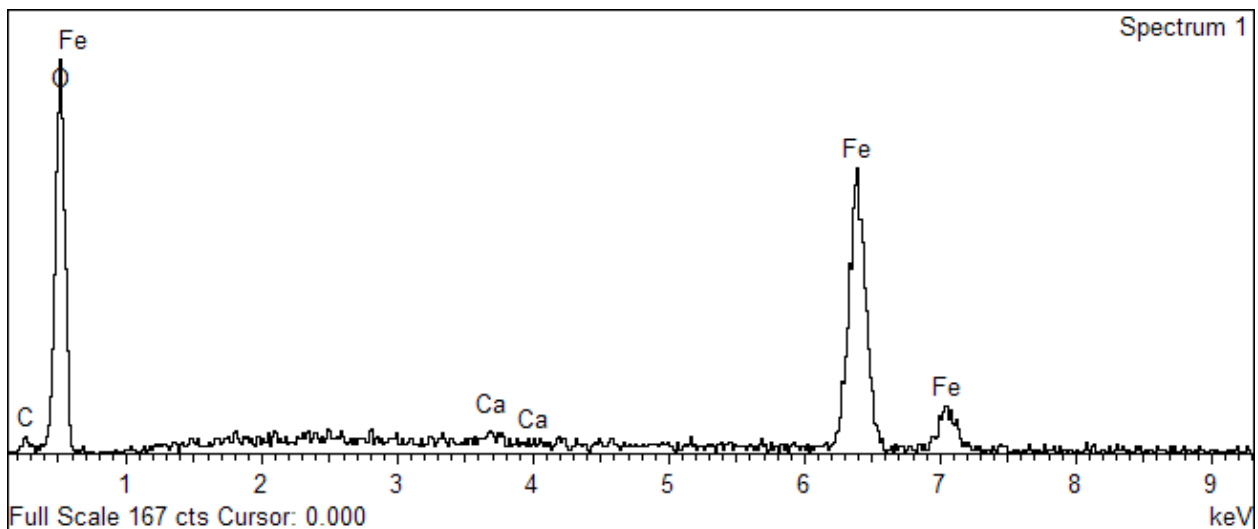


Figure 7.11: Energy dispersive system for spectrum 1

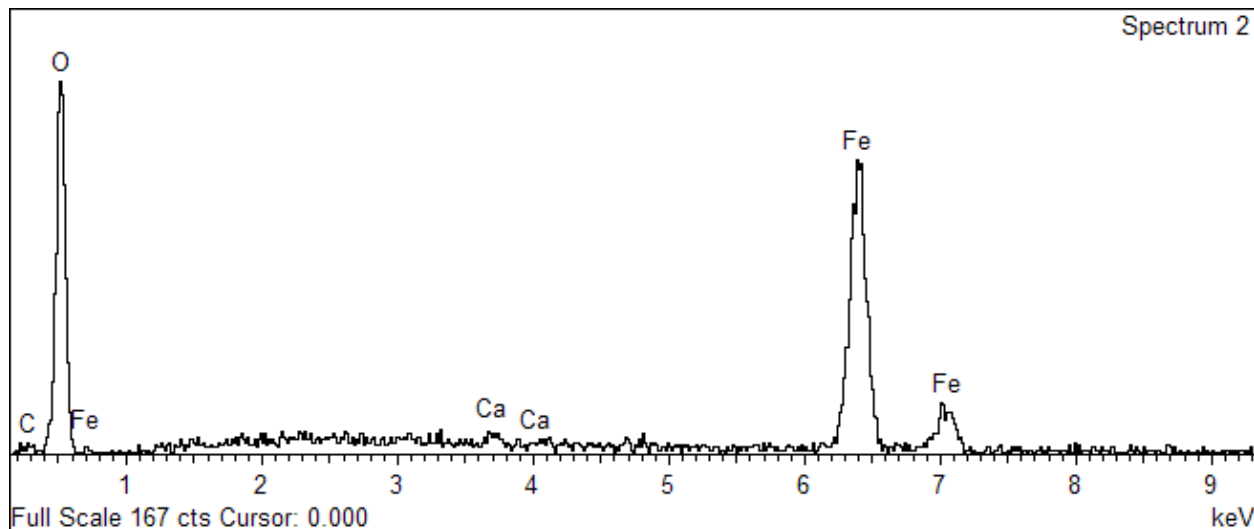


Figure 7.12: Energy dispersive system for spectrum 2

Figures 7.11 and 7.12 show that calcium is present at both pin-pointed locations. However, as the 2 spectrums analysed suffer from high background noise, it is difficult to determine whether the peaks observed are significant. However, both spectrums seem to indicate the presence of carbon depositing on the surface of the reacted iron oxide particle with the carbon peak on spectrum 1 being more pronounced than the carbon peak for spectrum 2. The carbon peaks suffer from the same high background noise observed for calcium but the background noise effect seems to be smaller due to the fact that carbon peaks are detected on the lower keV values.

As a result, it is believed that there is some form of carbon deposition on the surfaces of the iron oxide particles, but their exact location is very difficult to pin-point. However, the results from the energy dispersive system seem to be in agreement with the X-ray photoelectron spectroscopy data which will be discussed later in this chapter.

7.5 Copper Oxide

7.5.1 Cross-Sectional Scanning Electron Microscope Analysis

Figures 7.13 to 7.16 show the cross-sectional images of the copper oxide sample after 30 cycles. Figures 7.15 and 7.16 indicate that there is some form of segregation occurring in some of these particles whereby the lighter shaded areas are believed to be locations where the concentration of alumina is higher compared to the rest of the particles. However, these occurrences are small.

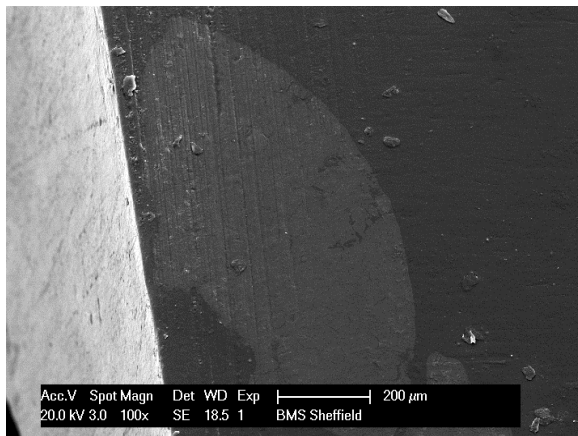


Figure 7.13: Cross-sectional SEM image of reacted copper oxide particles after 30 cycles

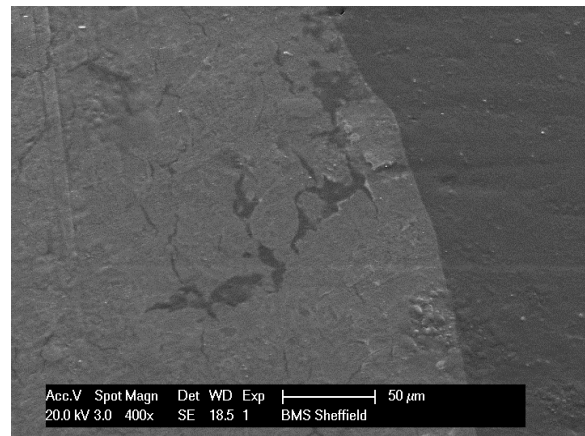


Figure 7.14: Magnified cross-sectional SEM image of reacted copper oxide particles after 30 cycles

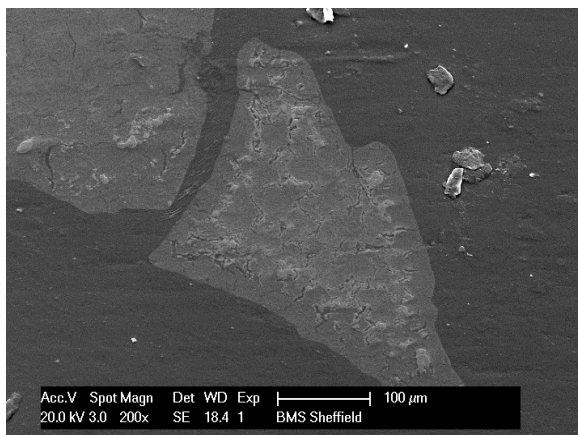


Figure 7.15: Cross-sectional SEM image of reacted copper oxide particles after 30 cycles

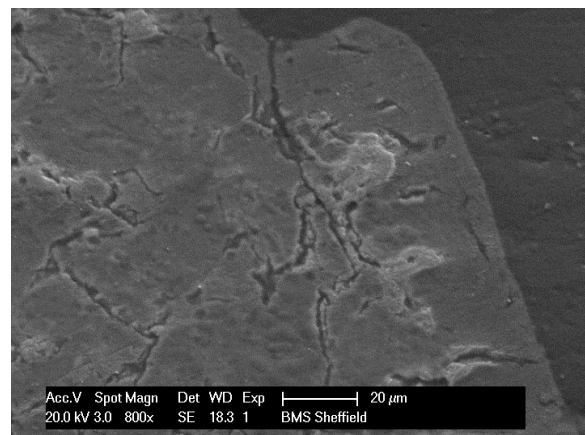
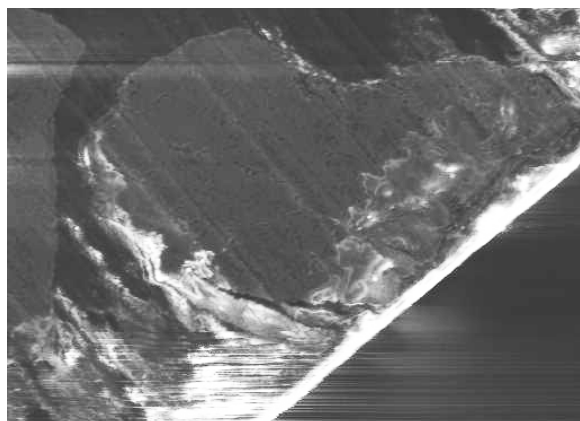


Figure 7.16: Magnified cross-sectional SEM image of reacted copper oxide particles after 30 cycles

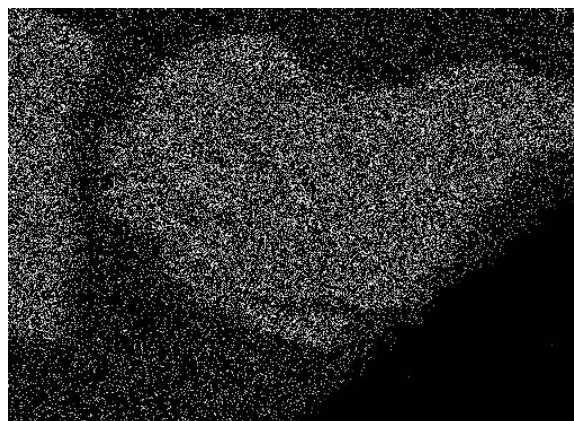
7.5.2 Energy Dispersive System Analysis

Figures 7.17 to 7.20 show the cross-sectional images and the energy dispersive system analysis of the fresh copper oxide sample. Figures 7.18 to 7.20 indicate that oxygen, copper and aluminium concentration are distributed randomly throughout the particle. The random distribution of copper throughout the particle (Figure 7.20) illustrates that this could be due to the fact that most of the copper present in the form of copper aluminate complexes.



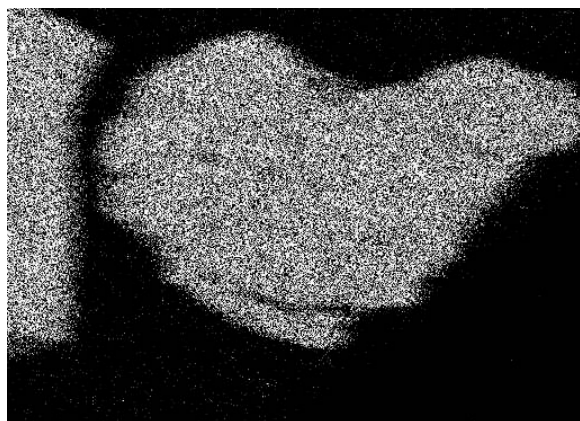
Electron Image 1

Figure 7.17: Cross-sectional SEM image of fresh copper oxide particles



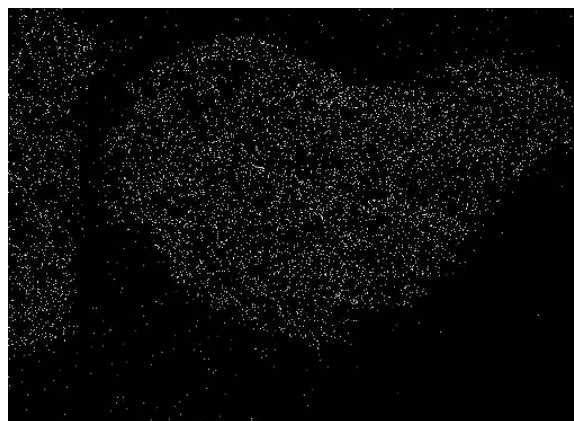
O Ka1

Figure 7.18: Oxygen mapping of fresh copper oxide particles



Al Ka1

Figure 7.19: Aluminium mapping of fresh copper oxide particles



Cu Ka1

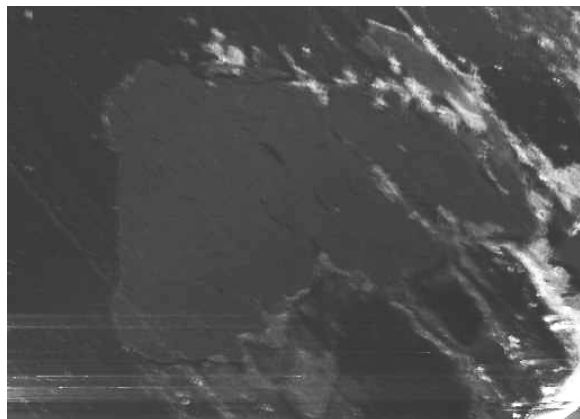
Figure 7.20: Copper mapping of fresh copper oxide particles

The scattering of aluminium, copper and oxygen throughout the particle confirms the XRD analysis conducted, whereby the majority of the compounds found in the copper oxide

samples were CuAl_2O_4 and Al_2O_3 . Note that this also correlates with the thermodynamic studies conducted by Jacob and Alcock (1975) whereby the stable form of a Cu_2O - CuO - Al_2O_3 for the temperature of operation in this study (800 – 1000°C) is CuAl_2O_4 and Al_2O_3 for 79 weight percent Al_2O_3 and 21 weight percent CuO .

Figures 7.21 to 7.24 show the cross-sectional images and the energy dispersive system analysis of the reacted copper oxide sample after 30 cycles. Figures 7.12 to 7.24 indicate that the concentration of oxygen, copper and aluminium are distributed randomly throughout the particle.

The scattering of aluminium, copper and oxygen throughout the particle confirms the XRD analysis conducted whereby the majority of the compounds found in the copper oxide samples were CuAl_2O_4 and Al_2O_3 .



Electron Image 1

Figure 7.21: Cross-sectional SEM image of reacted copper oxide particles after 30 cycles



O Ka1

Figure 7.22: Oxygen mapping of reacted copper oxide particles after 30 cycles

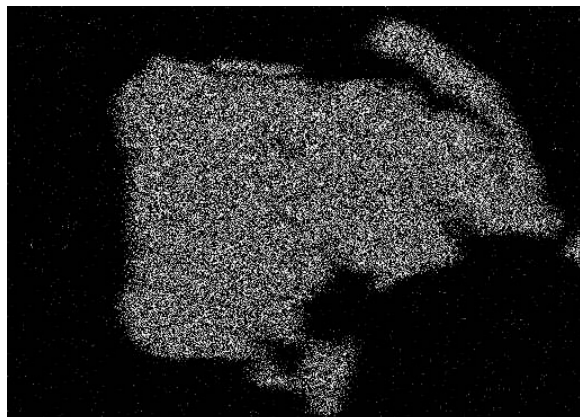


Figure 7.23: Aluminium mapping of reacted copper oxide particles after 30 cycles



Figure 7.24: Copper mapping of reacted copper oxide particles after 30 cycles

7.6 Iron Oxide X-Ray Photoelectron Spectroscopy Experiments

Figure 7.25 and Tables 7.1 and 7.2 show the XPS analysis for the fresh and reacted iron oxide. The tables show the atomic percentage and weight percentage of components found in the top 10 nm of the surface of the iron oxide particles. The variation in the concentration of carbon is mostly due to the variation in the thickness of the carbon coating used.

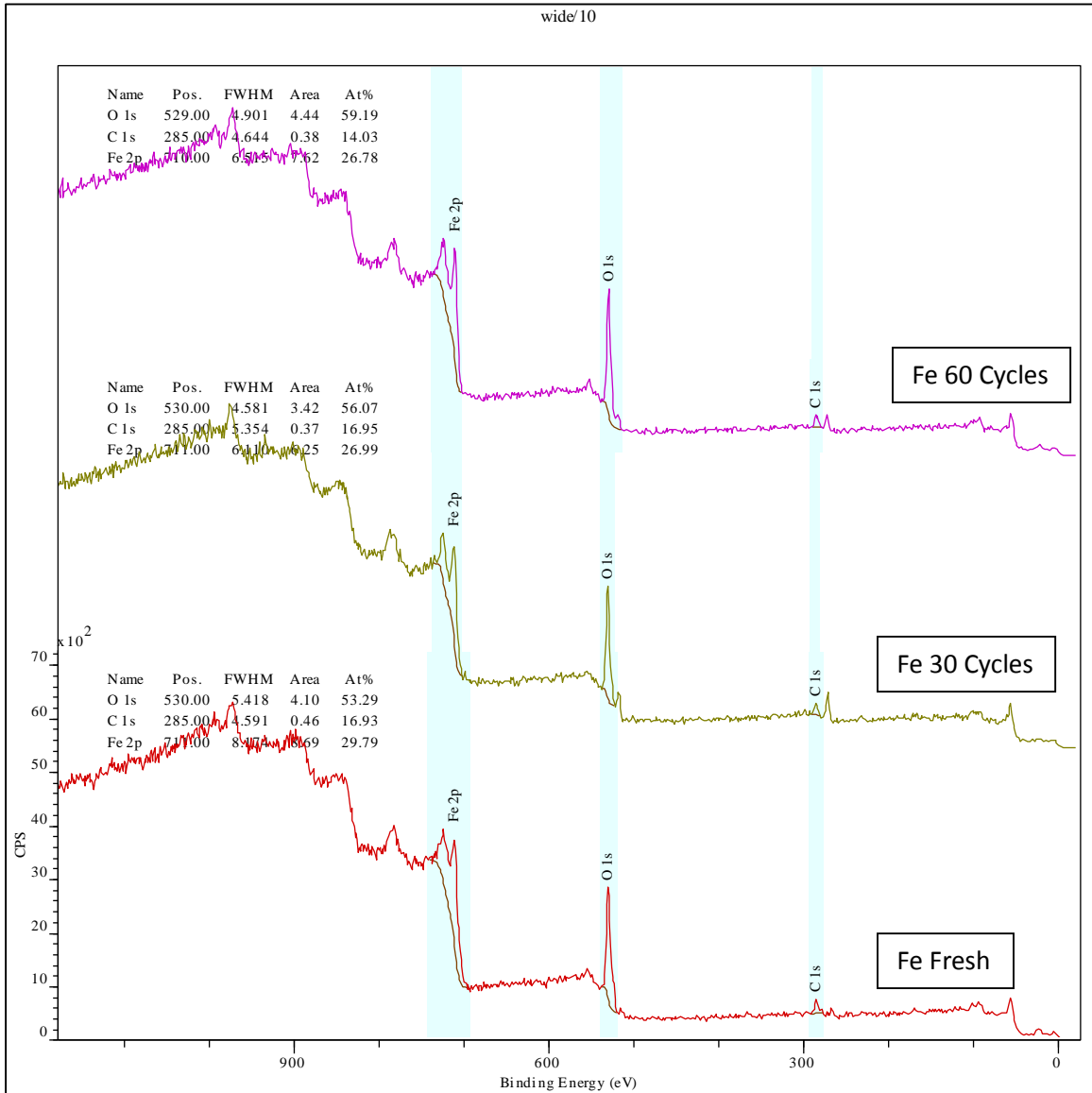


Figure 7.25: XPS data for fresh and reacted iron oxide

Table 7.1: Atomic percent of components on the surface of fresh and reacted iron oxide particles

Element	Fresh (1) (Atomic %)	Fresh (2) (Atomic %)	30 Cycles (1) (Atomic %)	30 Cycles (2) (Atomic %)	60 Cycles (1) (Atomic %)	60 Cycles (2) (Atomic %)
O	52.29	61.05	55.38	56.07	57	59.19
C	16.93	10.04	17.65	16.95	15.41	14.03
Fe	29.79	28.91	26.87	26.99	27.59	26.78

Table 7.2: Weight percent of components on the surface of fresh and reacted iron oxide particles

Element	Fresh (1) (Weight %)	Fresh (2) (Weight %)	30 Cycles (1) (Weight %)	30 Cycles (2) (Weight %)	60 Cycles (1) (Weight %)	60 Cycles (2) (Weight %)
O	30.95	36.02	34.10	34.40	34.58	36.27
C	7.52	4.45	8.16	7.81	7.02	6.45
Fe	61.53	59.53	57.74	57.79	58.41	57.27

The above tables show that the weight percent of iron oxide on the surface of the particles remains fairly consistent even after it has undergone multiple cycles of reduction and oxidation reactions. The tables also show the absence of calcium and magnesium from the surfaces of the iron oxide particles that is in sharp contrast to the inductively coupled plasma mass spectrometry (ICP-MS) and X-ray fluorescence (XRF) observations that showed the significant presence of calcium oxide and magnesium oxide in the iron oxide particles.

Based on the ionic diffusivity model, it is believed that when the oxygen ions diffuse to the surface of the metal oxide, it is possible some of the mineral matter to replace the space vacated by the oxygen ions. XRF and ICP-MS analysis shows that the amount of iron oxide in the particles decrease over successive reduction oxidation cycles. This shows that iron oxide molecules located at the core of the iron oxide particles must have diffuse to the surface of the particles to replace the elutriated iron oxide at the surface level. This is due to the fact

that iron oxide has a lower melting point compared to the mineral matter causing it to diffuse easily to the surface level. As a result, the amount of iron oxide at the surface level remains fairly consistent even though the collective amount of iron oxide decreases over successive reduction oxidation cycles. Even though this phenomenon is projected to occur continuously, it is believed that as the amount of mineral matter in the iron oxide particles increases, it will segregate iron oxide located on the surface level with those located at the core of the iron oxide particle. When this occurs, it will make it difficult for the oxygen atoms located at the core of the iron oxide particle to diffuse to the surface to react with the pyrolysis gases. This will result in the decrease in coal conversion over successive reduction cycles.

The surface melting model can also be used to explain the above phenomenon. Instead of taking over the vacated oxygen atoms, mineral matter will instead diffuse through the quasi-liquid layer and displace the iron oxide atoms located deeper in the particles due to its relatively higher melting point. It is possible that the quasi-liquid layer will dislodge from the surface of the particle to form its own particle during the oxidation stage. As the quasi-liquid layer is a very thin layer on the surface of the particle, the particle formed via the dislodging process is projected to have a small particle size. The newly generated particle will be easily elutriated from the fluidised bed due to its relatively low terminal velocity.

The XPS data also for the reacted iron oxide particles also shows the appearance of a double peak close to the binding energy of the elemental carbon that was not observed in the fresh iron oxide data. As carbon was used to coat the sample prior to the XPS analysis, the double peak is believed to be caused by the presence of carbonate or C-C on the surface of the particles. This has a major implication in that carbon depositing on the surface of the particles will reduce the contact between the pyrolysis gases and the iron oxide molecules on the surface of the particles. This will then result in lower pyrolysis gas conversion during the reduction stage.

The XPS data for the reacted iron oxide particles also shows the lack of sulphur containing species on the surfaces of the particles. This shows that all the sulphur in the fuel was

converted into sulphur dioxide and that the formation of iron sulphide is not preferred during the combustion process.

7.7 Copper Oxide X-Ray Photoelectron Spectroscopy Experiments

7.7.1 Carbon Calibration

Figure 7.26 shows the carbon peaks for the fresh and reacted copper oxide that were used for the calibration of the XPS data for further analysis. XPS data for the reacted copper oxide particles does not show the appearance of a double peak close to the binding energy of the elemental carbon that was observed in the reacted iron oxide data. However, the carbon bases for the reacted copper oxide are broader than the base for the fresh copper oxide and in cases with iron oxide. The broader base is due to the presence of potassium which has binding energy quite close to carbon. However, as the presence of potassium is small, their peaks appear to blend into the carbon peaks.

7.7.2 Copper Oxide Calibration

Figure 7.27 describes the calibration for the fresh and reacted copper oxide particles. The 4 peaks observed in the range of the binding energy spectrum correspond well to the data from literature, though some of the peaks seemed to have shifted slightly. This is believed to be caused by the presence of copper aluminate (CuAl_2O_4). As copper aluminate and copper oxide have very similar binding energy peak values, it is difficult to distinguish one from the other.

7.7.3 Copper Oxide X-ray Photoelectron Spectroscopy Results

Figure 7.28 and Tables 7.3 and 7.4 illustrate the XPS analysis for the fresh and reacted copper oxide. The tables show the atomic percentage and weight percentage of components found in the top 10 nm of the surface of the copper oxide particles. The variation in the concentration of carbon is mostly due to the variation in the thickness of the carbon coating used.

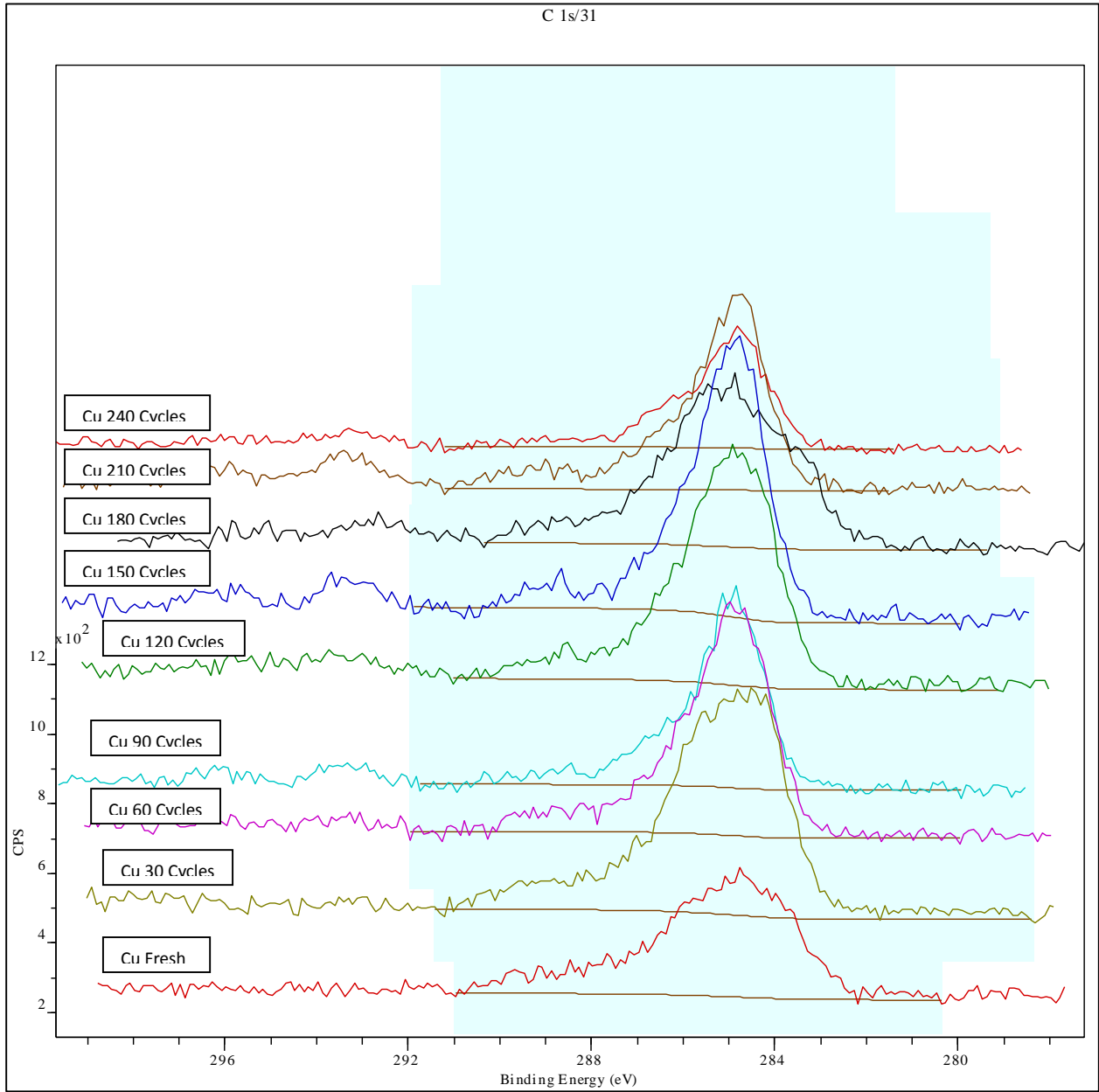


Figure 7.26: Carbon calibration for copper oxide

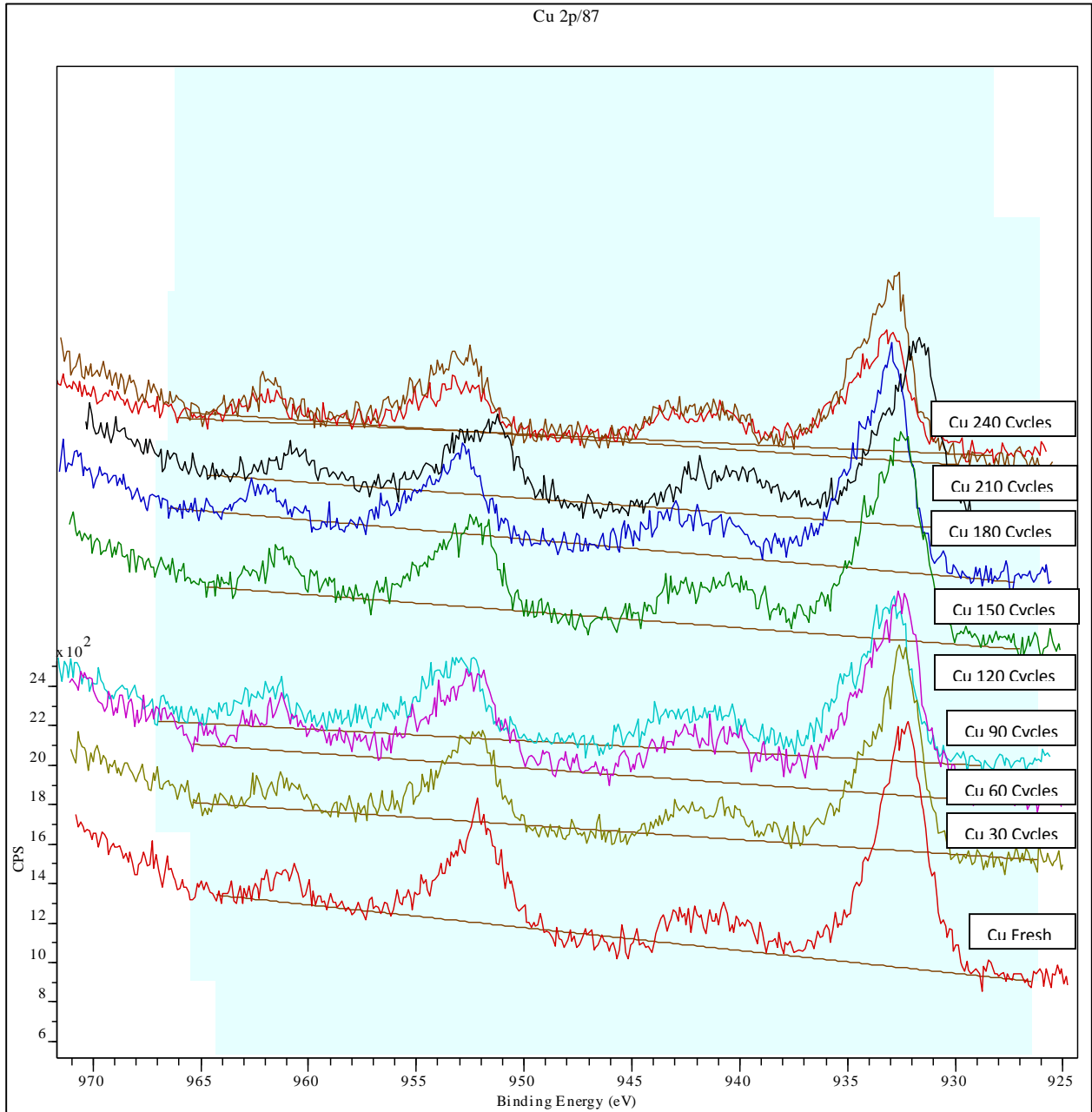


Figure 7.27: Copper oxide calibration

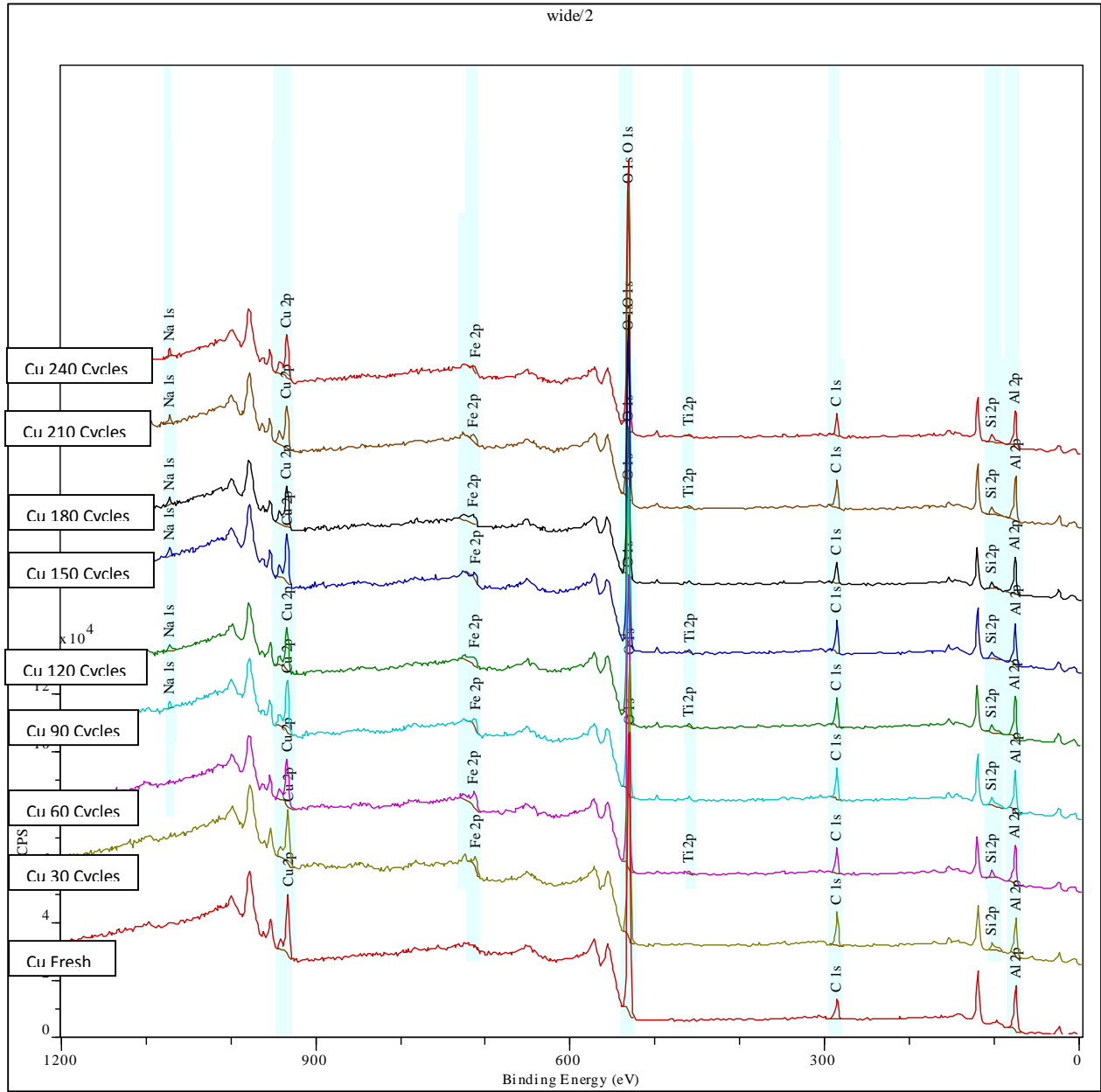


Figure 7.28: XPS data for fresh and reacted copper oxide

Table 7.3: Atomic percent of components on the surface of fresh and reacted copper oxide particles

Element	Fresh (Atomic %)	30 Cycles (Atomic %)	60 Cycles (Atomic %)	90 Cycles (Atomic %)	120 Cycles (Atomic %)	150 Cycles (Atomic %)	180 Cycles (Atomic %)	210 Cycles (Atomic %)	240 Cycles (Atomic %)
O	46.32	44.54	45.15	37.03	41.86	43.70	44.31	42.22	45.33
C	11.22	16.43	12.46	11.38	12.89	14.01	11.74	13.01	10.57
Na				0.20	0.46	0.54	0.49	0.50	0.54
Cu	1.73	1.68	1.54	1.08	1.20	1.48	1.69	1.49	1.72
Si		5.29	4.35	9.32	7.12	4.75	4.65	6.00	6.88
Al	40.72	31.44	34.74	40.77	35.22	35.13	35.81	36.03	34.53
Ti			0.23		0.22	0.17		0.29	0.15
Fe		0.61	1.53	0.22	1.03	0.20	1.32	0.47	0.27

Table 7.4: Weight percent of components on the surface of fresh and reacted copper oxide particles

Element	Fresh (Weight %)	30 Cycles (Weight %)	60 Cycles (Weight %)	90 Cycles (Weight %)	120 Cycles (Weight %)	150 Cycles (Weight %)	180 Cycles (Weight %)	210 Cycles (Weight %)	240 Cycles (Weight %)
O	35.55	34.80	33.98	27.22	31.45	33.71	33.14	31.88	34.19
C	6.46	9.64	7.04	6.28	7.27	8.11	6.59	7.37	5.98
Na	0.00	0.00	0.00	0.21	0.50	0.60	0.53	0.54	0.59
Cu	5.27	5.21	4.60	3.15	3.58	4.53	5.02	4.47	5.15
Si	0.00	7.26	5.75	12.03	9.39	6.43	6.11	7.95	9.11
Al	52.71	41.43	44.09	50.54	44.62	45.69	45.17	45.88	43.92
Ti	0.00	0.00	0.52	0.00	0.49	0.39	0.00	0.66	0.34
Fe	0.00	1.66	4.02	0.56	2.70	0.54	3.45	1.24	0.71

The above tables show that the weight percent of copper oxide on the surface of the particles remains fairly consistent even after it has undergone multiple cycles of reduction and oxidation reactions. The tables also show the absence of calcium and magnesium from the surfaces of the iron oxide particles and that the weight percent of silicon dioxide on the surface of the reacted copper oxide remains fairly consistent throughout the experimental study. This is in sharp contrast to the inductively coupled plasma mass spectrometry (ICP-MS) and X-ray fluorescence (XRF) observations that showed the significant and increasing presence of silicon dioxide, calcium oxide and magnesium oxide in the copper oxide particles as the number of reaction cycles increases. The reasoning for this phenomena was described in section 7.6.1 based on the hypothesis detailed in Chapter 3.

The XPS analysis for the copper oxide after 90 reaction cycles showed the least amount of copper on the surface of the particle among collected samples. This is believed to be due to the random error during the XPS analysis whereby the particle selected for analysis contained less copper than the other particles in the collected batch of copper oxide particles after 90 reaction cycles.

The XPS analysis detected the presence of sodium on the surfaces of the reacted copper oxide particles. The tails seen in the carbon calibration used for the copper oxide analysis seem to indicate the presence of potassium on the surface of the copper oxide particles. However, potassium is present in a very small amount that causes its peak to be blend into the binding energy of carbon.

The XPS data for the reacted iron oxide particles also shows the lack of carbon and sulphur containing species on the surfaces of the particles. This shows that all the sulphur in the fuel was converted into sulphur dioxide and that the formation of copper carbide and/or copper sulphide is not preferred during the combustion process.

7.8 Summary

In this chapter, the morphology and composition on the surface of the iron oxide and copper oxide were studied. SEM/EDX analysis conducted on the reacted iron oxide particles indicated the presence of carbon depositing on the surface of the iron oxide. The surfaces of the reacted iron oxide appeared to be smoother showing it has undergone sintering during the experiments.

The cross-sectional SEM analysis on the reacted copper oxide particles showed some form of segregation of silicon dioxide in the copper oxide particles. However, this was not detected via the EDX analysis highlighting that this phenomenon is probably dominant in some of the particles in the bed. EDX analysis for the fresh and reacted copper oxide particles after 30 reaction cycles showed that copper and alumina is distributed randomly throughout the entire particle with no form of segregation observed between them. This is due to the fact that most of the copper oxide are present in the form of CuAl_2O_4 and that the reduction of CuAl_2O_4 is believed to occur in the form of copper aluminate complexes rather than in the form of CuO to Cu .

XPS analysis for the metal oxide particles revealed that the amount of iron oxide and copper oxide on the surfaces of these particles fluctuates slightly and that they do not show a significant decrease in the core component as seen in the XRF and ICP-MS results.

Chapter 8 CONCLUSIONS & FUTURE WORK

8.1 Conclusions

The main conclusions from this research project are summarised as follows:

- Lignite coal and lignite char were found to be more reactive compared to activated carbon and the various bituminous coal used in this study. This makes lignite a major option for usage in chemical looping combustion with solid fuels as it can be easily gasified. The large accumulation of char in the bed when bituminous coal and activated carbon were used highlights one of the limitation in chemical looping combustion whereby the metal oxides will only react with the pyrolysis gases. Char will also reduce the carbon capture efficiency as the gas stream during the oxidation of char will consist of a mixture of nitrogen and carbon dioxide.
- XRF and ICP-MS results showed that the core components of the metal oxide particles decrease as the number of redox cycles increases. This is due to be the interaction between ash and the metal oxide particles. It is believed that mineral matter from ash will diffuse into the metal oxide particles resulting in the deformation in the morphology of the metal oxide particles. As a result, when the metal oxide particles collide among themselves as well as with the hard and abrasive mineral matter, metal oxide fines are generated and subsequently elutriated from the bed due to their relatively low terminal velocity.
- XPS results revealed that the core components on the surface of the metal oxide particles remained fairly unchanged over multiple redox cycles which is in sharp contrast to results obtained from XRF and ICP-MS. This is believed to be caused by the diffusion of the mineral matter into the core of the metal oxide particles. This is believed to indirectly cause the deactivation of the metal oxide particles as the mineral matter has the ability to segregate the core components located at the surface from those located at the core of the particles.

- Porosimetry analysis indicated that BET surface area appears to play a small part in the combustion process as the activity of the metal oxide particles decreased slightly over the entire course of the study whereas their BET surface area dropped significantly after the initial 30 redox cycles and appeared to level off during subsequent redox cycles. This shows that there is a large possibility that the reaction mechanism occurs either via ionic diffusion or surface melting rather than via the shrinking core model concept.
- SEM analysis highlighted the smoothing of molecules located on the surface of the particles. This is due to sintering as well as the possibility of melting occurring on the surface of these particles. The cross-sectional SEM analysis on the copper oxide particles showed some form of segregation occurring within the particles. However, EDS analysis performed on them did not provide a conclusive result.
- The overall conversion for the metal oxide particles were found to increase with time. This is believed to be largely due to the elutriation of the oxide fines from the fluidised bed as a result of attrition occurring in the fluidised bed. There is also the possibility that the oxide particles are starting to deactivate though the deactivation effect is believed to be small as the amount of carbon converted during reduction diminished slightly as the number of reaction cycles increased.
- The presence of support was found to increase the mechanical strength of the metal oxide particles thus allowing it to withstand a higher rate of attrition. This has a major impact in chemical looping combustion operation as a supported metal oxide can undergo a larger number of reduction cycles thus increasing their operational lifetime. This will reduce the cost associated with replacing the elutriated metal oxide.

- The preparation methods used for this PhD study were found to be relatively cheap and they can be easily scaled up for industrial application. Even though large amount of oxide materials could be produced at any given time, large quantity of oxide fines were generated due to the difficulty involved in trying to grind the oxide materials to the required size range.
- The semi-batch scheme involving the use of a single fluidised bed system has difficulty in scaling up for industrial applications due to the accumulation of char in the fluidised bed. There are two potential schemes that could be used for chemical looping combustion for solid fuels.
- One potential scheme that could be used is the dual fluidised bed setup with a reducer and an oxidiser reactor. With this reactor scheme, oxygen carrier will react with solid fuel in the reducing reactor. Unburned fuel will be separated from the reduced metal oxide before the metal oxide is channelled into the oxidation reactor. This will allow continuous operation of the chemical looping combustion process. However, it will increase the energy production cost as a second fluidised bed reactor is required.
- The second scheme that could be used is the triple fluidised bed setup. In this configuration, solid fuel will be gasified in the first reactor with a mixture of CO₂ and H₂O. The pyrolysis gases resulting from this process will then be channelled to the reduction reactor whereby it will react with the metal oxide in the second reactor. The reduced metal oxide will pass through the oxidation reactor. This will allow continuous operation of the process as stated previously and it has the added benefit in that char and ash will not interact with the metal oxide in the reducing reactor. This will thus increase the operational lifetime of the metal oxide particles. This will also cause the energy production cost to increase as a third fluidised bed reactor is required but the process is simplified in that the separation of the reduced metal oxide from the unburned fuel is not required.

- Ultimately, the initial increase in the starting up cost due to the additional required equipment should not be a major barrier to the commercialisation of chemical looping combustion. This is because it is projected that most of the cost associated with carbon capture and storage will arise from the compression, transportation and storage of the CO₂ stream into geological formation. Besides that, the additional equipment can be retrofitted into existing power plant thereby negating the need to build a new power plant for the purpose of chemical looping combustion.

8.2 Future Work

This work highlights two areas for further research:

- The design of the operation of the process in order to manage the accumulation of char and maximize capture of CO₂
- Development of durable oxygen carriers.

The operational design of this process could be achieved by combining further experimental investigations. In particular the following aspects of the process needs to be investigated:

- The optimal amount of oxygen carrier, fuel feeding rate and feeder positioning, for a given char reactivity which would minimize CO escape from the bed
- The optimal length of the feeding stage in order to maximize the CO₂ capture. Depending on the reactivity of the char, there will be an optimal point of carrier conversion when feeding of the fuel should be stopped and the char in the bed gasified.
- The ability to oxidise the oxygen carrier preferentially over the char needs to be further investigated in order to determine whether this is a feasible process option.

Since the accumulation of char is such a problem, alternative processes also need to be investigated such as chemical looping combustion coupled with oxyfuel combustion to deal with the char or running a gasifier coupled with chemical looping combustion of the syngas. To begin with, some flow sheeting studies should be performed to assess the impact of these hybrid schemes on the power cycle efficiency.

Besides that, the modelling of the ionic diffusivity mechanism as well as the surface melting mechanism via density function theory is essential to predict the main reduction mechanism occurring in the fluidised bed. This will lead to a better understanding of the interaction between coal and pyrolysis gases with the metal oxide particles.

REFERENCES

Adánez, J., Gayán, P., Celaya, J., de Diego, L.F., García-Labiano, F. and Abad, A. (2006) Chemical looping combustion in a 10kW_{th} prototype using a CuO/Al₂O₃ oxygen carrier: effect of operating conditions on methane combustion. *Industrial & Engineering Chemistry Research* 45(17), 6075-6080.

Australian Strategic Policy Institute (ASPI) (2007) *Power plays Energy and Australia's security*. Barton, ASPI.

Bailliez, S. and Nzihou, A. (2004) The kinetics of surface area reduction during isothermal sintering of hydroxyapatite adsorbent. *Chemical Engineering Journal* 98, 141-152.

Benson, S.M. and Surles, T. (2006) Carbon dioxide capture and storage: an overview with emphasis on capture and storage in deep geological formations. *Proceedings of the 2006 IEEE Conference* 94(10), 1795-1805.

Berguerand N. and Lyngfelt A. (2008) Design and operation of a 10kW_{th} chemical-looping combustor for solid fuels – testing with South African coal. *Fuel* 87(12), 2713–2726.

Berguerand N. and Lyngfelt A. (2008) The use of petroleum coke as fuel in a 10 kW_{th} chemical-looping combustor. *International Journal of Greenhouse Gas Control* 2(2) 169-179.

Bohn, C.D., Muller, C.R., Cleeton, J.P., Hayhurst, A.N., Davidson, J.F., Scott, S.A. and Dennis, J.S. (2008) Production of Very Pure Hydrogen with Simultaneous Capture of Carbon Dioxide using the Redox Reactions of Iron Oxides in Packed Beds. *Industrial & Engineering Chemistry Research* 47(20), 7623-7630.

Botterill, J.S.M. (1983) *Fluidised Bed Behaviour*. In Howard, J.R. (1983) *Fluidised Bed Combustion and Applications*. London: Applied Science Publishers, 1983. pp 1 – 36.

BP (2011) *Statistical review of world energy*.

Brinker, C.J. and Scherer, G.W. (1990) *The Physics and Chemistry of Sol-Gel Processing*. Academic Press, New York.

Brown, T.A. (2010) *Chemical looping Combustion with Solid Fuels*. PhD Dissertation, Department of Chemical Engineering and Biotechnology, University of Cambridge.

Caillet, D.A. and Harrisson, D.P. (1982) Structural property variations in the MnO-MnS system. *Chemical Engineering Science* 37, 625-636.

Cao, Y. and Pan, W.P. (2006) Investigation of chemical looping combustion by solid fuels. 1. Process analysis. *Energy & Fuels* 20(5), 1836–1844.

Cao, Y., Casenas, B. and Pan, W.P. (2006) Investigation of chemical looping combustion by solid fuels. 2. Redox reaction kinetics and product characterization with coal, biomass, and solid waste as solid fuels and CuO as an oxygen carrier. *Energy & Fuels* 20(5), 1845–1854.

Chirone, R., Massimilla, L. and Salatino, P. (1991) Comminution of carbons in fluidized bed combustion, *Progress in Energy and Combustion Science* 17(4), 297-326.

Cho, P., Mattisson, T. and Lyngfelt, A. (2004) Comparison of Iron-, Nickel-, Copper- and Manganese-Based Oxygen Carriers for Chemical-Looping Combustion. *Fuel* 83(9), 1215-1225.

Cho, P., Mattisson, T. and Lyngfelt, A. (2005) Carbon formation on nickel and iron oxide-containing oxygen carriers for chemical-looping combustion. *Industrial & Engineering Chemistry Research* 44(4), 668–676.

Chraibi, M. and Flamant, G. (1989) Kinetic, thermal and chemical attrition of manganese chloride particles in a fluidised bed. *Powder Technology* 59(2), 97-107.

Chuang, S.Y. (2009) Development and Performance of a Cu-based Oxygen carrier for Chemical-looping. PhD Dissertation, Department of Chemical Engineering and Biotechnology, University of Cambridge.

Corbella, B.M., de Diego, L., Garcia-Labiano, F., Adanez, J. and Palacios, J.M. (2005) The performance in a fixed bed reactor of copper-based oxides on titania as oxygen carriers for chemical looping combustion of methane. *Energy & Fuels* 19(2), 433–441.

Corbella, B.M., de Diego, L., Garcia-Labiano, F., Adanez, J. and Palacios, J.M. (2005) Characterization study and five-cycle tests in a fixed-bed reactor of titania-supported nickel oxide as oxygen carriers for the chemical-looping combustion of methane. *Environmental Science & Technology* 39(15), 5736–5803.

Davidson, J. and Thambimuthu, K. (2004) Technologies for Capture of Carbon Dioxide. Proceedings of the 7th International Conference on Greenhouse Gas Control Technologies, Vancouver, September 2004, Canada.

Davydov, A.A. (1990) Infrared Spectroscopy of Adsorbed Species on the Surface of Transition Metal Oxides, ed. Rochester, C.H., Jon Wiley and Sons, New York.

De Diego, L.F., Garcia-Labiano, F., Adanez, J., Gayan, P., Abad, A., Corbella, B.M. and Palacios, J.M. (2004) Development of Cu-Based Oxygen Carriers for Chemical-Looping Combustion. *Fuel*, 83(13), 1794-1757.

De Diego, L.F., Gayan, P., Garcia-Labiano, F., Celaya, J., Abad, A. and Adanez, J. (2005) Impregnated CuO/Al₂O₃ Oxygen Carriers for Chemical-Looping Combustion: Avoiding Fluidised Bed Agglomeration. *Energy & Fuels* 19(5), 1850-1856.

Dennis, J.S. (2009) Chemical-Looping Combustion: One Answer to Sequestering Carbon Dioxide: Proceedings of the 2009 European Combustion Meeting.

Dennis, J.S. and Scott S.A. (2010) In situ gasification of a lignite coal and CO₂ separation using chemical looping with a Cu-based oxygen carrier. *Fuel* 89(7), 1623-1640.

Department of Energy & Climate Change (DECC) (2010) www.decc.gov.uk.

Erri, P. and Varma, A. (2007) Solution Combustion Synthesized Oxygen Carriers for Chemical Looping Combustion. *Chemical Engineering Science*, 62(18-20), 5682-5687.

Erri, P. and Varma, A. (2007) Spinel-Supported Oxygen Carriers for Inherent CO₂ Separation during Power Generation. *Industrial & Engineering Chemistry Research* 46(25), 8597-8601.

Fan, L.S. (2010) *Chemical Looping Systems for Fossil Energy Conversions*. Jon Wiley and Sons, New York.

Forsythe, W.L. and Hertwig, W.R. (1949) Attrition characteristics of fluid cracking catalysts. *Industrial and Engineering Chemistry* 41(6) 1200-1206.

Gardner, R. and Austin, L. (1962) The Use of a Radioactive Tracer Technique and a Computer in the Study of the Batch Grinding of Coal. *Journal of the Institute of Fuel* 35, 173-177.

Gayan P., de Diego, L.F., Garcia-Labiano, F., Adanez, J., Abad, A. and Dueso, D. (2008) Effect of support on reactivity and selectivity of Ni-based oxygen carriers for chemical-looping combustion. *Fuel* 87(12), 2641-2650.

German, R.M. and Munir, Z.A. (1976) Surface area reduction during isothermal sintering. *Journal of American Ceramic Society* 59, 379-383.

Gwyn, J. (1969) On particle size distribution function and attrition of cracking catalysts. *AIChE Journal*, 15(1), 35.

Haber, J., Block, J.H. and Delmon, B. (1995) *Manual of Methods and Procedures for Catalyst Characterisation*. *Pure and Applied Chemistry*. 67(8-9), 1257-1306.

Holmgren, A. (1998) Monolith Catalysts for Car Exhaust: Experimental and Theoretical Studies of Oxygen Storage, Flow and Mass Transfer. PhD Dissertation, Chalmers University of Technology, Gothenburg, Sweden.

Hossain, M.M. and de Lasa, H.I. (2008) Chemical-looping combustion (CLC) for inherent CO₂ separations – a review. *Chemical Engineering Science* 63(18), 4433-4451.

Iablokov, V. (2011). Manganese and Cobalt oxides as highly active catalysts for CO oxidation. PhD Dissertation, Faculty of Sciences, University libre de Bruxelles.

Imperial College London (2010) Climate Change: A Short Introduction. Grantham Institute for Climate Change.

International Energy Agency (IEA) (2007) World energy outlook 2006, Organization for Economic Co-operation and Development. Paris.

IPPC (2005) Carbon Dioxide Capture and Storage.

IPPC (2007) Summary for policymakers. In: *Climate Change 2007 Mitigation. Contribution of Working group III to the fourth assessment report of the IPCC.*

IPPC (2007) Summary for policymakers. In: *Climate Change 2007 The physical Science Basis. Contribution of Working group I to the fourth assessment report of the IPCC.*

Ishida, M. and Jin, H. (1996) A Novel Chemical-Looping Combustor without NO_x Formation. *Industrial & Engineering Chemistry Research* 35(7), 2469-2472.

Ishida, M., Jin, H.G. and Okamoto, T. (1998) Kinetic Behaviour of Solid Particle in Chemical-Looping Combustion: Suppressing Carbon Deposition in Reduction, *Energy & Fuels* 12(2), 223-229.

Ishida, M., Yamamoto, M. and Ohba, T. (2002) Experimental Results of Chemical-Looping Combustion with NiO/NiAlO₄ Particle Circulation at 1200°C. *Energy Conversion and Management* 43(9-12), 1469-1478.

Ishida, M., Zheng, D. and Akehata, T. (1987) Evaluation of a chemical-looping-combustion power-generation system by graphic exergy analysis. *Energy* 12(2), 147.

Jacob, K.T. and Alcock, C.B. (1975) Thermodynamics of CuAlO₂ and CuAl₂O₄ and Phase Equilibria in the System Cu₂O-CuO-Al₂O₃. *Journal of the American Ceramic Society* 58(5-6), 192-195.

Jansson, J. (2000) Low-Temperature CO Oxidation over Co₃O₄/Al₂O₃. *Journal of Catalysis* 194, 55-60.

Jin, H. and Ishida, H. (2001) Reactivity Study on A Novel Hydrogen Fuelled Chemical-Looping Combustion. *International Journal of Hydrogen Energy* 26(8), 889-894.

Jin, H. and Ishida, H. (2002) Reactivity Study on Natural Gas Fuelled Chemical-Looping Combustion by a Fixed Bed Reactor. *Industrial & Engineering Chemistry Research* 41(16), 4004-4007.

Jin, H. and Ishida, M. (2004) A New Type of Coal Gas Fuelled Chemical-Looping Combustion. *Fuel* 83(17-18), 2411-2417.

Jin, H., Okamoto, T. and Ishida, M. (1998) Development of a Novel Chemical-Looping Combustion: Synthesis of a Looping Material with a Double Metal Oxide of CoO-NiO. *Energy & Fuels* 12(6), 1272-1277.

Jin, H., Okamoto, T. and Ishida, M. (1999) Development of a Novel Chemical-Looping Combustion: Synthesis of a Solid Looping Material of NiO/NiAl₂O₄. *Industrial & Engineering Chemistry Research* 38(1), 126-132.

Johansson M. (2007) Screening of oxygen-carrier particles based on iron-, manganese-, copper- and nickel oxides for use in chemical looping technologies. PhD Dissertation. Chalmers University of Technology.

Johansson, E., Lyngfelt, A., Mattisson, T. and Johnsson, F. (2003) Gas leakage Measurements in a Cold Model of an Interconnected Fluidised Bed for Chemical-Looping Combustion. *Powder Technology* 134(3), 210-217.

Johansson, M., Mattisson, T. and Lyngfelt, A. (2004) Investigation of Fe_2O_3 with MgAl_2O_4 for Chemical-Looping Combustion. *Industrial & Engineering Chemistry Research* 43(22), 6978-6987.

Kromer, B.R. (2008) Theoretical and Experimental Investigation of Heterogeneous Catalytic Reactions: Two Case Studies. PhD Dissertation, Purdue University, West Lafayette, Indiana.

Kunii, D. and Levenspiel, O. (1977) *Fluidisation Engineering*. Butterworth-Heinemann. United States.

Lindeberg, E. (1999) Future large-scale use of fossil energy will require CO_2 sequestering and disposal. Proceedings of the 1999 Minisymposium on the Carbon Dioxide Capture and Storage, Chalmers University of Technology and Goteborg University, Goteborg, 1-15.

Lu, D.Y., Hughes, R.W. and Anthony, E.J. (2008) Ca-based sorbent looping combustion for CO_2 capture in pilot-scale dual fluidized beds. *Fuel Processing Technology* 89(12), 1386-1395.

Maldonado Hodar, F.J. (2009) Heterogeneous catalysis (I). Advance Catalysis and Organometallic Chemistry Intensive Programs (IP), Lifelong Learning Program Erasmus, Camerino, Italy.

Manzoori, A.R. (1990) Role of the Inorganic Matter in Agglomeration and Defluidization During the Circulating Fluid Bed Combustion of Low Rank Coals. PhD Dissertation. The University of Adelaide, Adelaide.

Mars, P. and van Krevelen, D.W. (1954) Oxidations carried out by means of vanadium oxide catalysts. *Chemical Engineering Science* 3(1) 41-59.

Mattisson, T. and Lyngfelt, A. (2001) Capture of CO₂ using chemical-looping combustion. In: Proceedings of 1st Biennial Meeting of the Scandinavian-Nordic Section of the Combustion Institute, Goteborg, Sweden.

Mattisson, T., Jardnas, A. and Lyngfelt, A. (2003) Reactivity of Some Metal Oxides Supported on Alumina with Alternating Methane and Oxygen-Application for Chemical-Looping Combustion. *Energy & Fuels* 17(3), 643-651.

McBride, B.J., Zede, M.J. and Gordon, S. (2002) NASA Glenn coefficients for calculating thermodynamic properties of individual species. Cleveland, Ohio, US: National Aeronautics and Space Administration.

Merrett, K., Cornelius, R.M., McClung, W.G., Unsworth, L.D. and Sheardown, H. (2002) Surface analysis methods for characterising polymeric biomaterials – Review. *Journal of Biomaterials Science, Polymer Edition* 13(6), 593-621.

Niel, A. and Bridgwater, J. (1994) Attrition of particulate solids under shear. *Powder Technology*, 7(3), 183-197.

Pacala, S. and Socolow, R. (2004) Stabilization Wedges: Solving the Climate Problem for the Next 50 Years with Current Technologies. *Science (Washington D.C., United States)* 305 (5686), 968-972.

Patel, K., Nienow, A. and Milne, I. (1986) Attrition of urea in a gas fluidised bed. *Powder Technology* 47(3), 275-261.

Patrick, V. and Gavalas, G. (1990) Structure and Reduction of Mixed Copper-Aluminium Oxide. *Journal of the American Ceramic Society* 73, 358.

Pell, M. and Dunson, J.B. (1997) Gas-solids operations and equipment. In Perry, R.H. and Green D.W. (1997) *Perry's Chemical Engineers' Handbook*, 7th edition. McGraw-Hill, New York. pp. 17-1 – 17-59.

Pinchbeck, P.H. and Popper, F. (1956) Critical and terminal velocities in fluidisation. *Chemical Engineering Science* 6(2), 57-64.

Pluis, B., van der Gon, A.W.D., Frenken, J.W.M. and van der Veen, J.F. (1987) Crystal-Face Dependence of Surface Melting. *Physical Review Letters* 59 (23).

Ray, Y.C., Jiang, T.S. and Wen, C.Y. (1987) Particle attrition phenomena in a fluidized bed. *Powder technology* 49(3), 193-206.

Richter, H.J. and Knoche, K.F. (1983) Reversibility of Combustion Processes – Efficiency and Costing. *ACS Symposium Series* 235, 71.

Rubel, A., Zhang, Y., Liu, K. and Neathery, J. (2011) Effect of Ash on Oxygen Carriers for the Application of Chemical Looping Combustion to a High Carbon Char. *Oil & Gas Science & Technology* 66(2), 291-300.

Ryu, H.J. et al. (2003) Effects on reduction temperature of oxygen carrier particles on a fixed bed chemical-looping combustion. *Korean Journal of Chemical Engineering* 20(5), 960–966.

Sakka, S., Klein, L.C. and Pope, E.J.A. (1995) *Sol-Gel Science and Technology*. American Ceramic Society, Westerville, Ohio.

Salatino, P. (2007) A survey of particle attrition phenomena relevant to fluidized bed combustion and gasification of solid fuels. In 2007 8th UK Particle Technology Forum.

Scottish Carbon Capture & Storage (SCCS) (2008) CCS Education Centre: What are we doing about it? www.sccs.org.uk.

Sedlatschek, K. and Bass, L. (1953) Contribution to the theory of milling processes. Powder Metallurgy Bulletin 6, 148-153.

Sim, C.Y.; Brown, T.; Chen, Q.; Sharifi, V.; Swithenbank, J.; Dennis, J.; Scott, S. (2011) Particle characterisation in chemical looping combustion. Chemical Engineering Science 69, 211-224.

Siriwardane, R., Tian, H., Miller, D., Richards, G., Simonyi, T., Poston, J. (2010) Evaluation of reaction mechanism of coal-metal oxide interactions in chemical-looping combustion. Combustion and Flame 157 (11) 2198-2208.

Socolow, R.H. (2005) Can We Bury Global Warming? Scientific American, July 2005, 39-45.

Son, S.R. and Kim, S.D. (2006) Chemical-Looping Combustion with NiO and Fe₂O₃ in a Thermobalance and Circulating Fluidized Bed Reactor with Double Loops. Industrial & Engineering Chemistry Research 45(8), 2689-2696.

Soto, L.L. (2007) Studies of the Mars van Krevelen Mechanism in Hydrocarbon Selective Oxidation. PhD Dissertation. Faculty of Chemical Engineering, University of Delaware.

Valk, M. (1986) Fluidised Bed Combustors. In: Radovanovic, M. (1986) Fluidised Bed Combustion, Hemisphere Publishing Corporation. New York. pp. 7 – 36.

van der Veen, J.F. (1999) Melting and freezing at surfaces. Surface Science 433 – 435, 1-11.

Vannice, M.A. (2007) An analysis of the Mars-van Krevelen rate expression. *Catalysis Today* 123, 18-22.

Villa, R., Cristiani, C., Groppi, G., Lietti, L., Forzatti, P., Cornaro, U. and Rossini, S. (2003) Ni based mixed oxide materials for CH₄ oxidation under redox cycle conditions. *Journal of Molecular Catalysis A: Chemical* 204–205(15), 637–646.

Wolff, E.H.P, Gerritsen, A.W. and Verheijen, P.J.T. (1993) Attrition of an aluminate based synthetic sorbent for regenerative sulphur capture from flue gas in a fluidised bed. *Powder Technology*, 76(1), 47-55.

Yamasaki, A. (2003) An overview of CO₂ mitigation options for global warming-emphasizing CO₂ sequestration options. *Journal of Chemical Engineering of Japan*, 36(4), 361-375.

APPENDIX A

Calorific Value Determination

The calorific value of the fuels were conducted in the analytical laboratory in the department of Chemical and Process Engineering at the University of Sheffield using British Standard 1016-105 (1992).

Introduction

The calorific value of the fuel is derived as the heat released when it is completely burned at standard pressure (1 bar) and reference temperature (298 K)

Experimental Method

The sample is burned in a bomb calorimeter under the standardized conditions. The fuel is placed in the central bomb, which is surrounded by a water jacket. The fuel is ignited and the heat released is transferred to the water. The calorific value of the fuel is determined after abstracting the heat released due to the ignition of the wire. As it is customary to be quoted per kilogram of dry fuel, the moisture content must also be measured and the appropriate calculation made.

Procedures

- Weight about 1 gram of sample (to the nearest 0.1 mg) into a crucible
- Stretch a 10 cm length of nichrome wire between two poles of electrodes in the bomb cap. Place the bomb cap on the special stand and place the crucible in its holder, making sure that the wire is in contact with the sample
- Assemble the bomb with the correct position of the sealing ring in its groove in the bomb cap and tighten it by hand
- Pour 4 litres of cold water into the calorimeter vessel and place the vessel into the calorimeter so that the short locating peg on the side of the vessel engages the slot in the vertical part of the front left-hand foot of the spider support
- Connect the oxygen filling tube to the bomb
- Press the filling oxygen button on the calorimeter keyboard

- Remove the filing tube and lift the bomb into the calorimeter vessel by using a tommy bar
- Wait for a few seconds if there is no bubble rising, then gently close the lid of the calorimeter
- Check the standby light
- Press start and input identified number and weight of sample
- Press done when it is finished
- Remove the bomb from the calorimeter. Examine the contents of the bomb in order to ensure complete combustion. The test must be repeated if there is any presence of soot or residual carbon in the crucible

Data Analysis

Assuming that the bomb is perfectly insulated, then the heat absorbed by the water in the calorimeter is equal to the heat released by the fuel. The heat gained by water is given in the following equation:

$$Q = C\Delta T$$

$$C = \text{Bomb factor} = 11085 \frac{J}{^{\circ}C}$$

$$\Delta T = \text{Temperature rise of the water}$$

Calorific value of the fuel is calculated via:

$$CV = \frac{(\text{Bomb Factor} \times \text{Temperature Rise}) - \text{Heat Released from Wire}}{\text{Mass of the sample}}$$

Proximate and Ultimate Analysis

The proximate and ultimate analysis of the fuels were conducted in the analytical laboratory in the department of Chemical and Process Engineering at the University of Sheffield using British Standard 1016-6 and 1016-104. The analysis results are expressed as percentage in weight. The procedures are described as follows:

Proximate Analysis (BS 1016-6)

Moisture Content

- Weigh an empty crucible. Gradually add about 1 gram of sample (nearest 0.1 mg) and record the weight of the crucible and contents
- Tap the crucible gently to spread the sample evenly over the bottom of the crucible
- Place the crucible in an oven at a temperature of 105°C to 110°C for one hour
- Cool the crucible in a desiccator and reweigh. The percentage moisture is calculated via:

$$\% \text{Moisture} = \frac{\text{Mass of water removed}}{\text{Mass of original sample}} = \frac{M_2 - M_3}{M_2 - M_1} \times 100\%$$

M_1 = Mass of empty crucible

M_2 = Mass of crucible plus sample before heating

M_3 = Mass of crucible plus dried sample

Ash Content

- Weigh an empty crucible. Gradually add about 1 gram of sample (nearest 0.1 mg) and record the weight of the crucible content
- Tap the crucible gently to spread the sample evenly over the bottom of the crucible
- Place the crucible in a high temperature furnace of 750°C for one hour
- Remove the crucible from the furnace. Let it cool for approximately one minute in the laboratory and then place it in a desiccator until it has cooled to room temperature

- Reweigh the sample. The percentage of ash is calculated via:

$$\% \text{Moisture} = \frac{M_3 - M_1}{M_2 - M_1} \times 100\%$$

M_1 = Mass of empty crucible

M_2 = Mass of crucible plus sample before heating

M_3 = Mass of crucible plus residue

Volatiles Content

- Weigh an empty crucible plus lid
- Gradually add about 1 gram of sample and record the weight of the crucible (plus lid) and contents
- Place the covered crucible into a high temperature furnace of 925°C for exactly 7 minutes in the absence of air
- Remove the crucible from the furnace. Let it cool for about 1 minute in the laboratory and then place it in a desiccator
- Reweigh the sample
- The volatiles content is calculated via:

$$\% \text{Volatiles} = \frac{M_2 - M_3}{M_2 - M_1} \times 100\%$$

M_1 = Mass of empty crucible and lid

M_2 = Mass of crucible and lid plus sample before heating

M_3 = Mass of crucible, lid and residue after heating

Fixed Carbon Content

Fixed carbon is determined via:

$$\% \text{Fixed Carbon} = 100 - (\% \text{Moisture} + \% \text{Volatiles} + \% \text{Ash})$$

Ultimate Analysis

Quantitative analyses for carbon, hydrogen, nitrogen and sulphur are performed with the Carbo Erba Elemental Analyser EA 1108. The elemental analyser operation is based on the complete and instantaneous oxidation of the sample via flash combustion whereby the all organic and inorganic substances are converted into combustion products.

The sample is placed in a tin capsule and is introduced into the instrument automatically via the autosampler (AS-200LS). The autosampler tray holds 49 samples. The autosampler operates via the following manner. The sample container drops from the autosampler tray into the cavity of the autosampler slide where it is continuously purged with a constant flow of carrier gas (helium, 100 mL/min). It then drops into the first of two serially connected reaction columns. The first column, the combustion reactor tube, is made of transparent quartz and is filled with the catalyst, chromic oxide (Cr_2O_3 , 8 cm height) over silvered cobaltous cobaltic oxide ($\text{Co}_3\text{O}_4/\text{Ag}$, 6 cm height). The column is maintained at 1020°C . The second column, the reduction reactor tube, is also made of transparent quartz and is maintained at 650°C . It is filled with reduced copper wire (Cu) and cupric oxide (CuO) layers above and below the copper wire.

After the samples are dropped into the combustion reactor tube, the helium stream is temporarily (2 seconds) enriched with pure oxygen. Oxidation of the tin capsule results in a violent exothermic reaction known as flash combustion. Flash combustion causes oxidation of 85 – 95% of the sample. Complete oxidation of reduced carbon and sulphur is achieved when the mixture of gases passes over the catalyst layer of chromic oxide. The silvered cobaltous cobaltic oxide in the combustion reactor tube removes SO_x , halogens (except fluorine) and acid halides through chemi-adsorption. Once the combustion gases have passed through the combustion reactor tube, they enter the reduction reactor tube. In this reactor, CO and H_2 are oxidized (on the CuO layers) while O_2 is removed and N_xO_y species are reduced to N_2 (on Cu layer). At this point, the gas mixture is composed of N_2 , CO_2 , H_2O and fluorinated gases. The gas mixture is then directed through a water filter (filled with anhydrous magnesium perchlorate) and onto the chromatographic column. Separation of N_2 and CO_2 (in that order) occurs in a 2 meter stainless steel column, 6 mm outer diameter and

4 mm internal diameter, packed with Porapak QS (80 – 100 mesh). Fluorinated gases are chemi-adsorbed to the stationary phase. The column is held at 60°C. A thermal conductivity detector measures the individual components of the gas mixture (N₂, CO₂) as they elute from the column. The signal produced from the thermal conductivity detector is passed to an A/D converter and the peaks are integrated by the EAGER 200 data system. The percentage of carbon, nitrogen, hydrogen and sulphur is computed automatically by the data system.

APPENDIX B

List of Journal Publications

- Sim, C.Y.; Brown, T.; Chen, Q.; Sharifi, V.; Swithenbank, J.; Dennis, J.; Scott, S. (2011) Particle characterisation in chemical looping combustion. *Journal of Chemical Engineering Science*, 69, pp 211-224.
- Sim, C.Y.; Sharifi, V.; Swithenbank, J. (2012) Morphological and compositional changes of oxygen carriers in chemical looping combustion with solid fuels. *Industrial & Engineering Chemistry Research*. Submitted for publication, under review.

Conferences

- Sim, C.Y.; Sharifi, V.; Swithenbank, J. (2012) Particle Characterisation in Chemical Looping Combustion. Conference poster for the 5th International Freiberg Conference on IGCC & XtL Technologies. 21st – 24th May 2012, Leipzig, Germany.
- Sim, C.Y.; Sharifi, V.; Swithenbank, J. (2012) Particle Characterisation in Chemical Looping Combustion with Solid Fuels. Presentation for the 4th IEAGHG High Temperature Solid Looping Cycles Network. 20th – 22nd August 2012, Tsinghua University, China.

Presentations

- Sim, C.Y.; Sharifi, V.; Swithenbank, J. (2010) Initial study on chemical looping combustion. EPSRC UK-China H₂ Network meeting, Cranfield University, 20th January 2010.
- Sim, C.Y.; Sharifi, V.; Swithenbank, J. (2010) Particle Morphology in Chemical Looping Combustion System. EPSRC UK-China H₂ Network meeting, Imperial College, London, 12th October 2010.

- Sim, C.Y.; Sharifi, V.; Swithenbank, J. (2011) Particle Morphology and Characterisation in Chemical Looping Combustion System. EPSRC UK-China H₂ Network meeting, Imperial College, London, 13th July 2011.
- Sim, C.Y.; Sharifi, V.; Swithenbank, J. (2011) Engineering Issues in Chemical Looping Combustion. EPSRC UK-China H₂ Network meeting, University of Sheffield, 16th November 2011.

Department Seminars

- Sim, C.Y.; Sharifi, V.; Swithenbank, J. (2011) Particle Characterisation in Chemical Looping Combustion System. 24-month departmental poster presentation, University of Sheffield.
- Sim, C.Y.; Sharifi, V.; Swithenbank, J. (2012) Morphology and Characterisation of Particles in Chemical Looping Combustion System with solid fuels. 30-month departmental presentation, University of Sheffield, 6th June 2012.

APPENDIX C

Chemical Engineering Science 69 (2012) 211–224



Contents lists available at ScienceDirect

Chemical Engineering Science

journal homepage: www.elsevier.com/locate/ces



Particle characterisation in chemical looping combustion

Chern Yean Sim^{a,*}, Tamaryn Brown^{b,c}, Qun Chen^a, Vida Sharifi^a, Jim Swithenbank^a,
John Dennis^{b,c}, Stuart Scott^{b,c}

^a Department of Chemical and Biological Engineering, University of Sheffield, Mappin Street, Sheffield S1 4DU, United Kingdom
^b Department of Chemical Engineering and Biotechnology, University of Cambridge, Pembroke Street, Cambridge CB2 3RA, United Kingdom
^c Department of Engineering, University of Cambridge, Trumpington Street, Cambridge CB2 1PZ, United Kingdom

ARTICLE INFO

Article history:
 Received 23 February 2011
 Received in revised form
 6 October 2011
 Accepted 11 October 2011
 Available online 28 October 2011

Keywords:
 Chemical looping combustion
 Solid fuels
 Iron oxide
 Copper oxide impregnated alumina
 Semi-batch
 Fluidised bed

ABSTRACT

In a chemical looping combustion process, as the oxygen carrier circulates the system, it is subjected to morphological and compositional changes such as sintering, attrition and reaction between metal oxides and fuels. These changes may cause the deactivation of the oxygen carrier to decrease over time. This research work is carried out to investigate and characterise the iron oxide and copper oxide particles used in a chemical looping combustion system after 20 reduction-oxidation cycles with 5 different fuels, (i.e. Hambach lignite coal, Hambach lignite char, activated carbon, Taldinski bituminous coal and US bituminous coal). Oxygen carriers used in this study were subjected to analyses with X-ray diffraction (XRD), inductive coupled plasma mass spectrometry (ICP-MS), scanning electron microscope (SEM) and BET surface area and full isotherm analysis.

XRD analysis on these particles showed that the reduced particles were reoxidised back to their original form with trace amounts of impurities such as silicon dioxide (SiO₂) on the iron oxide particles whereas similar impurities plus copper complexes such as copper aluminate were detected on the copper oxide particles. ICP-MS analysis on these particles revealed that the concentration of the core metal elements (iron, copper and alumina) decreased after 20 reaction cycles which in turn decreased the total concentration of the metal elements in the particles. BET surface area analysis on these particles indicated that the total surface area of these particles decreased by more than 50% of their original values. Full isotherm analysis on the copper oxide particles showed that the total pore volume of the particles decreased after 20 reaction cycles even though the pore sizes of the particles increased slightly. SEM analysis showed the iron oxide particles underwent severe attrition whereas the copper oxide particles showed signs of agglomeration due to the high operating temperature.

© 2011 Elsevier Ltd. All rights reserved.

1. Introduction

It is well known that carbon dioxide is a greenhouse gas that contributes to the global warming. Nowadays a third of the worldwide anthropogenic CO₂ emissions come from fossil fuels fired power production (Yamasaki, 2003; IEA, 2007). Meanwhile, fossil fuels will continue to be the main source of energy consumption for the foreseeable future (EIA, 2010). The increasing threat posed by enhanced global warming as well as the requirement to secure energy supplies around the world have led to the development of several novel technologies to produce clean energy from fuels (Rigueiro et al., 2008). Among these new technologies is chemical looping combustion (CLC) which uses a solid metal oxide (oxygen carrier) to react with fuels (Richter and Knoche, 1983; Ishida et al., 1987). This technology has the potential advantage to produce a pure stream of carbon dioxide (CO₂) which can then be utilised or sequestered.

In a CLC process, the oxygen carrier is reduced by fuels in one reactor while being reoxidised by air in a separate reactor. The typical operating conditions for a CLC system is 800–1200 °C and under pressurised or atmospheric pressure. The low temperature range used in a CLC system ensures that thermal NO_x does not form as a side reaction in the system (Ishida and Jin, 1996; Son and Kim, 2006).

As the oxygen carrier circulates the system, it is subjected to morphological and compositional changes such as sintering, attrition and reaction between metal oxides and fuels. These changes might cause the reactivity of the oxygen carrier to decrease over time. Earlier studies conducted on CLC focuses on oxygen carriers, reactor design and thermodynamic efficiency of the system with gaseous fuels. Lindemolm et al. (2008) studied the performance of NiO/Ni₂O₃ oxygen carrier in a 10 kW reactor for 160 h. They observed no decrease in the reactivity of the oxygen carrier during the test. The particle lifetime was estimated

^{*} Corresponding author.
E-mail address: cppt@kys@shef.ac.uk (C.Y. Sim).

0009-2502/\$ – see front matter © 2011 Elsevier Ltd. All rights reserved.
doi:10.1016/j.ces.2011.10.026

to be about 4500 h based on fines loss calculations. Zafar et al. (2006) found that the reactivity of NiO/SiO₂ decreased as a function of the cycle number at 950 °C but this effect was not observed for temperatures below 850 °C. The decay in reactivity is found to be due to the formation of nickel complexes.

Mattisson et al. (2001, 2004) studied the performance of iron ores (haematite) under multiple reduction and oxidation cycle with CH₄ and air at 950 °C. They found that the surface of the particles changes to a coarser texture with cracks and fissures after multiple oxidation–reduction cycles. Copeland et al. (2002) studied unsupported Fe₂O₃ at 720–800 °C and found that it showed good chemical stability and that they observed no loss in reactivity over multiple oxidation–reduction cycle. However, agglomeration was observed at 900 °C at a slow rate. Leion et al. (2008) studied the performance of ilmenite and found that the particles showed no decrease in reactivity after 37 reduction oxidation cycles. Zafar et al. (2005, 2006) studied Fe₂O₃ supported on SiO₂ and found that the particles showed high reactivity during the initial reduction oxidation cycles. However, Fe₂O₃ reacts with SiO₂ to form Fe₂SiO₅, iron silicates which will reduce the amount of available oxygen.

Some researchers studied CuO supported on Al₂O₃ (Adán et al., 2004, 2006; Cho et al., 2004; Corbella et al., 2005a, 2005b; de Diego et al., 2004, 2005; García-Labiano et al., 2006; Mattisson et al., 2003). Scanning electron microscope (SEM) images of reduced CuO/Al₂O₃ particles showed the presence of particle agglomeration such that the reactivity of the particles decreased between two consecutive reduction oxidation cycles. At high temperatures, agglomeration decreases the reactivity of the particles and causes the bed to defluidise. Aluminate formation is also another problem found with CuO/Al₂O₃ particles. de Diego et al. (2005) found CuO content in CuO/Al₂O₃ greater than 20 wt% agglomerates whereas CuO content in CuO/Al₂O₃ of less than 10 wt% does not agglomerate. Besides that, the reactivity of CuO/Al₂O₃ was high during the reduction and oxidation and was not affected by the number of cycles.

However, only limited research conducted on chemical looping with solid fuels as the oxygen carrier particles are not easily separable from the fuel or the ash particles. Without separation, the solid fuels would enter the air reactor along with the oxygen carrier and give CO₂ in the off-gas. As a result, a few techniques have been developed (Dennis and Scott, 2010; Brown et al., 2010; Mattisson et al., 2009a, 2009b; Leion et al., 2009a, 2009b; Shulman et al., 2009; Rydén et al., 2010).

The deactivation of the oxygen carries in the chemical looping process with solid fuels due to morphological and compositional have not been studied extensively. Berguerand and Lyngfelt

(2008) studied the performance of ilmenite with petroleum coke in a 10 kW_{th} CLC. They observed a low loss of noncombustible fines from the system which indicates low attrition of the ilmenite particles. The main objective of this research work is to investigate and characterise the morphological and compositional changes in oxygen carrier particles such as Fe₂O₃ and CuO after multiple reduction oxidation cycles with solid fuels. The results can then be used to optimise the overall performance of the looping process.

2. Experimental

2.1. Apparatus

Experiments were carried out in a fluidised bed (inner diameter of 25 mm), constructed from 316 stainless steel, heated to a maximum temperature of 1273 K by an external electric furnace. The bed was fluidised with mixtures of nitrogen, air and CO₂ with $U/U_{mf} \sim 7$, with U being the superficial velocity at the temperature of the bed with $U = U_{mf}$ at incipient fluidisation. A screw feeder was used to deliver fuel continuously to the top of the bed. All of the flue gases leaving the reactor were directed to a condenser via a tube, trace-heated to 523 K to prevent the tar and water from condensing. The condenser was cooled with ice water and was packed with glass ballotini to increase the surface area for heat exchange and condensation. When the gases left the condenser, they were passed through a drying tube filled with CaCl₂. A fraction of the off gases was then pumped through an infrared analyser measuring 0–100 mol% CO, 0–100 mol% CO₂, and 0–10,000 ppmv SO₂ and a paramagnetic analyser which measured 0–100 mol% O₂. Fig. 1 shows the layout of the CLC system designed for the purpose of this research.

2.2. Procedures

At the start of an experiment, the empty reactor was filled with either 20 g of iron oxide and then heated to 1223 K with the bed fluidised at a rate of 40 ml/s consisting of 50 mol% air in nitrogen [all flow rates are given at standard temperature and pressure (STP)]. Once the operating temperature had been reached, the fluidising gas was switched to 40 ml/s consisting of 50 mol% CO₂ in N₂. When the outlet concentration of CO₂ was steady, Hambach lignite coal was fed continuously into the bed. The continuous feeding was stopped when a carbon monoxide breakthrough was achieved. At the end of the feeding period, CO₂

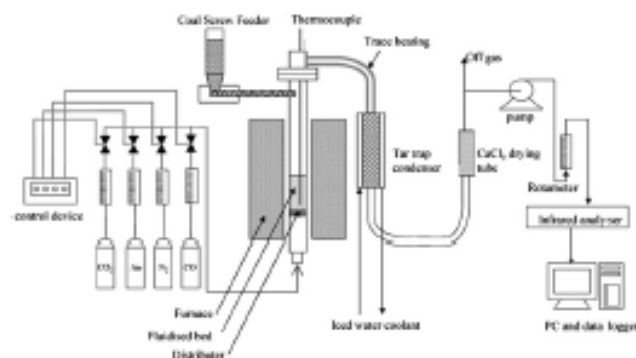


Fig. 1. Schematic of the chemical looping combustion system used in this experiment (Brown et al., 2010).

and fuel were switched off simultaneously and the bed was purged with 40 mL of N_2 /s. After 60 s of purging, the purge N_2 was switched to 40 mL/s consisting of 50 mol% air in N_2 to burn off the carbon in the bed and, when the bed material was iron oxide, to regenerate the carrier back to Fe_2O_3 . Once oxidation was complete and all of the remaining carbon in the bed had been combusted, as measured by the absence of CO and CO_2 detected in the sampled gases, the next feeding period was commenced and the process was repeated for another 19 cycles.

The procedures were then repeated with 4 different fuels (Hambach lignite coal, activated carbon, Taldinski bituminous coal and US bituminous coal) as well as with copper oxide impregnated with alumina as the oxygen carrier. Properties of the 5 fuels as well as their ash contents used in this study are shown in Tables 1 and 2.

2.3. Iron oxide preparation

The iron oxide particles were prepared by using the mechanical mixing method. This method consists of spraying high-purity powdered haematite (Fe_2O_3) (> 99 wt%, sized to < 10 μm , Fisher Scientific Ltd.) with a fine mist of water. The water caused the fine particles to form agglomerates, which were then sieved to the size range of 300–600 μm , and then roasted at 1173 K for 3 h, after which, the particles were sieved again to the size range of 300–425 μm (Brown et al., 2010).

Table 1
Fuels analysis.

	Hambach lignite coal	Hambach lignite char	Activated carbon	Taldinski bituminous coal	US Bituminous Coal
Moisture content (K)	7.15	4.69	6.43	4.59	4.44
Volatiles (K)	57.75	13.17	12.02	30.77	37.23
Ash (K)	3.70	8.62	12.72	15.87	13.06
N (dry K)	0.90	0.62	0.62	1.72	1.41
C (dry K)	61.80	65.66	70.34	71.92	75.73
H (dry K)	4.80	0.90	0.74	3.99	4.48
S (dry K)	0.00	0.00	0.00	0.01	2.03
O_2 (dry K)	32.51	32.82	28.30	22.37	16.35

Table 2
Fuels' ash content analysis.

Element	Ash 1 (mg/kg)	Ash 2 (mg/kg)	Ash 3 (mg/kg)	Ash 4 (mg/kg)	Ash 5 (mg/kg)
Al	11,024.9	11,663.1	651.04	22,323.7	32,688.5
B	1405.0	152.50	33.7	181.1	154.4
Ba	5148.9	3105.1	6342.8	2253.0	1594.6
Ca	318,648.5	336,504.5	9304.7	38,475.1	30,486.7
Cu	624.8	73.68	10,706.1	288.1	232.7
Fe	123,506.6	12,461.29	1743.4	26,381.2	14863.2
Ga	192.1	129.0	247.5	92.4	75.7
Mg	98,596.8	10,321.0	2263.4	7155.0	4406.8
Mn	2391.3	262.85	63.2	828.6	365.1
Se	3248.3	3277.0	701.5	660.3	2140.0
V	34.6	30.2	67.6	95.9	105.1
K	3854.0	176.9	622.2	1888.8	1561.7
Na	9908.2	797.7	4221.1	2978.5	1110.0

Ash 1: Hambach lignite coal's ash.
Ash 2: Hambach lignite char's ash.
Ash 3: Activated carbon's ash.
Ash 4: US bituminous coal's ash.
Ash 5: Taldinski bituminous coal's ash.

2.4. Copper oxide impregnated on alumina preparation

A solution containing 762 g $Cu(NO_3)_2 \cdot 2.5H_2O$ and 400 g $Al(NO_3)_3 \cdot 9H_2O$ was made up in 200 cm^3 of deionised water at 318 K, at which temperature the whole of the copper nitrate was just soluble. This solution was added, with stirring, to a tapped volume of alumina trilobes of 1400 cm^3 (JM plc., Orchard Road, Royston, UK, Product Code 110010A, 1.2 mm nominal diameter). It was then sieved to a size range of 600–1190 μm by maintaining the temperature above 313 K throughout the sieving process to avoid crystallisation of the copper nitrate from the solution. The slurry was then allowed to stand for 18 h at 335 K, with care being taken to prevent evaporative losses. At the end of this period, it was found that the alumina trilobes had absorbed all of the solution without any excess liquid remaining. The resulting material was transferred to a large evaporating basin and dried for 19 h at 423 K. This temperature was chosen such that copper nitrate does not decompose. Finally, the solids were calcined at 1098 K by feeding them at rate of 2.5 $g\ min^{-1}$ to the electrically heated fluidised bed. The low rate of feeding of solids was necessary to avoid excessive off-gas concentrations of NO_2 formed during the decomposition of the nitrates. For the calcination, the bed initially contained 215 g pure alumina sand (mean diameter 0.46 mm, about 100 cm^3 at incipient fluidisation) and the bed was fluidised by 500 $cm^3\ s^{-1}$ measured at 293 K and atmospheric pressure. The tapped, bulk density of the final oxygen carrier was 1450 $kg\ m^{-3}$ with a skeletal density of about 2550 $kg\ m^{-3}$. The bed was fluidised with 470 $cm^3\ s^{-1}$ air, as measured at 293 K and atmospheric pressure, to reduce all compounds present to their oxides. This mode of preparation gave a robust carrier containing 21 wt% CuO, based on the quantitative masses of materials used in its preparation (Dennis and Scott, 2010).

2.5. Morphological and chemical characterisation

After looping experiments, attempts were made to separate the oxygen carrier particles from the ash particles with Micromeritics' Particle Insight Dynamic Image Analyser/Particle Shape Analyser. This instrument has the ability to separate a sample population into individual particles thereby allowing the user to single out whether a particular particle is the oxygen carrier or ash based on the circularity and smoothness of the particle. Initial attempts were carried out to separate the copper oxide particles from the ash particles. One of the attempts include visualising the particles with Particle Insight (Micromeritics) and trying to single them out according to the smoothness and circularity of these particles.

X-ray diffraction (XRD) and BET surface area of the fresh and reacted oxygen carrier particles were conducted with Phillips X'Pert and Micromeritics' Tristar II 3020, respectively. Scanning electron microscope images of the particle morphology were taken with Phillips XL-20 SEM.

The chemical composition of the fresh and reacted oxygen carrier particles were analysed using inductive coupled plasma-mass spectrometry (ICP-MS) on PerkinElmer ELAN DRC II. The samples were prepared via an open digestion whereby the solid samples were digested in 20% nitric acid (HNO_3) at 80 °C for 12 h, diluted before running them through ICP-MS.

3. Results and discussion

3.1. Iron oxide

Fig. 2 shows two successive reaction cycles between iron oxide and Taldinski bituminous coal. It can be seen that at the beginning of the reduction period, only a small amount of bituminous

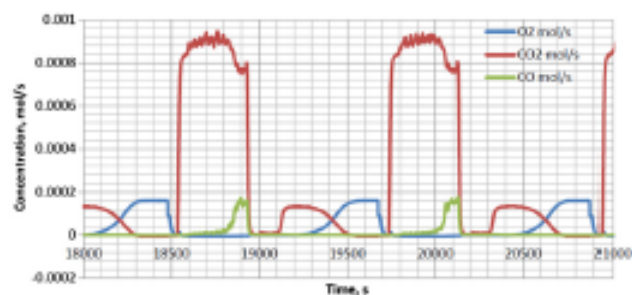


Fig. 2. Exit gas profile for 2 reaction cycles between iron oxide and Taldinski bituminous coal.

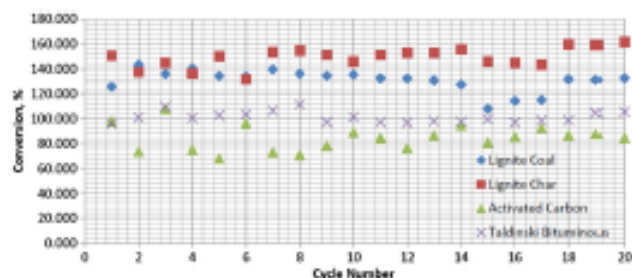


Fig. 3. Iron oxide conversion for different fuels system during reduction.

coal is being converted to carbon dioxide due to the small feeding rate. However, after a few minutes of continuous feeding, a sharp increase in the concentration of carbon dioxide is observed. This increase coincides with the formation of carbon monoxide and this observation continues until a carbon monoxide breakthrough (sharp increase in the concentration of carbon monoxide) is observed which sharply decrease the concentration of carbon dioxide from the bed. Carbon monoxide liberated is believed to be due to the formation of char in the bed as a result of the incomplete oxidation of fuel via pyrolysis. This will occur when there is insufficient amount of oxygen available in the system for complete combustion to occur.

Carbon monoxide breakthrough is believed to be due to fact that the reverse Boudouard reaction, i.e. $\text{CO}_2 + \text{C} \rightarrow 2\text{CO}$, became the dominant reaction towards the end of the reduction period. This is believed to occur when most of the Fe_2O_3 in the bed has been converted into Fe_3O_4 . However, the conversion of Fe_3O_4 to FeO is believed to be thermodynamically non-feasible unless the ratio between the partial pressure of carbon dioxide and the partial pressure of carbon monoxide, $p_{\text{CO}_2}/p_{\text{CO}}$ in the bed falls below 2 (Bohn et al., 2008). As a result, it is believed carbon dioxide fed into the bed might have reacted with the fuel to form carbon monoxide via the reaction stated above.

During the initial oxidation stage, very small amount of oxygen or carbon dioxide was detected even though the temperature in the fluidised bed increases rapidly during the initial oxidation period. This is because most of the oxygen introduced into the bed during this period is spent to reoxidise the reduced iron oxide (FeO and Fe_3O_4) Fe_2O_3 and Fe_2O_3 to and that the oxidation of the reduced iron oxide is an exothermic process. It also indicates that reduced iron oxide (FeO and Fe_3O_4) is more reactive and has a higher affinity for oxygen compared to the unburned char. The unburned char will then combust with

oxygen introduced into the bed once most of the reduced iron oxide has been reoxidised. This causes the delay in the increase in the concentration of carbon dioxide during the oxidation period. This was then followed by a sharp increase in the concentration of oxygen till it reached equilibrium.

3.2. Iron oxide conversion analysis

Fig. 3 shows the percentage of Fe_2O_3 converted Fe_3O_4 during the reduction period while Fig. 4 shows the percentage of Fe_3O_4 oxidised back into Fe_2O_3 . It can be deduced from both figures that the percentage of iron oxide being converted during reduction and oxidation follows a similar pattern as the fuel feeding rate (Fig. 5) where a higher feeding rate produces a higher iron oxide conversion ratio and vice versa. This is true for all cases except for the case with activated carbon. For the case with activated carbon, iron oxide conversion oscillates till it reaches a stable value towards the end of the experimental run.

The conversion of Fe_3O_4 to FeO was believed to be thermodynamically non-feasible in these experiments. As a result, it was believed that the conversion of over 100% of Fe_2O_3 to Fe_3O_4 could have been caused by the reverse Boudouard reaction but was instead being attributed to the conversion of Fe_3O_4 to FeO . However, due to the conversion of more than 120% seen for cases with lignite coal and lignite char, it is believed that there is a possibility that Fe_3O_4 might have converted to FeO towards the end of the reduction period.

3.3. Copper oxide

Fig. 6 shows two successive reaction cycles between copper oxide and lignite coal. It can be seen that oxygen is released during the initial stage of feeding. This occurs due to the low partial pressure of oxygen in the bed thereby allowing copper (II)

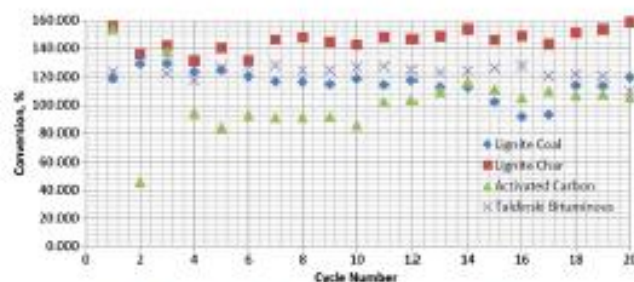


Fig. 4. Iron oxide conversion for different fuel systems during oxidation.

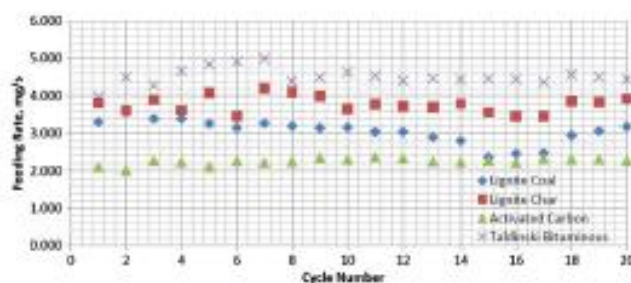


Fig. 5. Feeding rates for the different types of fuels for the iron oxide system.

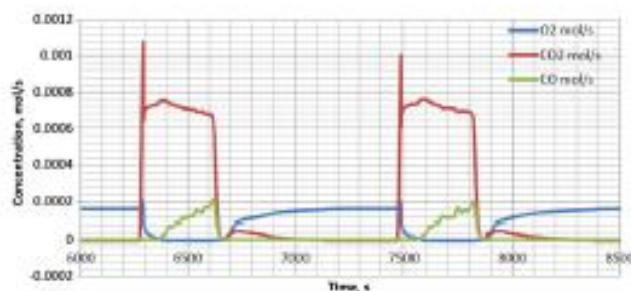


Fig. 6. Exit gas profile for 2 reaction cycles between copper oxide and lignite char.

oxide to decompose into copper (I) oxide and possibly to copper during that initial period of time. Calculations indicated that between 10% and 14% of the oxygen from copper oxide is released during this period.

This indicates that there are two possible reaction mechanisms occurring in the bed during the feeding period. The first mechanism is via the gas–solid interaction. This is due to the fact that the decomposition of copper (II) oxide to copper (I) oxide occur till all copper (II) oxide has been converted to its lower oxidation form due to the low partial pressure of oxygen in the bed. As a result, the oxygen released via the decomposition of copper oxide reacts with lignite coal which is fed into the bed. The second mechanism is via direct reaction between copper oxide and lignite coal. As a result the initial carbon dioxide released is due to the faster first mechanism while carbon dioxide and carbon monoxide releases in the later stages are due to the second mechanism.

The figure also shows that carbon monoxide is formed as soon as the concentration of oxygen falls to zero indicating that the amount of oxygen available in the bed is insufficient to achieve complete combustion. As a result, some of the fuel fed into the bed will only be partially oxidised via pyrolysis. Similar reduction stage phenomenon was observed for lignite char. However for the case with activated carbon, the concentration of carbon dioxide released from the reaction is constant throughout the cycle indicating that activated carbon is not as reactive when compared to lignite coal and lignite char.

During the oxidation stage, a sharp increase in oxygen was observed during the initial oxidation period followed by a gradual increase in the concentration of oxygen till equilibrium was reached. This is in sharp contrast to cases with iron oxide whereby a sharp increase is observed a few minutes after air is introduced into the bed and reaches equilibrium within a short period of time after that.

The sharp increase in the concentration of oxygen during the initial oxidation stage can be attributed to 3 factors. The first is due to the fact that most of the fuel fed into the bed has been fully combusted or partially oxidised via pyrolysis. Pyrolysis of fuel creates char which is less reactive thereby requiring a longer period of time for the combustion to proceed to completion. As a result, the initial sharp increase in the concentration of carbon dioxide seen in cases with lignite char and activated carbon can be attributed to the unreacted fuel. Carbon dioxide released during the later stages of the oxidation period can be attributed to the unreacted char. The second factor is due to the fact that an equilibrium oxygen partial pressure would need to be achieved before copper and copper (I) oxide react with oxygen in air to form copper (II) oxide. Finally, alumina which is present as a support in copper oxide causes the copper oxide particles to be more stable and have a lower affinity for oxygen. The second and third factor is believed to be the cause for the longer time required for complete oxidation.

Sharp spike in the concentration of CO_2 during the initial period of feeding was observed for cases with lignite coal. This could be due to rapid decomposition of the copper oxide particles to balance off the sudden drop in the partial pressure of oxygen in the reactor. The rapid increase in the concentration of oxygen released during this time could have reacted with the lignite coal. This is believed to occur till equilibrium in the partial pressure of oxygen in the reactor is achieved. It was noted that there was an increase in the temperature of the bed during the initial oxidation period and this is associated with the burning off of the carbon inventory in the bed. Fluctuations in mole fractions of CO_2 and CO during the feeding period are attributed to the unsteady state feeding of the coal screw feeder.

3.4. Copper oxide conversion

Fig. 7 shows the percentage of CuO is converted to Cu during the reduction period while Fig. 8 shows the percentage of Cu which is oxidised back into CuO . It can be deduced from both figures that the

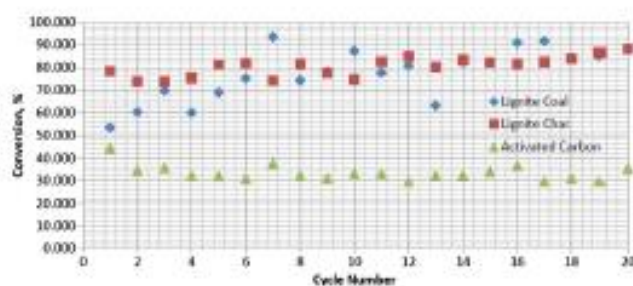


Fig. 7. Copper oxide conversion for different fuels system during reduction.

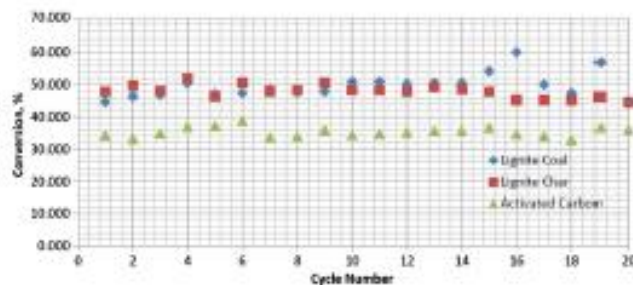


Fig. 8. Copper oxide conversion for different fuels system during oxidation.

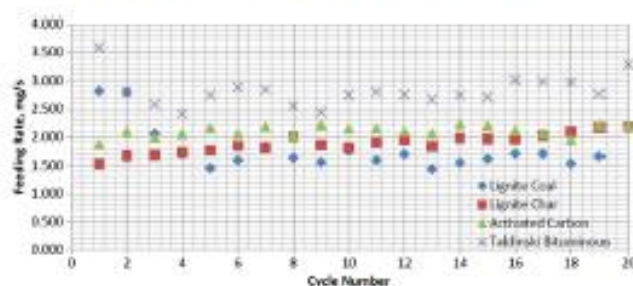


Fig. 9. Feeding rates for the different types of fuels for the copper oxide systems.

percentage of copper oxide being converted during reduction and oxidation follows a similar pattern as the fuel feeding rate (Fig. 9), where a higher feeding rate produces a higher copper oxide conversion ratio and vice versa. This is true for all cases except for the case with lignite coal. Besides that, it is also noted that the amount of copper oxide converted during oxidation is quite similar for the case with activated carbon but differs significantly for cases with lignite coal and lignite char. As alumina is an inert compound which does not react with fuel and is very difficult to decompose, it is believed that the difference is mainly due to the error involved

in the gas analyses. This error is believed to have occurred during the initial feeding period as a sharp increase in the concentration of oxygen was observed for cases with lignite coal and lignite char but not observed in the case with activated carbon. Since the conversion of copper oxide during reduction is calculated based on the sum of amount of copper oxide which is decomposed during the initial feeding period and the amount of copper oxide which reacts with fuel fed into the bed, this phenomenon will thereby increase the estimated conversion of copper oxide during reduction.

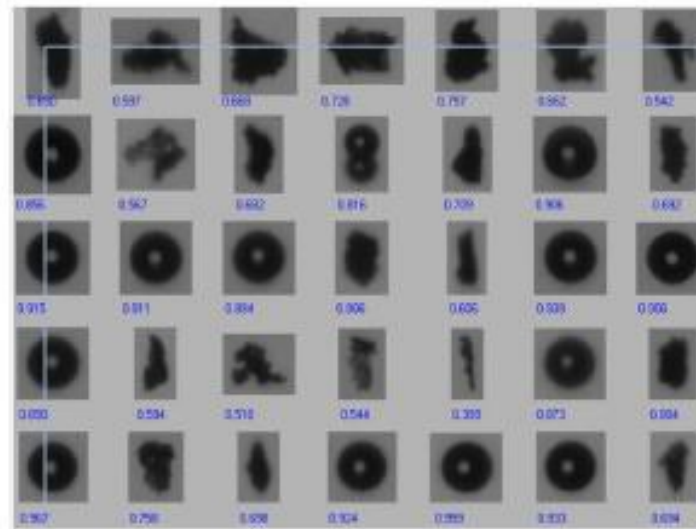


Fig. 10. Reacted copper oxide particle smoothness.

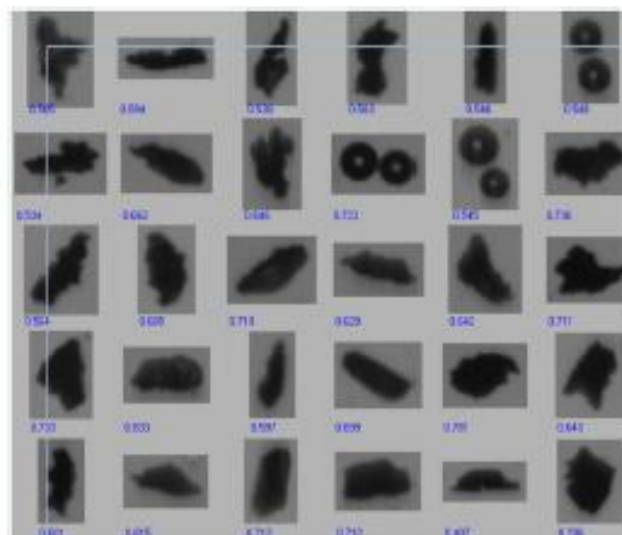


Fig. 11. Reacted copper oxide particle circularity.

3.5 Copper oxide separation from ash

Figs. 10 and 11 present the smoothness and circularity analysis of copper oxide particles by using Particle Insight. It was found that copper oxide comes in a variety of shapes thereby making it difficult to single them out for separation from the rest of the sample. Besides that, it was believed that particles which demonstrated a 'donut' like shape are air bubbles due to the fact that all particles with smoothness and circularity of above 0.8 demonstrate this feature. Besides that, scanning electron microscope images suggest that the copper oxide particles comes in various shapes and none of them indicate that they have a circular shape. As a result, the proceeding particle analyses were conducted without any sort of ash separations from the oxygen carrier particles.

3.6 Crystal structure of oxygen carriers

Fig. 12 shows the X-ray diffraction (XRD) analysis for both the fresh and reacted iron oxide particles. XRD analysis showed that iron oxide reduced during the continuous feeding stage was reoxidised back to its original form during the oxidation stage. However, minor traces of impurities such as silicon dioxide (SiO_2) were found on some of these particles (I5 and I11) indicating that SiO_2 from the ash or fuel particles deposited onto the surface of the iron oxide particles. It was also found that SiO_2 can react with iron oxide to form fayalite (FeSiO_3) as seen I1. However, SiO_2 and FeSiO_3 impurities detected on these particles did not affect the reactivity of the iron oxide particles throughout the experiment. This could be due to the fact that they appear in small quantities thereby their effect on the reactivity of the iron oxide particles could not be detected over a small number of redox cycle.

Fig. 13 shows the X-ray diffraction (XRD) analysis for the fresh and reacted copper oxide particles. XRD analysis shows that the copper (II) oxide which was reduced into copper (I) oxide and copper during the reduction period was reoxidised back to its original form during the oxidation stage. However, it was found that some of the copper oxide reacted with its support, alumina, during preparation to form copper aluminium oxide (CuAl_2O_4). It was also found that the interaction between the oxygen carrier and its support continued throughout the experimental run. This was highlighted by the detection of a different form of copper aluminium oxide (CuAl_2O_4). Minor traces of impurities such as silicon dioxide (SiO_2) were found on some of the particles

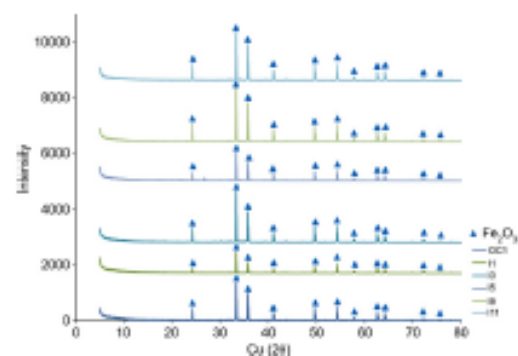


Fig. 12. X-ray diffraction analysis of fresh and reacted iron oxide particles. Note: OC1: Fresh iron oxide particles, I1: Iron oxide with Hambach lignite coal after 20 redox cycles, I3: Iron oxide with Hambach lignite char after 20 redox cycles, I5: Iron oxide with activated carbon after 20 redox cycles, I9: Iron oxide with US bituminous after 20 redox cycles, I11: Iron oxide with Taldinski bituminous coal after 20 redox cycles.

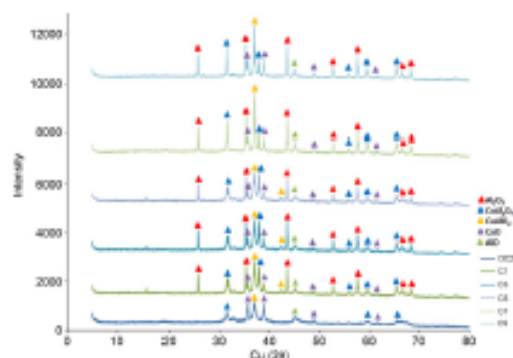


Fig. 13. X-ray diffraction analysis of fresh and reacted copper oxide particles. Note: OC2: Fresh copper oxide particles, C1: Copper oxide with Hambach lignite coal after 20 redox cycles, C3: Copper oxide with Hambach lignite char after 20 redox cycles, C5: Copper oxide with activated carbon after 20 redox cycles, C7: Copper oxide with US bituminous after 20 redox cycles, C9: Copper oxide with Taldinski bituminous coal after 20 redox cycles.

Table 3
BET surface area of the iron oxide particles.

Sample	BET surface area (m^2/g)
OC1	1.2
I1	0.3
I3	0.3
I5	0.5
I9	0.6
I11	0.3

OC1: Fresh iron oxide particles.

I1: Iron oxide with Hambach lignite coal after 20 redox cycles.

I3: Iron oxide with Hambach lignite char after 20 redox cycles.

I5: Iron oxide with activated carbon after 20 redox cycles.

I9: Iron oxide with US bituminous after 20 redox cycles.

I11: Iron oxide with Taldinski bituminous coal after 20 redox cycles.

indicating that SiO_2 from the ash or fuel interacted with the copper oxide particles. However, it was found that SiO_2 did not react with the copper oxide particles as found in cases with iron oxide. The impurities were found to have no effect on the reactivity of the copper oxide particles as only a very small amount of them were detected. The formation of copper aluminium oxide (CuAl_2O_4) did not seem to have an effect on the reactivity of the copper oxide particles over successive reduction oxidation cycles even though it has been reported in the literature that the formation of copper aluminate complexes reduces the amount of oxygen available for combustion (Abad et al., 2006; de Diego et al., 2005).

Thermodynamics studies conducted by Jacob and Alcock (1975) and Gadalla and White (1964) showed that CuAl_2O_4 and Al_2O_3 are the stable compounds for a $\text{Cu}_2\text{O}-\text{CuO}-\text{Al}_2\text{O}_3$ system for the ratio of $\text{CuO}/\text{Al}_2\text{O}_3$ used in the preparation of the particles as well as the preparation and operating temperatures used in this study.

3.7. Surface area and pore structure of oxygen carriers

Tables 3 and 4 show the BET surface area for the fresh and reacted iron oxide and copper oxide particles. As shown in both tables, the BET surface area of the reacted particles decreased by more than 50% of their original value for all cases. The decrease in the surface area may be caused by sintering. Sintering occurs

Table 4
BET surface area of the copper oxide particles.

Sample	BET surface area (m^2/g)
OC2	899
C1	327
C1	301
C5	324
C7	215
C9	215

OC2: Fresh copper oxide particles.
 C1: Copper oxide with Harbach lignite coal after 20 redox cycles.
 C5: Copper oxide with Harbach lignite char after 20 redox cycles.
 C7: Copper oxide with activated carbon after 20 redox cycles.
 C9: Copper oxide with Taldinski bituminous coal after 20 redox cycles.

because the surface of the particles is in a region with high energy. As a result, atoms on the surface of the particles will thermodynamically try to minimise this energy by merging these atoms to form fewer bigger atoms (Bowker, 1998). Sintering causes both the specific surface area and the porosity to decrease while increasing the density of the particles as well as improving surface coordination (Bowker, 1998).

The reduction in BET surface area of the particles while the particles are able to achieve identical conversion ratio during the successive redox cycles can be explained via the unreacted shrinking core model. The model suggests that during the initial reaction stage, carbon from fuels will react with the surface iron oxide. As the reaction proceeds, carbon reacts with iron oxide deeper in the particle but the reaction does not penetrate into the core of the iron oxide particles. As a result, when the reduced iron

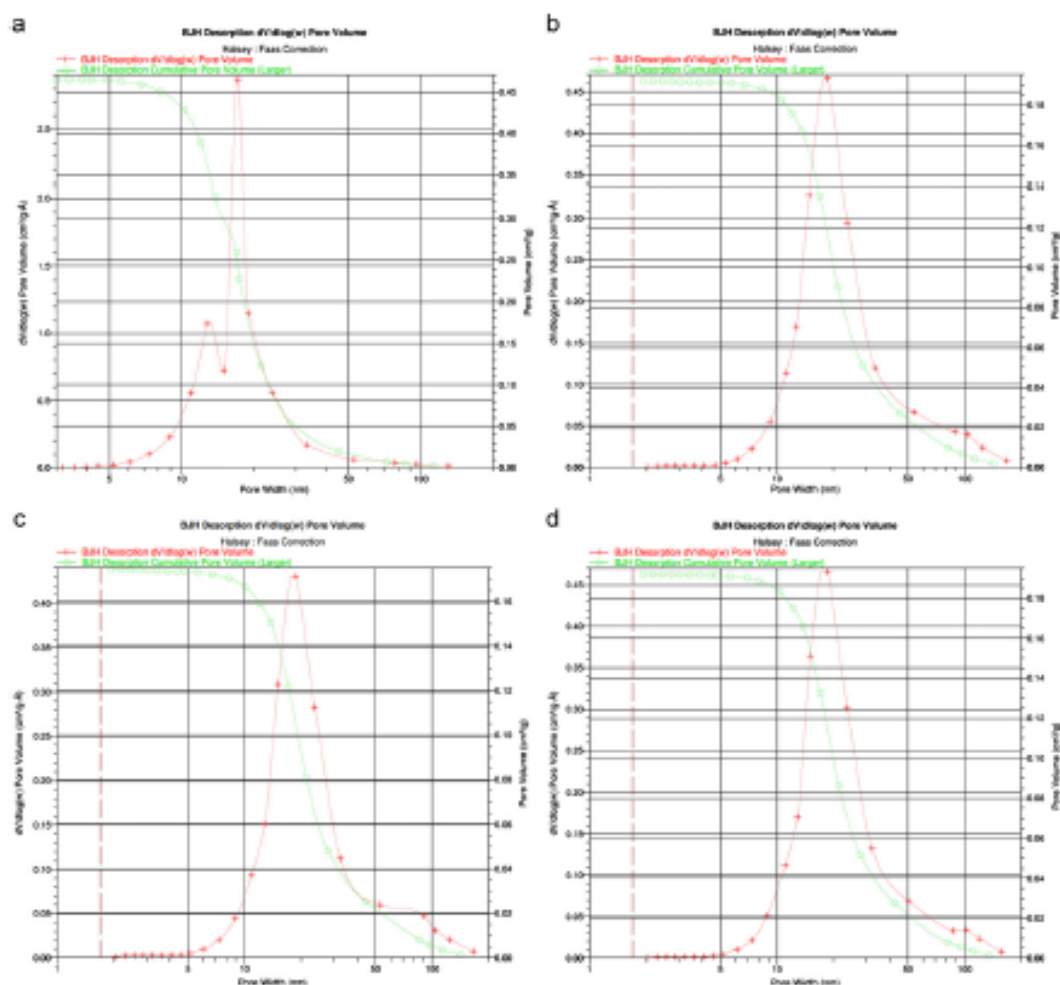


Fig. 14. (a) BJH analysis for fresh copper oxide particles, (b) BJH analysis for copper oxide particles reacted with lignite coal, (c) BJH analysis for copper oxide particles reacted with lignite char, (d) BJH analysis for copper oxide particles reacted with activated carbon.

oxide particles are regenerated, it is possible that the pores in the core of the particles are completely closed when the inner iron atoms react with oxygen whereas pores in the regenerated layer remain almost unchanged. This will thus create the effect that the reaction and conversion ratios remain almost identical even though the surface area decreases during successive reduction oxidation cycles.

Fig. 14a–d show the BJH analysis for the fresh and reacted copper oxide particles. As shown in the figure that the majority of the pores lie in the range of 10–25 nm and 15–35 nm for the fresh and reacted particles, respectively. This indicates that the pores on the copper oxide particles became larger after 20 reaction cycles.

Even though the pore size of the reacted particles became larger, it was found that the pore volume of the reacted particles was smaller compared to the fresh particles. It was deduced that this could be due to the fact that closed pores were created around the core of the particles when the inner copper atom reacts with oxygen in the particles. As a result, this will decrease the amount of adsorbate being adsorbed, which will reduce the total pore volume of the particles. In addition, the decrease in pore volume explains the decrease in the BET surface area of the reacted particles. The number of open pores became lesser as the experiment progresses thereby reducing BET surface area of the particles. However, the enlargement of pore size makes the gaseous reactants more easily diffuse into the copper oxides and get oxidised. This cancelled out the negative effect of surface area reduction on the reactivity of the particles. As a result, similar conversion ratio and rate of reaction was observed throughout the 20 cycles.

3.8 Morphology of oxygen carriers

Fig. 15 shows the images obtained from scanning electron microscope for the iron oxide particles. As shown in Fig. 15a, the fresh iron oxide particle displayed a smooth surface while particles after multiple oxidation and reduction cycles (Fig. 15b)

displayed a surface that had undergone attrition during the experiment. Attrition in these experiments is caused mainly by interactions between: (i) the carriers, (ii) the carriers and fuel fed into the bed and (iii) the carriers and the wall of the fluidised bed. As a result, large cracks can be seen on the surface of these particles. Besides, some particles demonstrated a layer of coating on the iron oxide particles (Fig. 15c). This phenomenon is confirmed in whereby a number of orange particles were observed via the stereo microscope. As the occurrences of these particles are in a very small number, it was deduced that this phenomenon occurred towards the end of the feeding period when Fe_2O_3 was converted into FeO. This layer is believed to be made of fused carbon or ash due to the fact that it has a rather smooth surface with no indication of pores on its surface as shown in Fig. 16. However, XRD analysis did not detect carbon on these samples indicating that this could be due to the fact that the amount of carbon is very small which makes it difficult

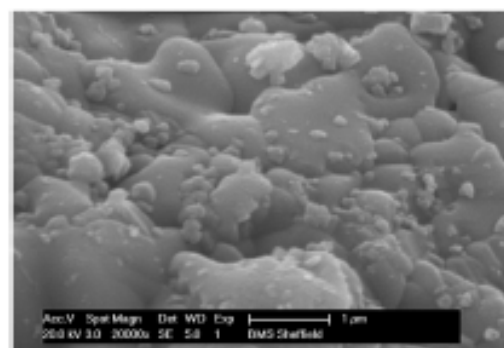


Fig. 16. SEM image of coated layer on iron oxide particles.

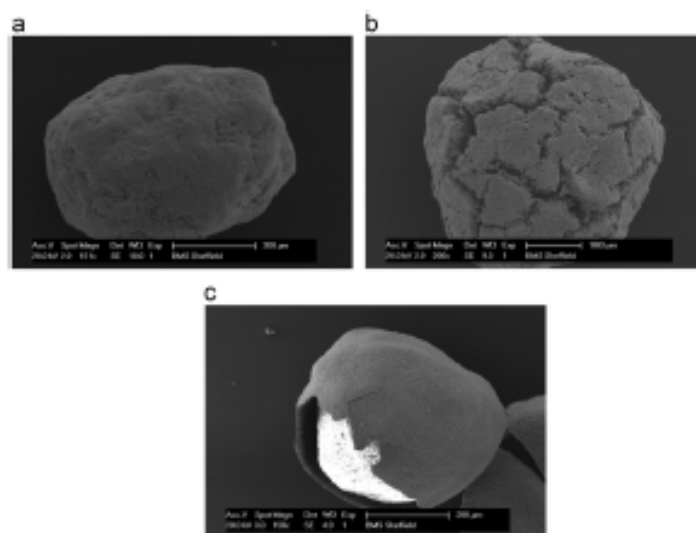


Fig. 15. SEM images of fresh and reacted iron oxide particles. (a) Fresh iron oxide particles, (b) iron oxide with Harbach lignite coal after 20 redox cycles, and (c) iron oxide with Harbach lignite char after 20 redox cycles.

to distinguish between the lesser peaks on the XRD graphs. Some of the peaks could be due to carbon but ended up being attributed to background noise. In addition, the presence of potassium, sodium and phosphate in the ash particles also causes the ash to fuse together due to the low melting points of these elements.

Fig. 17 shows the magnified surface of the fresh and reacted iron oxide particles. The images showed that the fresh iron oxide

particles have a rather polished surface. The reacted iron oxide particles have a rough surface due to impurities or the change in orientation/placement of the iron oxide particles when it undergoes multiple redox cycles. It is also shown in Fig. 17c that some of the sub-particles appeared to have swelled thereby changing the size and shape of the sub-particles. This could be due to surface melting. Surface melting on the iron oxide particles occur due to the fact that these particles have a Tammann temperature of

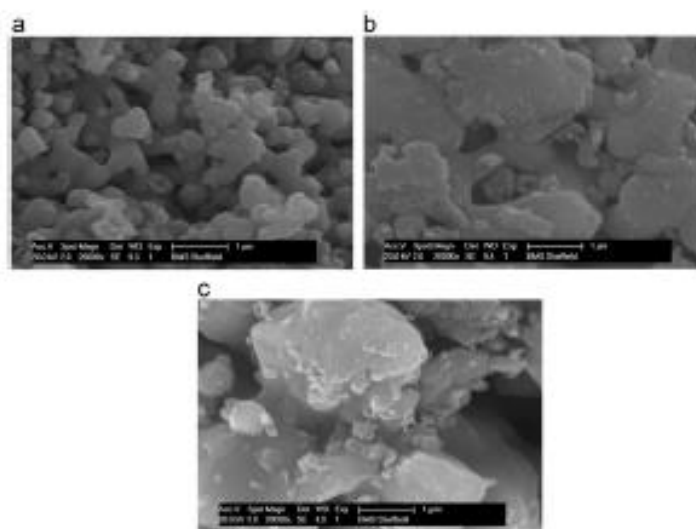


Fig. 17. SEM images of fresh and reacted iron oxide particles. (a) Fresh iron oxide particles, (b) iron oxide with Harbath lignite coal after 20 redox cycles, and (c) iron oxide with Harbath lignite coal after 20 redox cycles.

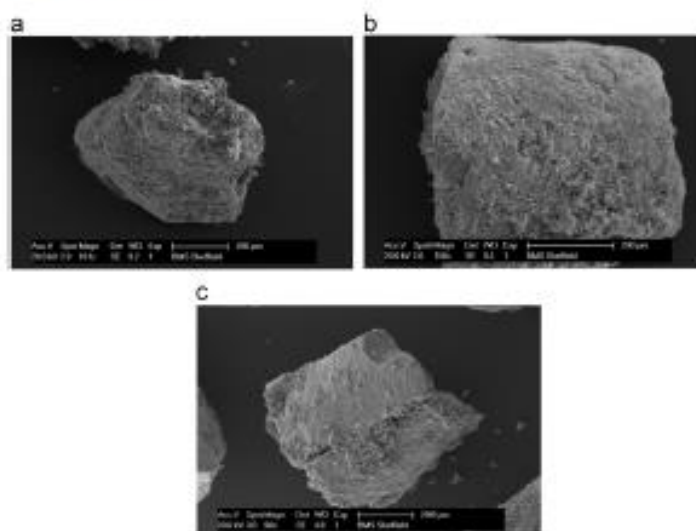


Fig. 18. SEM images of fresh and reacted copper oxide particles. (a) Fresh copper oxide particles, (b) copper oxide with Harbath lignite coal after 20 redox cycles, and (c) copper oxide with Talidimki bituminous coal after 20 redox cycles.

769 °C even though their melting point is 1538 °C (Galvita et al., 2008). This phenomenon will be discussed in the next section.

Fig. 18 shows images obtained from scanning electron microscope for the copper oxide particles. The images showed that copper oxide impregnated with alumina has a high resistance to attrition as cracks on the surface of the reacted particles were not observed. However, Fig. 18c shows that there is a possibility that agglomeration of the copper oxide particles might have occurred, as it appears to be two separate particles sticking onto one another.

Fig. 19 shows the magnified surface of the fresh and reacted copper oxide particles. The images showed that the fresh copper oxide particles have a rough surface whereas the reacted copper oxide particles have a slightly smoother surface with some impurities deposition. Some of the sub-particles appeared to have swelled thereby changing the size and shape of the sub-particles.

One possible reason for the smoothing effect on the surface of the particles is due to surface melting (Li et al., 1989). Surface melting causes a layer of metallic copper to be formed initially on the CuO surface. As a result, carbon will react with the bulk CuO through the liquid layer. SEM images taken by Sriwardane et al. (2010) showed that the CuO surface became smoother when the C/CuO samples are heated to various temperatures in nitrogen due to melting of copper at 500–700 °C. Besides, they observed melted copper particles adhered to carbon particles at 600 °C. Even though copper has a melting point of 1080 °C, it has a Tammann temperature of 405 °C. Li et al. (1989) observed surface melting at a temperature lower than the melting temperature of the bulk thereby indicating that carbon might have reacted with the bulk CuO through the liquid copper layer. Carbon may also react with oxygen diffused out from the bulk CuO to the surface

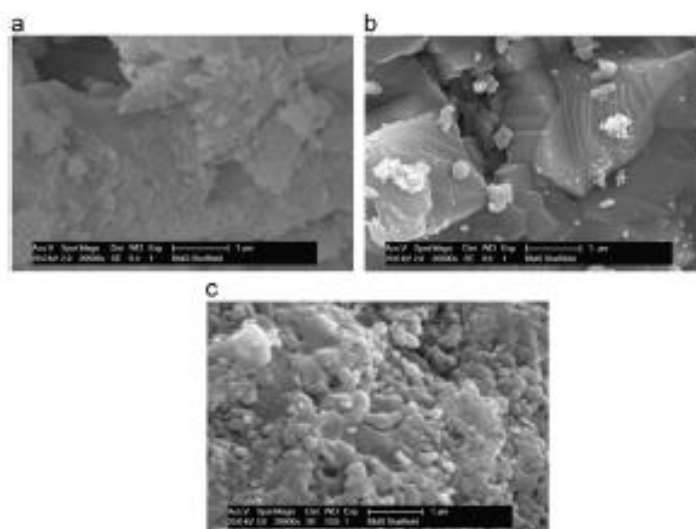


Fig. 19. SEM images of fresh and reacted copper oxide particles. (a) Fresh copper oxide particles, (b) copper oxide with Harbath lignite coal after 20 redox cycles, and (c) copper oxide with Harbath lignite char after 20 redox cycles.

Table 5
ICP-MS of fresh and reacted iron oxide particles.

Element	OC1 (mg/kg)	I1 (mg/kg)	I3 (mg/kg)	I5 (mg/kg)	I9 (mg/kg)	I11 (mg/kg)
Al	170.2	721.1	141.1	203.1	494.4	848.3
Si	1.0	29.5	78.4	209.7	73.2	33.8
Ca	21.7	468.0	590.0	802.9	753.3	109.8
Cr	13.2	4.69	746.3	3.8	8.6	2.2
Cu	42.88	1.423	51.6	23.3	64.6	46.5
Fe	57391.03	132096	45.952.2	9509.4	18805.8	11,115.3
Mg	19.8	5.145	220.72	12.46	78.1	106.4
Mn	13.435	518.0	949.8	11.1	115.2	21.1
Mo	2.7	535.7	174.31	139.3	20.3	11.8
Ni	91.6	4.444	162.12	10.62	23.1	34.2

OC1: Fresh iron oxide particles.

I1: Iron oxide with Harbath lignite coal after 20 redox cycles.

I3: Iron oxide with Harbath lignite char after 20 redox cycles.

I5: Iron oxide with activated carbon after 20 redox cycles.

I9: Iron oxide with US bituminous coal after 20 redox cycles.

I11: Iron oxide with Taldinski bituminous coal after 20 redox cycles.

Table 6
ICP-MS of fresh and reacted copper oxide particles.

Element	OC2 (mg/kg)	C1 (mg/kg)	C3 (mg/kg)	C5 (mg/kg)	C7 (mg/kg)	C9 (mg/kg)
Al	311,160.1	164,308.5	163,481.4	2009,54.8	121,984.1	130,295.4
Ca	312.9	0.0	0.0	0.0	371.3	690.4
Cu	194,018.0	117,581.9	116,544.3	1,226,40.4	82,550.7	93,017.8
Fe	490.7	55.5	146.0	208.2	353.5	328.7
Mg	182.6	138.7	197.2	163.7	373.3	308.4

OC2: Fresh copper oxide particles.
C1: Copper oxide with Hambach lignite coal after 20 redox cycles.
C3: Copper oxide with Hambach lignite char after 20 redox cycles.
C5: Copper oxide with activated carbon after 20 redox cycles.
C7: Copper oxide with US bituminous after 20 redox cycles.
C9: Copper oxide with Taldinski bituminous coal after 20 redox cycles.

layers containing Cu_2O with relatively low activation energy (Cheng and Berry, 1992).

3.9. Chemical composition of oxygen carriers

Tables 5 and 6 show the inductive coupled plasma mass spectrometry (ICP-MS) analysis of fresh and reacted iron and copper oxide particles after 20 reduction–oxidation cycles. XRD analysis showed that the fuel and ash particles had very minor effects on the oxygen carriers. However, it was noticed from the ICP-MS analysis that the concentration of key metal elements such as copper, iron and alumina in these particles decreased quite significantly after 20 reduction–oxidation cycles. Part of this can be attributed to errors involved when reading the off-peak data of the key elements. It was also found that the total concentration of the metal elements decreased after 20 reduction–oxidation cycles. As 0.1 g of each sample was used in the ICP-MS analysis, this suggests that the concentration of non-metal impurities such as carbon, silicon, fluorine, chlorine and oxygen have increased and that they could not be detected with the ICP-MS. Moreover, the increase in concentration for certain elements can be attributed to the fact that some of the ash particles deposited onto the surface of these particles.

4. Conclusions

In this paper, the iron oxide and copper oxide particles used in a chemical looping combustion system after 20 reduction–oxidation cycles with 5 different fuels, (i.e. Hambach lignite coal, Hambach lignite char, activated carbon, Taldinski bituminous coal and US bituminous coal) were investigated to characterise the changes in the crystal structure, morphology, pore structure and chemical composition.

XRD analysis on these particles showed that the reduced particles were reoxidised back to their original form with trace amounts of impurities such as silicon dioxide (SiO_2) on the iron oxide particles. Similar impurities plus copper complexes such as copper aluminate were detected on the copper oxide particles.

ICP-MS analysis on these particles revealed that the concentration of the core metal elements (iron, copper and alumina) decreased after 20 reaction cycles which in turn decreased the total concentration of the metal elements in the particles.

BET surface area analysis on these particles indicated that the total surface area of these particles decreased by more than 50% of their original values. The copper oxide particles showed that the total pore volume of the particles decreased after 20 reaction cycles whereas the pore sizes of the particles increased slightly.

SEM images of the reacted iron oxide particles showed that some of these particles were coated with a layer of fused ash or carbon during reduction and that the iron oxide particles have undergone

quite severe attrition during the experiment. The alumina support impregnated onto the copper oxide particles increases its resistance to attrition. However, some of these particles showed signs of agglomeration due to the high operating temperature.

Further research efforts are needed to investigate the effects of properties changes on the oxygen carrier deactivation behaviour by running the experiments over a larger number of reduction–oxidation cycles.

Acknowledgements

The authors would like to acknowledge the Engineering and Physical Sciences and Research Council (EPSRC) for financial support.

References

- Ahad, A., Mattsson, T., Lyngfelt, A., Rydén, M., 2006. Chemical-looping combustion in a 300 W continuously operating reactor system using a manganese-based oxygen carrier. *Fuel* 85 (9), 1174–1185.
- Adriano, J., de Diego, L.F., García-Labiano, F., Gayán, P., Abad, A., Palacios, J.M., 2004. Selection of oxygen carriers for chemical-looping combustion. *Energy Fuels* 18 (2), 371–377.
- Adriano, J., Gayán, P., Gelaya, J., de Diego, L.F., García-Labiano, F., Abad, A., 2006. Chemical looping combustion in a 10 kW_{th} prototype using a CuO/NiO oxygen carrier: effect of operating conditions on methane combustion. *Ind. Eng. Chem. Res.* 45 (17), 6075–6080.
- Bergstrand, N., Lyngfelt, A., 2008. The use of petroleum coke as fuel in a 10 kW_{th} chemical-looping combustor. *Int. J. Greenhouse Gas Control* 2 (2), 169–179.
- Behr, C., Müller, C., Clifton, J.P., Hayhurst, A.N., Davidson, J.F., Scott, S.A., Dennis, J.S., 2008. Production of very pure hydrogen with simultaneous capture of carbon dioxide using the redox reactions of iron oxides in packed beds. *Ind. Eng. Chem. Res.* 47 (20), 7623–7630.
- Bowker, M., 1988. *The Basic and Applications of Heterogeneous Catalysis*. Oxford University Press, New York, United States.
- Brown, T.A., Dennis, J.S., Scott, S.A., Davidson, J.F., Hayhurst, A.N., 2010. Gasification and chemical-looping combustion of a lignite char in a fluidised bed of iron oxide. *Energy Fuels* 24 (5), 3034–3048.
- Cheng, H.P., Berry, R.S., 1992. Surface melting of dusts and implications in bulk matter. *Phys. Rev. A* 45 (11), 7989–7993.
- Cho, P., Mattsson, T., Lyngfelt, A., 2004. Comparison of iron-, nickel-, copper-, and manganese-based oxygen carriers for chemical-looping combustion. *Fuel* 83 (9), 1215–1225.
- Copeland, R.J., Alptekin, G., Gosato, M., Gombanovich, Y., 2002. Sorbent energy transfer system (SETS) for CO_2 separation with high efficiency. In: Proceedings of the 27th International Technical Conference on Coal Utilization & Fuel Systems, Clearwater, Florida, USA.
- Corbella, B.M., de Diego, L.F., García-Labiano, F., Adriano, J., Palacios, J.M., 2005a. The performance in a fluid bed reactor of copper-based oxides on titanite as oxygen carriers for chemical looping combustion of methane. *Energy Fuels* 19 (2), 433–441.
- Corbella, B.M., de Diego, L.F., García-Labiano, F., Adriano, J., Palacios, J.M., 2005b. Characterization study and five-cycle tests in a fluid-bed reactor of titanite-supported nickel oxide as oxygen carriers for the chemical-looping combustion of methane. *Environ. Sci. Technol.* 39 (15), 5736–5803.
- de Diego, L.F., García-Labiano, F., Adriano, J., Gayán, P., Abad, A., Corbella, B.M., Palacios, J.M., 2004. Development of Cu-based oxygen carriers for chemical-looping combustion. *Fuel* 83 (13), 1749–1757.

- de Diego, L.F., Gayán, P., García-Labiano, F., Celaya, J., Abad, A., Adánez, J., 2005. Impregnated CuO/Al₂O₃ oxygen carrier for chemical-looping combustion: avoiding fluidized bed agglomeration. *Energy Fuels* 19 (5), 1850–1856.
- Demko, J.S., Scott, S.A., 2010. In situ gasification of a lignite coal and CO₂ separation using chemical looping with a Cu-based oxygen carrier. *Fuel* 89 (7), 1623–1640.
- EIA, 2010. International Energy Outlook 2010.
- Figueroa, J.D., Foust, T., Flayhugi, S., Medvedev, H., Srivastava, R.D., 2008. Advances in CO₂ capture technology—The U.S. Department of Energy's Carbon Sequestration Program. *Int. J. Greenhouse Gas Control* 2 (1), 9–20.
- Gadella, A.M.M., White, J., 1964. Equilibrium relationships in the system CuO–Cu₂O–Al₂O₃. *Trans. Br. Ceram. Soc.* 63 (1), 39–52.
- Galvis, V., Hessel, P., Lorenz, H., Böker, R., Mackensen, L.K., Sandmacher, K., 2008. Deactivation of modified iron oxide materials in the cyclic water gas shift process for CO-free hydrogen production. *Ind. Eng. Chem. Res.* 47 (2), 303–310.
- García-Labiano, F., Adánez, J., de Diego, L.F., Gayán, P., Abad, A., 2006. Effect of pressure on the behavior of copper-, iron-, and nickel-based oxygen carrier for chemical-looping combustion. *Energy Fuels* 20 (1), 25–33.
- International Energy Agency (IEA), 2007. World Energy Outlook 2006. Organization for Economic Co-operation and Development, Paris.
- Inhida, M., Jin, H., 1996. A novel chemical-looping combustor without NO_x formation. *Ind. Eng. Chem. Res.* 35 (7), 2469–2472.
- Inhida, M., Zheng, D., Aohata, T., 1987. Evaluation of a chemical-looping-combustion power-generation system by graphic energy analysis. *Energy* 12 (2), 147–154.
- Jacob, K.T., Alcock, C.B., 1975. Thermodynamics of CuAD₂ and CuAl₂O₄ and phase equilibria in the system Cu₂O–CuO–Al₂O₃. *J. Am. Ceram. Soc.* 58 (5–6), 192–195.
- Leino, H., Lyngfelt, A., Johansson, M., Jorndal, E., Mattsson, T., 2008. The use of ilmenite as an oxygen carrier in chemical-looping combustion. *Chem. Eng. Res. Design* 86 (9), 1017–1025.
- Leino, H., Lanting, Y., Bakken, E., Brudeen, R., Mattsson, T., Lyngfelt, A., 2009a. Use of CaMn_{0.25}Fe_{0.125}O₃ as oxygen carrier in chemical-looping with oxygen uncoupling. *Energy Fuels* 23 (10), 5276–5283.
- Leino, H., Mattsson, T., Lyngfelt, A., 2009b. Using chemical-looping with oxygen uncoupling (CLOU) for combustion of six different solid fuels. *Energy Procedia* 1 (1), 447–453.
- Li, J., Wang, S.Q., Mayer, J.W., Tu, K.N., 1989. Oxygen-diffusion-induced phase boundary migration in copper oxide thin films. *Phys. Rev. B* 39 (16), 12367–12370.
- Lindholm, C., Abad, A., Mattsson, T., Lyngfelt, A., 2008. 160 h of chemical-looping combustion in a 10kW reactor system with a NiO-based oxygen carrier. *Int. J. Greenhouse Gas Control* 2 (4), 520–530.
- Mattsson, T., Lyngfelt, A., Cho, P., 2001. The use of iron oxide as an oxygen carrier in chemical-looping combustion of methane with inherent separation of CO₂. *Fuel* 80 (13), 1953–1962.
- Mattsson, T., Jorndal, E., Lyngfelt, A., 2003. Reactivity of some metal oxides supported on alumina with alternating air and oxygen—application of chemical-looping combustion. *Energy Fuels* 17 (3), 643–651.
- Mattsson, T., Johansson, M., Lyngfelt, A., 2004. Multicycle reduction and oxidation of different types of iron oxide particles—application to chemical-looping combustion. *Energy Fuels* 18 (3), 628–637.
- Mattsson, T., Leino, H., Lyngfelt, A., 2009a. Chemical-looping with oxygen uncoupling using CuO/ZnO with petroleum coke. *Fuel* 88 (4), 683–690.
- Mattsson, T., Lyngfelt, A., Leino, H., 2009b. Chemical-looping with oxygen uncoupling for combustion of solid fuels. *Int. J. Greenhouse Gas Control* 3 (1), 11–19.
- Richard, H.J., Knoche, K.F., 1983. Reversibility of combustion processes—efficiency and costing. *ACS Symp. Ser.* 235 (3), 71–85.
- Rydén, M., Lyngfelt, A., Mattsson, T., 2010. CaMn_{0.25}Fe_{0.125}O₃ as oxygen carrier for chemical-looping combustion with oxygen uncoupling (CLOU)—experiments in a continuously operating fluidized-bed reactor system. *Int. J. Greenhouse Gas Control*. doi:10.1016/j.ijggc.2010.08.004.
- Shalman, A., Cheverton, E., Mattsson, T., Lyngfelt, A., 2009. Manganese/iron, manganese/nickel, and manganese/dilution oxides used in chemical-looping with oxygen uncoupling (CLOU) for combustion of methane. *Energy Fuels* 23 (10), 5269–5275.
- Srivastava, R., Tian, H., Miller, D., Richards, G., Simonyi, T., Poston, J., 2010. Evaluation of reaction mechanism of metal-oxide interactions in chemical-looping combustion. *Combust. Flame* 157 (11), 2198–2208.
- Son, S.R., Kim, S.D., 2006. Chemical-looping combustion with NiO and Fe₂O₃ in a thermobalance and circulating fluidized bed reactor with double loops. *Ind. Eng. Chem. Res.* 45 (8), 2689–2696.
- Yamasaki, A., 2003. An overview of CO₂ mitigation options in global warming emphasizing CO₂ sequestration options. *J. Chem. Eng. Japan* 36 (4), 361–375.
- Zafar, Q., Mattsson, T., Grewer, B., 2005. Integrated hydrogen and power production with CO₂ capture using chemical-looping reforming-oxide reactivity of particles of CuO, Mn₂O₃, NiO, and Fe₂O₃ using SiO₂ as a support. *Ind. Eng. Chem. Res.* 44 (10), 3485–3496.
- Zafar, Q., Mattsson, T., Grewer, B., 2006. Redox investigation of some oxides of transition-state metals Ni, Cu, Fe, and Mn supported on SiO₂ and MgAl₂O₄. *Energy Fuels* 20 (1), 34–44.